The 17th CEReS International Symposium

Proceedings

March 1, 2012
Keyaki Kaikan (Chiba University Convention Hall)
Chiba, Japan

Center for Environmental Remote Sensing (CEReS)
Chiba University

Cover Image:
TerraSAR-X DInSAR image of Tokyo Station, Japan and its surrounding area
TerraSAR-X data provided by PASCO Corp
Analyzed by Josaphat Microwave Remote Sensing Laboratory, CEReS, Chiba University

TABLE OF CONTENTS

ORAL SESSION

POSTER SESSION

DEVELOPMENT OF CIRCULARLY POLARIZED SYNTHETIC APERTURE RADAR ONBOARD UNMANNED AERIAL VEHICLE (CP-SAR UAV)

Josaphat Tetuko Sri Sumantyo

Center for Environmental Remote Sensing, Chiba University, 1-33, Yayoi-cho, Inage-ku, Chiba-shi 263-8522 Japan Tel.+81-43 2903840 Fax +81-43 2903857 (jtetukoss@faculty.chiba-u.jp)

ABSTRACT

Synthetic Aperture Radar (SAR) is well-known as a multi-purpose sensor that can be operated in all-weather and day-night time. The past SAR sensors for Earth observation mission are commonly operated in linear polarization that sensitive to Faraday rotation effect, especially in low frequency. This paper introduce our Circularly Polarized Synthetic Aperture Radar onboard Unmanned Aerial Vehicle (CP-SAR UAV) that is developed to retrieve the physical information of Earth surface for Earth diagnosis mission. The CP-SAR system is considered as small, light in weight and low power consumption system. The CP-SAR sensor is employing elliptical wave propagation and scattering phenomenon by radiating and receiving the elliptically polarized wave, including the special polarization as circular and linear polarizations. This paper introduces the CP-SAR and UAV system, including simulated full polarimetric CP-SAR images.

Index Terms— CP-SAR, Synthetic Aperture Radar, Unmanned Aerial Vehicle (UAV)

1. INTRODUCTION

Synthetic Aperture Radar (SAR) is well-known as a multi-purpose sensor that can be operated in all-weather and day-night time. Past missions of SAR sensors are operated in linear polarization (HH, VV, HV and VH) with high power, sensitive to Faraday rotation effect in low frequency, i.e. L band. In this research, we propose Circularly Polarized Synthetic Aperture Radar onboard microsatellite (CP-SAR μSAT) to retrieve the physical information and land deformation on Earth surface for Earth diagnosis mission [1]. Fig. 1 shows the illustration of CP-SAR μSAT that is being developed in Josaphat Microwave Remote Sensing Laboratory, Center for Environmental Remote Sensing, Chiba University, Japan. Table I shows the specification.

In this research, the CP-SAR sensor is employing the elliptical wave propagation and scattering phenomenon by radiating and receiving the elliptically polarized wave,
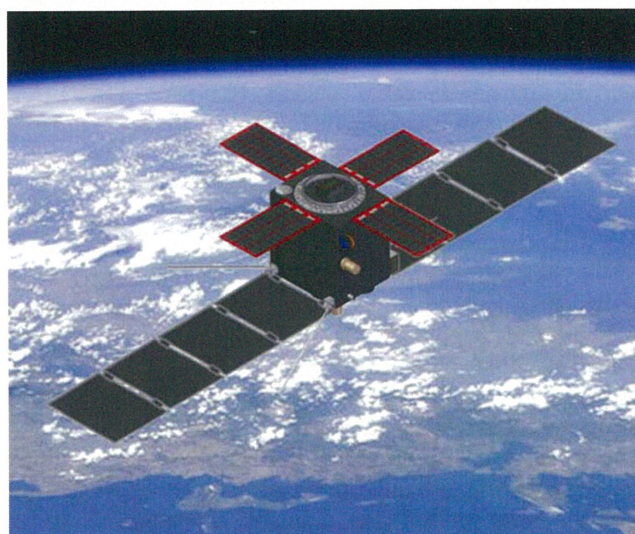
Fig.1. Illustration of Circularly Polarized Synthetic Aperture Radar onboard microsatellite (CP-SAR μSAT)

TABLE I. SPECIFICATION OF CP-SAR ONBOARD MICROSATELLITE

Altitude	500 ~ 700 km
Inclination angle	97.6 degrees
Frequency / wavelength	1.27 GHz (L Band) / 24 cm
Polarization	TX : RHCP+LHCP RX : RHCP+LHCP
Gain / Axial ratio	> 30 dBic / < 3 dB (main beam)
Off-nadir angle	29 degrees (center)
Swath width	50 km
Spatial resolution	30 m
Peak power	90 ~ 300 W (PRF 2000~2500 Hz, Duty 6% : average 5.6 W)
Bandwidth	Chirp pulse : 10 MHz
Platform size	1 m x 1 m x 1 m
Weight	200 kg
Antenna size	Elevation 1.0 m x Azimuth 4.0 m x 2 panels for RHCP and LHCP

including the specific polarization as circular and linear polarizations. CP-SAR is as active sensor that could transmit and receive the L band chirp pulses with PRF 2,000 to 2,500 Hz. The sensor is designed as a low cost, light, low power or safe energy, low profile configuration to transmit and receive left-handed circular polarization (LHCP) and right-handed circular polarization (RHCP). Then these circularly polarized waves are employed to generate the axial ratio image (ARI), ellipticity, tilt angle etc. This sensor is considered not depending to the platform posture, and it is available to reduce the effect of Faraday rotation during propagating in Ionosphere. Therefore, the high precision and low noise image is expected to be obtained by the CP-SAR. For this purpose, we are also developing the CP-SAR onboard unmanned aerial vehicle (CP-SAR UAV) for ground testing of this sensor.

2. CP-SAR MISSION

The main mission of our CP-SAR (see Fig. 2) is to hold the basic research on elliptically polarized scattering and its application developments. In the basic research, we will investigate the elliptical (including circular and linear polarizations) scattering wave from the Earth surface, circularly polarized interferometric technique (CP-InSAR), generation of axial ratio image (ARI), ellipticity and tilted angle images etc. We hold the analysis and experiment of circularly polarized wave scattering on vegetation, snow, ice, soil, rock, sand, grass etc to investigate the elliptical scattering wave. In experiment of CP-InSAR, we will hold some experiments to compare the InSAR technique by using circular and linear polarizations. This technique will be implemented to extract the tree trunk height, DEM etc by using the elliptical polarization. The axial ratio image (ARI), ellipticity, tilted angle, polarization and other images will be extracted by using the received RHCP and LHCP wave. The principle of CP-SAR UAV is shown in see Fig.3. This figure shows CP-SAR sensor transmits only one polarization, RHCP or LCHP, then we receive RHCP and LHCP scattering waves simultaneously. Then this image is employed to investigate the relationship between the ARI and physical characteristics of vegetation, soils, snow etc. The image of tilted angle as the response of Earth surface also will be extracted to mapping the physical information of the surface, i.e. geological matters, contour, tree trunk structure and its characteristics, snow-ice classification, vegetation characteristics etc.

In application development, CP-SAR sensor will be implemented for land cover mapping, disaster monitoring, Cryosphere monitoring, oceanographic monitoring etc. Especially, land cover mapping will classify the forest and non-forest area, estimation of tree trunk height, mangrove area monitoring, Arctic and Antarctic environment monitoring etc. In disaster monitoring, CP-SAR sensor will

Fig.2. Josaphat Laboratory Experimental CP-SAR onboard Unmanned Aerial Vehicle (CP-SAR UAV : JX-1)
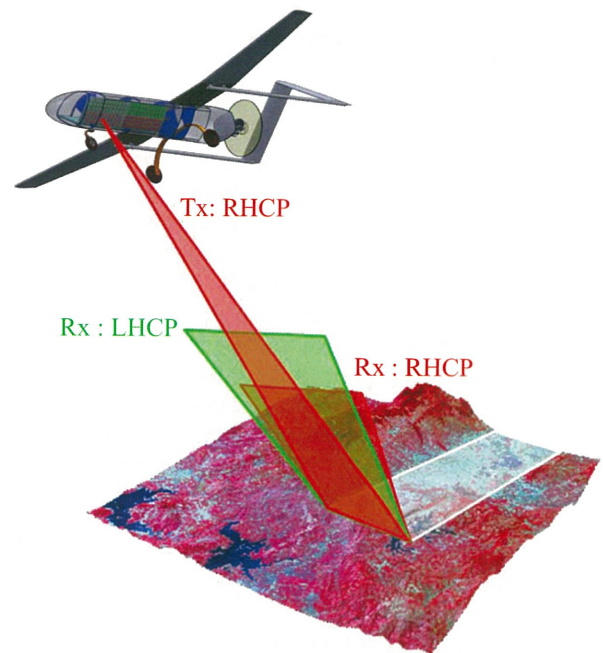
Fig. 3. Principle of CP-SAR sensor onboard UAV
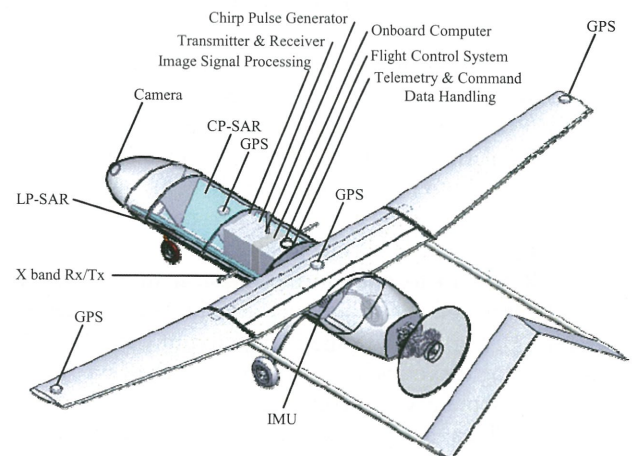
Fig. 4. CP-SAR UAV Sub-system

be employed for experiment of CP Differential InSAR in earthquake area, volcano activity etc.

TABLE II. CP-SAR UAV SPECIFICATION

Parameter	Value
Altitude	1 to 4 km
Frequency range	1270 MHz ± 150 MHz
Baseband range	DC to 150 MHz
Pulse transmission output power	50 W, Pulse width 10 μs (max), Duty circle 2% (max)
Polarization	TX & RX : RHCP+LHCP
Transmission system gain	+ 47 dB (min)
Receiver system gain	+ 60 dB (min)
Gain flatness	± 1.5 dB (max)
Receiver noise ratio	3.5 dB (max) @+25°C
Modulator	(RX and TX) QPSK
Output higher harmonic wave	-30 dBc (max)
Output spurious	-60 dBc (max)
Transmission system gain tuning function	1/2/3/8/16 dB (0 to -31 dB)
Receiver system gain tuning function	1/2/3/8/16 dB x 2 (0 to -62 dB)
Impedance	50 Ω
Transmission system output VSWR	1.5 : 1 (typ.)
Receiver system input VSWR	1.5 : 1 (typ)
Transmission system antenna switching speed	1μs (typ.) / 2 μs (max)
Receiver system antenna switching speed	1μs (typ.) / 2 μs (max)
Transmission system On/Off speed	100 ns (max)
Receiver system On/Off speed	100 ns (max)
Power voltage	DC +28 V (DC +25 to + 35 V switchable)
Current consumption	5A (max)
Temperature	+0°C to 45°C
Saving temperature	-20°C to 80°C
RF connector	SMA-Female
Power connector	N/MS3102A10SL-3P
Control connector	D-Sub-37P
Weight	10 kg (max)
Size	W250mm x H100mm x D300mm
Pulse Length	4.33 up to 47.63 μs
Off Nadir	30° up to 60°
Resolution	Up to 1 m
Swath Width	1 km
Antenna Size	0.75 x 0.2 m (4 panels)
Axial Ratio	≤3 dB
Antenna Gain	14.32 dBic
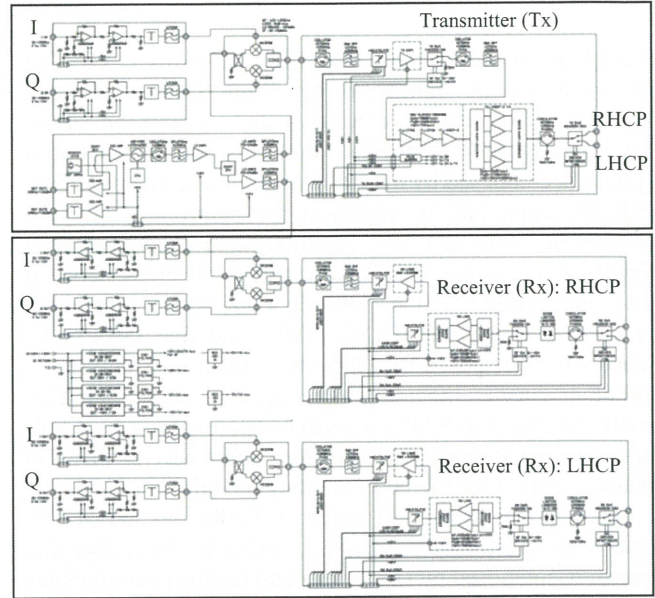
Fig. 5. Block diagram of CP-SAR system
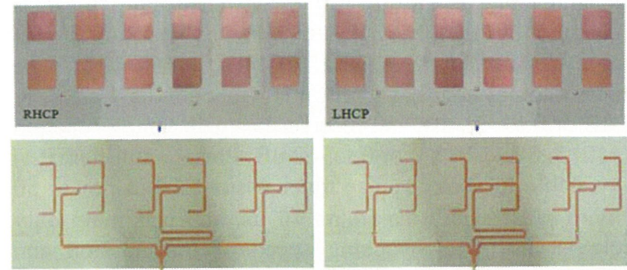
Fig.6. Microstrip antenna for Tx and Rx of CP-SAR [2]
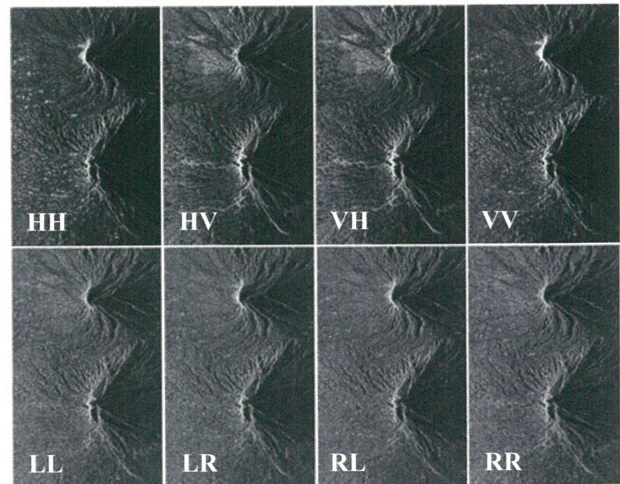
Fig.7. Images of linear and circular polarization

3. CP-SAR SYSTEM

Fig. 4 shows sub-systems installed in CP-SAR UAV. The system is mainly composed by Flight Control System, Onboard Computer, Telemetry and Command Data Handling, Attitude Controller, and Sensors. Flight Control System is composed by manual and automatic flight module. Onboard computer is employed for controlling all sub-systems in CP-SAR UAV. Telemetry and Command Data Handling subsystems use X-band communications between UAV and ground station. Attitude Controller is composed by Inertial Measurement Unit (IMU) and four GPS units. Sensors are composed by CP-SAR as main mission sensor, and other sensors, including hyper spectral camera and five small cameras. CP-SAR sub-system is composed by Chirp pulse generator module, Transmitter and Receiver (Tx-Rx) module, and Image Signal Processing module.

Fig. 5 shows the circuit block of Tx-Rx module of CP-SAR with specification shown in Table II. Basically, this system is composed by transmitter and receiver sub modules. The input of transmitter is In-phase (I) and Quadrature (Q) signal of chirp pulse generated by pulse generator with baseband range is DC to 150 MHz. Then chirp pulse is modulated by frequency 1,270 MHz, where our Tx-Rx system has frequency range 1270 MHz ± 150 MHz. The transmission system has gain tuning function as 1, 2, 3, 8, 16 dB or 0 to -31 dB, and receiver has gain tuning function as 1, 2, 3, 8 and 16 x 2 or 0 to -62 dB. Power amplifier (PA) is available to control pulse transmission output power 50 W with pulse width maximum 10 μs, and maximum duty circle is 2%. The switching speed of transmission and receiver system antennas (RHCP and LHCP) is typically 1 μs and maximum 2 μs. The antenna is composed by two sets of CP microstrip array antenna (LHCP and RHCP panels) as shown in Fig. 6, totally 4 panels to realize full polarimetric CP-SAR sensor. Size of Tx and Rx unit is W250 mm x H100 mm x D300 mm as one module in our CP-SAR system as shown in Fig. 4.

4. CP-SAR ONBOARD UNMANNED AERIAL VEHICLE (CP-SAR UAV) SYSTEM

In this research, the CP-SAR onboard unmanned aerial vehicle (CP-SAR UAV) as shown in Fig. 2 is developed for ground testing of CP-SAR before installing this sensor on our microsatellite. The platform called Josaphat Laboratory Experimental CP-SAR UAV (JX-1) has 25 kg of payload availability for various microwave sensors (CP-SAR, GPS-SAR, and GPS-Radio Occultation) and optic sensors, i.e. hyper spectral camera. The operation altitude is 1,000 m to 4,000 m. As shown in Table II, the specification of CP-SAR sensor for UAV is center frequency 1,270 MHz, ground resolution up to 1 m, pulse length could be tuned from 4.5 to 48 μs, pulse bandwidth 150 MHz, off nadir angle 30° to 60°, swath width 1 km, antenna size for 4 panels of CP-SAR

1.5 m x 0.4 m, antenna radiation efficiency >80%, PRF 1,000 Hz, and peak power 8.65 W (1 km) to 95 W (4 km). We plan to hold ground experiment with altitude less than 2 km with pulse transmission output power 50 W. The CP-SAR has receiver antenna composed by LHCP and RHCP antenna. The data retrieved by LHCP and RHCP antenna is employed to investigate the characteristics of elliptical polarization, including circular and linear polarizations.

We have simulated circularly polarized waves with full polarization (LL, LR, RL and RR) as shown in Fig. 7 by using ALOS PALSAR polarimetric mode images. Where L and R is left handed circular polarization and right handed circular polarization, respectively. LR means LHCP transmission and RHCP receiving. This image shows that circularly polarized images show more clear than linear polarized image, and less foreshortening and shadowing effects. It is assumed that the geometrical effect of object (volcano) is strongly affecting to linear polarized images, but less to circularly polarized waves. In the near future, further investigation of characteristics of circular polarization will be done by using our CP-SAR UAV and microsatellite. CP image will be used to retrieve the physical information of Earth surface, i.e. soil moisture, biomass, Cryosphere, agriculture, ocean dynamics, land deformation, disaster monitoring, DEM etc. In the UAV, we also install the linearly polarized SAR (LP-SAR) in same frequency. The LP-SAR data will be compared with CP-SAR data, and employ for some applications.

5. SUMMARY

In this paper, we introduce the circularly polarized Synthetic aperture radar onboard Unmanned Aerial Vehicle (CP-SAR UAV) for ground experiment to investigate performance of CP-SAR sensor. The CP-SAR is designed as the small, light in weight and low power consumption system. The CP-SAR sensor is developed to radiate and receive elliptically polarized wave, including circularly and linearly polarized waves. In the near future, this sensor will be installed in our microsatellite that will be applicable for land cover mapping, disaster monitoring, snow cover and oceanography monitorig etc.

REFERENCES

[1] Josaphat Tetuko Sri Sumantyo, "Microwave Remote Sensing Research and Education at Center for Environmental Remote Sensing, Chiba University," IEEE Geoscience and Remote Sensing Society (GRSS) Newsletter, Issue #159, pp. 32-38, June 2011.

[2] Yohandri, V. Wissan, I. Firmansyah, P. Rizki Akbar, J.T. Sri Sumantyo, and H. Kuze, "Development of Circularly Polarized Array Antenna for Synthetic Aperture Radar Sensor Installed on UAV," Progress in Electromagnetics Research C, Vol. 19, pp. 119-133, January 2011.

Activities of AIT for Sustainable Capacity Building in Asia on Space Based Technologies

Lal Samarakoon

Director, Geoinformatics center
Asian Institute of Technology, Thailand

Information
- About 2000 students from 46 countries
- 14,000 alumni from 74 countries
- 22,000 short-term trainees from 71 countries
- 100 faculty from 26 countries
- 30 Board of Trustees members from 25 countries

Structure
- School of Engineering & Technology
- School of Environmental Resources and Development
- School of Management

Establish in 1959 as a Post Graduate School
Catering for higher education in Asia

AIT Academic Structure
Highlight GIS related Fields

School of Engineering and Technology		School of Environment Resources and Development	School of Management	AIT Extension (Non-degree training, consultancy and services)
Computer Science	Construction, Engineering and Infrastructure Management	Agricultural Systems and Engineering	International Business	Agriculture, Resources and Rural Development
Design and Manufacturing Engineering		Aquaculture and Aquatic Resources Management	International Public Management	Business Management
Industrial Engineering and Management	Geotechnical and Geoenvironmental Engineering	Energy		
		Environmental Engineering and Management	Management of Technology	Development Management
Information Management	Structural Engineering	Food Engineering and Bioprocess Technology		
Remote Sensing and Geographic Information Systems	Transportation Engineering	Gender and Development Studies	Service Marketing and Technology	Education and Training Development
		Natural Resources Management	Executive MBA EMBA Bangkok EMBA Vietnam EMBA-HRM	Environment, Infrastructure and Urban Development
Telecommunications	Water Engineering and Management	Pulp and Paper Technology		
Information and Communications Technologies	Disaster Preparedness Mitigation & Management (DPMM)	Regional and Rural Development Planning		Information and Communications Technology
Mechatronics		Urban Environmental Management		
Microelectronics	GIC			

Sustainable approach for Capacity Development

Risk, Hazard, Suitability, Adaptability, Allocation, Relocation ....
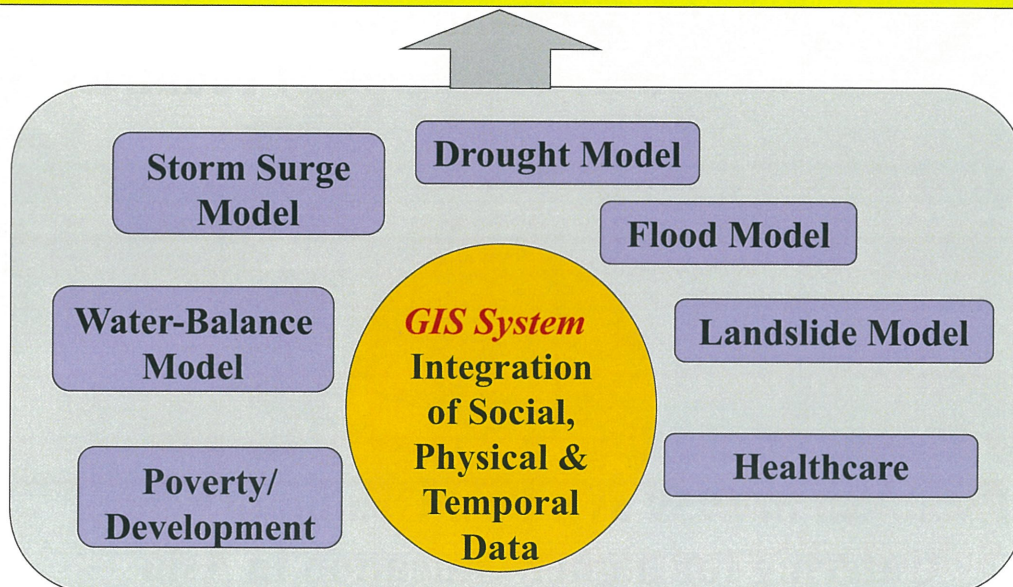
- Storm Surge Model
- Drought Model
- Flood Model
- Water-Balance Model
- **GIS System** Integration of Social, Physical & Temporal Data
- Landslide Model
- Poverty/ Development
- Healthcare

**Geoinformatics Center
Established in 1999
(Self Funded)**

Staff Profile
5 PhD
5 MSc
3 BSc

www.geoinfo.ait.ac.th

Modes of Technology Transfer of AIT

1. **Higher Education (Graduate & Undergraduate)**
   - ✓ **Long-term planning**
   - ✓ **High and indirect investment**
   - ✓ **Comprehensive and robust**
2. **Diploma & Certificate (3-6 Months)**
   - ✓ **Target oriented**
   - ✓ **Direct investment**
3. **Short-term target oriented training (1-4 weeks)**
   - ✓ **Targeted audience**
   - ✓ **Application oriented & Readiness in implementation**
   - ✓ **Conducted locally or at AIT**
4. **Seminars & Workshops (1-2 Days)**
   - ✓ **Indirect investment**
   - ✓ **Awareness raising**
   - ✓ **Address larger audience, senior officials**

Main Services Of GIC/AIT

➢ **Training Programs**

➢ **Receiving & Distributing MODIS/NOAA satellite data**

➢ **Consulting Works**

➢ **Rapid mapping support for Sentinel Asia & IDC**

➢ **Conduct Workshops and Conferences**

➢ **Applied Research (Disaster, poverty, aquatic ..)**

➢ **Publications: journal, reports, manuals, results**

➢ **Collaboration (exchange programs, Students, experts ..)**

Ongoing and Recent Activities

✓ *Completed Mini-Project Training in 8 countries in February 2012 (JAXA)*

✓ *Completed use of RS/GIS in agriculture for Ministry of Agriculture, Indonesia, December 2011 (Government of Indonesia)*

✓ *Completed training program for technicians from 8 African countries on remote sensing application on forest fire management, February 2012 (JICA)*

✓ *Mini-Project Training for 10 countries concluded in February 2010 and start of 8 new projects for 2011 (JAXA)*

✓ *Phase II of the Poverty Mapping for ASEAN was started on March 2, 2009. Poverty Mapping Workshop in June 11-12 (ASEAN Foundation)*

✓ *One month Training on MODIS data handling and application for Remote Sensing Center of Mongolia, May 2009 (Mongolian RS Center)*

✓ *Extreme Flood Event Forecasting – 5 countries in Asia: (2010, United Nations University, Tokyo)*

Ongoing and Recent Activities

✓ *Asian Node in Second Administrative Level Boundary data initiative of WHO handling 36 countries, on going*

✓ *Capacity Building Project on Space Data for DRR for ADRC in ASEAN countries (2009-2011, Asian Disaster Reduction Center).*

✓ *Technical support for Space Application for Environment (SAFE) of JAXA*

✓ *Forest Mapping and Database Development for Dept. of Forestry Lao PDR, 2010 - 2011 (JICA)*

✓ *Professional Development Training Program on "Project Management, PPP and Good Governance" for Manipur State Officials (09-13 May 2011)*

✓ *Professional Development Training cum study visit on "Application of GIS and RS for Ground Water Salinity and NRM" for Bangladeshi Officials (11-15 July 2011)*

Terra/Aqua MODIS Receiving, Archiving and Processing Systems in Geoinformatics Center (GIC), AIT

- Operational since May 2001 – present
- More than 20,000 Scenes for Terra/Aqua(day and night)
- Covering 19 countries (South and Southeast Asia)
- Products include:
  Land, Ocean, Atmosphere and Cryosphere disciplines
- Most products are Standard NASA Products
- Mostly use NASA ATBD (Algorithm Theoretical Basic Documents) for data processing
- Operating System : Linux (only!)

Concept of Processing System:
- Automatic
- Near Real-time
- Daily (6-8 image scenes/day)
- Online Product Access for 24 hours
- Easy-to-use Data format Products

Receiving System
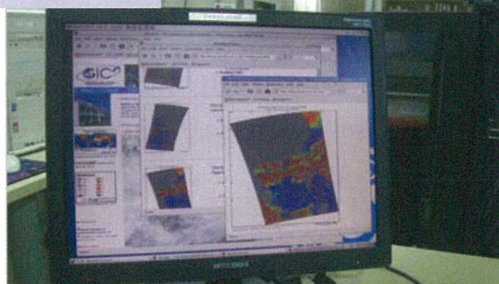
Automatic Near Real-Time Processing Systems
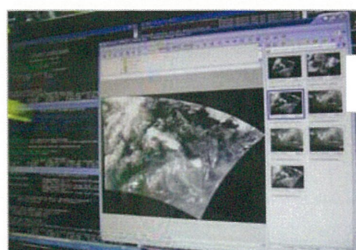
Backup Storage:
- External USB Hard disks (2.0 TB)
- DLT Tapes (40 Gigabytes)

GIC/AIT Near Real time Automatic MODIS
Receiving, Processing, Archiving, Transferring and Distributing Systems
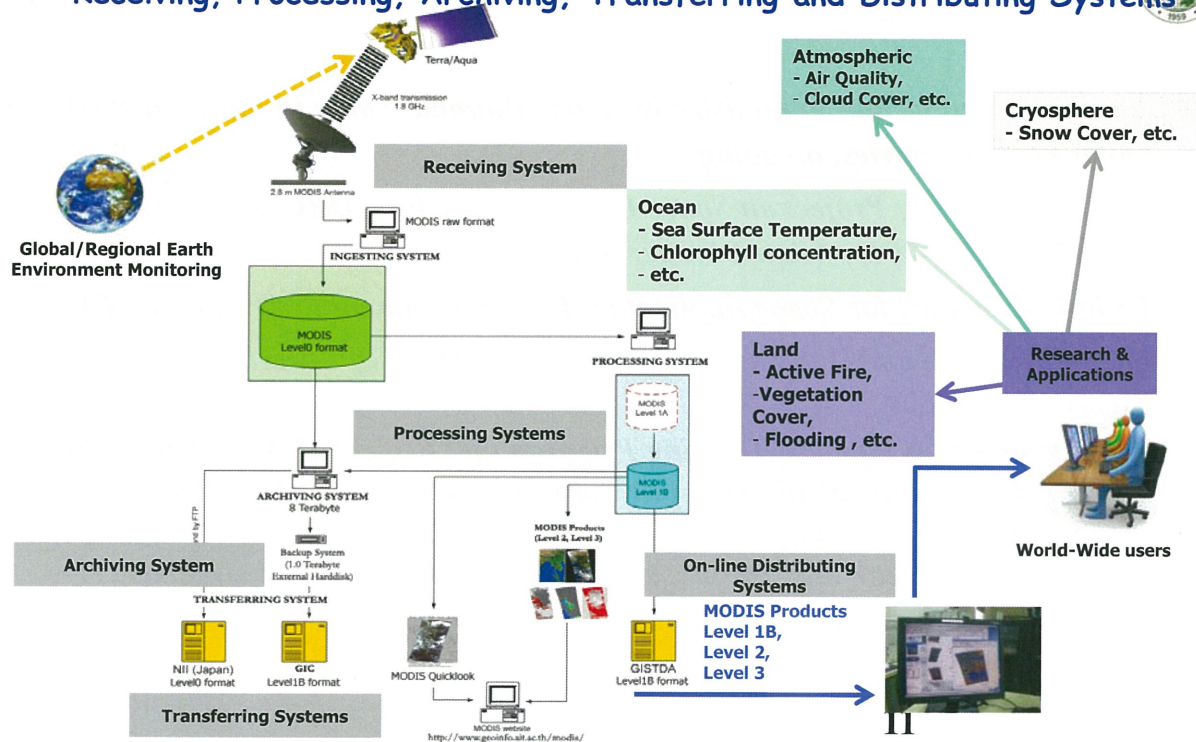
---

NTRIP

- "Networked Transport of RTCM via Internet Protocol" (NTRIP) stands for an application-level protocol streaming Global Navigation Satellite System (GNSS) data over the Internet.

  - Eliminate need of Radio Unit for RTK.
  - Coverage is not limited. (compared to radio unit)
  - Easy to use.
  - VRS(Virtual Reference Station) can be used to calculate precise correction.
  - Number of uses per Base station is not limited.

NTRIP setup at GIC/AIT
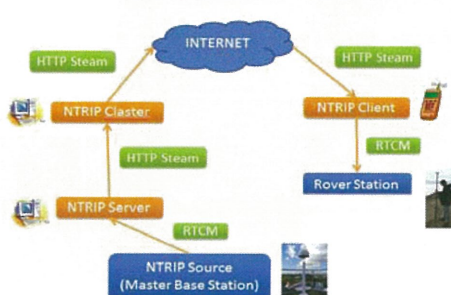
NTRIP flow diagram
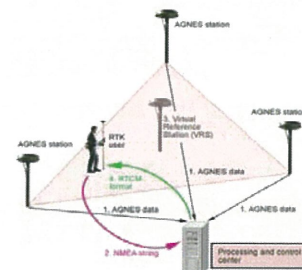
VRS setup

QZSS

- The Quasi-Zenith Satellite System (QZSS), is a proposed three-satellite regional time transfer system and Satellite Based Augmentation System for the Global Positioning System,

- QZSS will enhance GPS services in two ways
    - Availability enhancement
    - Performance enhancement
- Transmitting Signals
    - L1C/A signal, L1C signal, L2C signal and L5 sign
    - L1-SAIF and LEX ,performance enhancement signals(DGPS data)

- Applications
    - Precise vehicle navigation
    - Automated farming
    - Precise Point Positioning
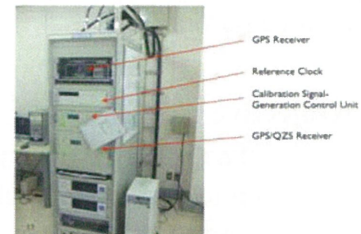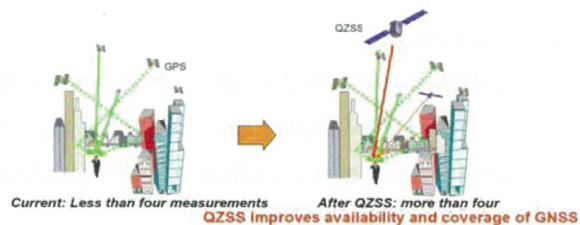
QZSS Monitoring Station at GIC/AIT

Current: Less than four measurements

After QZSS: more than four

QZSS improves availability and coverage of GNSS

Growing NAVIS

The project is coordinated by
Instuto Superiore Mario Boella, Italy.

Targets:

1. Research in Asia on ionospheric condition, algorithm development, Algorithm enhancement

2. Multi GNSS signal and receivers, signal processing

3. Wireless communication

4. Training, seminars and awareness raising programs

Partners: Italy, Spain, France, Vietnam, Thailand, Malaysia, Australia

JAXA Multi-GNSS Joint Experiment

Effectiveness of QZSS-LEX signal compared to DGPS and IGS PPP data for Thailand

• The project will be done as static and RTK modes. Study area will cover urban and semi urban environments.

• Objective
  – To Quantitatively measure the improvement in positioning due to precise ephemeris and clock from QZSS-LEX, compared to DGPS and PPP calculation from IGS data.
  – Evaluation of GPS positioning improvement techniques.

• Expected results
  – QZSS is expected to give ±10cm positioning accuracy .
  – Comparably high accuracy than IGS real time PPP data.
  – Quantitative evaluation of GPS positioning improve techniques.

Mini-Project Training
(Sponsored by Japan Aerospace Exploration Agency)

Application oriented & Locally Selected projects conducted at GIC-AIT since 2004.

Procedure:

a. Applications for New Mini-Projects are called in December each year

b. Selection is done in March (by GIC and JAXA)

c. Initial training/procedure development in July-August (1 month in AIT)

d. Fieldwork is carried out during Sep-December

e. Analysis and output generation is done in Jan-Feb (1 month in AIT)

More Information: www.geoinfo.ait.ac.th/training/miniproject.php

Mini-Projects - conducted in 2009-2010

✓ *Training and capacity building through* <u>*real-world projects*</u> *such as flood, landslides, climate change, mapping etc. (individual)*

✓ *Involve data/service provider agencies and services/products user agencies, (Institutional/Systematic)*

✓ *Calibration/validation through* <u>*field observations*</u>

1. *Landslide related Risk Analysis – Indonesia (LAPAN)*
2. *Land use mapping & Monitoring – Cambodia (Ministry of Land)*
3. *Cyclone Risk Mapping – Bangladesh (LGED)*
4. *Drought Analysis – Mongolia (Remote Sensing Center)*
5. *Landslide Mapping – Nepal (Survey Dept.)*
6. *Wildlife Mapping & Monitoring – Pakistan(WWF)*
7. *Watershed Management – Thailand (National Parks and Forest)*
8. *Mangrove Monitoring– Thailand (Chulalongkorn University)*
9. *Flood Risk Mapping – Sri Lanka (DMC, Survey Dept)*
10. *Flood Risk Mapping – Vietnam (STI, MONRE)*
11. *Flood Risk Mapping – Lao PDR (DMC and Hydrology Dept)*

Mini-Projects - conducted in 2008-09

1. *Landslide relted Risk Analysis – Bhutan (Geological Survey)*
2. *Land use mapping/flood – Cambodia (Ministry of Land)*
3. *Flood Mitigation – Bangladesh (SPARSSO/LGED/FFWC)*
4. *Drought Analysis and Global Warming – Philippines (PhilRice)*
5. *Drought Analysis – Mongolia (Remote Sensing Center)*
6. *Mangrove/coastal Monitoring – Malaysia (Fishery Dept.)*
7. *Risk due to Sea Level Rise – Sri Lanka (CCD/Survey Dept.)*
8. *Flood Risk mapping – Thailand (Irrigation Dept)*
9. *Forest Fire Risk Analysis – Indonesia (LAPAN)*
10. *Flood mitigation – Vietnam (STI, MONRE)*
11. *Flood Mitigation – Lao PDR (DMC and Hydrology Dept)*

Capacity building on the use of Space based Technologies in ASEAN

Project:
ADRC-ASEAN Project on Satellite Data for Disaster Risk Reduction under Japan-ASEAN Integrated Fund

CYCLONE

DROUGHT

TSUNAMI

Ministry of Science & Technology, Myanmar

National Geography Department, Cambodia

WREA, Laos

LAPAN, Indonesia

ASEAN COUNTRIES

PHIVOLCS, Philippines

Remote Sensing Center, MONRE, Vietnam

GISTDA, Thailand

Survey Department, Brunei Darussalam

FLOODS

Project Coordination :

Dr. Lal Samarakoon
Director, GIC/AIT
PO Box 4, Klong Luang, Pathumthani,
Thailand 12120
Tel: +66-2-524-6487, Fax: +66-2-524-6147
E-mail: lal@ait.ac.th;
www.geoinfo.ait.ac.th

Mr. Naoki Yamaguchi
Senior Researcher of ADRC
Hitomiraikan 5F, 1-5-2
Wakinohamakaigan-dori
Chuo-Ku, Kobe 651-0073, Japan
E-mail: ny-yamaguchi@adrc.asia;
www.adrc.asia

Mr. Emir Rio Krishna
Technical Officer of S&T Division
ASEAN Socio-Cultural Community (ASCC)
Department
ASEAN Secretariat
A 70A, Jalan Sisingamangaraja, Jakarta 12110,
Indonesia
Tel: +6221 - 726 2991, 724 3372
Tel: +6221 - 739 8234, 724 3504, 720 0848
E-mail: emir@asean.org

Web Site : http://www.geoinfo.ait.ac.th/adrc/

Space Applications for Environment (SAFE)
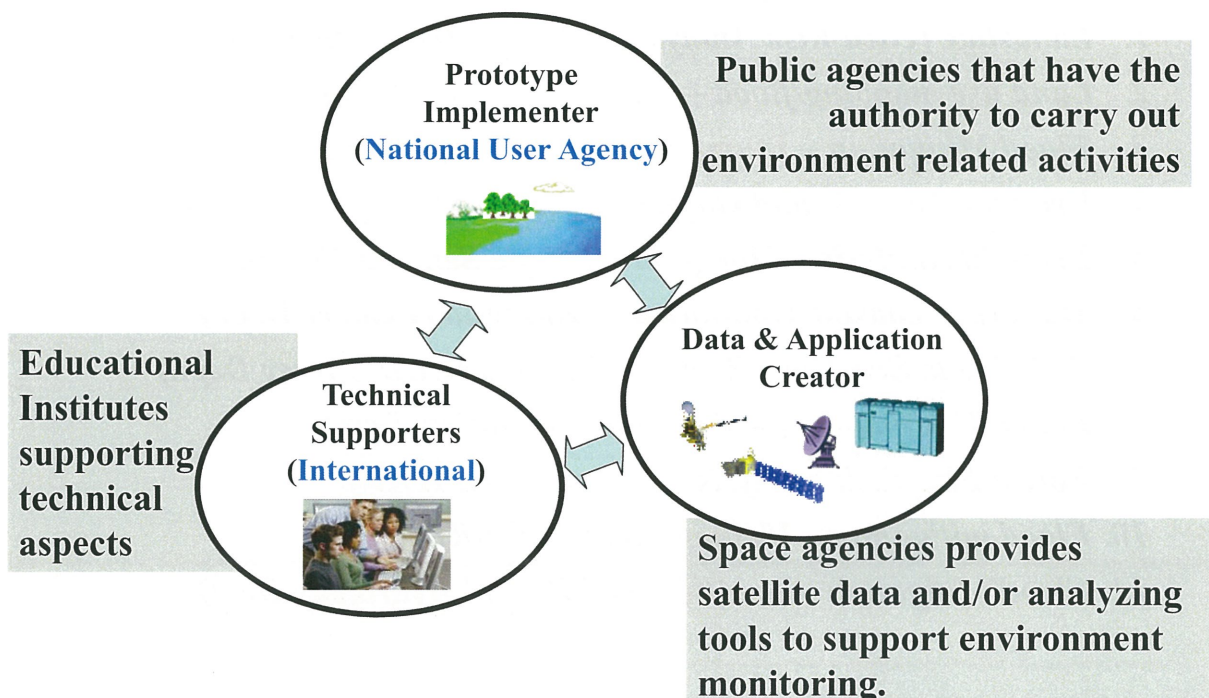
Prototype Implementer (National User Agency)

Public agencies that have the authority to carry out environment related activities

Educational Institutes supporting technical aspects

Technical Supporters (International)

Data & Application Creator

Space agencies provides satellite data and/or analyzing tools to support environment monitoring.

SAFE Prototyping Status

Country	Theme	Technical Collaborator
VIETNAM	Forest monitoring	IIS/University of Tokyo
CAMBODIA	Water Cycle and Agricultural Activities	University of Tokyo
LAO PDR	Forest monitoring and management	IIS/University of Tokyo
INDONESIA	Potential Drought Monitoring	IIS/University of Tokyo
SRI LANKA	Risk of Sea Level Rise on Coastal Zone	University of Tokyo
PAKISTAN	Monitoring Water Cycle Variations & Assessing Climate Change Impacts	IIS/University of Tokyo
SRI LANKA	Modeling ocean frontal zones using high resolution satellite and float data to locate tune fish aggregations	Fishery Research Agency, Japan
Thailand	Use of satellite data derived ocean color and SST information for Thailand Fishery	Kyoto University

Case Study: Flood Risk Mapping
Irrigation Dept and Survey Dept of Sri Lanka
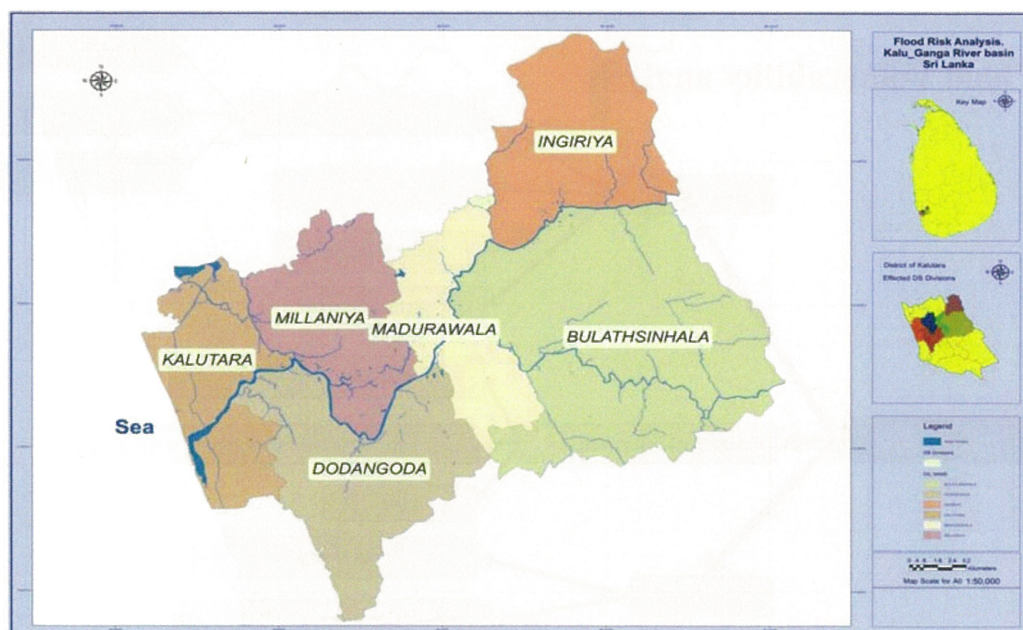
Flood Risk Mapping – Summary
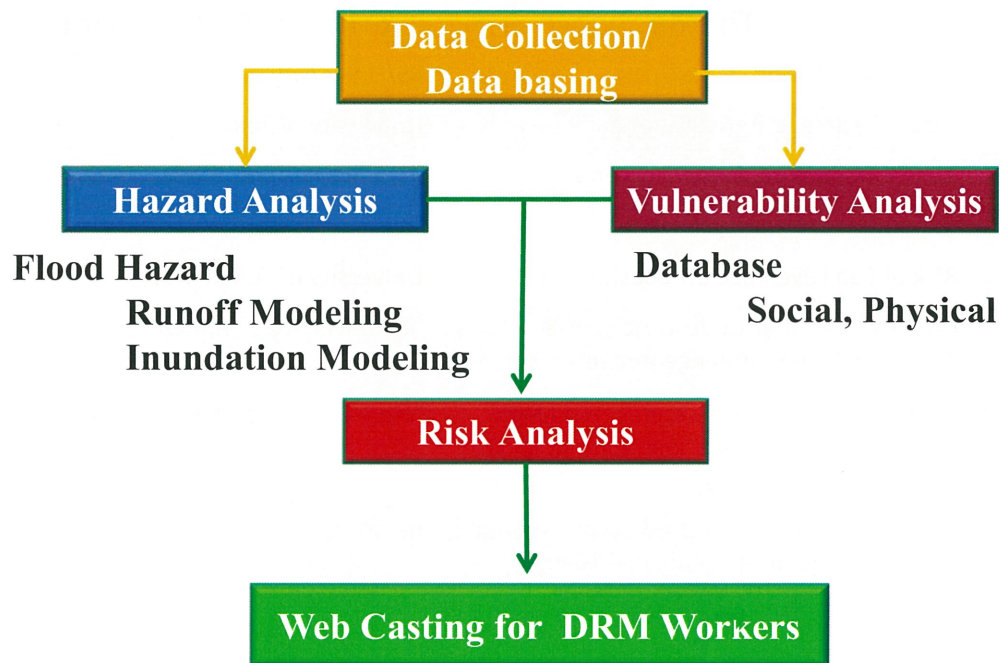

```
          Data Collection/
           Data basing
         ┌───────┴───────┐
         ↓               ↓
  Hazard Analysis   Vulnerability Analysis
```

Flood Hazard   **Database**
  Runoff Modeling   **Social, Physical**
  Inundation Modeling

```
              Risk Analysis
                   ↓
       Web Casting for DRM Workers
```

Methodology

Flood Vulnerability Analysis based on Household Survey

Household Vulnerability Analysis
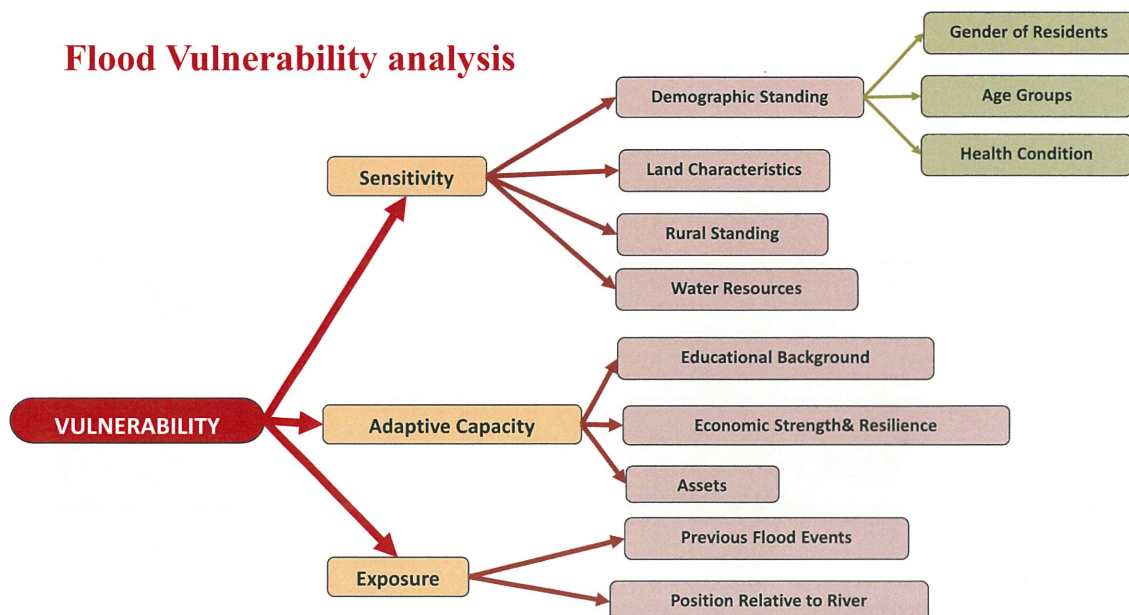
Flood Vulnerability analysis

- VULNERABILITY
  - Sensitivity
    - Demographic Standing
      - Gender of Residents
      - Age Groups
      - Health Condition
    - Land Characteristics
    - Rural Standing
    - Water Resources
  - Adaptive Capacity
    - Educational Background
    - Economic Strength& Resilience
    - Assets
  - Exposure
    - Previous Flood Events
    - Position Relative to River

Flood Hazard Maps from HEC-RAS
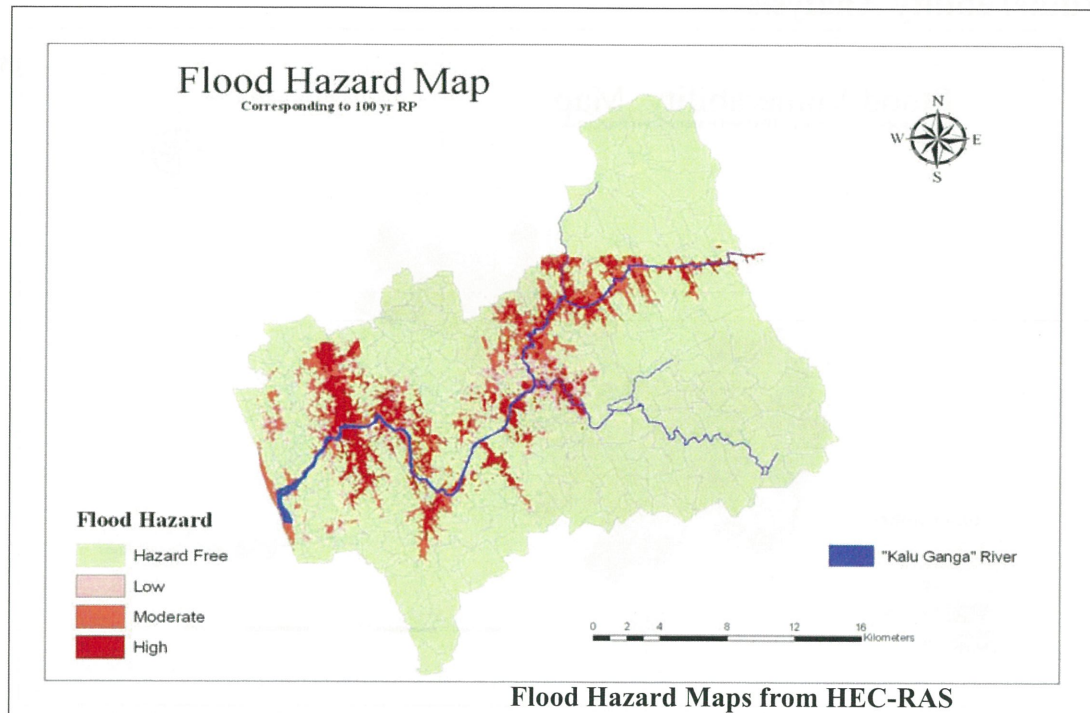
Results

b. Hazard Analysis

Verification of model result by satellite data

Model
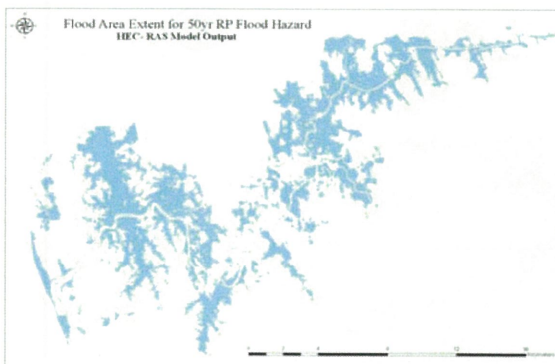
PALSAR
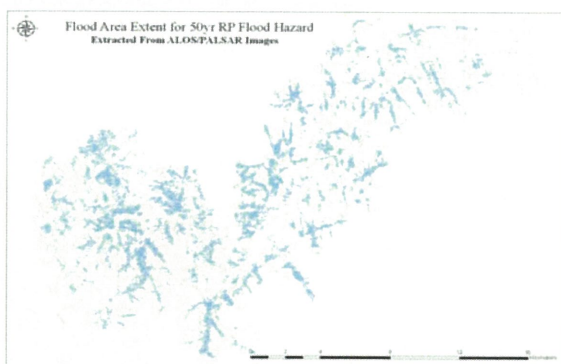
Comparison of the Flood extent derived from HEC-RAS model and Satellite image
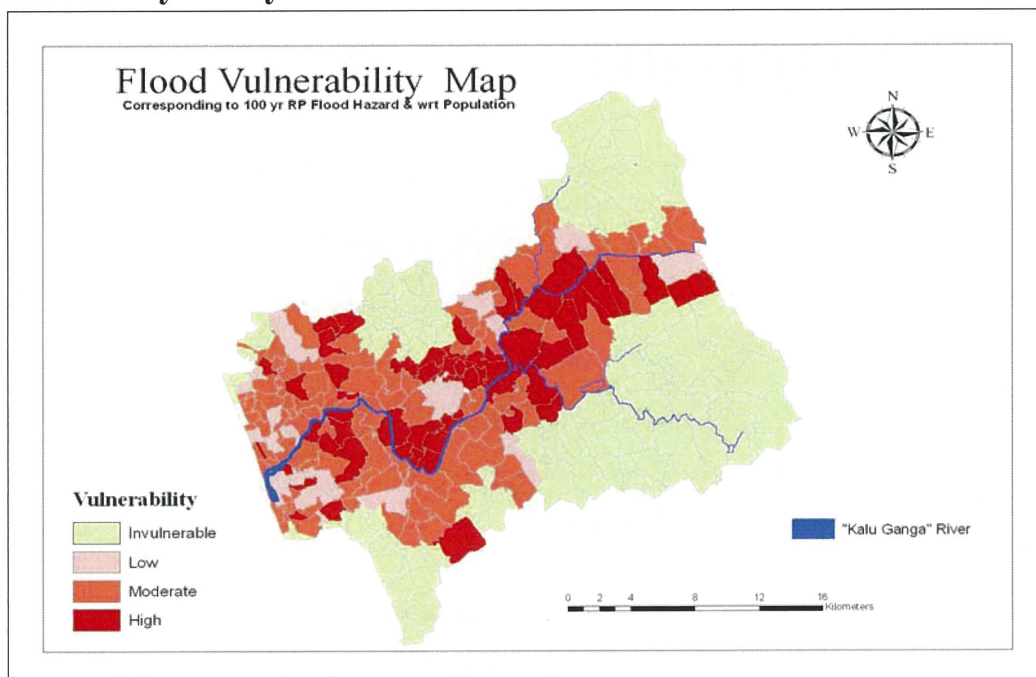
Results

Vulnerability Analysis

Flood Vulnerability Map
Corresponding to 100 yr RP Flood Hazard & wrt Population

Vulnerability
- Invulnerable
- Low
- Moderate
- High

"Kalu Ganga" River

Analysis

Results

Risk Analysis

Buildings (Physical) Risk Analysis
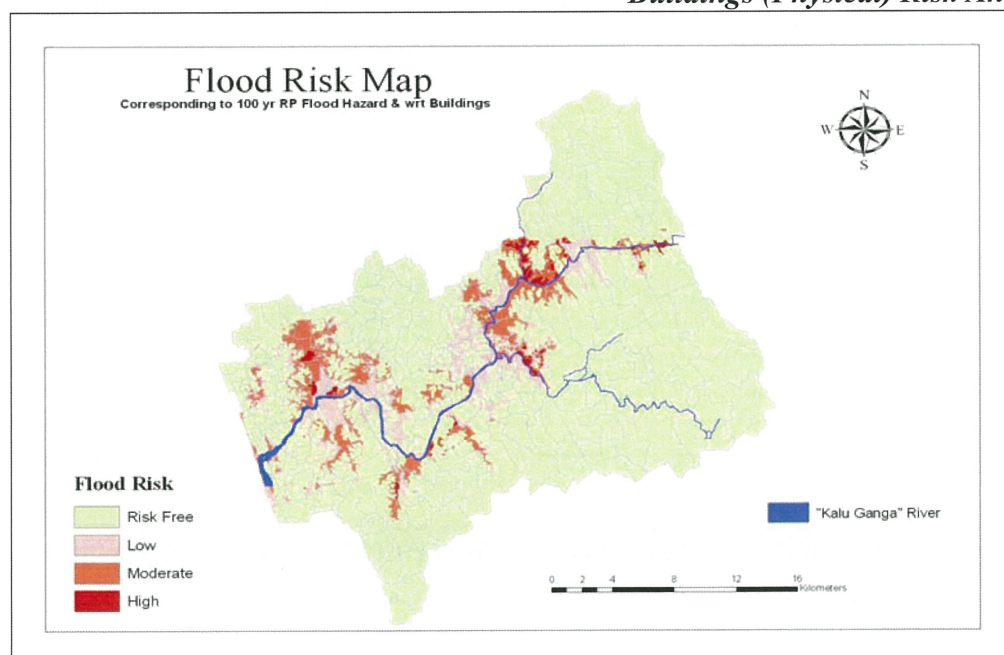
Flood Risk Map
Corresponding to 100 yr RP Flood Hazard & wrt Buildings

Flood Risk
- Risk Free
- Low
- Moderate
- High

"Kalu Ganga" River

Information Sharing

Mini-Project 2009-2010

Mini-Project 2008-2009

Mini-Project 2007-2008

Mini-Project 2006-2007

Mini Projects
2007 - 2008

Introduction

JAXA

Presentations

Sponsored by
Japan Aerospace Exploration Agency (JAXA)

Conducted by
Geoinformatics Center
Asian Institute of Technology

Sample

Collaboration under Sentinel Asia
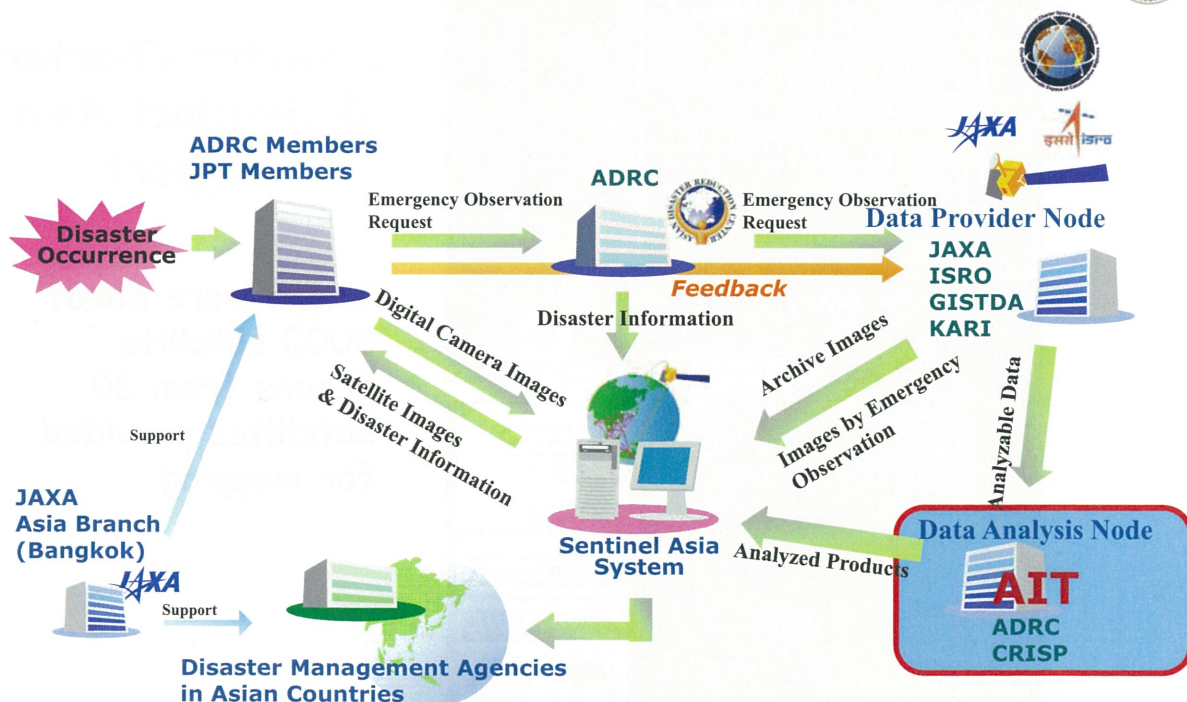
ADRC Members
JPT Members

Disaster
Occurrence

Emergency Observation
Request

ADRC

Emergency Observation
Request

Data Provider Node

JAXA
ISRO
GISTDA
KARI

Feedback

Disaster Information

Digital Camera Images

Satellite Images
& Disaster Information

Archive Images

Images by Emergency
Observation

Analyzable Data

Support

JAXA
Asia Branch
(Bangkok)

Support

Sentinel Asia
System

Analyzed Products

Data Analysis Node

AIT

ADRC
CRISP

Disaster Management Agencies
in Asian Countries
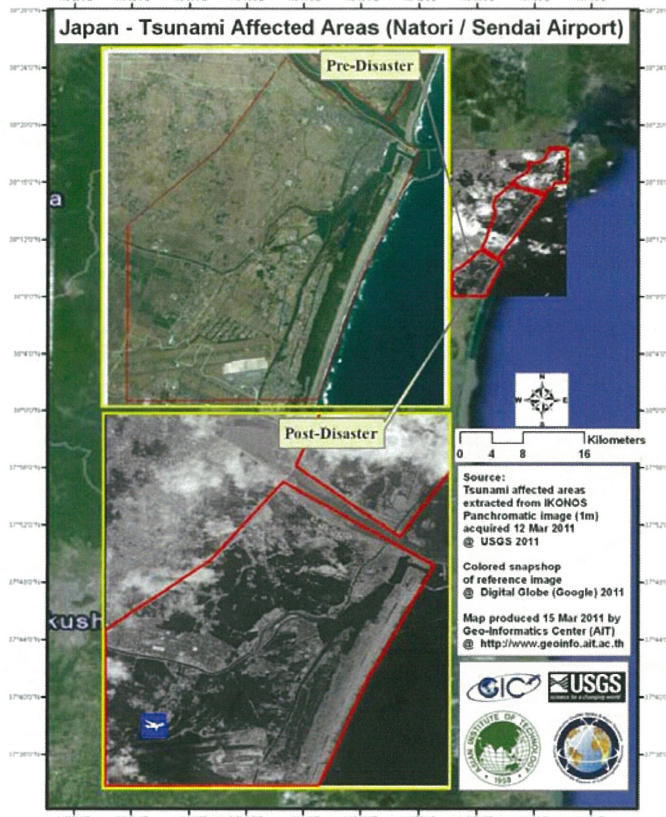
Disaster Charter & Sentinel Asia Support

There were about 5000 satellite images from 30 satellites provided for mapping

Regional Human Network

JAXA HUMAN RESOURCE NETWORK
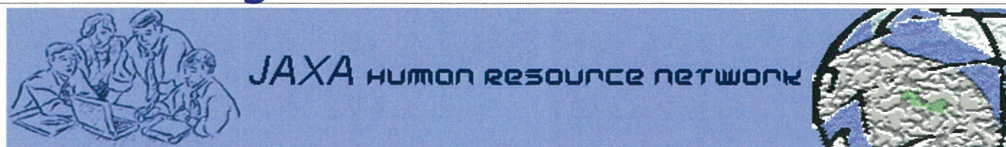
JAXA HRNet (March 2008) NEW

⊞ JAXA HRNet Final Report

⊞ JAXA HRNet Database (This DB is password protected & only JAXA & GIC members are permitted to access it. Request for password)

Provided by IFNet and Sentinel Asia
⊞ Daily Accumulated Precipitation Site

⊞ 3, 7, 30, 60, 100-day Accumulated Precipitation Site

August, 2007
⊞ Web Mapping more

July, 2007
⊞ Mini Project Field Data Site
⊞ Upload Waypoint Site

March, 2006
⊞ HRN Meeting at Bangladesh more
⊞ HRN Meeting at Nepal more
⊞ HRN Meeting at Indonesia more
⊞ HRN Meeting at Thailand more

WELCOME

Japan Aerospace Exploration Agency (JAXA) previously known as National Space Development Agency (NASDA) of Japan has been contributing to capacity building in remote sensing and related space technologies in Asian region with the cooperation of Geoinformatics Center (GIC) previously named as GIS Application Centre (GAC) of Asian Institute of Technology since 1995. The first training course under JAXA sponsorship was launched in 1995 inviting twenty participants from Asia to GIC. The title of the course was PC based GIS Information System, which was appropriate at that time due to very limited awareness of these new technologies.

JAXA supported capacity building and information sharing in the region was carried out in number of initiatives since 1995, namely, Structured Training Programs, Caravan Training Programs, Mini-Projects, and Workshops. Structured training programs were carried out at GIC inviting participants from the region who are working in national agencies. Structured courses were conducted for two weeks at GIC with full sponsorship of JAXA. This activity was continued until year 2003 satisfactorily training more than 400 people. During training at AIT, participants were benefited with access to the library of the institute and opportunities to meet faculty members of AIT to further exchange information and develop future collaborative opportunities.

Another type of training program that is conducting by GIC for JAXA sponsorship is referred to as Caravan Training. These programs are being conducted locally with the collaboration of local agencies. It is expected that this program could offer opportunities to a larger audience to increase awareness in remote sensing, GIS and GPS by conducting locally. Generally, the duration is five days targeting a topic that is relevant to the country concerned. Since 1997, after two years of first structured training program, Caravan type training programs were started and the first training program was conducted in Philippines. Since then seventeen Caravan training programs were conducted in ten countries. more

17th CEReS International Symposium, 1st March 2012, Chiba University, Japan

Student Internships

GIC Internships at GIC | GeoInformatics Center - Asia...   Page ▾ Tools

Faculty of Geomatics, Sabaragamuwa University of Sri Lanka

"Internship at GIC was a wonderfull experience for me. I had first hand experience with real data and real situation, selecting the appropriate data for the project, downloading freely available data, accuracy assessment of result. Web GIS and SAR interferometry were another new subject that i was able to study in depth with the help from the expert staff at the center. The atmosphere at GIC was very pleasant, the staff was very kind enough to explain any question that I came a cross. Every day was a new experience learning some thing new. If you are planning to work in the fields of GIS and Remote Sensing GIC is the place to be in your Internship, the experience you gain will help you through out your career. Finlay I must thank Dr. Lal and all the other staff member at GIC for giving me this wonderful opportunity which i will never forget."

Apiwat Thongchan

Faculty of Electronic and telecommunication Engineering, Rajamangala University of Technology(Jun 2009 - Oct 2009)

"Internship at Geoinformatics Center helped me to gain a good working experience with Network , IP address, Windows server and related technologies. I also learned about field of Geoinfomations such as Digitizing Map and involved some of training programs. This center was my first international work place, I had practiced and learned English language from working experience. The staff was very friendly and their work style like family. I have good friends and good experiences from GIC that i have never had before"

Kushani Tharangika Wickramasekara

Faculty of Engineering, University of Moratuwa, Sri Lanka (October 2008 –March 2009)

"I consider the oppertunity i got to work as an Intern at the Geoinformatics Center one of the main highlights of my undergraduate period. Apart from the multinational work environment it provided i had the chance to be exposed to the latest technological advances in the field of Remote Sensing and GIS. Not only did i have the privilage of working with the specialists in that area the training sessions under the industry experts had been an invaluable experience. i will always be indebted to the Director, Dr Lal Samarakoon and the Staff of the GIC for that amazing opportunity and i hope that they will continue their wonderful work of lending a hand to enlighten the young minds with

17th CEReS International Symposium, 1st March 2012, Chiba University, Japan

JICA Training on Forest Fire
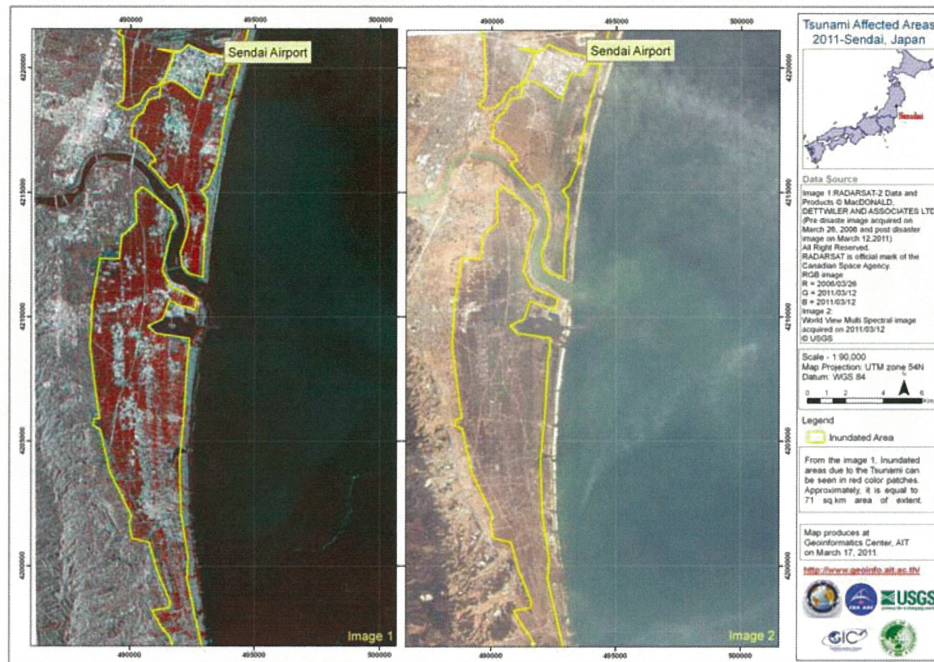

17th CEReS International Symposium, 1st March 2012, Chiba University, Japan

Spectrometer

Field Verification

Interpretation – Optical & SAR

GPS survey

17th CEReS International Symposium, 1st March 2012, Chiba University, Japan

Seminar at Local Institutes

Laos

Vietnam

Sri Lanka

Bangladesh

17th CEReS International Symposium, 1st March 2012, Chiba University, Japan

Lao PDR

Bhutan

Cambodia

Vietnam

Field Work in Philippines

Field Observations in Thailand

Community Based Survey in Nepal

Community based survey

Mud houses
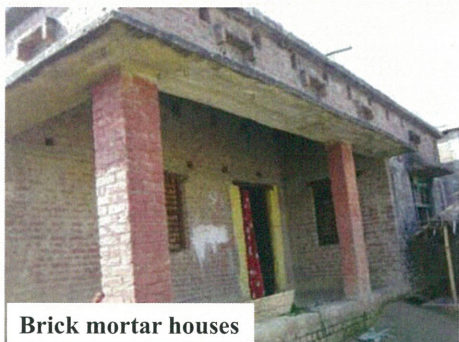
Brick mortar houses
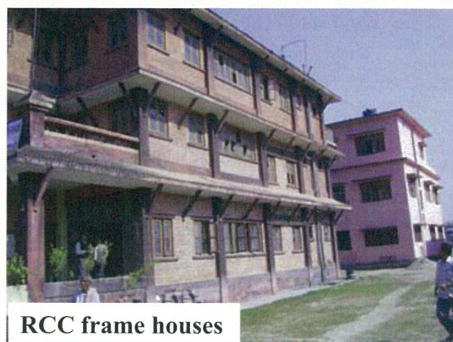
RCC frame houses

Drought Studies in Philippines
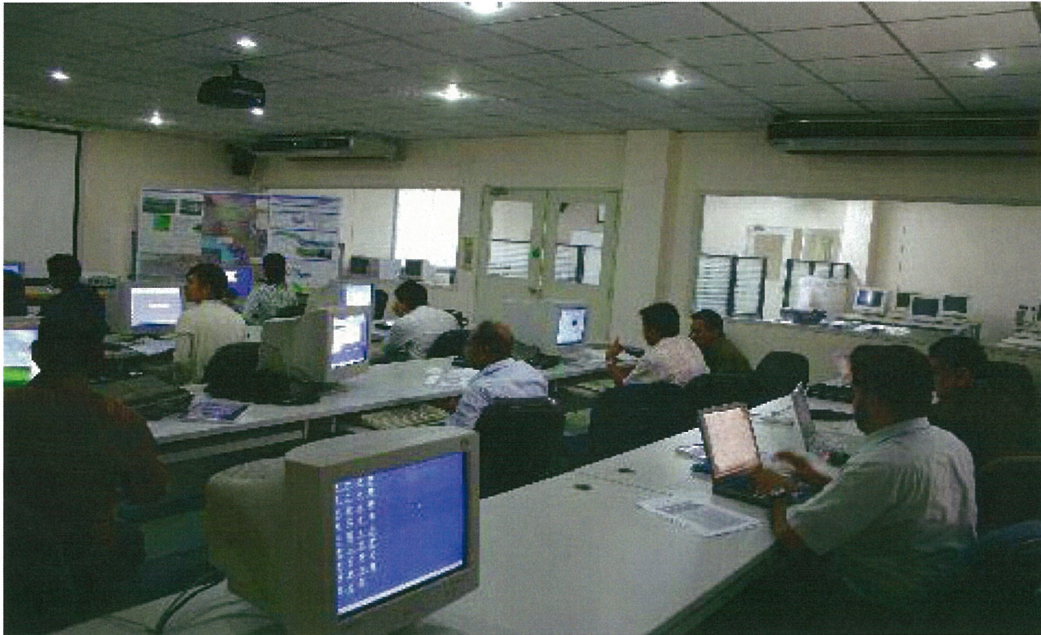
GIC/AIT Working Environment

GIC/AIT Working Environment
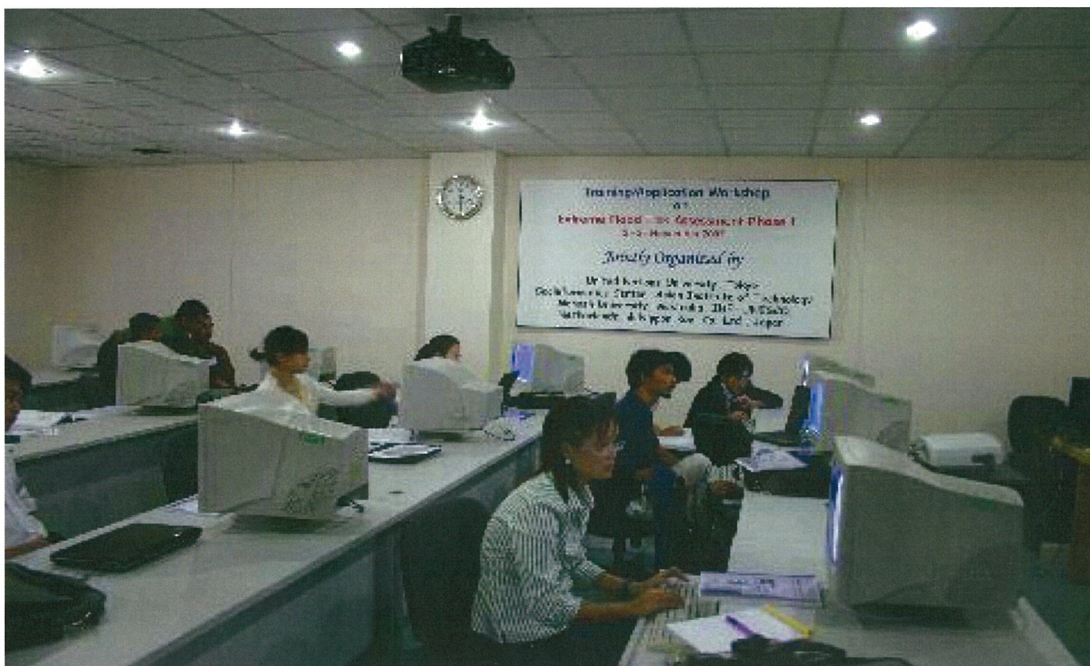
Summary

1. AIT contributes to capacity building in space based technologies in Asia with various programs,
2. GIC/AIT provides opportunities for joint research works on MODIS and multi-sensor GPS technologies,
3. Truly international institute work without boarders,
4. Knowledge is shared through publications, accepting internships, and through conferences presentations.

Ccapacity Building and Technological Support

Geoinformatics Center, AIT

www. geoinfo.ait.ac.th

geoinfo@ait.ac.th

Introduction of Advanced small satellite for earth observation

Tomoki TAKEGAI[1] Toshiaki OGAWA[1] Yasuhiro UCHIBORI[1] Koichi KISHI[2] Tsuyoshi OISHI[1]

[1] *Space Systems Division, NEC Corporation.   1-10 Nisshin-Cho, Fuchu, Tokyo, 183-8501, Japan*
[2] *Satellite Business Development Office, NEC Corp.   3-20-2 Nishi-Shinjuku, Shinjuku, Tokyo, 163-1403, Japan*
E-mail: [1]{t-takegai@bu, t-ogawa@dt, y-uchibori@cj, t-ooishi@cj}.jp.nec.com,   [2]k-kishi@aj.jp.nec.com

Abstract

The Earth observation system by using advanced small satellite bus of "NEXTAR (NEC Next Generation Star)" developed by NEC is introduced in this paper. NEXTAR-300L and NEXTAR-100L are one of NEXTAR series buses, respectively. NEXTAR is designed as standard bus , which we can realize advanced small satellite for earth observation only by combining with high performance sensors .

Keywords : Small Satellite, NEXTAR, ASNARO, SERVIS-3, Earth Observation

1. Introduction

NEC are proceeding to the development of standard advanced small satellite bus based on our technologies which was established at more than 40 years experience on space development with JAXA. This advanced small type standard satellite bus is called as "NEXTAR". NEXTAR-300L and NEXTAR-100L are one of NEXTAR series buses, respectively. NEXTAR-300L was adopted as "ASNARO" (Advanced Satellite with New system ARchitecture for Observation) ,and NEXTAR-100L was adopted as "SERVIS-3"(Space Environment Reliability Verification Integrated System 3) project. Both projects are under the contract of Institute for Unmanned Space Experiment Free Flyer (USEF) and Ministry of Economy, Trade and Industry (METI). By using this NEXTAR, we can provide high performance satellite equivalent with a medium or large type satellite at low cost and short duration for development.

1. Overview of NEXTAR System

1.1. Overview

NEXTAR is the spacecraft platform whose purpose is standardization and designed based on the advancing various recent technology innovations. These include the innovative "miniaturization" technology for small scientific satellites. Such advances are helping to provide the "Multi-functionality" and "high performance" of large satellites while maintaining the features of small satellites such as "light weight", "low price" and "short delivery term". Structural/thermal/electrical designs of bus and mission are independent for each other. That means bus design is standardized and can be compatible with several type of mission hardware without any modification of bus design.

The concept of NEXTAR bus is shown in Fig 1.
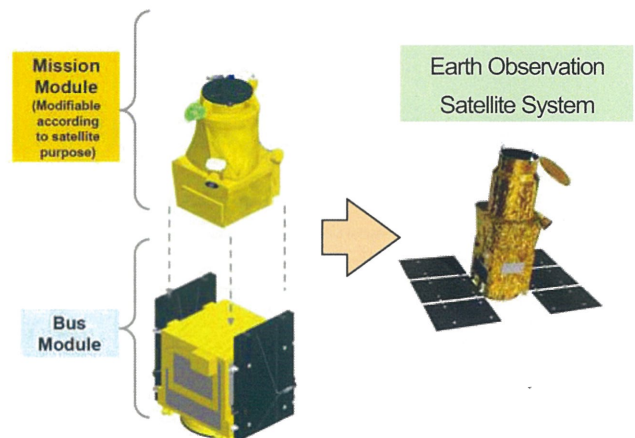
Fig 1 Concept of NEXTAR standard bus

NEC has several types of NEXTAR bus (including 100L and 300L) as an advanced small satellite for earth observation. The size and weight of NEXTAR -100L is smaller than that of 300L.The line-up of earth observation satellite using NEXTAR series are shown in Fig 2.

The satellite with high resolution optical sensor on NEXTAR-300L is developed as "ASNARO" project (in Section 2) and the satellite with medium optical sensor on NEXTAR-100L is developed as "SERVIS-3" project (in Section 3). And the satellite with X band SAR sensor on NEXTAR-300L is ready for development as ASNARO-2. This satellite has resolution of less than 1m at 10km swath.

Furthermore, a hyper spectrum sensor with many detection band up to 185 bands(with a resolution of 30m at 30km swath) or a multi spectrum sensor for wide area detection (with a resolution of less than 5m at 90km swath) is under development by NEC. Each sensor will be

integrated onto NEXTAR-500L bus system, which is a larger type standard bus system than NEXTAR-100L /300L.

	Medium resolution optical sensor 1	High resolution optical sensor	Hyper sensor
Development Status	Just starting of development (as a "SERVIS-3" project)	Under development (as "ASNARO" Project)	Under development
Outside of Satellite			
Sensor performance	Panchromatic/Multi Resolution: 2.5~5m Swath: 20~50km	Panchromatic/Multi (6bands) Resolution: <0.5m (Pan) Swath: 10km	VIS~SWIR, 185 bands Resolution: <30m Swath: 30km
Type of Bus	NX-100L	NX-300L	NX-500L
	Medium resolution optical sensor 2	SAR Sensor	Optical sensor for wide area detection
Development Status	Under development (as "ASNARO-2" project)	Under development (as "ASNARO-2" project)	Under development
Outside of Satellite			
Sensor performance	Panchromatic/Multi Resolution: ~1.2m Swath: ~10km	X band Resolution: <1m Swath: 10km	Multi (4 bands) Resolution: <5m Swath: 90km
Type of Bus	NX-100L	NX-300L	NX-500L

Fig 2 Line-up of earth observation satellite with NEXTAR-100L/300L/500L bus.

1.2. Space Wire Technology

A technology of SpaceWire RMAP (Remote Memory Access Protocol) is adopted as a one of standardization features of NEXTAR. The CPU boards of computers equipped on traditional satellites as well as other functions such as the data control, attitude control and mission control functions have been developed individually according to the mission requirements of each satellite. With the NEXTAR, this method has been changed to use a standardized computer that implements the functions required of the bus for the entire network (Fig 3).

As a result, the previous method of implementing the data control, attitude control, and mission control using three different computers is now enabled with the use of a small common computer "SpaceCube2" (which was launched on SDS-1 project by JAXA) which contributes significantly to a reduction in the size and price of satellites (Fig 4).
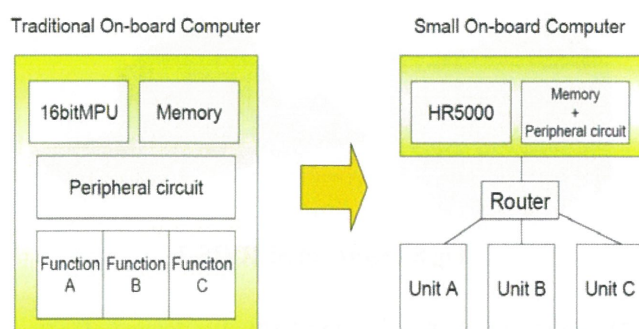
Fig 3 Use of SpaceWire networking technology
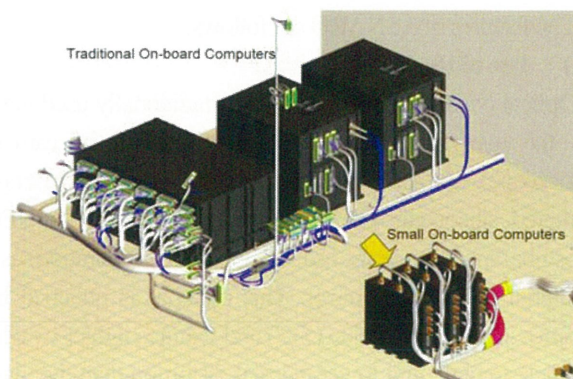
Fig 4 Compact satellite-born computer in NEXTAR

2. Introduction of ASNARO with NEXTAR-300L

The satellite which accommodates high resolution optical sensor is now under development as ASNARO (Advanced Satellite with new system Architecture for Observation, which is the first satellite using NEXTAR bus (Fig 5) and will be launched in FY2012.As shown in Table 1, ASNARO introduces new technology including NEXTAR bus technology for a small satellite of about 500kg in order to implement a performance equivalent to that of a satellite weighing a few tones.

Table 1 Performance comparison with ASNARO

	ASNARO	WorldView-2	GeoEye-1
Launch year, External view	2012(Scheduled)	2009	2008
Developing country	Japan	U.S.A.	U.S.A.
Orbit	504km Sun synchronous	770km Sun synchronous	684km Sun synchronous
Mission Life	3years	7.25years	7years
Satellite mass	<500kg	2800 kg	2000 kg
Ground sampling distance (GSD) Swath	< 0.5m(Pa) <2m(Mu) 10km	0.46m(Pa) 1.84m(Mu) 15.8km	0.41m(Pa) 1.65m(Mu) 14.4km
Data rate	832Mbps	800Mbps	740Mbps
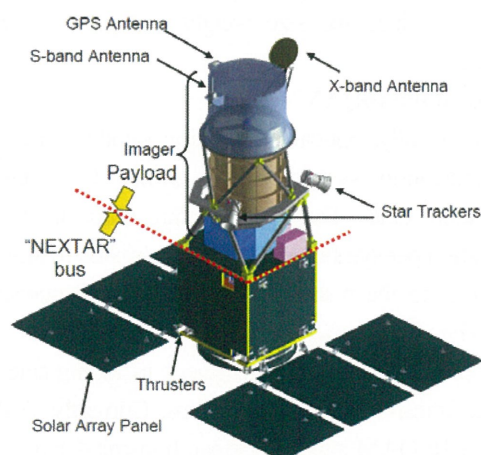
Fig 5   ASNARO Overview

The features of ASNARO are follows:

(1) Use of the NTSIC Mirror

Optical observation satellites have traditionally used glass as the material for the primary mirror of the camera (telescope), but ASNARO adopts a high-strength, reaction sintered, silicon carbide(NTSIC, developed jointly by NEC Toshiba Space Systems, Ltd. and Toshiba Corporation) as a material of primary mirror. This material is obtained by improving silicon carbide (SiC) and features lighter weight, higher strength, and lower thermal distortion than the glass material (Fig 6). NTSIC features a higher strength than the ordinary SiC material and has a dense and no pores on the surface.
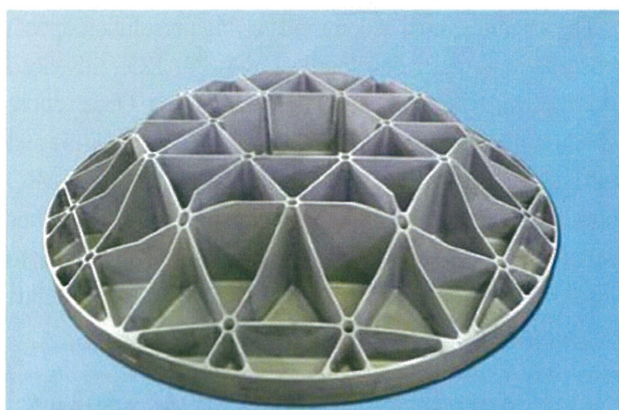
Fig 6 Primary mirror made from NTSIC material

(2) Use of flash memory

The mainstream memory used hitherto in the data recorder for storing the observation data of traditional optical observation satellites has been the SD-RAM that features high-speed processing and high reliability. On the other hand, ASNARO adopts a flash memory that features lower heat dissipation, lower power consumption, lower price, same size and larger capacity than the SD-RAM in order to reduce the size weight and price of the data recorder.

(3) Use of the 16QAM system

Traditionally, optical observation satellites used to use the modulation system called QPSK for transmitting observation data. This system can transmit 2 bits of information per symbol and the rate is limited to around 400 Mbps due to the restriction of the 8GHz frequency band used. Therefore, larger satellites had to have two sets of 400Mbps communication equipment, including antennas, in order to transmit data at 800 Mbps. Currently, ASNARO adopts a 16 QAM system that can transmit 4 bits, which is twice that of the QPSK, per symbol. It can thereby achieve the same 800Mbps transmission as larger satellites using a

single set of communication equipment and as a consequence enable reductions in the size, weight, and price of the satellite (Fig 7).

Based on upon features, we can obtain high performance equivalent to that of a satellite weighing a few tones at low cost and short duration for development.
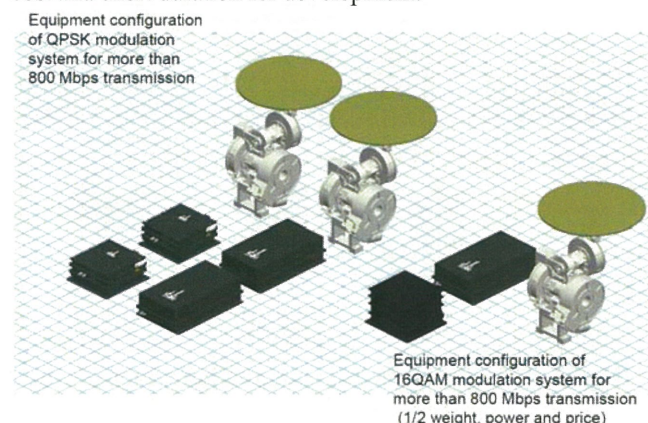
Fig 7 Configuration of data transmission system

3. Introduction of SERVIS-3 with NEXTAR-100L

SERVIS-3 is a satellite to demonstrate NEXTAR-100L bus with some mission payload using some commercial parts. The specifications of SERVIS-3 are shown in Table 2.

Table 2 Specification of SERVIS-3

Items	Specification
Size	1068 x 1059 x H900 mm (Launch) 2458 x 1059 x H900 mm (On orbit)
Mass	< 170 kg (Total)
Power Generation	> 370W (EOL)
Power consumption	About 200W (For bus system)
Communication	S-band 1MBps
Data Recorder	> 1 Gbyte

The figures of SERVIS-3 are shown in Fig 8 (for Launch and On orbit Configuration).
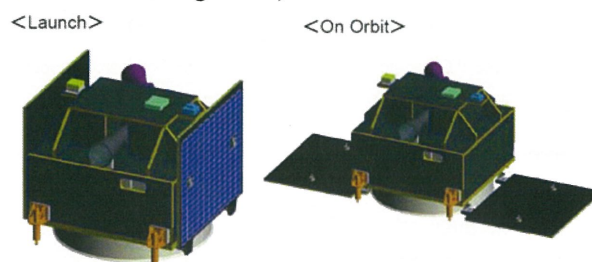
Fig 8 Figures of SERVIS-3

The system block diagram of SERVIS-3 is shown in Fig 9. SERVIS-3 has three types of reaction control system , Reaction Wheel Assembly (RWA), Magnetic Torque (MTQ), and Thruster system. Because of these system, SERVIS-3

can comply with various system with enough pointing and attitude control performance.
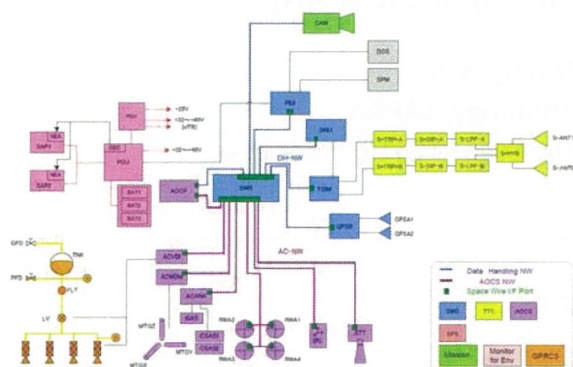
Fig 9 System Block diagram of SERVIS-3.

The features of SERVIS-3 are follows.

(1) Dual Launch

The SERVIS-3 is suitable for dual launch as a sub satellite and has a compatibility with world major satellite. Therefore, the size of SERVIS-3 is very small enough to be launched at lower side of Payload Attachment Mechanism which is the mechanical connection between main satellite and launch rockets. The dual launch configuration is shown in Fig 10. All of the interface (including adapter to maintain enough height for SERVIS-3 under a mechanical interface for main satellite) was already developed.
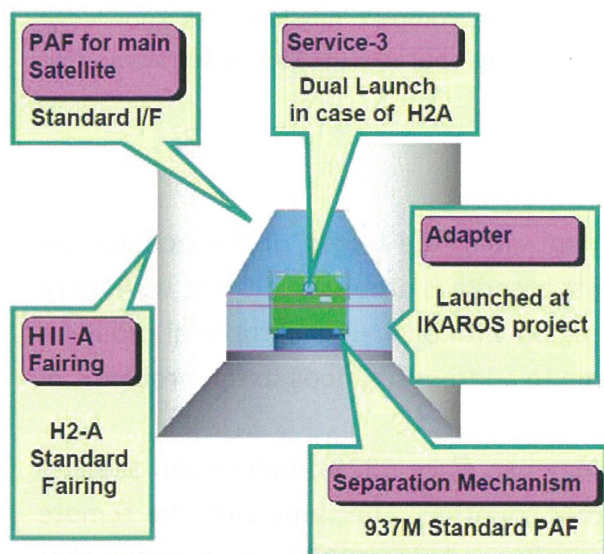
Fig 10 SERVIS-3 Launch configuration (Dual launch at H2A)

(2) Reduction of Interface Board
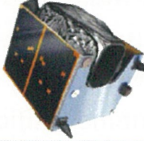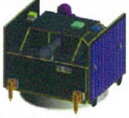
In NEXTAR-300L architecture, there are many interface exchange board to accommodate existing/experienced sensors/ actuators with Space Wire bus system. That is a reason for NEXTAR-300L to have large compatibility with existing hardware. But in SERVIS-3 configuration, interface boards are deleted by mounting them into inside of each sensor/actuator. Therefore, though SERVIS−3 has limited flexibility with various sensor/actuator , it can achieve smaller size than ASNARO architecture. This means that SERVIS-3 is easier to be integrated as satellite system.

(3) High Mission Installation capability

SERVIS-3 has equivalent or higher mission installation capability than that of other world popular bus system with equivalent size (about 100kg). Table 3 shows a comparison with other world popular bus system (about 100kg).

Table 3 Comparison with other bus (about 100kg)

	SSTL-150	Myriade	SERVICE-3 NEXTARL-100L
Item	Specification		
Bus system Mass	103kg	About 100kg	About 100kg
Mission Mass	50kg	<40-60 kg	80kg
Total Mass	150kg	<140kg	< 200kg
Mass Ratio	33%	33%	< 40%
Satellite Size	730 x 455 x 744 mm	600 x 600 x 800 mm	950 x 950 x 900 mm

4. Summary

NEC is developing advanced standard bus systems of NEXTAR series. The first satellite of NEXTAR-300L was adopted as ASNARO, and the first satellite of NEXTAR -100L was adopted as SERVIS-3. ASNARO has high resolution optical sensor equivalent with the world's finest optical sensor on orbit. SERVIS-3 has simplified architecture which is suitable for a training of bus development process.

By using this NEXTAR, we can provide high performance satellite equivalent with medium or large type satellite at low cost and short duration for development.

Reference

[1]   Ogawa," Development of the ASNARO, an Advanced Space System", NEC TECHNICAL JOURNAL, Vol.64, No.1, P32-P35,March 2011

[2]   HIHARA Hiroki ・ YOSHIDA Teiji ・ TANAMACHI Takehiko ・ KUMASHITA Kyousuke ・ KOBAYASHI Akihide,"NEXTAR Standard Platform for Quick Startup of Remote Sensing Operations", NEC TECHNICAL JOURNAL, Vol.64, No.1, P75-78, March 2011

[3]   Tomoki Takegai ・Toshiaki OGAWA ・Koichi KISHI ・Tsuyoshi OISHI, "Introduction of Earth Observation Small Satellite", ICSANE2011, IEICE, October 17-19, 2011

Development of Micro-satellite Technology at the Indonesian National Institute of Aeronautics and Space (LAPAN)

Robertus Heru Triharjanto
Center For Satellite Technology, LAPAN
jl. Cagak Satelit km.4 Rancabungur, Bogor 16310, Indonesia
rtriharjanto@yahoo.com

ABSTRACT

The evolution of desain of LAPAN's micro-satellite will be presented in here. Micro satellite systems have been chosen for space technology development in Indonesia due to the cost effectiveness. Starting in 2003, LAPAN has implemented LAPAN-TUBSAT micro-satellite program, which has successfully carried its mission as experimental Earth observation satellite and capacity building tools. The satellite is currently serving its 5th year of operation. Since 2008, LAPAN is preparing two satellites; named LAPAN-ORARI and LAPAN-IPB. The mission for LAPAN-ORARI is Earth observation using RGB camera, maritime traffic monitoring using AIS, and amateur radio communication (text & voice). The satellite will be launched as auxiliary payloads for ASTROSAT mission which has orbit of be 650 km circular at inclination of 8^0, expectedly before the end of 2012. The purpose of the project is to develop capability to design, Assembly, Integration and Test (AIT) process of micro-satellite in Indonesia. LAPAN-IPB will cary an experimental 4-bands multispectral imager, as well as AIS and communication for Amateur Radio Community, and to be flown by PSLV SSO mission expectedly before the end of 2013. The three projects shows LAPAN's micro-satellite bus development, that grow in complexity to accomodate more complex mission. The knowledge advancement is expected to prepare the Center for developing operational satellite for supporting the food security program in Indonesia.

I.   Introduction

Indonesia is located approximately 5,150 km along the length of the equator (or about 1/8th of earth circumference), and the widest breadth is around 1,750 km, with more than 220 million population. With the extensive region with diverse geographical problem, the utilization of satellites is important for Indonesia to address solutions to the problems of the nation.

Despite the extensive of satellite technology use since 1970s, Indonesian satellite communication system is still purchased from other countries. The same with the remote sensing satellite system, which have been extensively used since 1980s. It is known that during the Aceh tsunami, the disaster management support is heavily dependent on foreign satellite services. Economically, in the long term, the technology dependency created great loss for Indonesia. In addition to that, the dependency made Indonesia prone to political pressure from technology supplier countries.

The development of micro-satellites has become an opportunity for LAPAN in developing its satellite program. The development of such satellites requires only limited budget and facilities, compared to the development of big satellites. Meanwhile, the

capability to develop micro-satellite will brings LAPAN to the readiness state to implement a future space program that will have measureable economic impact, and therefore contribute to the country's sustainable development effort.

II. LAPAN-A1 Satellite

The development of LAPAN-A1, Indonesian 1st microsatellite which is also named LAPAN- TUBSAT, was started in 2003. Its Assembly Integration and Test was done in 2004-2005 in Technical University of Berlin, Germany. The satellite payload is a COTS video camera with 1000 mm lens, resulting into nadir resolution of 5 m and nadir swath of 3,5 km from 650 km altitude. In addition to that the satellite carries another video camera with 50 mm lens, resulting into 200 m resolution video image with swath of 80 km at nadir. The *uplink* and *downlink* for *telemetry, tracking and command* (TTC) is done in UHF and *downlink* for video is done in S-band analog. The satellite is successfuly launched to SSO of 635 km as auxiliary payload in *Polar Satellite Launch Vehicle* (PSLV) C7 from Sriharikota, India on January 10th, 2007, and now has entered its fifth year of operation and still in good condition.

Figure 1. 3-roda cement factory, West Java (taken by LAPAN-TUBSAT 25 May 2010)

III. LAPAN-A2 Satellite

Gaining experience in developing, launching, and operating micro-satellite as well as in developing and operating satellite's ground station, LAPAN continue in developing its 2nd satellite, named LAPAN-A2. The mission for LAPAN-A2 is Earth observation using RGB digital camera, maritime traffic monitoring, and amateur radio communication.

Since Indonesian territory is spread along the equator, LAPAN study the operation of satellite at low inclination orbit, so that the satellite may pass Indonesia as much as SSO orbit pass the North/South pole (14 times in 24 hours at 600 km orbit). The study shows that in order to be able to cover the entire Indonesia with surveilance camera oriented at nadir, the inclination needed is 10^0. Therefore, when ISRO announce that it would launch ASTROSAT mission which has orbit of be 650 km circular at inclination of 8^0, LAPAN decided to put the satellite as auxiliary payloads for the mission. With frequent pass over Indonesia, the missions are expected to be more useful.

The objective of LAPAN-A2 satellite project is to achieve the design, integration and operation of micro satellite in Indonesia. LAPAN-A2 main mission is Earth Observation using digital RGB camera (5 m resolution). In addition to that the satellite carry AIS (Automatic Identification System) receiver to monitor maritime trafic, a reaction wheel made by LAPAN for space proofing, and an amateur radio Automatic Packet Reporting System (APRS), as well as amateur radio voice repeater, for Indonesian Amateur Radio Organization (ORARI). Due to this cooperation, LAPAN-A2 is called LAPAN-ORARI.
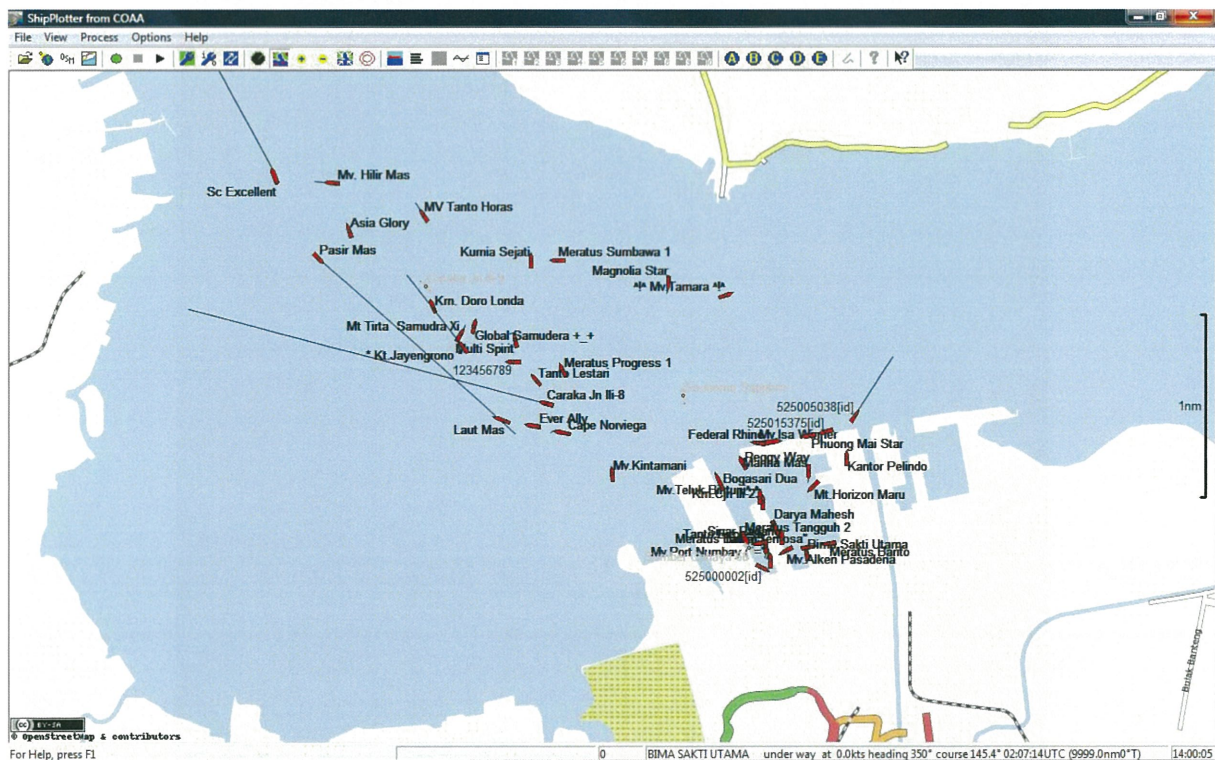
Figure 2. AIS payload test result, Surabaya, East Java, 2010

LAPAN-A2 satellite is planned to has two picture operation modes : automatic target pointing and interactive operation. The 1st mode will employ close loop process between Star Sensor, GPS, and the attitude control actuator. The 2nd mode is the same as the

operation of LAPAN-TUBSAT, in which the video camera mode will be used to find the target, before the high resolution picture is taken.

IV.   LAPAN-A3 Satellite

The objective of LAPAN-A3 satellite project is to support the national food sustainability program. Therefore the payload requirement is defined by Institut Pertanian Bogor (IPB). IPB in an academic institution that specialized in agricultural science and technology, which is awarded as national academic reference for Indonenesian food sustainability program. Based on such cooperation, the satellite is also named LAPAN-IPB satellite. The multi-spectral imager will serve the data acquisition related to crop growth/yield estimation as well as coastal environment monitoring, which are important for the food security management. The satellite is planned to be launched to SSO altitude 650 km by PSLV expectedly mid 2013.

The main payload of the satellite is a 4-band multi-spectral imaging line imager (using 4 Kodak 8023 sensor with spectral filter on 450 - 520 nm, 520-600 nm, 630-690 nm, and 760-900 nm) with 1000 mm Nikor Lens, to produce spatial resolution of 18 m, swath width of 110 km. The satellite will also carry digital camera similar to LAPAN-A2 with 1,6 m lens, so that it may provide image with 3,5 m resilution. In addition to that, the satellite will carry AIS and APRS to support global maritime monitoring mission and worldwide radio amateur community.
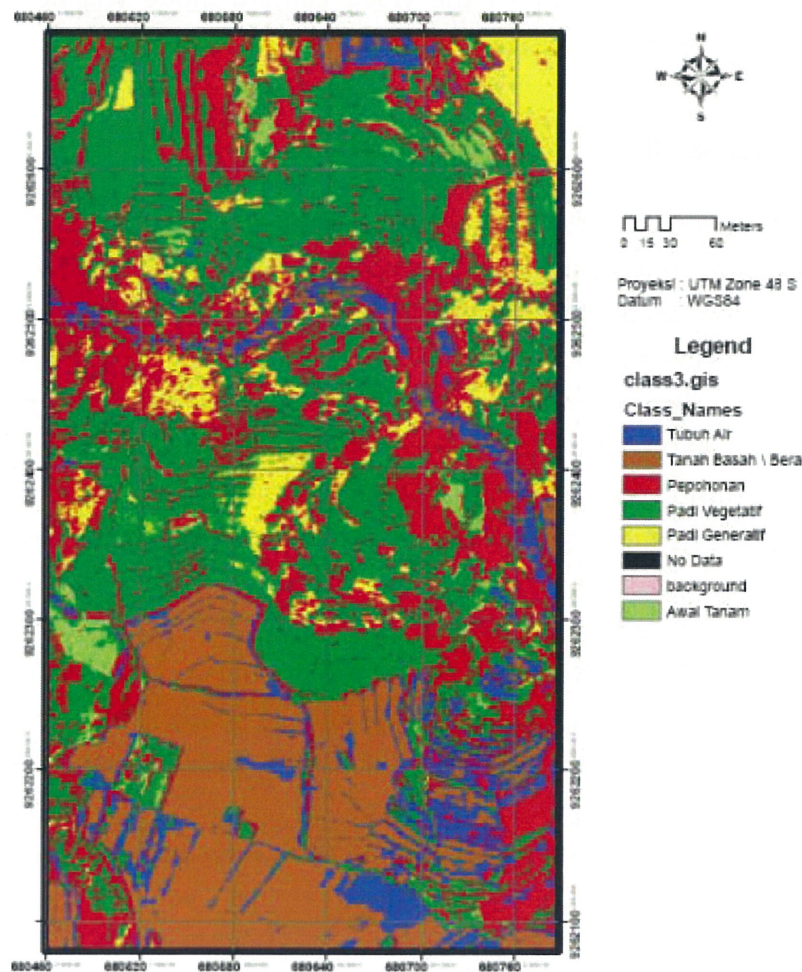
Figure 3. Multispectral imager flight test, Bogor, West Java, 2010

V. Upgrade on satellite bus

Table 1. Advancement in LAPAN's satellite bus

	LAPAN-TUBSAT	LAPAN-ORARI LAPAN-IPB
Power generation	4 Silicium solar panels (432x243 mm). Each panel has 34 cells in series, provide 14 W max power	4 GaAs Solar panels (465x262 mm). Each panel has 30 cells in series, provide 32 W max Power
Power storage	5 NiH2 batteries, configured in series. The batteries would provide nominal voltage of 12.5 V, 8 Ah capacity	3 Lithium-Ion batteries in paralel, 4 Cells per pack in series, 15 V Nominal Voltage, 17 Ah total capacity
Attitude sensor	1 CMOS star sensor	1 CMOS star sensor + 1 CCD star sensor

	4 solar panel + 2 solar cell sun sensor	6 solar cell sun sensor
Orbit determination	None	GPS
ACS mode	Manual drive mode & support anti-sun camera pointing mode (close loop main computer, -Z solar panel, and Wheel Drive Electronics	support automatic orientation of the camera to capture specific target location (close loop Star Sensor, GPS, main computer and Wheel Drive Electronics)
Payload data support	Analog data switch	solid state memory & multi-payload data handling system
Payload data transmision system	S-band analog	LAPAN-A2 : S-band analog & digital (6 Mbps) LAPAN-A3 : X-band digital (100 Mbps)

Table 1 shows that the capacity of LAPAN's satellite bus increases from its 1st generation to the next. LAPAN's 1st satellite weights around 55 kg, its 2nd generation weight arround 70 kg. Structural layout of each satellite is as follows.
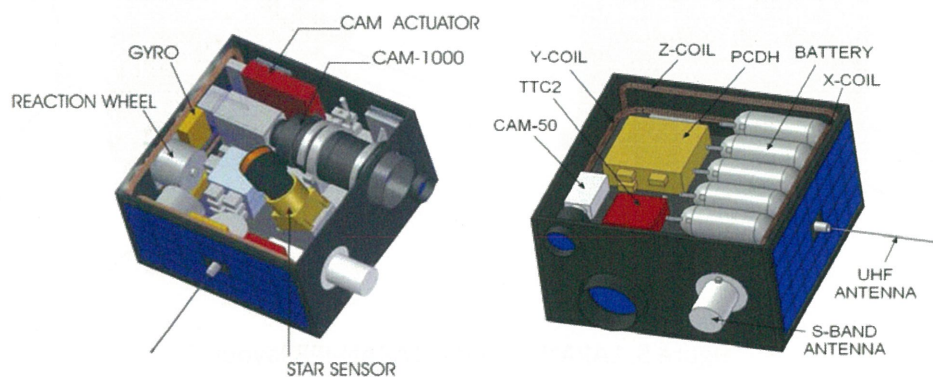
Figure 4. LAPAN-TUBSAT layout
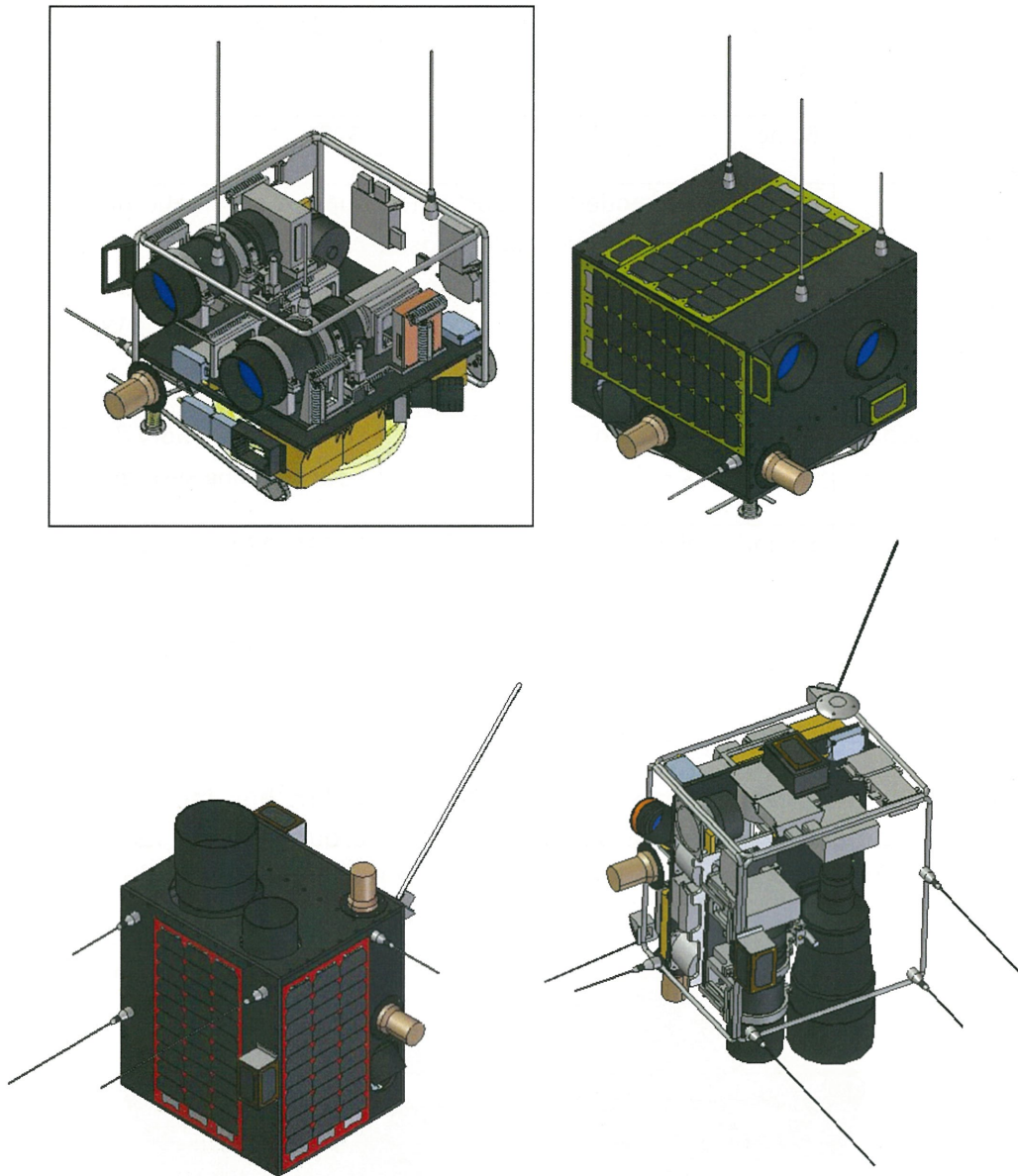
Figure 5. LAPAN-ORARI & LAPAN-IPB layout

The commonality in LAPAN's satellite buses are the mechanical packaging, i.e using the 2-shelves base, and star-configuration type computing system. Extrapolating the capacity of the Center for Satellite Technology for the next 5 years, LAPAN would be capable to develop 100 kg class satellite. Such satellite bus would be able to support battery capacity 34 Ah (at 15 V) and charging capacity 120 W, which will be able to serve more power demanding mission.
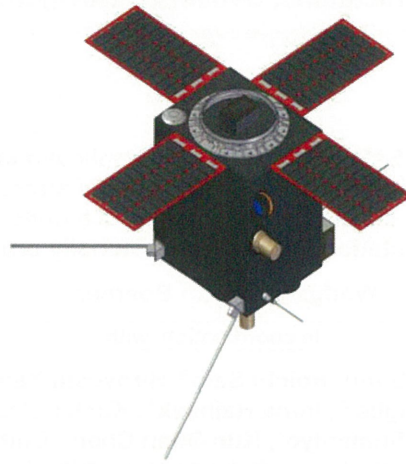
Figure 6. LAPAN's 100 kg class satellite

VI.   Conclusions

From the facts above, it can be seen that LAPAN's satellite program is technology is growing, froim simple satellite for capacity building puposes to more complex satellite designed to serve more complex mission.

In developing its satellite program, LAPAN always involve partnership with other institution interestd in satellite tehnology. LAPAN will always looking for new partner, as well as maintain its current partner, to work together on its next satellite program.

VII.   References

1. Triharjanto, R.H.; Hasbi, W.; Widipaminto, A.; Mukhayadi, M; Renner, U.; *LAPAN-TUBSAT : Micro-Satellite Platform for Surveillance and Remote Sensing*; Proceeding of Small Satellite System and Services Symposium; La Rochelle, France, 2004
2. Hardhienata, S; Triharjanto, R.H. (Editors); *LAPAN-TUBSAT : From Concept to Early Operation*; Lembaga Penerbangan dan Antariksa Nasional; 2007
3. Hasbi, W.; Widyastuti, R.; *The Use Of LAPAN-TUBSAT Satellite Video Data For Earth Observation*; Earth Observation Small Satellites for Remote Sensing Application Conference, Kuala Lumpur, November 2007
4. Triharjanto, R.H.; Widipaminto, A.; *Video Camera System on LAPAN-TUBSAT Micro-Satellite*; 3rd Asian Space Conference, Singapore March 2007
5. Triharjanto, R.H.; Mukhayadi, M; *LAPAN-TUBSAT Attitude Control : Operational Implementation of Angular Momentum Bias on SSO Satellite*; 6th Regional Conference on Aerospace Science, Technology and Industry; Bandung, June 2007
6. Renner, U.; Buhl, M; *First Flight Result with LAPAN-TUBSAT*; 6th Symposium Small Satellite for Earth Observation, Berlin, 2007
7. Renner, U.; Buhl, M.; *High Precision Interactive Earth Observation With LAPAN-TUBSAT*; Proceedings of the 4S Symposium Small Satellites, Systems and Services, Rhodos, Greece, May 2008
8. Hasbi, W.; Mukhayadi, M.; Budiantoro, P.A.; Syafrudin, H.; Tahir, A.M.; Kadri, T.M.; *Penentuan Spesifikasi Optik Kamera Pengamatan Bumi di Satelit LAPAN-A2 dan LAPAN-A3*; Satelit Mikro untuk Mitigasi Bencana dan Ketahanan Pangan; IPB Press; November 2010
9. www.lapantubsat.org

Future perspectives of SAR polarimetry with applications to multi-parameter fully polarimetric pol-sar remote sensing & geophysical stress-change monitoring with implementation to natural disaster assessment and monitoring within the "*Pacific Ring of* Fire" by implementation of polar & equatorially orbiting satellite sensors

Wolfgang-Martin Boerner[1-7]

In coordination with

Yoshio Yamaguchi[2], Akinobu Sato[2], Roichi Sato[2], Hiroyoshi Yamada[2]; Alberto Moreira[3], Gerhard Krieger[3], Andreas Reigber[3], Irena Hajnsek[3], Kostas Papathanassiou[3]; Katsumi Hattori[4], Josaphat Tetuko Sri Sumantyo[4], Kun-Shan Chen[5], Chih-Yuan Chu[5], Chih-Tien Wang[5], Jong-Sen Lee[5]; Enrico Paringit[6]; Roberto Heru Triharjanto[7], Mahmud Raimadoya[7]

1 University of Illinois at Chicago, UIC-ECE/CSN, Chicago, IL/USA
2 Niigata University, Electronic Information Engineering, Ikarashi, Niigata, Japan
3 DLR-HR, Oberpfaffenhofen, Bavaria, Germany
4 Chiba University, Earthquake Research Center & CEReS, Chiba, Japan
5 National Central University, NCU-CSRSR/MRSL, Jhongli, Taoyuan, Taiwan ROC
6 UPD-GE, Diliman, Quezon City, Metro-Manila, Philippines
7 LAPAN, Jakarta; BAC-CEE/RAWG, Jalan Meranti Dramaga Campus, Bogor, Java, Indonesia

Exploitation of fully polarimetric Satellite POLSAR modes for natural hazard detection and subsequent disaster reduction of SE-Asian/Pacific earthquakes, volcano eruptions and taiphoons – Japan, Taiwan, Philippines and Indonesia

Abstract: The outstanding performance capabilities of the three Satellite POLSAR sensors are well established; and in this exposition the exploitation of the fully polarimetric ALOS-PAL=PPL=SAR mode is demonstrated by implementing the NIIGATA-UNIVERSITY four-scatterer SAR image decomposition with coherency-matrix rotation proving the superior imaging capabilities of the fully polarimetric SAR modes not only for the ALOS-PALSAR L-Band and similarly to the S-Band, C-Band and X-Band. The novel fully polarimetric POL-SAR image processing techniques are then applied to natural hazard detection and subsequent disaster reduction of taiphoons with land-slides, volcano eruptions with plume aftereffects & landslides, and of earthquakes with drop-slips experienced within the SE-Asian/Pacific Ring-of-Fire including next to Japan in Taiwan, the Philippines and Indonesia, promoting equatorially orbiting Single and TanDEM L-/S-/X-Band POLSAR sensor deployment.

Apollo 11: 1969 July 16 - 24

WIDEBAND INTERFEROMETRIC SENSING AND IMAGING POLARIMETRY   4

Hydrologic cycle with volcanologic & seismic activity
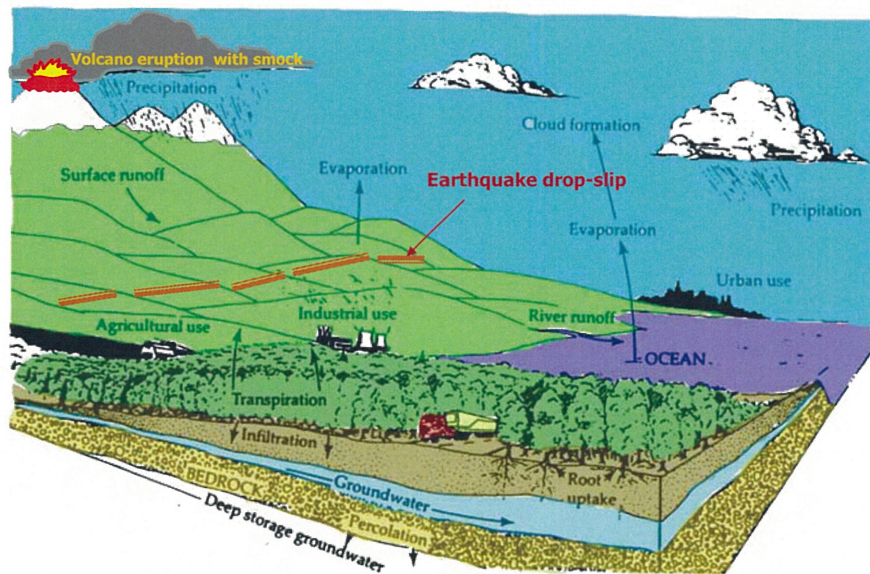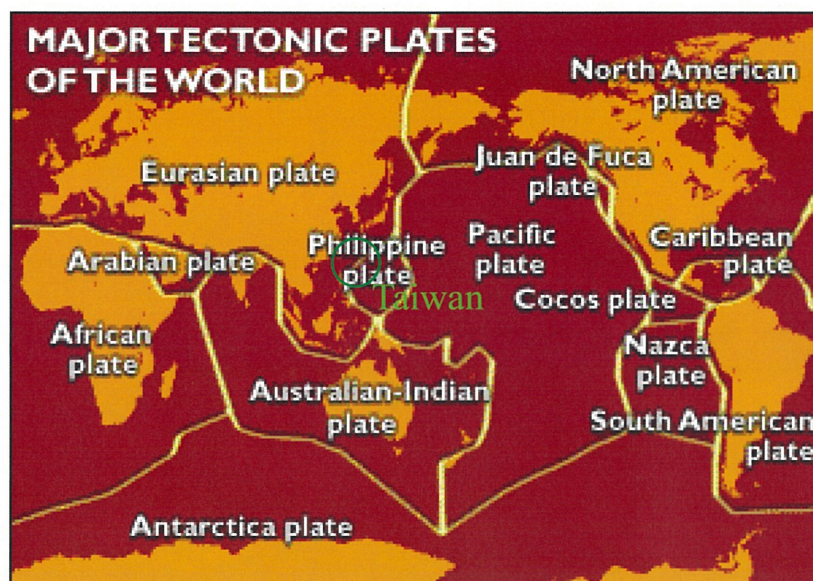
From BBC news site

The terrestrial tectonology: Alfred Wegener's tectonic plate theory and the two major seismic belts

Belt 2,   Circum-Pacific belt
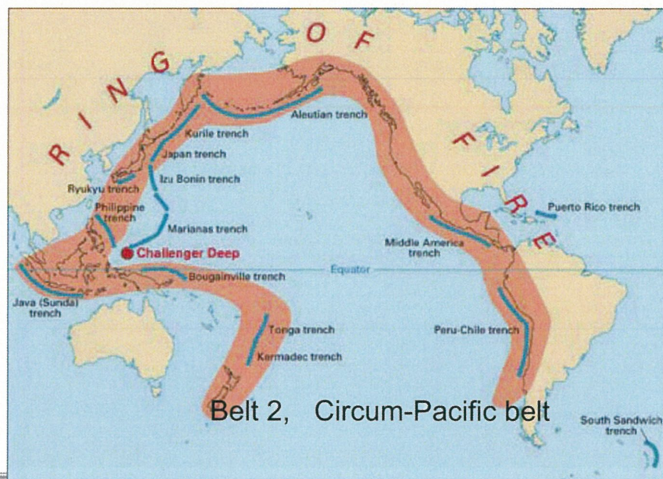
LAPAN-A2 ORBIT PROFILE
(14 pass per 24 hr / orbit time 100 minutes and stay above horizon at about 10 minutes)
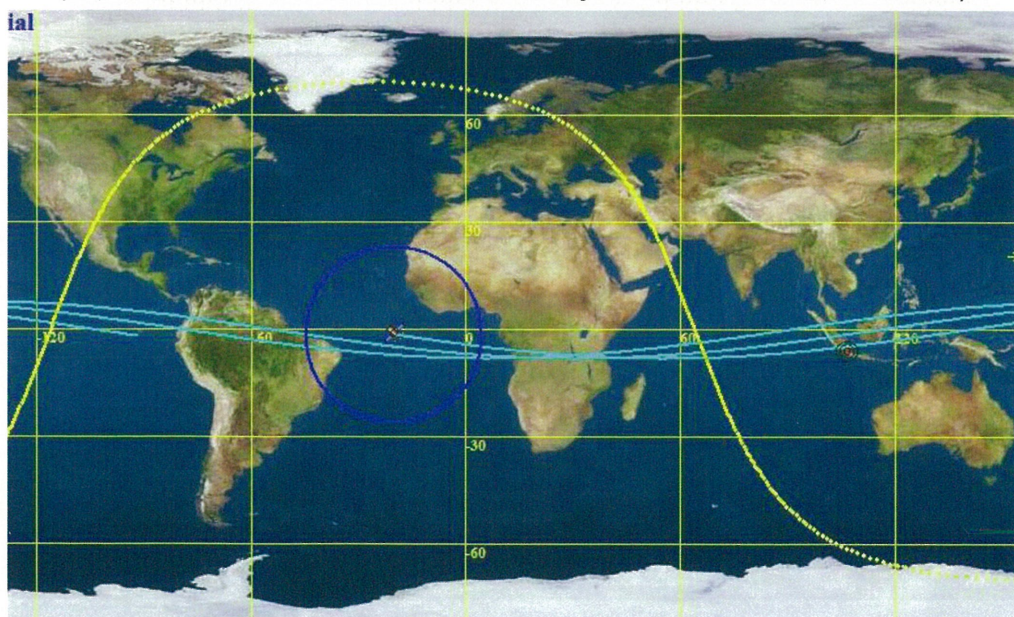
TUB-LAPAN-ORARI ORBIT PROFILE
(14 pass per 24 hr / orbit time 100 minutes and stay above horizon at about 10 minutes)
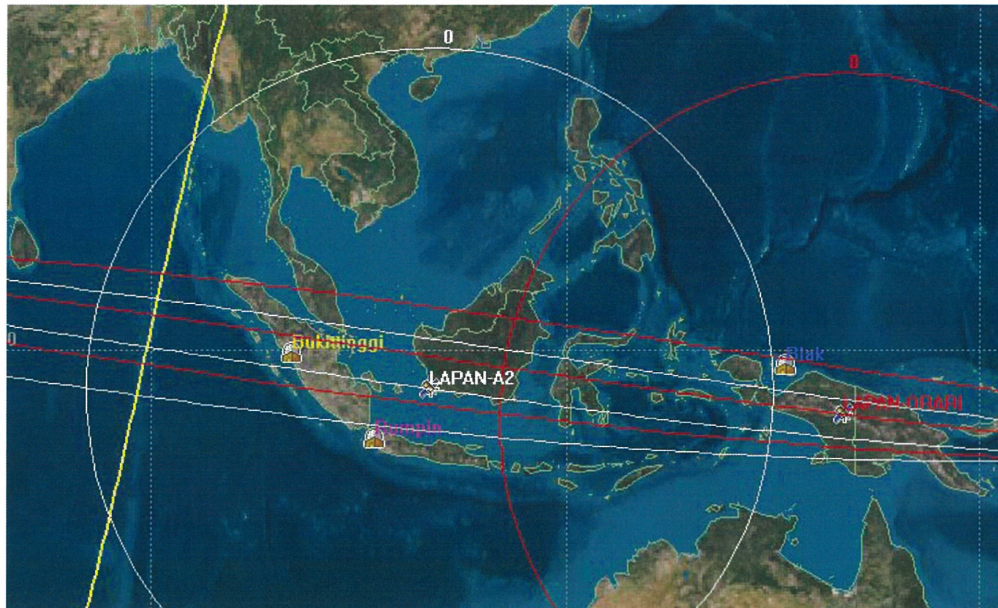
WIDEBAND INTERFEROMETRIC SENSING AND IMAGING POLARIMETRY   9

Table 1. Comparison of High-Level Parameters			
Parameter	**PALSAR**	**RADARSAT-2**	**TerraSAR-X**
Orbit: LEO, circular	Sun-synchronous	Sun-synchronous	Sun-synchronous
Repeat Period (*days*)	46	24	11
Equatorial Crossing time (*hrs*)	22:30 (ascending)	18:00 (ascending)	18.00 (ascending)
Inclination (*degrees*)	98.16	98.6	97.44
Equatorial Altitude (*km*)	692	798	515
Wavelength (*Band*)	23 cm (*L*)	5.6 cm (*C*)	3 cm (*X*)
Fully polarimetric mode	Yes	Yes	Yes

ALOS / PALSAR
Japanese Space Agency (JAXA)
L-Band (quad), 2006

RadarSAT-II
Canadian Space Agency (CSA)
C-Band (quad), 2007

TerraSAR-X
German Aerospace Center (DLR) / Astirum
X-Band (quad), 2007

WIDEBAND INTERFEROMETRIC SENSING AND IMAGING POLARIMETRY   10
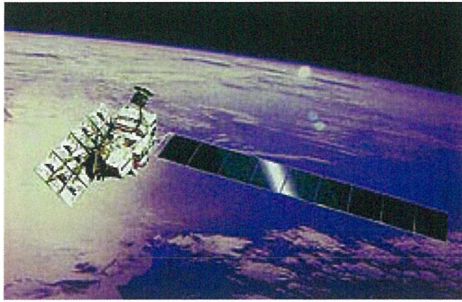
ALOS is one of the largest Earth observing satellites ever developed, at 3850 kg. It is in a near-exact 45-day repeat sun-synchronous orbit, 690 km altitude above the equator. The active phased array SAR antenna is obliquely Earth-facing, aligned with the spacecraft velocity vector. The solar array is arranged at right angles to the orbit plane, consistent with the near-mid-day orbit phasing. The X-band down-link must be shared with optical instruments, which constrains SAR operation times.

Table 1. Selected PALSAR Mode Parameters				
Mode (selected)	**Resolution (m)**	**Swath (km)**	**Looks**	**Polarization**
Standard, stripmap	20 x 10	70	2	HH or VV
Fine	10	70	1	HH or VV
ScanSAR (5-beam)	~ 100	350	8	HH or VV
Dual polarization	(as above)	(as above)	(as above)	(HH, HV), (VV, VH)
Quad-pol	30 x 10	30	2	Full polarization
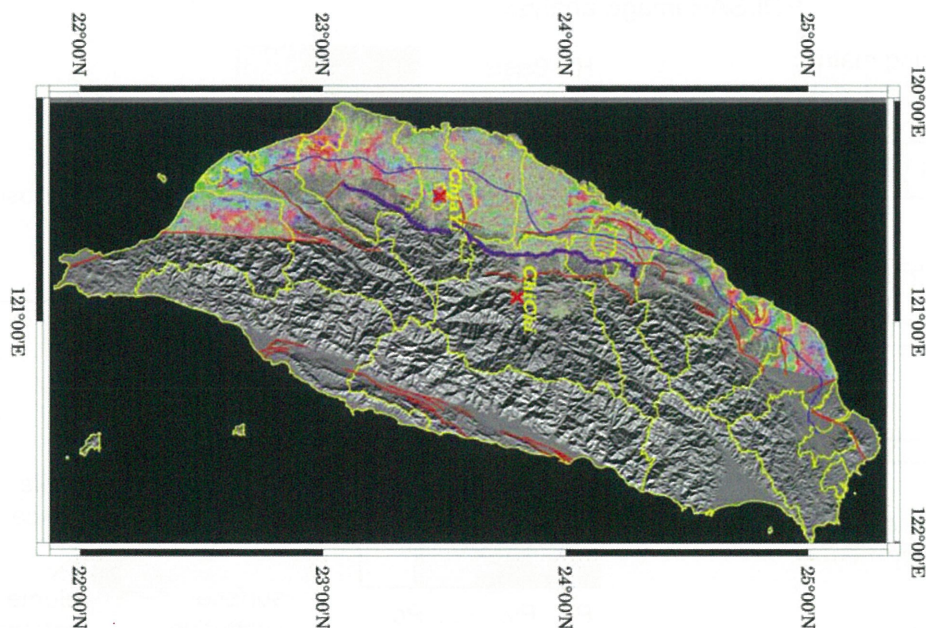
3.4.5.6.7.8

Polarimetric mode

Incident angle :23.1°

Date:2009/05/01

Path:442

Frame:430(3),440(4)

450(5),460(6)

470(7),480(8)

POLSAR image analysis

Scattering matrix = Quad. Pol. data

HH HV VV

<Average>

Covariance matrix
Coherency matrix

HV Basis

HH, 2HV, VV

Pauli Basis

HH-VV, 2HV, HH+VV

Color-Composite

Eigenvalue   Entropy, Alpha-angle, Anisotropy

λ1 λ2 λ3

Scattering Power Decomposition

Pd, Pv, Ps, Pc

Pd double bounce

Ps surface scattering

Pv volume scattering

Surface scattering **+** Double bounce **+** Volume scattering **+** Helix scattering

expansion matrix

$$\frac{1}{30}\begin{bmatrix} 15 & 5 & 0 \\ 5 & 7 & 0 \\ 0 & 0 & 8 \end{bmatrix}$$

$$\begin{bmatrix} 1 & \beta^* & 0 \\ \beta & |\beta|^2 & 0 \\ 0 & 0 & 0 \end{bmatrix} \qquad \begin{bmatrix} |\alpha|^2 & \alpha & 0 \\ \alpha^* & 1 & 0 \\ 0 & 0 & 0 \end{bmatrix} \qquad \frac{1}{4}\begin{bmatrix} 2 & 0 & 0 \\ 0 & 1 & 0 \\ 0 & 0 & 1 \end{bmatrix} \qquad \frac{1}{2}\begin{bmatrix} 0 & 0 & 0 \\ 0 & 1 & \pm j \\ 0 & \mp j & 1 \end{bmatrix}$$

$$\frac{1}{30}\begin{bmatrix} 15 & -5 & 0 \\ -5 & 7 & 0 \\ 0 & 0 & 8 \end{bmatrix}$$
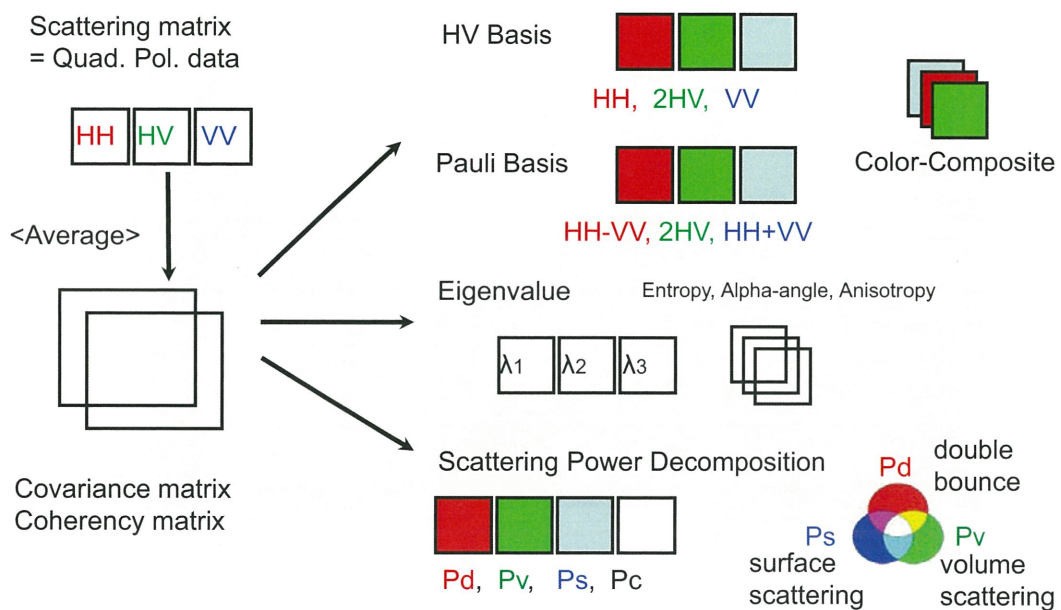
Scattering Power
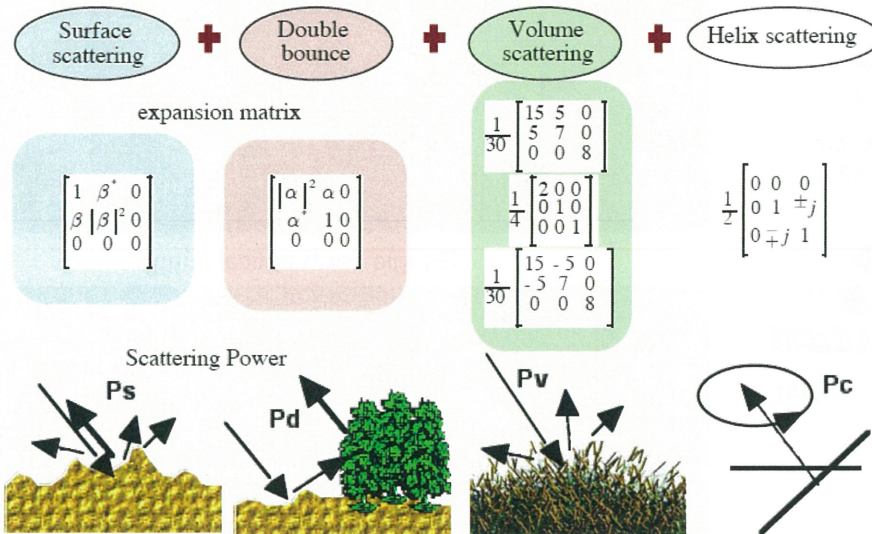
Ps   **Pd**   **Pv**   **Pc**

The four-component decomposition of scattering powers Ps, Pd, Pv, and Pc

---

4-compornent scattering power decomposition algorithm using rotated coherency matrix

Radar line of sight

Deorientation

$[T(\theta)]$ θ $[T]$

Rotation of imsge
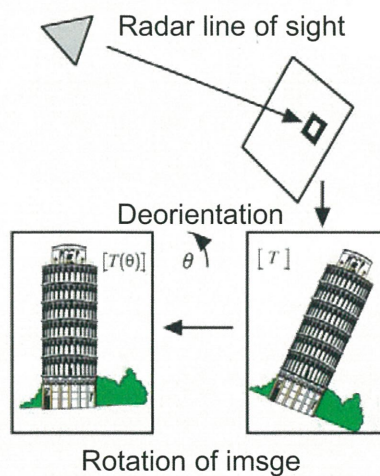
Taiwan

23.703N
120.875E

PASL110090501
14242009070200
02

Pd

Ps   Pv

Niigata University
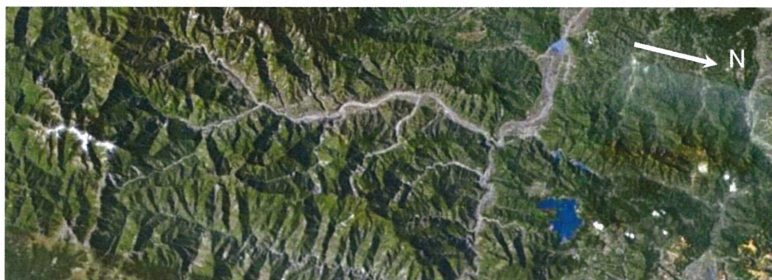
©METI, ERSDAC

2009/5/1

Google earth optical image

Scattering power decomposition (Pd, Ps, Pv)

Sun-Moon Lake

Scattering power decomposition

Pd
Ps   Pv

Niigata University

Pauli-basis

Taiwan
23.703N
120.875E

HV-basis

2009/5/1

PASL11009050114242200907020002

©METI, ERSDAC
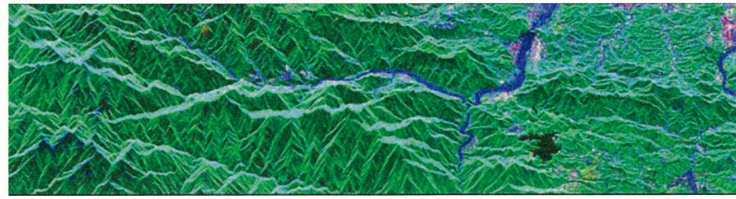
Pd, Pv, Ps
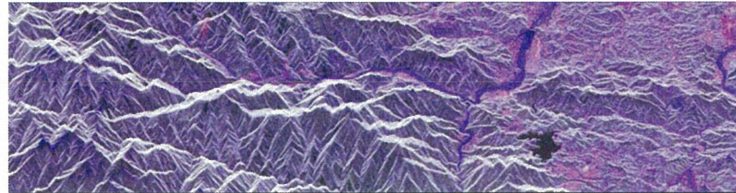
HH-VV, 2HV, HH+VV
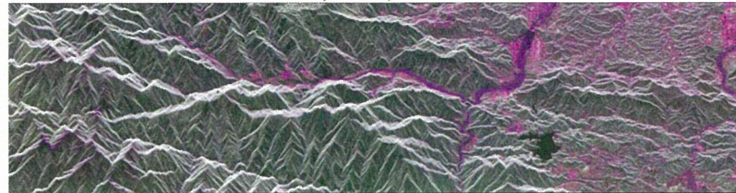
HH, 2HV, VV

The destruction along the Cheleng-Pu fault caused by the Chi-Chi earthquake of 1999 September 21

Scattering power decomposition

Pd
Ps · Pv

Niigata University
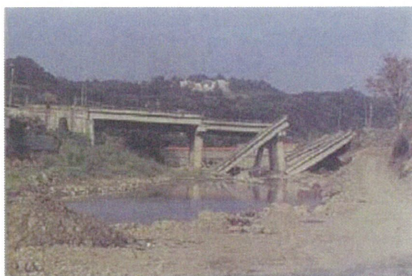
T33 Rotation

Pauli-basis

Taiwan
23.703N
120.875E

HV-basis

2009/5/1

PASL11009050114242200907020002

©METI, ERSDAC

Pd, Pv, Ps

HH-VV, 2HV, HH+VV

HH, 2HV, VV

ALOS-PALSAR Polarimetric Mode

Philippines

Ascending
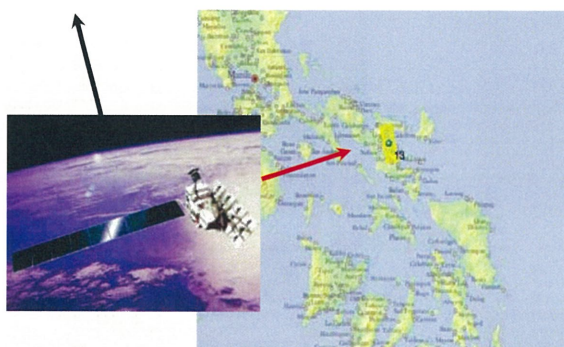
13.501N
123.551E

2009/5/30

Data no.
ALPSRP178330
260

© METI, JAXA

Yoshio Yamaguchi   **Niigata University**

WIDEBAND INTERFEROMETRIC SENSING AND IMAGING POLARIMETRY   22

Mt. Mayon – The pearl of the Orient

Philippines

13.498N
123.561E

2010/1/15

Data no.
ALPSRP211880260

©METI, JAXA

Scattering power
Decomposition

Mt. Mayon

Google Earth optical image
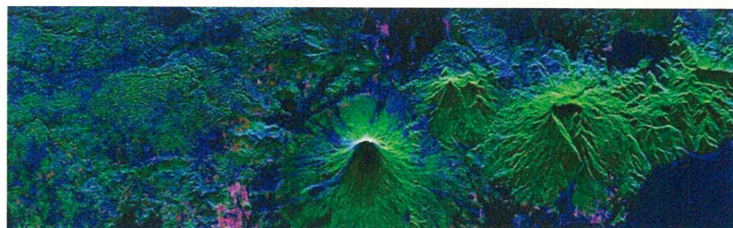
Decomposed image (Ps, Pd, Pv) with rotation 2*12 window

South-East Asia
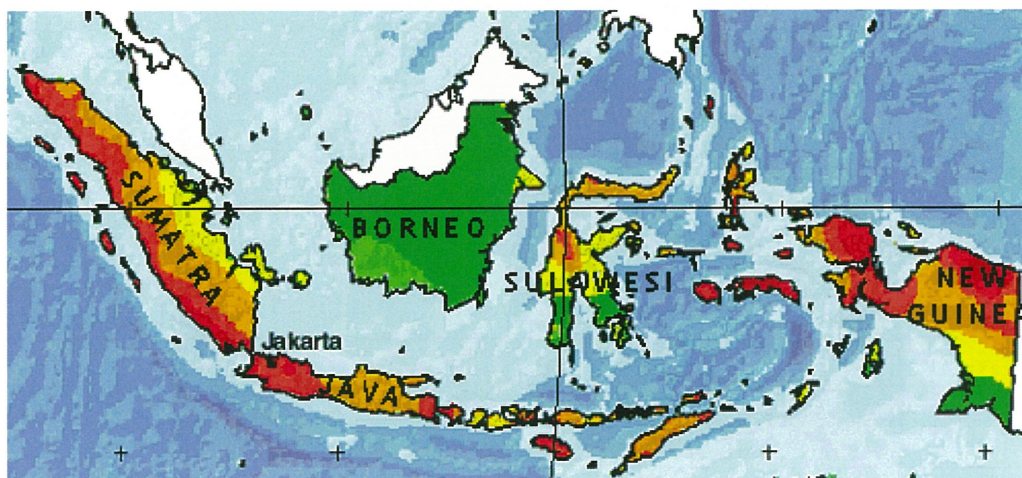
ALOS-PALSAR Polarimteric Mode

Ascending   Indonesia   2007/3/10

Data no.
ALPSRP059887030
ALPSRP059887040

2009/3/15

Data no.
ALPSRP167247030
ALPSRP167247040

Java
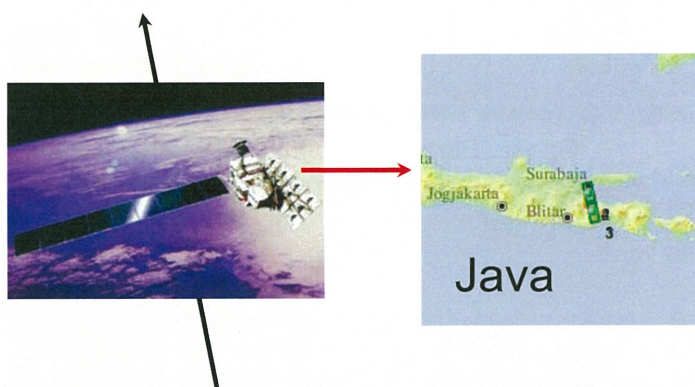
©JAXA, METI

Yoshio Yamaguchi

Niigata University

TUB-LAPAN-ORARI ORBIT PROFILE
(14 pass per 24 hr / orbit time 100 minutes and stay above horizon at about 10 minutes)

Indonesia

−7.942N
112.870E

2007/3/10

ALPSRP059887030-P1.1__A

©JAXA, METI

Scattering power
Decomposition
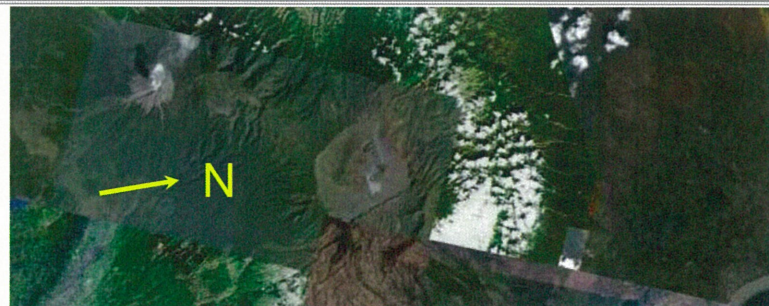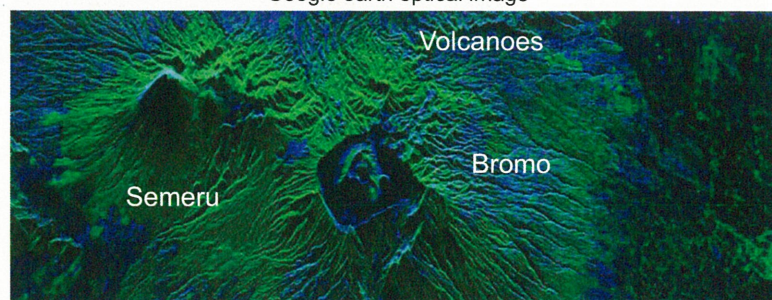
Pd

Ps   Pv

Niigata University

Google earth optical image

Decomposed image (Ps, Pd, Pv)

Mount Semeru puffs steam behind a cloud of sulphur gas from Mount Bromo in the Tengger caldera on Java.

WIDEBAND INTERFEROMETRIC SENSING AND IMAGING POLARIMETRY   29

Scattering power decomposition

Pd

Ps   Pv

Niigata University

2007/3/10

Pauli-basis

−7.942N

112.870E

HV-basis
Indonesia

ALPSRP059887030-P1.1__A
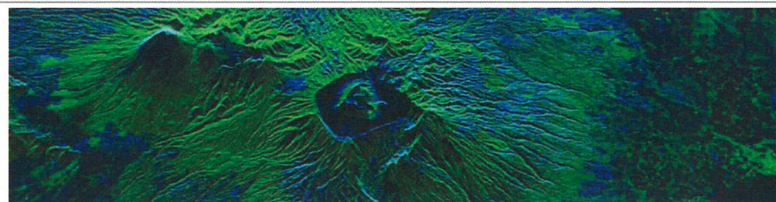
©JAXA, METI
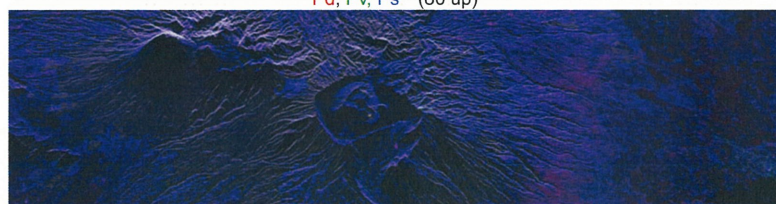
Pd, Pv, Ps (80 up)

HH-VV, 2HV, HH+VV (0-50 up)
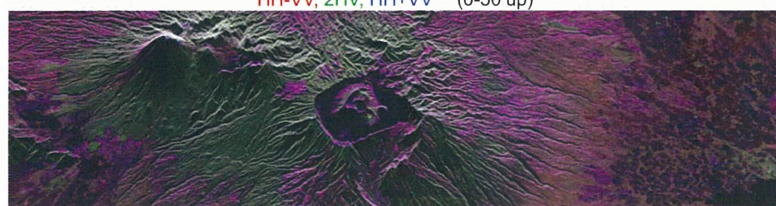
HH, 2HV, VV (50 up)

WIDEBAND INTERFEROMETRIC SENSING AND IMAGING POLARIMETRY   30

Scattering power decomposition

Pd
Ps   Pv
Niigata University

2007/3/10

T33 Rotation

Pauli-basis

HV-basis

Indonesia
−7.942N
112.870E

ALPSRP059887030-P1.1__A

©JAXA, METI

Pd, Pv, Ps (80 up)
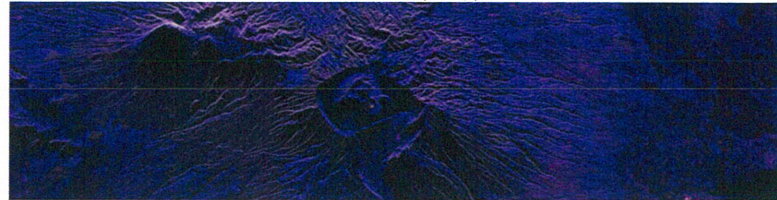
HH-VV, 2HV, HH+VV (80 up)
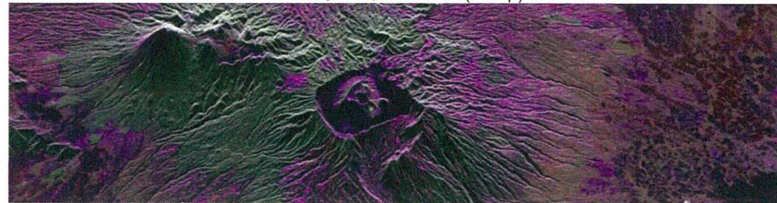
HH, 2HV, VV (50 up)

WIDEBAND INTERFEROMETRIC SENSING AND IMAGING POLARIMETRY   31
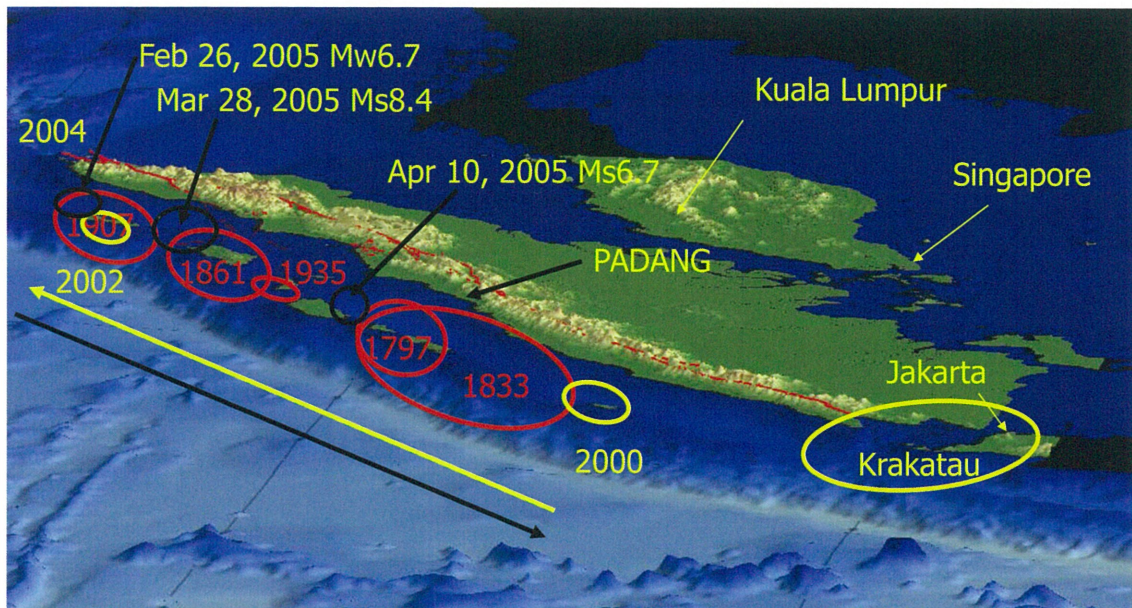
A flurry of ruptures have occurred since 2000

WIDEBAND INTERFEROMETRIC SENSING AND IMAGING POLARIMETRY   32

From Simkin and Fiske, 1983

Krakatau

8/26/1883

Next major eruption within 20 years

Indian Ocean Tsunamis: 1833 & 2004
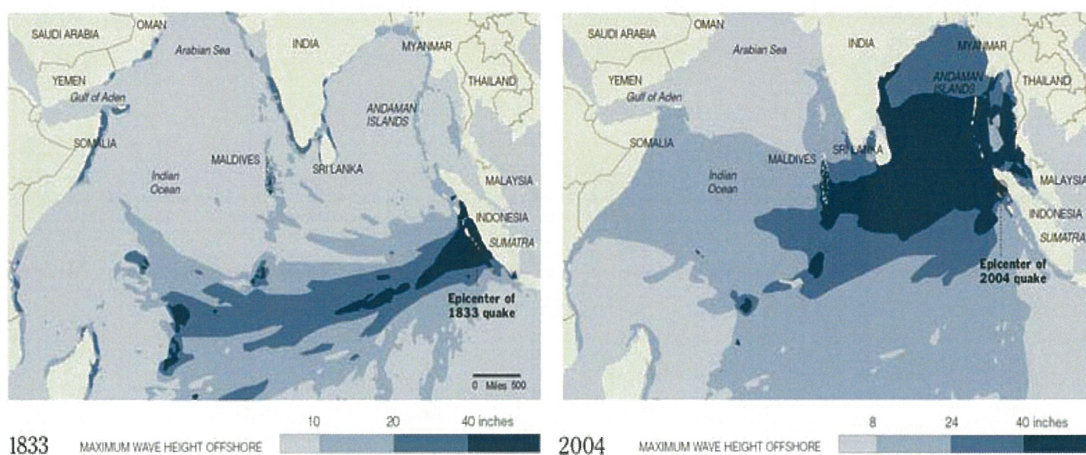
Hannah Fairfield/The New York Times, Science Section, January 4, 2005

Iceland, Eyjafjallajökull Volcano

Iceland, Eyjafjallajökull Volcano
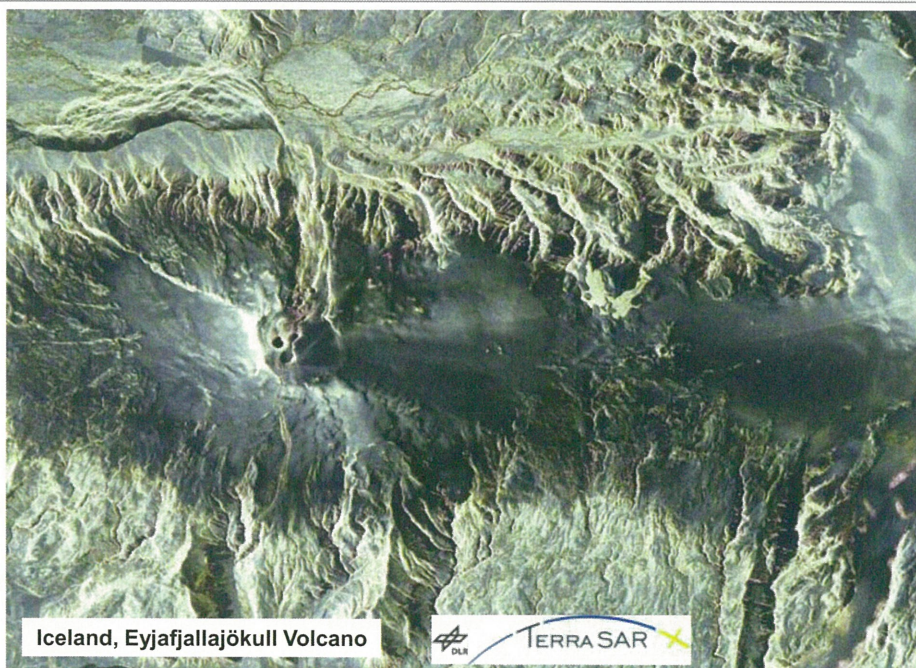
USGS ShakeMap : NEAR THE EAST COAST OF HONSHU, JAPAN
Fri Mar 11, 2011 05:46:23 GMT M 8.9 N38.32 E142.37 Depth: 24.4km ID:c0001xgp
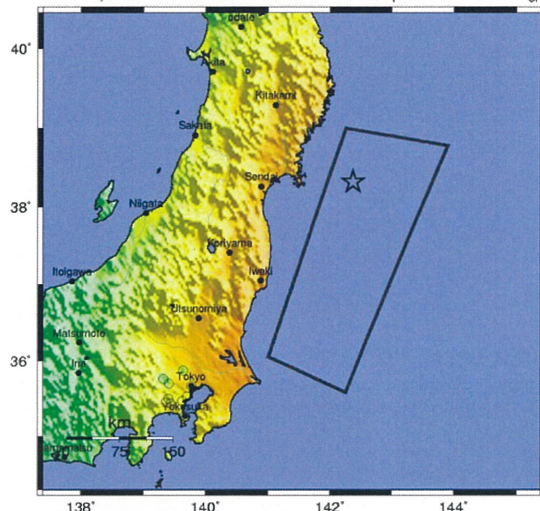
Map Version 4 Processed Fri Mar 11, 2011 01:23:57 AM MST – NOT REVIEWED BY HUMAN

PERCEIVED SHAKING	Not felt	Weak	Light	Moderate	Strong	Very strong	Severe	Violent	Extreme
POTENTIAL DAMAGE	none	none	none	Very light	Light	Moderate	Moderate/Heavy	Heavy	Very Heavy
PEAK ACC.(%g)	<.17	.17-1.4	1.4-3.9	3.9-9.2	9.2-18	18-34	34-65	65-124	>124
PEAK VEL.(cm/s)	<0.1	0.1-1.1	1.1-3.4	3.4-8.1	8.1-16	16-31	31-60	60-116	>116
INSTRUMENTAL INTENSITY	I	II-III	IV	V	VI	VII	VIII	IX	X+

Off-Tohoku M9 Seaquake & Tsunami 110311

Friday, March 11, 2011 at 05:46:23 UTC
Friday, March 11, 2011 at 02:46:23 PM at epicenter
Epicenter
38.322°N, 142.369°E

110311-Tsunami
OFF-TOHOKU-COASTAL-DISATER
Map-book, 2011 March/April

Clearly interpreting the Japanese

Expression Tsu-nami 津波
= Harbor-wave

Note that every harbor along the affected Eastern Off-Tohoku coastal corridor was severely damaged by the incoming and outgoing tsunami water-walls

ALOS/PALSAR Footprint

60.5km •Epicenter
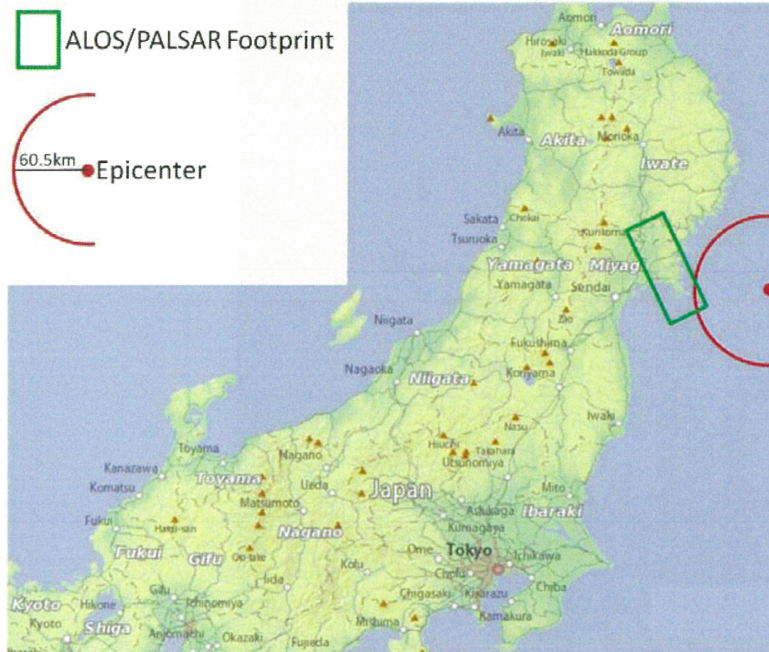
Off-Tohoku 9.0 Earthquake with Super-Tsunami
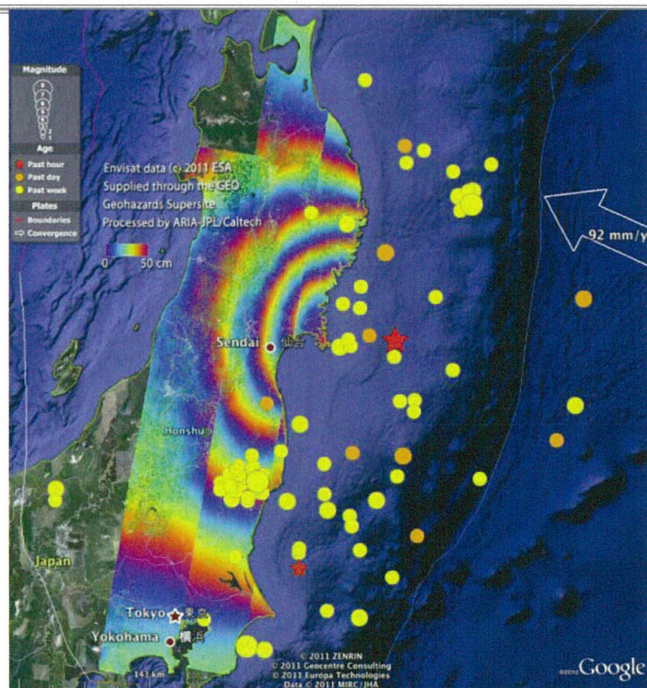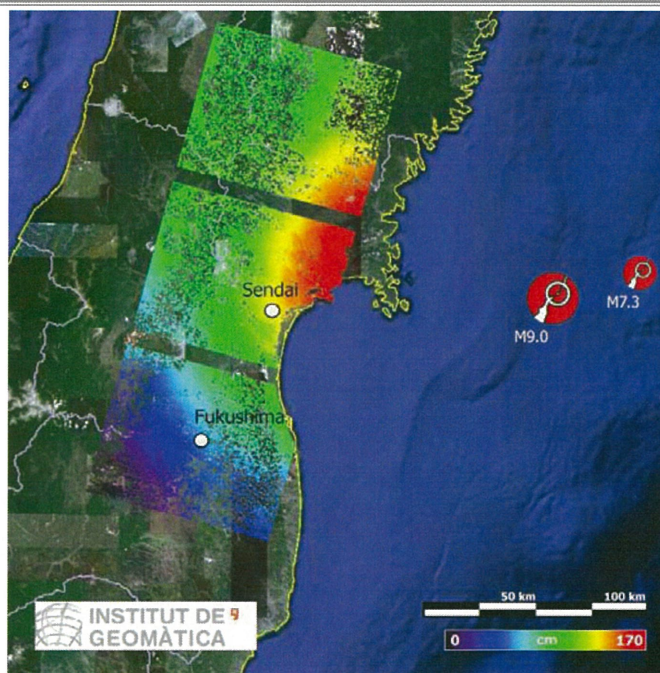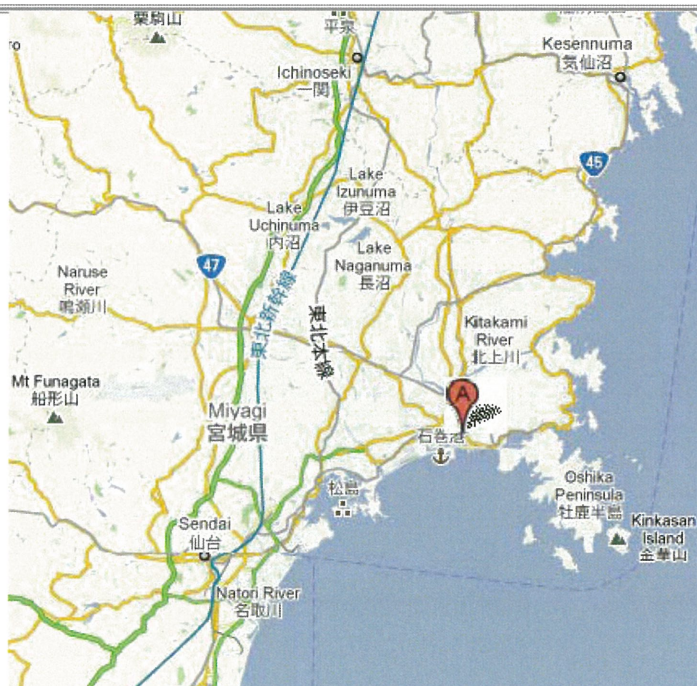
**Ishinomaki harbor
38*25'N, 141*18'E**

Destruction of City and Harbor of Ishinomaki by 110311 Tsu-nami (Harbor-Wave)

Off-Tohoku M9 Seaquake & Tsunami 110311
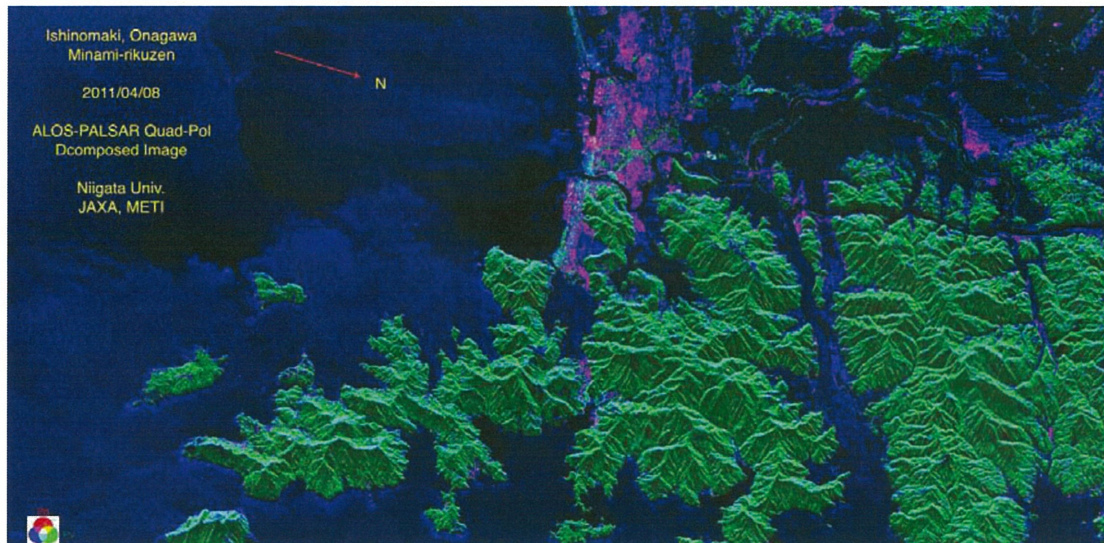
Ishinomaki, Onagawa
Minami-rikuzen

2011/04/08

ALOS-PALSAR Quad-Pol
Dcomposed Image

Niigata Univ.
JAXA, METI

Off-Tohoku M9 Seaquake & Tsunami 110311

ALPSRP257090760-P1.1__A

Scattering power
decomposition
S4R

20101121

Ishinomaki

Patch A

Patch B

ALPSRP277220760-P1.1_A

Scattering power
decomposition
S4R

20110408

Ishinomaki

Off-Tohoku M9 Seaquake & Tsunami 110311

collapsed by tsunami

covered by tsunami
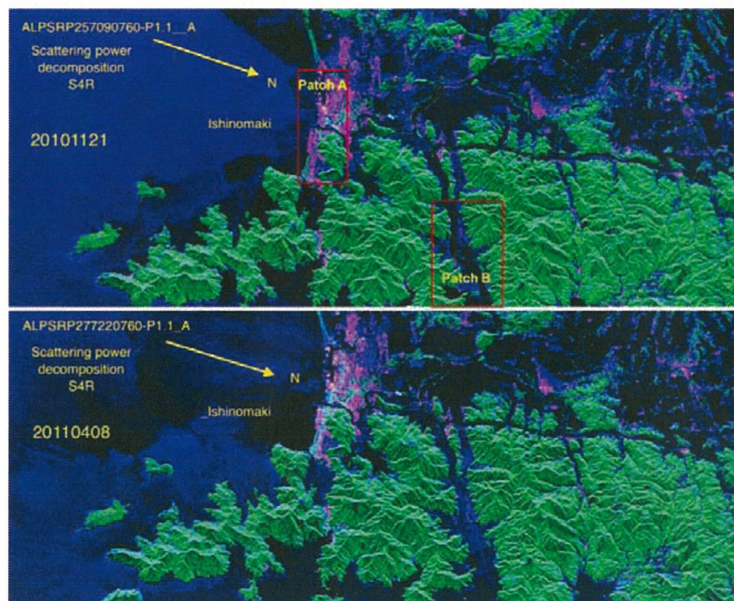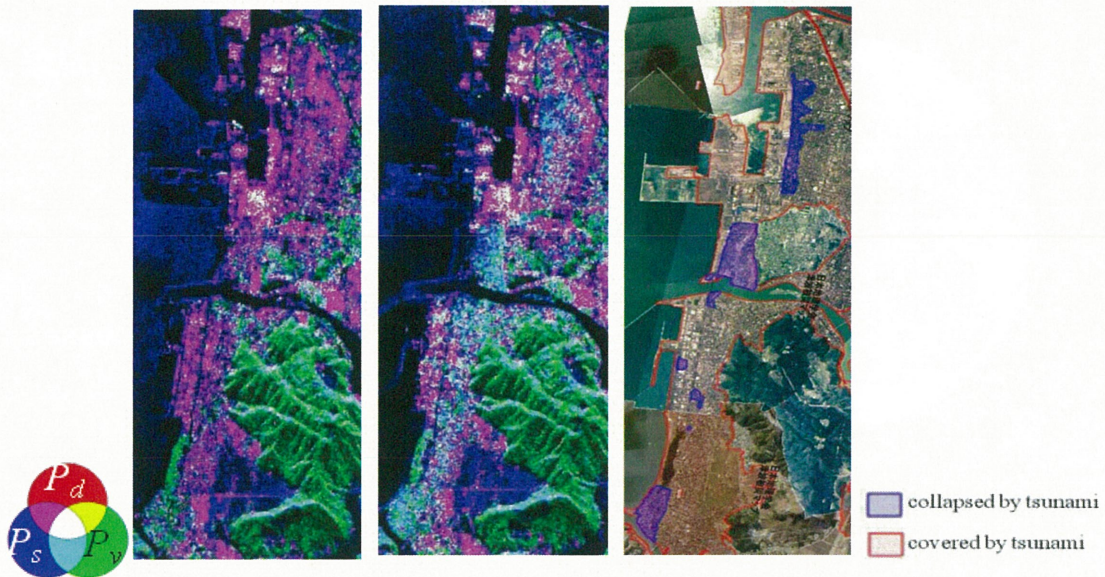
WIDEBAND INTERFEROMETRIC SENSING AND IMAGING POLARIMETRY   47

Off-Tohoku M9 Seaquake & Tsunami 110311

collapsed by tsunami

covered by tsunami
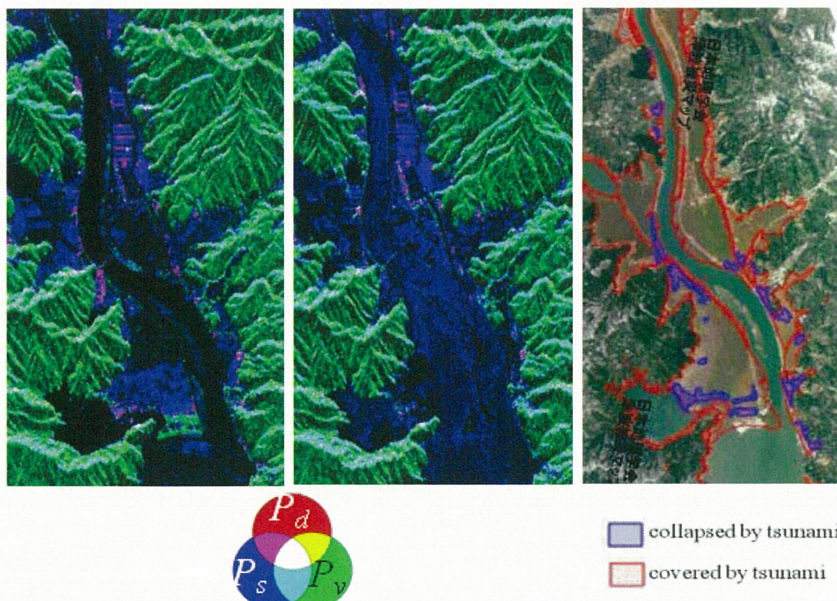
WIDEBAND INTERFEROMETRIC SENSING AND IMAGING POLARIMETRY   48
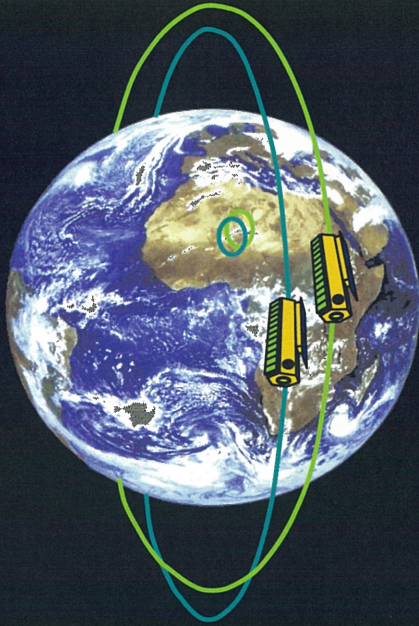
Global Monitoring of Bio-, Geo-, Cryo- and Hydrosphere processes with hith temporal and spatial resolution.
(Prof. A. Moreira – POLINSAR09)

Radar Interferometry

WIDEBAND INTERFEROMETRIC SENSING AND IMAGING POLARIMETRY   49
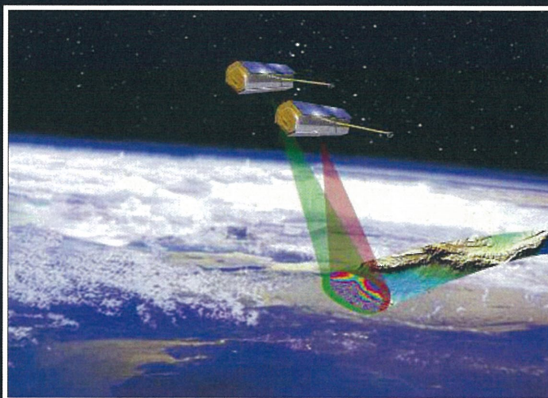
TerraSAR – X (1 & 2)
(2010)
Pol – InSAR Sensors
TanDEM-X
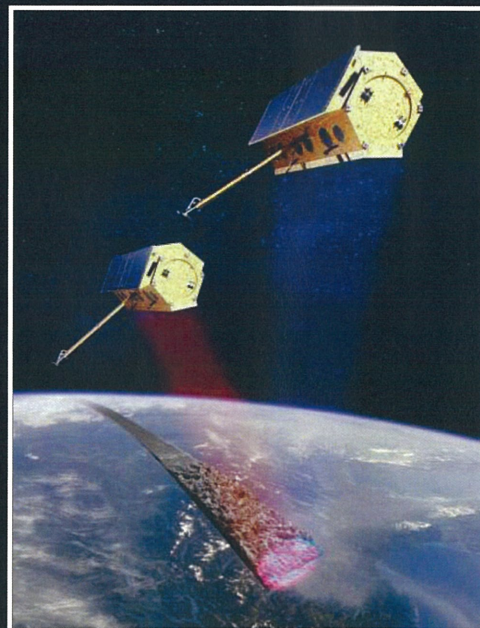
WIDEBAND INTERFEROMETRIC SENSING AND IMAGING POLARIMETRY   50

TandemSAR-L (Destiny): JPL & DLR
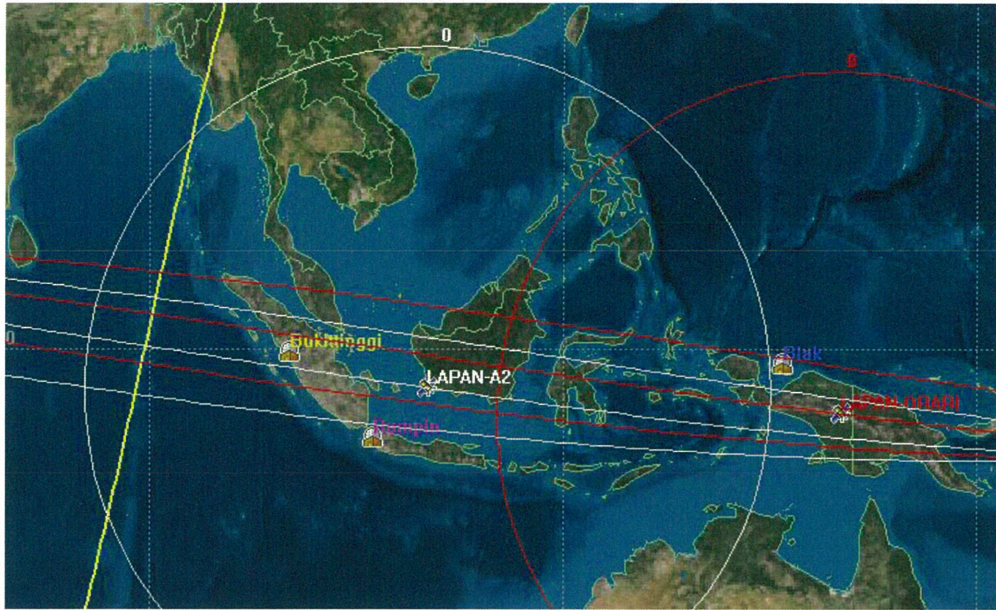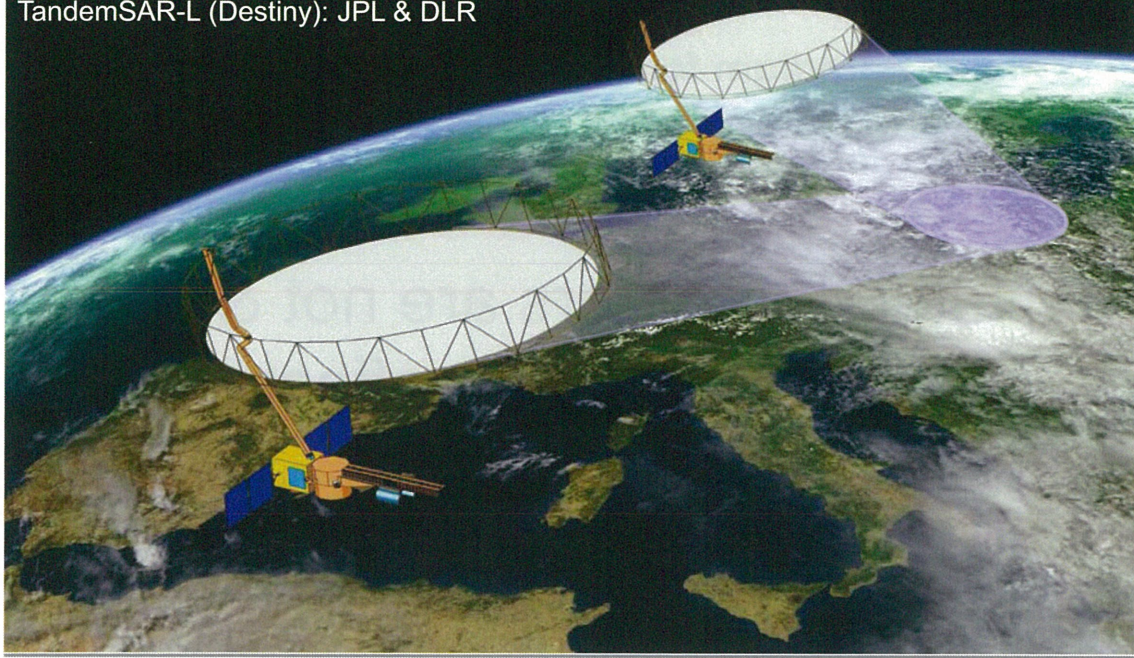

WIDEBAND INTERFEROMETRIC SENSING AND IMAGING POLARIMETRY   51

TUB-LAPAN-ORARI ORBIT PROFILE
(14 pass per 24 hr / orbit time 100 minutes and stay above horizon at about 10 minutes)
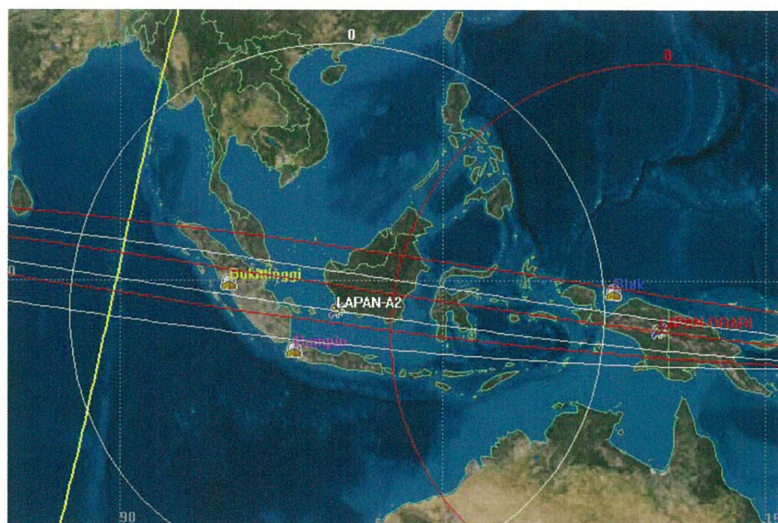
WIDEBAND INTERFEROMETRIC SENSING AND IMAGING POLARIMETRY   52

## Major Paradigm for Remote Sensing from Air and Space of the Terrestrial Covers:

"Natural hazards are inevitable! Natural disasters are not & how can we reduce aftereffects?"

Accomplished with the aid of fully Polarimetric POLinSAR Sensors at Very High Resolution and all pertinent bands:

ACQUISITION OF NEW BANDS FOR PASSIVE & ACTIVE SENSING

- **Deep earth sounding**   **ULF - LF**

- **Ground penetrating radar**   **LF - VHF**

- **Mineral resource exploration**   **HF - UHF**

- **Biomass and vegetative cover estimation**   **HF – EHF (P/L/C-Band)**

- **Man made surface structure monitoring**   **HF – EHF (C/X/K-Band)**

- **Atmospheric passive remote sensing**   **cm – sub-mm**

◊   We need to put our act together as the global remote sensing community and request from ITU/WMO the protection of the "fundamental natural resource: the e-m spectrum", and for providing the spectral bands for us to fulfill our professional duties as

"The Remote Sensing Pathologists and Radiologists of Earth and Planetary Covers"

Table - EESS (active) Frequency Bands between P-band and Ka-band (Huneycutt)

IEEE Band Designation	Frequency Band (MHz)	Bandwidth (MHz)	Allocation Status
P-band	432-438	6	Secondary (WRC'03)
L-band	1215-1300	85	Primary (WRC'97)
S-band	3100-3300	200	Secondary (WRC'97)
C-band	5250-5570	320	Primary (WRC'97)
X-band	8550-8650	100	Primary (WRC'97)
X-band	9300-9900	600	Primary (WRC'97, WRC'07)
Ku-band	13250-13750	500	Primary (WRC'97)
Ku-band	17200-17300	100	Primary (WRC'97)
K-band	24050-24250	200	Secondary (WRC'97)
Ka-band	35500-36000	500	Primary (WRC'97)

F-SAR technical characteristics (Reigber)

	X	C	S	L	P
RF [GHz]	9.6	5.3	3.25	1.325	0.35/0.45
Bw [MHz] PRF	760	400	300	150	100/50
[kHz] PT [kW]	5	5	5	10	10
Rg res. [m] Az	2.5	2.2	2.2	0.9	0.9
res. [m]	0.2	0.4	0.5	1.0	1.5
Rg cov. [km]	0.2	0.3	0.35	0.4	1.5
Sampling	12.5 (at max. bandwidth)				
Channels Data	8 bit real, 1000MHz				
rate	4	2	2	2	1
	247 MByte/s (per channel)				

FOUNDATIONS AND RELEVANCE OF MODERN EARTH REMOTE SENSING & ITS APPLICATIONS BY IMPLEMENTING SPACE-BORNE POL-IN-SAR

Conclusions:

The Electromagnetic **Vector (Polarization) Wave** Spectrum:
A Natural Global Treasure

Terrestrial Remote Sensing with POLinSAR for
The *Diagnostics of the Health of the Earth*

MMU UAVSAR: A Miniature C-band Synthetic Aperture Radar for Remote Sensing

Koo Voon Chet[1]

[1]*Multimedia University, Faculty of Engineering and Technology,*
Jalan Ayer Keroh Lama, 75450 Melaka, Malaysia, vckoo@mmu.edu.my

Abstract

A new miniature C-band SAR onboard an unmanned aerial vehicle (UAV) has been developed at the Multimedia University (MMU), Malaysia. Its major components include a microstrip antenna, a C-band RF transceiver, an onboard SAR recording and processing unit, and an embedded motion sensing system. The overall dimension of the system is approximately 1 ft^3, with total weight of 12 kg, thus suitable for a small UAV operation. This paper highlights the design, development and field measurement of the UAVSAR system.

Keywords : Synthetic Aperture Radar, Unmanned Aerial Vehicle, SAR processing

1. Introduction

Radar is a common tool used in many applications such as imaging, missile guidance, remote sensing and global positioning [1]. The Synthetic Aperture Radar (SAR) was first proposed by Carl Wiley in 1951 [2] which described the use of Doppler frequency analysis to improve radar image resolution. SAR has been proven to be very useful over wide ranges of applications, including high resolution geological and topological mapping, snow monitoring, military surveillance, and classification of earth terrain [3]-[4].

An Unmanned Aerial Vehicle (UAV) is an aircraft that is capable of operating without the presence of pilot or crew in the aircraft's cabin. It can be found extensively in the area of reconnaissance and surveillance as well as military purposes [5]. In recent years, UAV has become an alternative platform for Synthetic Aperture Radar (SAR). As compared to conventional airborne or space-borne SAR systems, UAV-based SAR system has lower operation cost, lower risk, and suitable for *in-situ* measurement where frequent revisit is required. The potential of UAVSAR in a diverse range of applications has led to the development of a number of UAVSAR systems [6]-[12].

In 2010, an experimental UAVSAR had been developed by the Multimedia University (MMU), under the collaboration with the Malaysian Remote Sensing Agency (ARSM) [13]. The platform used is a small UAV with allowable payload less than 25 kg and working space less than 1 ft^3.

2. System Overview

The specifications of the MMU UAVSAR system are summarized in Table 1. This SAR sensor operates at 5.3 GHz with moderate chirp bandwidth of 80 MHz. VV-polarization is chosen since it is sensitive to the vegetation's vertical canopy structure, and thus allowing crop type and growth stage discrimination. The backscattering data is collected in stripmap mode with nominal incidence angle of 30 degree. It can produce SAR imagery of all classes of terrain with backscattering coefficient between 0 and –30dB. The nominal speed and altitude of the UAV is 30 m/s and 1000 m, respectively.

Due to the limited payload capacity of the UAV, the SAR sensor must be very compact and small in size. Most of the subsystems are custom-built since there is no room to mount standard instruments such as signal generator and workstation onto the UAV platform. Figure 1 shows the overall arrangement of various subsystems housed in a three-layer chassis. Its total weight is approximately 12 kg.

Table 1 MMU UAVSAR's Specifications

System Parameters	Specifications
Mode of Operation	Stripmap
Operating Frequency	5.3 GHz (C-band)
Bandwidth	80 MHz
Polarization	Single, VV
Spatial Resolution	3 m × 3 m
Nominal Platform Speed	30 m/s
Nominal Platform Height	1000 m
Payload Weight	< 25 kg
Allowable Working Space	12" (L) × 9" (W) × 12" (H)
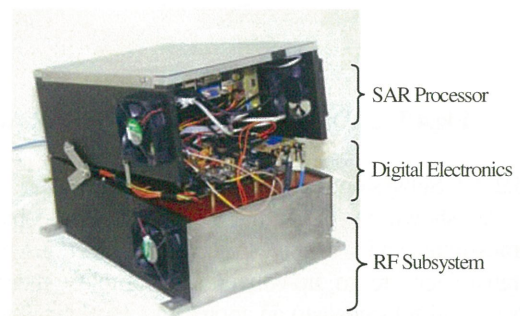
Fig.1 The MMU UAVSAR Sensor

3. Subsystem Design

3.1. Antenna Design

Based on the specifications above, a lightweight, small size, linearly polarised microstrip array antenna panel is required. The centre frequency for the antenna array is set at 5.3 GHz, with SWR less than 2. The directive gain of the panel is more than 25dBi for good detection in the presence of noise. Fig. 2 shows the typical slant range geometry of the UAVSAR.
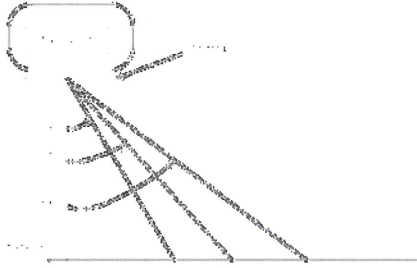
Fig.2 Slant Range Geometry

The azimuth array is designed with 16 elements spaced 44 mm apart [14]. The 3 dB beamwidth is about 4°. No amplitude variation is planned in the azimuth plane, thus power will be uniformly fed resulting in a sharp pencil beam . The final antenna prototype is shown in Fig.3 and the three-dimensional radiation pattern of the array is given in Fig.4.
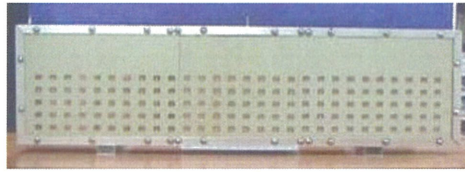
Fig.3 The UAVSAR Antenna Prototype
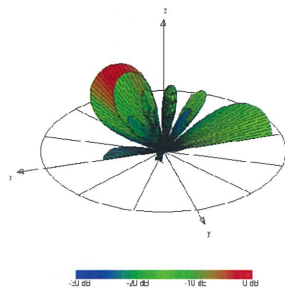
Fig.4 The 3D Radiation Pattern of the SAR Antenna

3.2. RF Subsystem Design

As shown in Fig.5, the RF subsystem consists of a transmitter and a receiver. The main functions of the RF transmitter are to up-convert and amplify the incoming baseband IQ signals to an appropriate level suitable for long distance transmission. The desired chirp signals (IQ) are generated using FPGA-based DDS architecture [15]. These signals are fed into the RF subsystem. Dual antenna system is employed in this design to provide high isolation between the transmitter and the receiver. The received echoes are further amplified and down-converted to baseband IQ signals, which will then be fed to a dual-channel high speed ADC.
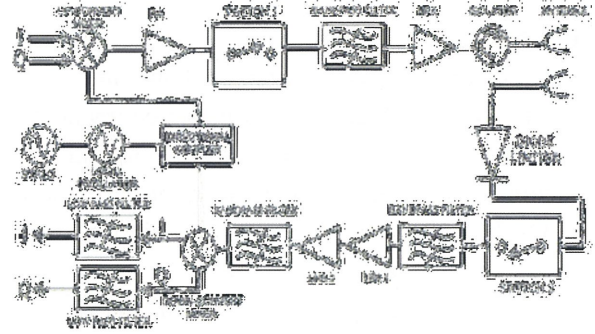
Fig.5 RF Transceiver Design

3.3. Embedded UAVSAR Recording and Processing Unit

Fig. 6 shows the general flow of the embedded UAVSAR data recording and processing unit. The raw data is acquired using a high speed 12-bit dual channel analog-to-digital converter (ADC) with data rate of 7.5 Mbps. The digitized raw data are stored in a solid-state drive and a copy of it will be sent to the onboard SAR processor. The onboard SAR processor is implemented using an embedded high performance computer [16]. Range-doppler algorithm is employed for real-time imaging, while omega-*k* algorithm is used for high-resolution image formation.
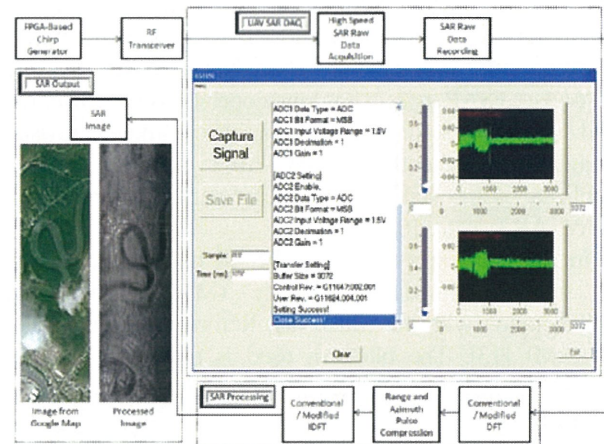
Fig.6 Overview of the UAVSAR Recording and Processing

3.4. Embedded Motion Sensing Unit

The embedded motion sensing unit consists of two main components namely the Inertial Measurement unit (IMU) and the Global Positioning System (GPS) receiver. The integrated IMU-GPS system provides all the necessary motion data (such as platform speed, acceleration, yaw-pitch-roll angles) in real-time for precise motion sensing. Fig.7 shows the embedded motion sensing unit with built-in

IMU and GPS receiver. A 8-bit microcontroller is used to read and transfer both the IMU and GPS data to a single board computer for recording and further processing.
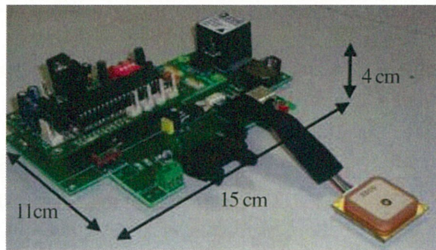
Fig.7 The Embedded Motion Sensing Unit

4. SAR Experiments and Preliminary Flight Tests

In order to verify the performance of the SAR system before the UAV flight mission, a series of ground experiments has been conducted. Fig.8 shows the measurement setup where the SAR system was mounted onto a truck. The truck was then travelled at a constant speed for approximately 1 km to perform SAR imaging. The processed SAR image is shown in Fig.9. It is clearly shown that multiple strong targets are observed at distance more than 1.2 km.

Fig.8 Ground-based SAR Experiment
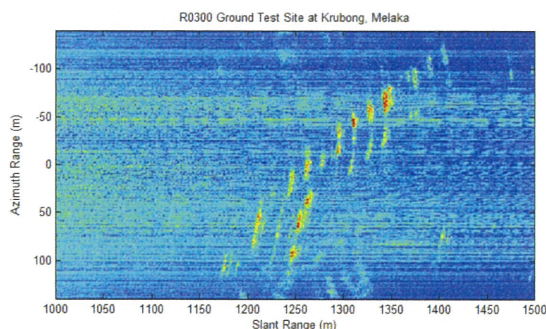
Fig.9 SAR Image of a Ground Test Site

Finally, the SAR sensor was installed into a small UAV for flight test. As shown in Fig.10, the allowable working space is a small opening of approximately 12" (L) × 9"(W) × 12" (H). The SAR antenna was mounted underneath the UAV's fuselage as illustrated in Fig.11.

Fig.10 Installing SAR Sensor into UAV

Fig.11 SAR Antenna Mounted Underneath the Fuselage

A sample of the SAR images captured on December 2010 is presented in Fig.12, with comparison to the Google Earth map of the same site. Clear signatures of river, roads, urban and vegetated areas are observed.

Fig.12 A Sample of SAR Image Taken at Mersing Test Site, Johor, Malaysia on December 2010

5. Summary

A new miniature C-band SAR onboard an unmanned aerial vehicle (UAV) has been successfully developed at the Multimedia University (MMU), Malaysia. It will be used for remote sensing and surveillance applications in near future.

Acknowledgements

References

[1] Skolnik, M. I., *Radar Handbook*, McGraw-Hill, New York, 1970

[2] Wiley, C. A., "Pulse Doppler radar methods and apparatus", *United States Patent*, No. 3, 196, 436, Filed, August 1954, 1965.

[3] Storvold, R., E. Malnes, Y. Larsen, K. A. Hogda, S.-E. Hamran, K. Mueller, and K. Langley, "SAR remote sensing of snow parameters in Norwegian areas — Current status and future perspective," *Journal of Electromagnetic Waves and Applications*, Vol. 20, No. 13, 1751–1759, 2006.

[4] Kong, J. A., S. H. Yueh, H. H. Lim, R. T. Shin, and J. J. van Zyl, "Classification of Earth terrain using polarimetric synthetic aperture radar images," *Progress In Electromagnetics Research*, PIER 03, 327–370, 1990.

[5] Taylor, A. J. P., *Jane's Book of Remotely Piloted Vehicles*.

[6] Zaugg EC, Hudson DL, Long DG, "The BYU SAR: A Small, Student-Built SAR for UAV Operation", *IEEE International Geoscience and Remote Sensing Symposium*, 2006, 411-414, 2006.

[7] Wheeler, K., Hensley, S., Lou, Y., Miller, T., Hoffman, J., "An L-band SAR for repeat pass deformation measurements on a UAV platform", *Proceedings of the IEEE Radar Conference*, 317-322, 2004.

[8] Rosen, P.A., Hensley, S., Wheeler, K., Sadowy, G., Miller, T., Shaffer, S., Muellerschoen, R., Jones, C., Zebker, H., Madsen, S., "UAVSAR: a new NASA airborne SAR system for science and technology research", *IEEE Conference on Radar*, 22-29, 2006.

[9] Weiss, M., Peters, O., Ender, J., "A three dimensional SAR system on an UAV", *IEEE International Geoscience and Remote Sensing Symposium*, 5315-5318, 2007.

[10] Seong Kim, Al Pergande, Hughen, J., "Low cost ka band SAR/ISAR for UAV applications", *Proceedings IEEE Aerospace Conference*, Vol. 2, 1097-1102, 2005.

[11] Wells, L., Sorensen, K., Doerry, A., Remund, B., "Developments in SAR and IFSAR Systems and Technologies at Sandia National Laboratories", *Proceedings IEEE Aerospace Conference*, Vol.2, 1085-1095, 2005.

[12] Josaphat Tetuko Sri Sumantyo: *Development of Circularly Polarized Synthetic Aperture Radar (CP-SAR) Onboard Small Satellite*. PIERS Proceedings, Marrakesh, MOROCCO, March 20-23, 334-341, 2011.

[13] Y.K. Chan, V.C.Koo, C.Y.Ang, K.S.Yee, and M.Y.Chua, "Design and Development of A C-Band RF Transceiver for UAVSAR", *Progress In Electromagnetics Research C* (PIER C), Vol.24, pp.1-12, 2011.

[14] P. N. Tan, T. S. Lim, V. Gobi, and Y. K. Chan, "Design and Development of a Dual Operating Mode Microstrip Patch Antenna for Unmanned Aerial Vehicle Synthetic Aperture Radar", *Progress In Electromagnetics Research C* (PIER C), Vol.27, pp.143-156, 2012.

[15] M.Y. Chua and V.C. Koo: *FPGA-based Chirp Generator for High Resolution UAV SAR*. Progress In Electromagnetics Research (PIER), Vol.99, 2009, pp.71-88.

[16] C. H. Lim, C. S. Lim, M. Y. Chua, Y. K. Chan, T. S. Lim, and V. C. Koo: *A New Data Acquisition and Processing System for UAVSAR*. IEICE Electronics Express, Vol.8, No.20, 2011, pp.1716-1722.

Polarimetric Synthetic Aperture Radar: Theory and Applications

Yoshio Yamaguchi

Dept. of Information Eng., Niigata University, 950-2181 Japan, yamaguch@ie.niigata-u.ac.jp

Abstract

Scattering power decomposition theory and some images of fully polarimetric synthetic aperture radar data are presented for disaster monitoring. Utilization of fully polarimetric data can derive full color images with red–green–blue color coding, red for the double-bounce power, green for the volume scattering power, and blue for the surface scattering power, for which each color brightness corresponds to the magnitude. Since disaster causes the change of each scattering power, it becomes easy for everyone to recognize the change by color in the decomposition image when time series data sets are available. By applying the four-component scattering power decomposition to fully polarimetric data acquired with Advanced Land Observing Satellite (ALOS) Phased Array type L-band Synthetic Aperture Radar (PALSAR), we present several images for natural disaster monitoring on volcano activity, snow accumulation, land slide and tsunami effect caused by great earthquake. It is seen in the polarimetric decomposition images that most disaster areas show increasing surface scattering power compared to those in normal situations.

Keywords: Polarimetric Synthetic Aperture Radar, Scattering power decomposition

I. Introduction

Since the launch of ALOS-PALSAR in 2006, a large number of fully polarimetric (Quad-pol) data sets have been acquired from space [1]-[2]. Although the fully polarimetric mode is hitherto an experimental one, it has provided us with precious data sets of various places spread over the planet earth. The total number of scenes exceeds more than 274,000.

There are various image analysis methods for fully polarimetric data sets [3]-[8]. The representative and fundamental methods are based on incoherent analysis dealing with ensemble averaging of several pixels retaining the second order statistics of polarimetric information. The most frequently used method is the H-Alpha-Anisotropy developed by Cloude and Pottier [3]-[5] based on the eigenvalues of coherency matrix. The second one is the scattering power decomposition method [6]-[8] based on physical scattering models, which was first developed by A. Freeman and S. Durden [6]. The current paper describes the four-component decomposition with rotation of the coherency matrix for more accurate polarimetric synthetic aperture radar (POLSAR) image decomposition and scatterer classification.

The scattering power decomposition scheme divides polarimetric data of the imaging pixel area into surface scattering, double bounce scattering, volume scattering, and helix scattering components. These scattering powers are calculated very easily, and are used to compose full color images with RGB color-coding. They have been successfully applied to POLSAR image analysis since color-coded images are easier to understand, and since each color represents a specific scattering mechanism.

II. Scattering Power Decomposition

If scattering matrix data set of the imaging pixel area is acquired, the corresponding coherency matrix can be created, which retains the second order statistics of polarimetric information. The ensemble average of the coherency matrix is given as

$$\langle [T] \rangle = \langle k_P k_P^\dagger \rangle \ , \ \text{with} \quad k_P = \frac{1}{\sqrt{2}} \begin{bmatrix} S_{HH} + S_{VV} \\ S_{HH} - S_{VV} \\ 2S_{HV} \end{bmatrix} \tag{1}$$

where $\dagger$ denotes complex conjugation and transposition, $<\ >$ denotes ensemble average.

Then the measured coherency matrix is rotated by the angle $\quad 2\theta = \frac{1}{2} \tan^{-1} \left(\dfrac{2 \, \text{Re} \, (T_{23})}{T_{22} - T_{33}} \right)$ $\tag{2}$

so as to minimize the T33 term in (1) using

$$\langle [\ T(\theta)\ ]\rangle = [R_P(\theta)]\,\langle [\ T\ ]\rangle\,[R_P(\theta)]^{\dagger}\ ,\text{with}\quad [\ R_p(\theta)\ ] = \begin{bmatrix} 1 & 0 & 0 \\ 0 & \cos 2\theta & \sin 2\theta \\ 0 & -\sin 2\theta & \cos 2\theta \end{bmatrix} \tag{3}$$

Then the rotated coherency matrix (measured) is expanded into four sub-matrices which correspond to surface scattering, double bounce scattering, volume scattering, and helix scattering mechanisms

$$\langle [T(\theta)]\rangle = f_s\,\langle [T]\rangle_{surface} + f_d\,\langle [T]\rangle_{double} + f_v\,\langle [T]\rangle_{vol} + f_c\,\langle [T]\rangle_{helix} \tag{4}$$

where $f_s, f_d, f_v,$ and f_c are the expansion coefficients to be determined. These four terms have been derived based on the physical scattering models as shown in Fig. 1. The derivation of scattering power is provided in [8]. The algorithm for the four-component scattering power is shown in Fig. 2.
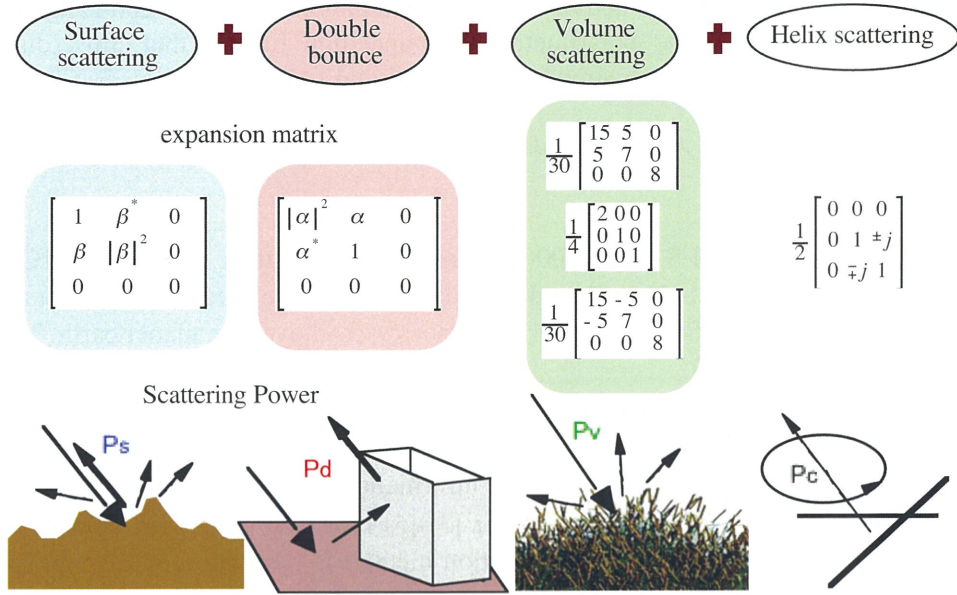
Fig. 1 The four-component decomposition of scattering powers Ps, Pd, Pv, and Pc.

III.   Decomposition Results for Disaster Monitoring

A great earthquake with magnitude 9.0 hit East Japan on March 11, 2011. This disaster was accompanied by a huge tsunami which attacked the eastern seashore of Tohoku area in Japan. ALOS-PALSAR had acquired fully polarimetric data over Ishinomaki area before and after the earthquake on 20101121 and 20110408, respectively. The area was heavily destroyed not only by the earthquake by also by the tsunami. The major part of Ishinomaki-city and neighboring Onagawa-cho were completely destroyed and washed out by the tsunami. Fig. 3 shows the corresponding ALOS-PALSAR polarimetric images of Ishinomaki-city before and after the earthquake together with ground truth data. Although the second data take (April 8) was 28 days after the earthquake (March 11), it is possible to confirm several changes: red color (man-made) area turned into blue color (surface scattering due to completely washed out area by tsunami) near by seashore in Fig. 3 (a) and (b). The ground truth was carried out by Association of Japanese Geographers and Geospatial Information Authority of Japan. Fig. 3 (c) shows the extent of disaster area with blue indicating destroyed by tsunami and with orange indicating flooded by tsunami. The legend color "orange" in Fig. 3 (c) denotes the flooded area where the tsunami hit. But there still remain some buildings/houses and man-made structures after the tsunami. The "blue" color in Fig. 3 (c) denotes the area where almost all buildings/houses and man-made structures were collapsed/destroyed and washed by the tsunami, leaving bare suf: on the ground. We can see fairly well correspondence in Fig. 3 (b) and (c).

Rotation of data matrix

$$\langle [T] \rangle = \begin{bmatrix} T_{11} & T_{12} & T_{13} \\ T_{21} & T_{22} & T_{23} \\ T_{31} & T_{32} & T_{33} \end{bmatrix} = \frac{1}{n} \sum^{n} k_p k_p^{\dagger} \qquad \theta = \frac{1}{4} \tan^{-1}\left(\frac{2 \operatorname{Re}\{T_{23}\}}{T_{22} - T_{33}} \right)$$

$$\langle [T'] \rangle = [R(\theta)] \langle [T] \rangle [R(\theta)]^{\dagger} \qquad [R(\theta)] = \begin{bmatrix} 1 & 0 & 0 \\ 0 & \cos 2\theta & \sin 2\theta \\ 0 & -\sin 2\theta & \cos 2\theta \end{bmatrix}$$

Four-component decomposition

$$P_c = 2\left| \operatorname{Im}\left(T'_{23}\right) \right| \qquad \text{Helix scattering power}$$

Volume scattering power

$$10 \log \left| \frac{T'_{11} + T'_{22} - 2\operatorname{Re}\left(T'_{12}\right)}{T'_{11} + T'_{22} + 2\operatorname{Re}\left(T'_{12}\right)} \right|$$

-2 dB 2 dB

$$P_v = \frac{15}{4} T'_{33} - \frac{15}{8} P_c \qquad P_v = 4 T'_{33} - 2 P_c \qquad P_v = \frac{15}{4} T'_{33} - \frac{15}{8} P_c$$

$$\text{if} \quad P_v < 0, \ \text{then } P_c = 0 \quad (\text{remove helix scattering})$$

$$S = T'_{11} - \frac{1}{2} P_v \qquad\qquad S = T'_{11} - \frac{1}{2} P_v \qquad\qquad S = T'_{11} - \frac{1}{2} P_v$$

$$D = T'_{22} - \frac{7}{30} P_v - \frac{1}{2} P_c \qquad D = T'_{22} - T'_{33} \qquad D = T'_{22} - \frac{7}{30} P_v - \frac{1}{2} P_c$$

$$C = T'_{12} - \frac{1}{6} P_v \qquad\qquad C = T'_{12} \qquad\qquad C = T'_{12} + \frac{1}{6} P_v$$

$$TP = T'_{11} + T'_{22} + T'_{33} \qquad P_v + P_c > TP \qquad \text{yes} \qquad P_s = P_d = 0$$

no

$$C_0 = T'_{11} - T'_{22} - T'_{33} + P_c$$

$$C_0 > 0$$

Surface scattering — yes Double bounce scattering — no

$$P_s = S + \frac{|C|^2}{S} \qquad\qquad P_d = D + \frac{|C|^2}{D}$$

$$P_d = D - \frac{|C|^2}{S} \qquad\qquad P_s = S - \frac{|C|^2}{D}$$

$$\text{if} \quad P_s > 0, P_d > 0 \ \mid \ P_s > 0, P_d < 0 \ \mid \ P_s < 0, P_d > 0$$

Decomposed power			P_c
P_s, P_d, P_v, P_c	$P_v, P_c \quad P_d = 0$	$P_v, P_c \quad P_s = 0$	$P_s = P_d = 0$
$TP = P_s + P_d + P_v + P_c$	$P_s = TP - P_v - P_c$	$P_d = TP - P_v - P_c$	$P_v = TP - P_c$
Four comp.	Three comp.	Three comp.	Two comp.

Fig. 2 Four-component scattering power decomposition algorithm using rotated coherency matrix

<div align="center">(a)   (b)   (c)</div>

Fig. 3   Ishinomaki area suffered from tsunami caused by great earthquake of East Japan 2011. (a) before, (b) after the earthquake and tsunami. Color composite images are generated by scattering power decomposition with surface scattering (Blue), double bounce scattering (Red), and volume scattering (Green), (c) ground truth data: Blue color areas show totally destroyed areas by tsunami. Orange color denotes the area flooded by tsunami, provided by Association of Japanese Geographers, and Geospatial Information Authority of Japan.

IV. Concluding remarks

It is seen in the polarimetric decomposition images that most disaster areas show increasing surface scattering power compared to those in normal situations.

References

[1]   [Online]. Available: http://www.eorc.jaxa.jp/ALOS/en/about/palsar.htm

[2]   [Online]. Available: http://www.palsar.ersdac.or.jp/e/index.shtml

[3]   J. S. Lee and E. Pottier, *Polarimetric radar imaging from basics to applications*, (398 pages), CRC Press, 2009

[4]   S. R. Cloude and E. Pottier, "A review of target decomposition theorems in radar polarimetry," *IEEE Trans. Geosci. Remote Sens.*, vol. 34, no. 2, pp. 498-518, Mar. 1996.

[5]   E. Pottier and J. S. Lee, "Application of the <<H/A/ $\overline{\alpha}$ >> polarimetric decomposition theorem for unsupervised classification of fully polarimetric SAR data on the Whishart distribution," *Proc. of EUSAR2000*, pp. 265-268, May 2000

[6]   A. Freeman, and S. Durden, "A three-component scattering model for polarimetric SAR data," *IEEE Trans. Geosci. Remote Sens.*, vol. 36, no. 3, pp. 963-973, May 1998.

[7]   Y. Yamaguchi, T. Moriyama, M. Ishido, and H. Yamada, "Four-component scattering model for polarimetric SAR image decomposition," *IEEE Trans. Geosci. Remote Sens.*, vol. 43, no. 8, pp. 1699-1706, Aug. 2005.

[8]   Y. Yamaguchi, A. Sato, W. -M. Boerner, R. Sato, H. Yamada, "Four-component scattering power decomposition with rotation of coherency matrix," *IEEE Trans. Geosci. Remote Sens.*, vol. 49, no. 6, pp. 2251-2258, June 2011.

CERES Symposium, Chiba, 1st March 2012

Synthetic Aperture Radar Interferometry: techniques and applications

Daniele Perissin

daniele.perissin@cuhk.edu.hk

ISEIS, CUHK, Hong Kong

Foreword

The Speaker

2002 Master in Telecommunication Engineering, Politecnico di Milano, Italy
2006 PhD degree in Information Technology, Politecnico di Milano, Italy
Till 2009 Assistant researcher in Politecnico di Milano, Italy

Since 2nd October 2009, Research Assistant Prof., ISEIS, CUHK

The Chinese University of Hong Kong
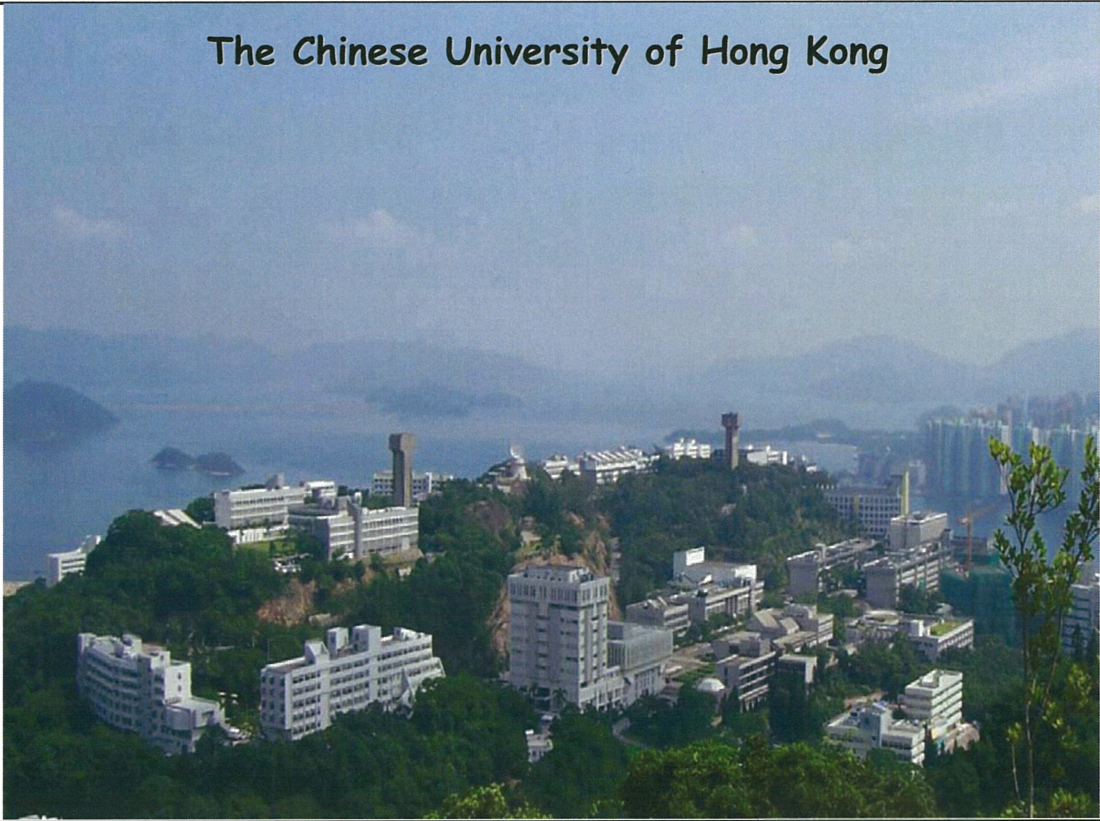
Techniques (1)

Synthetic Aperture Radar Interferometry

InSAR

Vertical gorund displacement with centimeter precision

Interferogram

Colour map of the variation of the sensor-target distance as fractions of the wavelength

$$\frac{2\Delta r}{\lambda}$$

Each fringe indicates

$$\Delta r = \frac{\lambda}{2} \approx 2.8cm$$

of displacement
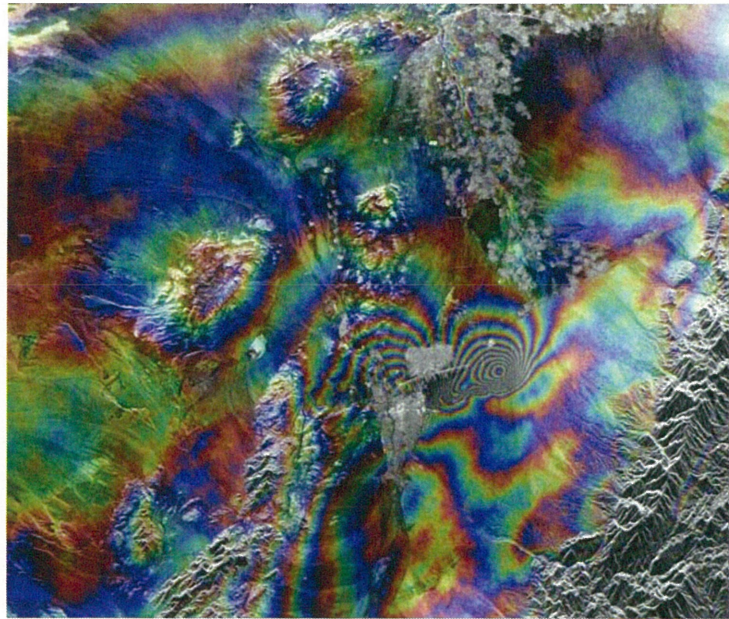
Bam (IRAN)   Earthquake, Dec. '03

Techniques (2)

The Permanent Scatterers (PS) Technique

InSAR Permanent Scatterers (PS)

Scatterers that do not change their electromagnetic behavior (Houses, manmade constructions, exposed rocks)

Many repeated images (>20) are needed!

R_1 R_2 D_r

VS VS PS VS VS PS
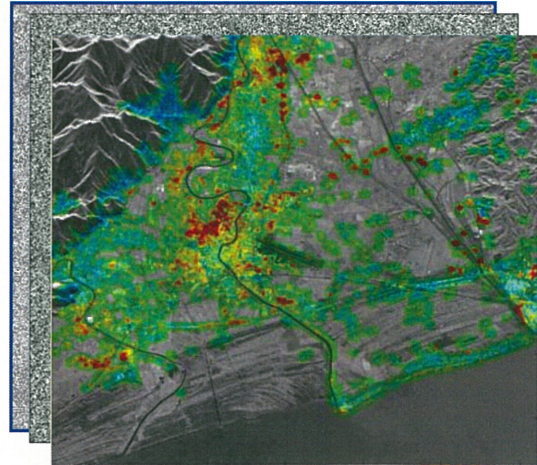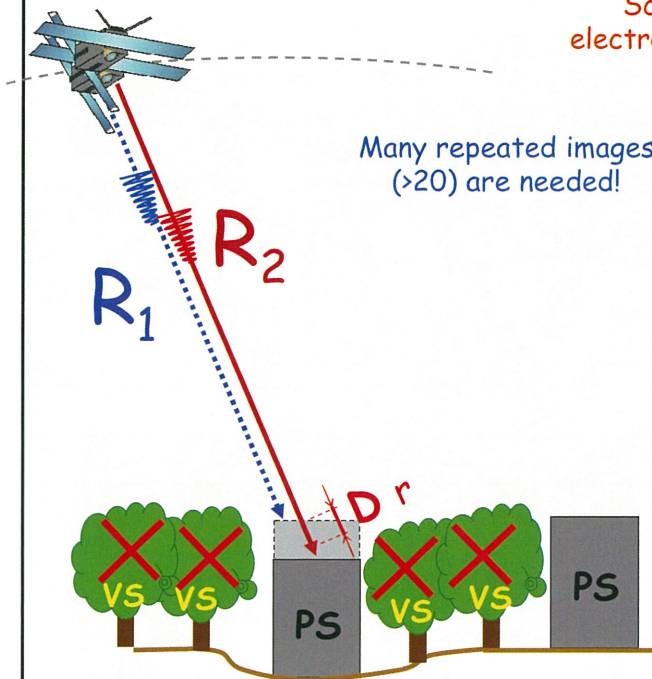
PSInSAR

The Permanent Scatterers (PS) technique
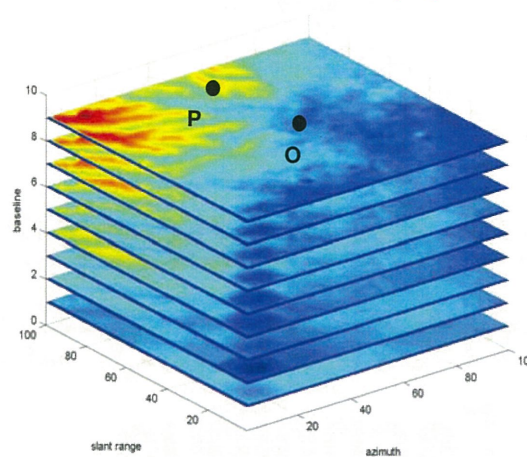
We can estimate the height between P and O only if P and O are *permanent* targets

$$\Delta h_{PO} = \arg\max\left\{\left|\frac{1}{N}\sum_{i=1}^{N}e^{j\phi_i}\cdot e^{-jK_h\Delta h_{PO}B_{n,i}}\right|\right\}$$

Non-linear problem, can be solved through a periodogram

The Height of PS's in Hong Kong

TSX data
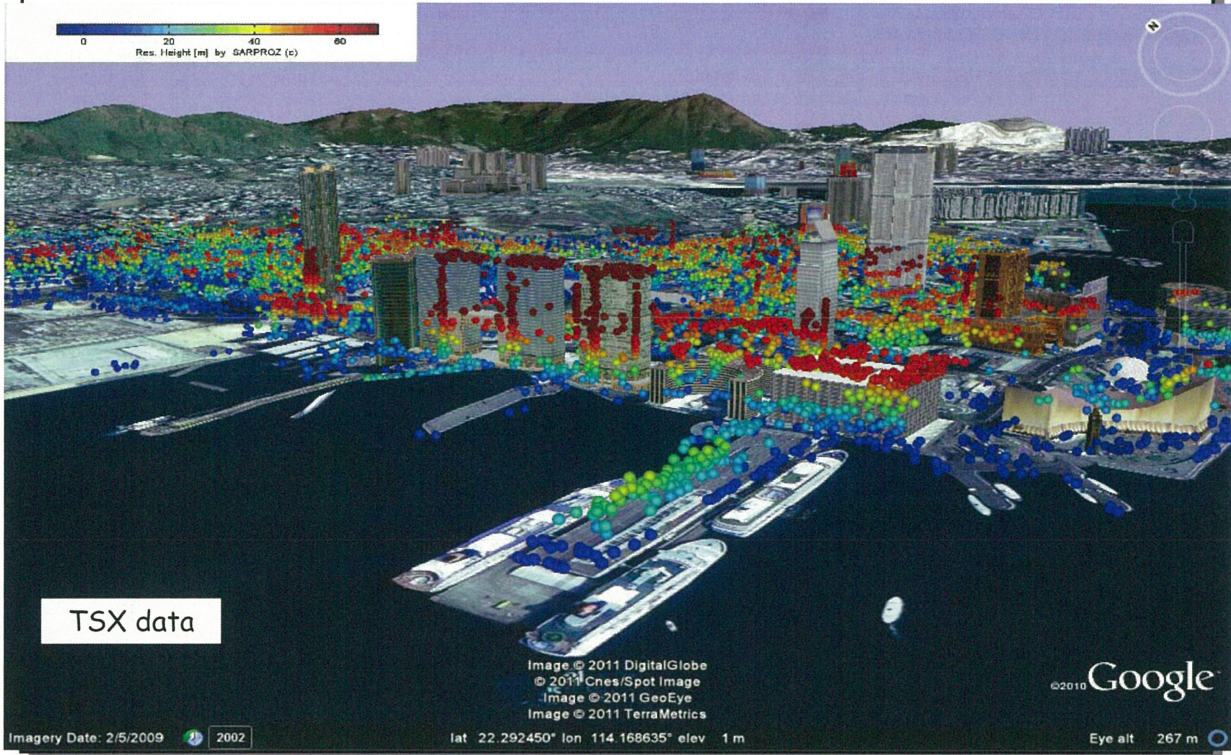
PSInSAR technique to monitor ground deformation

CUHK

2cm/year

1cm/year

Subsiding areas

TSX data

Hong Kong with TerraSAR-X data

ID: 169765
Ellipsoidal Height (WGS84) [m]: 33
Res. Height [m]: 15.8
Velocity [mm/year]: -14.1
Displ. to Temper. Ratio [mm/degC]: 0.04
Temporal Coherence: 0.83
Sample: 9667, Line: 4632

by SARPROZ (c)
Directions: To here - From here

Cosmo SkyMed, Shanghai

~1.5 Million PS's

CERES, Chiba University   Daniele Perissin   ISEIS-CUHK   12/37

Shanghai Subway Tunnel monitoring (Cosmo data)
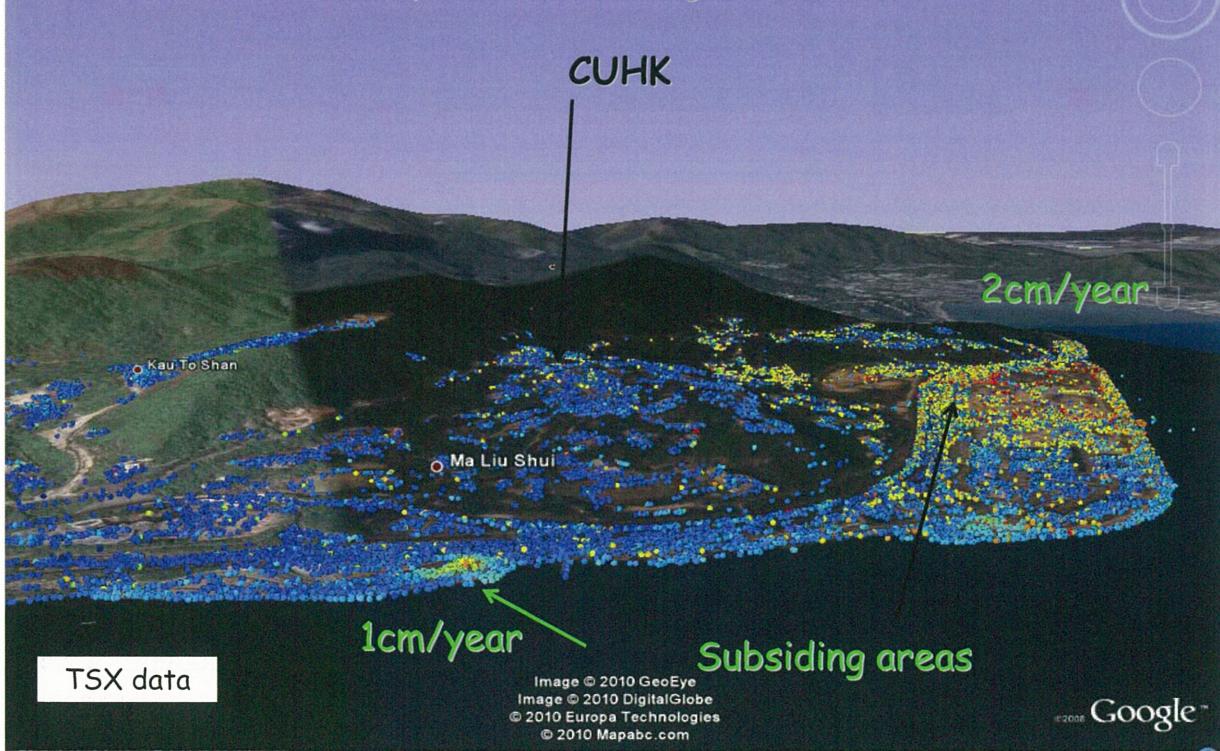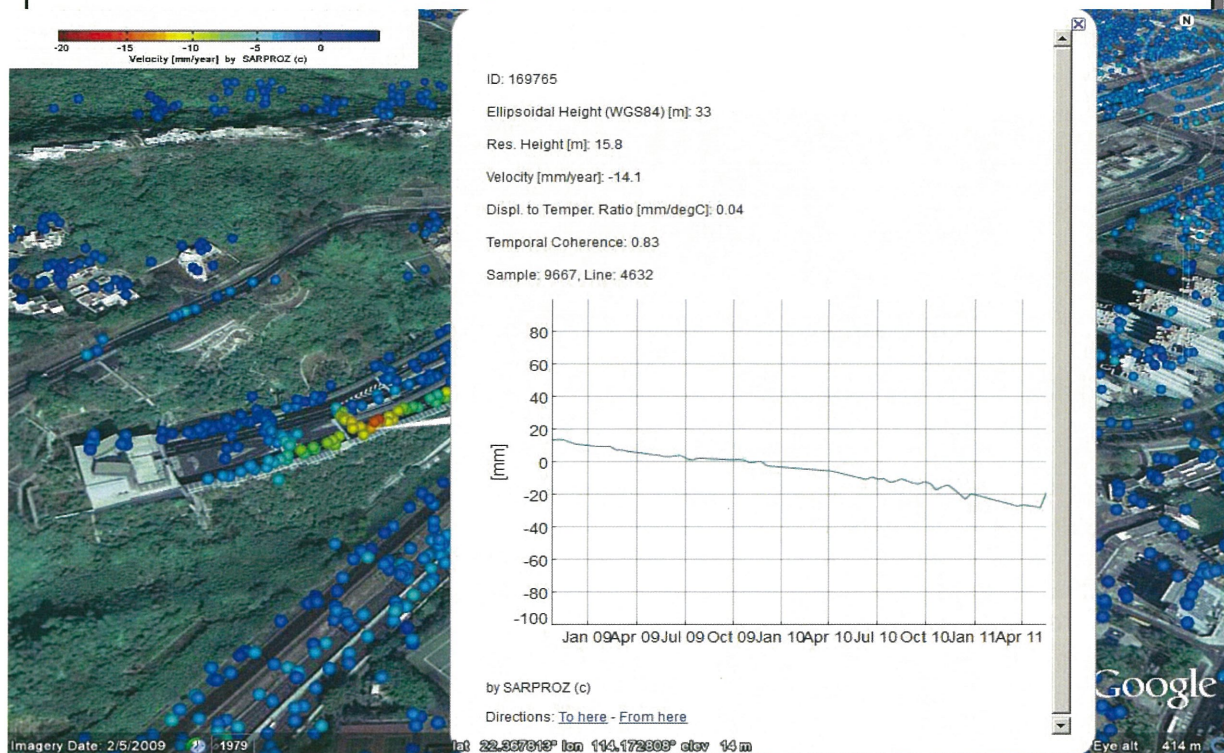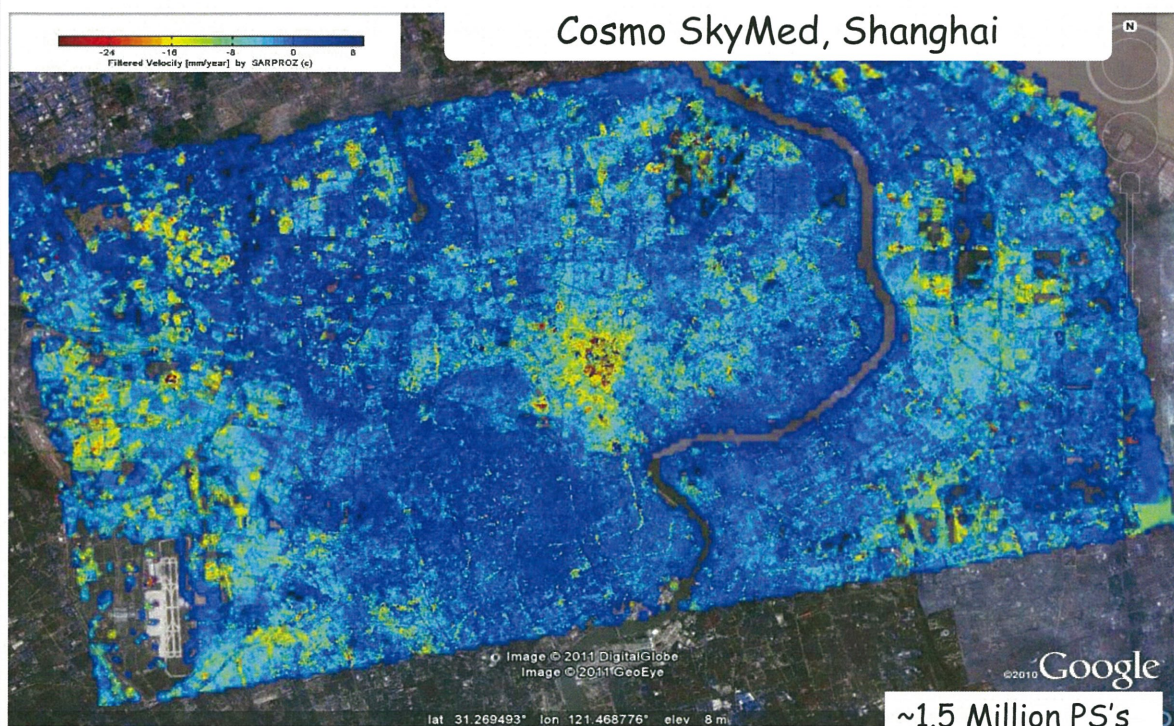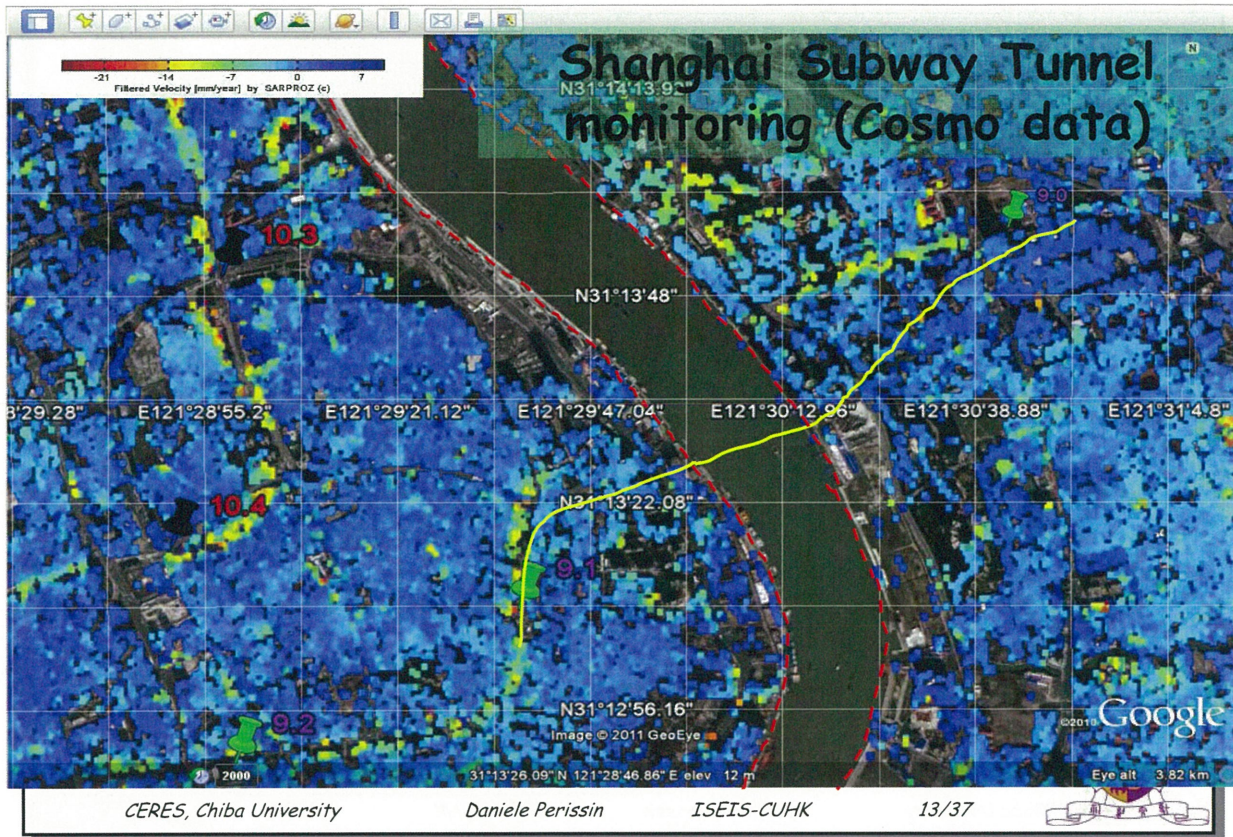
Techniques (3)

The ADVANCED Permanent Scatterers analysis

What are PS's?

Many repeated acquisitions taken at different times, with different geometries, polarizations, ...
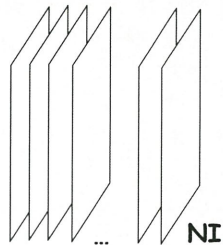
Point targets extraction

... NI

Estimation of RCS, size, resonance, height, ...

Characterization and classification
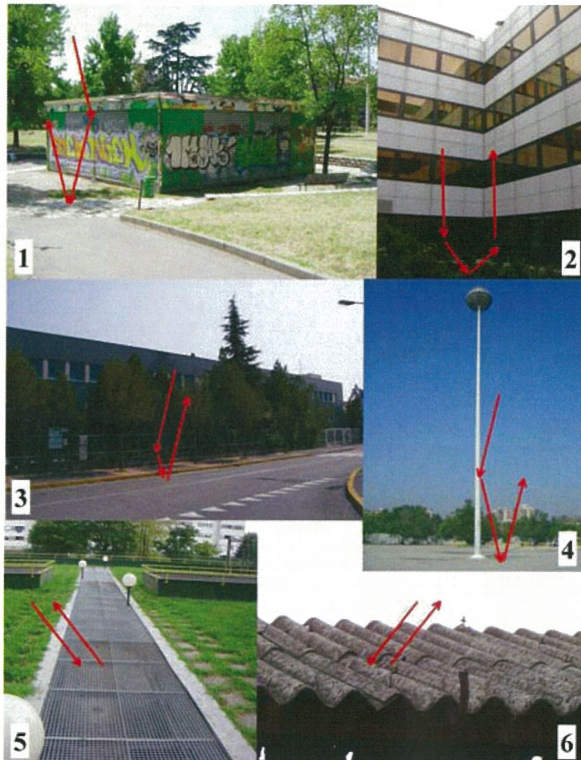
Multi-platform PS's

Trihedral

Different attitudes, Different incidence angles

Parallel orbits

Dihedral

Ascending

Descending

Pole
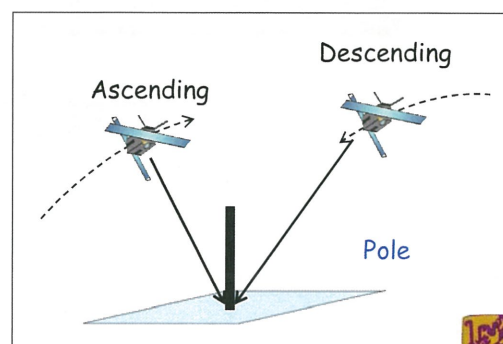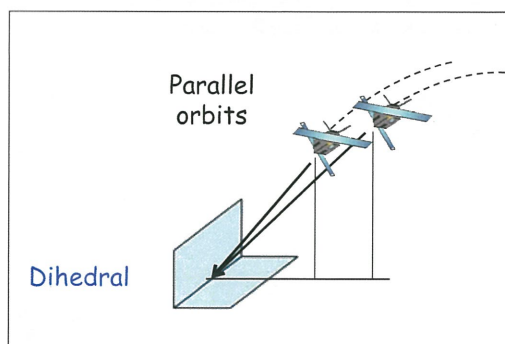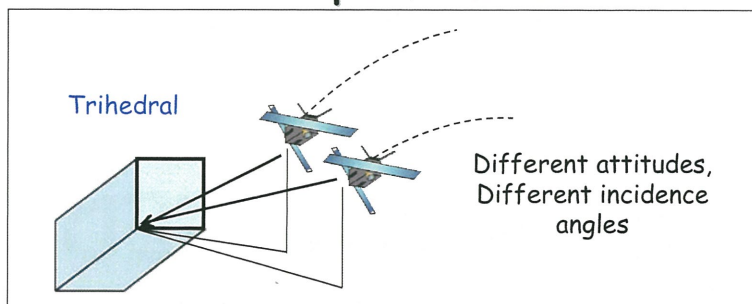
Details of PS density from 3 tracks

ERS data in Milan
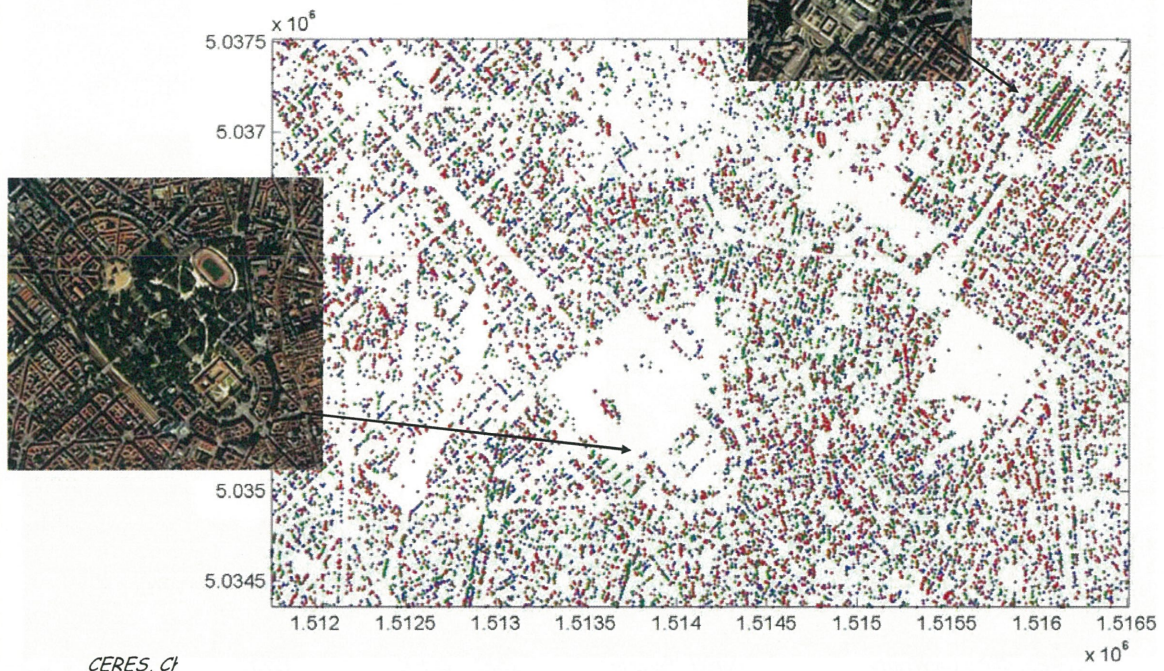
CERES, Cr

Parallel tracks combination, ERS + Envisat

Seasonal displacement time series of a DIHEDRAL PS in Milan
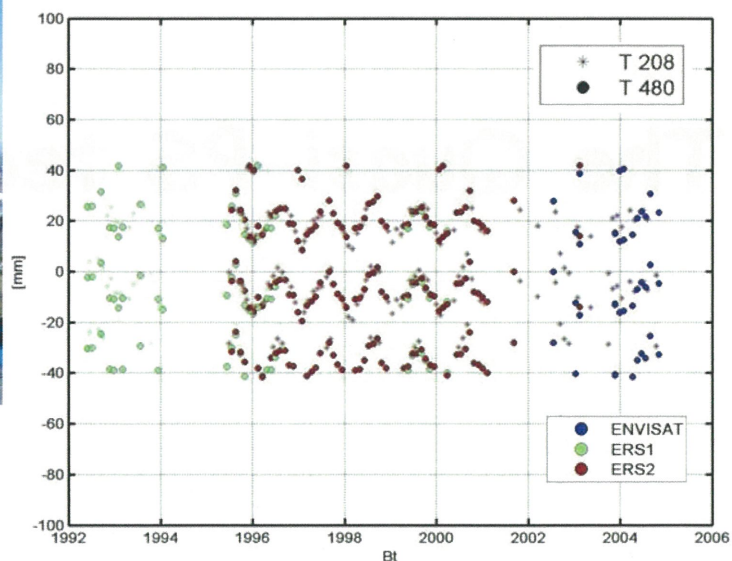
CERES, Chiba University
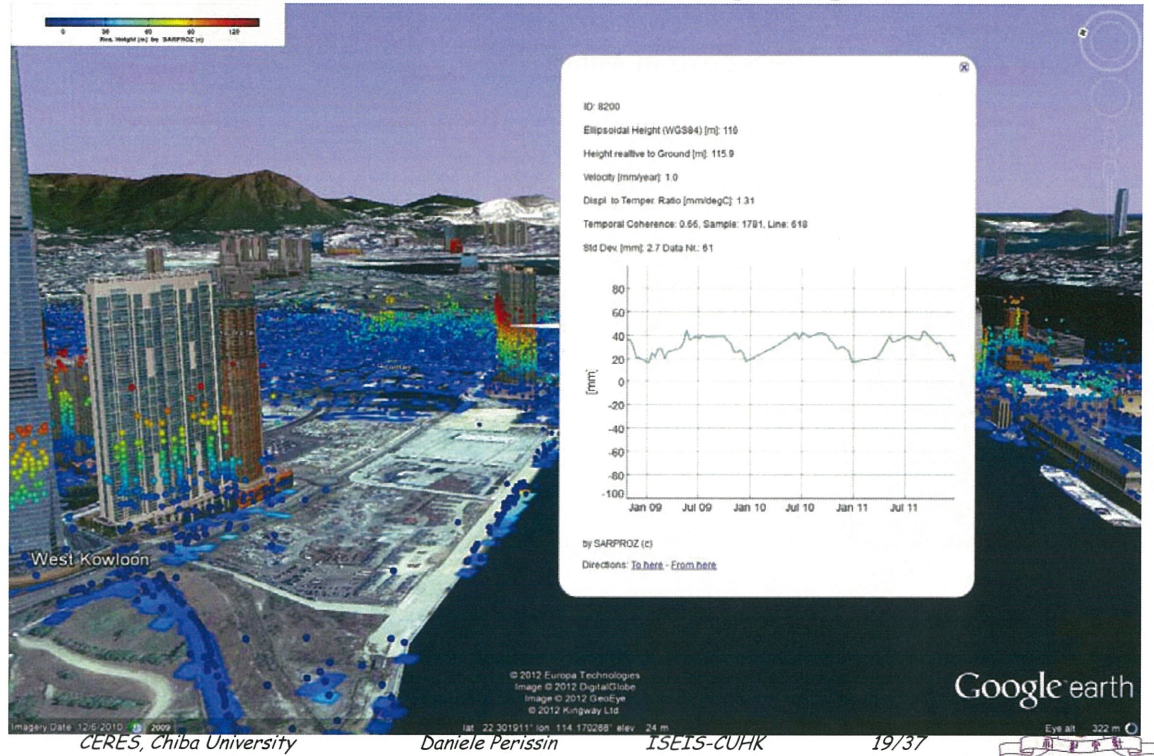
Techniques (4)

The Quasi-PS technique

On mountains or in vegetated areas, there are no PS's

Amplitude Mean

The Quasi-PS analysis

The core concept

Coherent connections

Time

SAR sampling grid
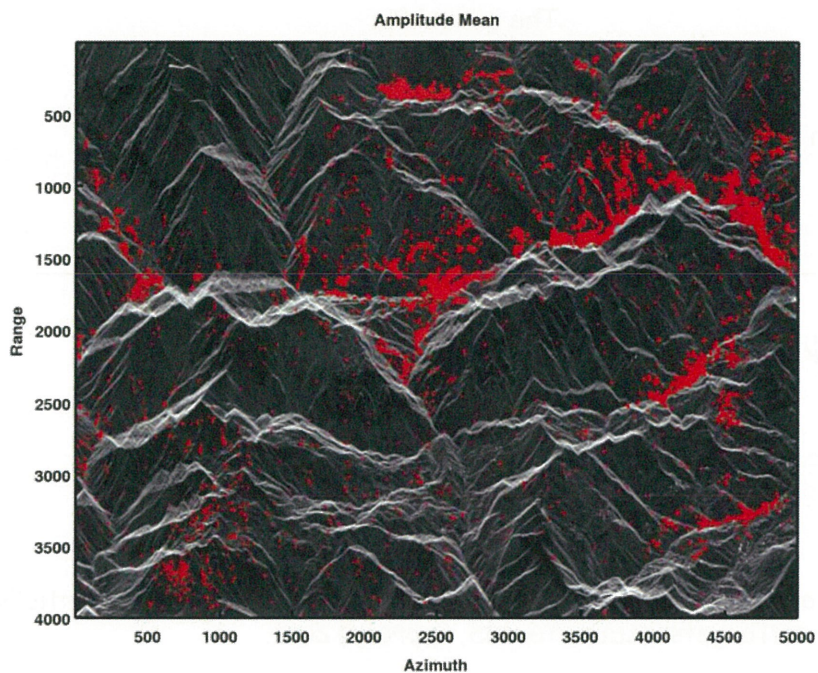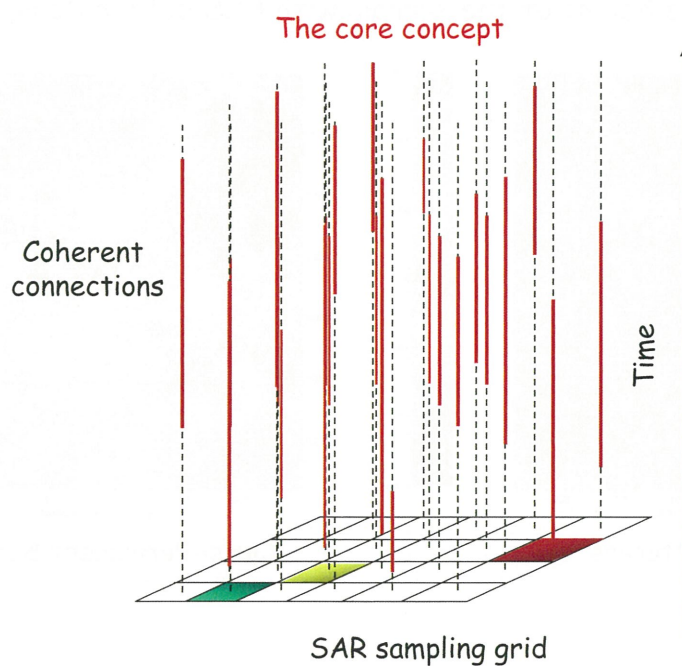
The Quasi-PS analysis

The basic idea

Model used in the PS analysis for estimating PS height and velocity

Modifications w.r.t the classic technique

$$\sum_{(i,k)} \left| \gamma_p^{i,k} \right| e^{j\left(\Delta\phi_{pq}^{i,k} - \Delta\phi_{Model}^{i,k} \right)}$$

ik Images Graph

pq PSC Graph

Processing weights

D. Perissin and T. Wang, "Repeat-pass SAR Interferometry with Partially Coherent Targets", IEEE TGARS, in press, 2011.

Quasi-PS: an example

Estimating the height of the terrain with ERS data in Rome, Italy
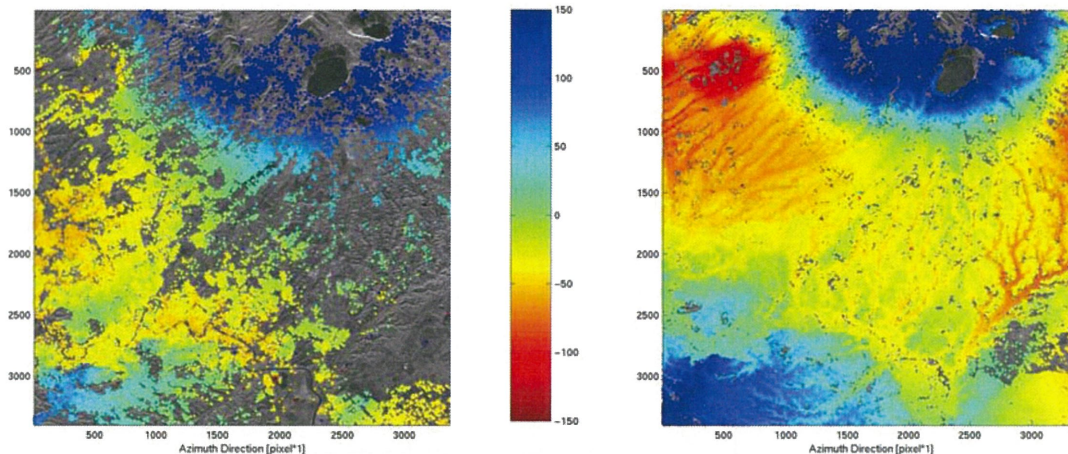
Permanent Scatterers

Quasi-Permanent Scatterers

Case study: Tibet with ALOS data

The movement
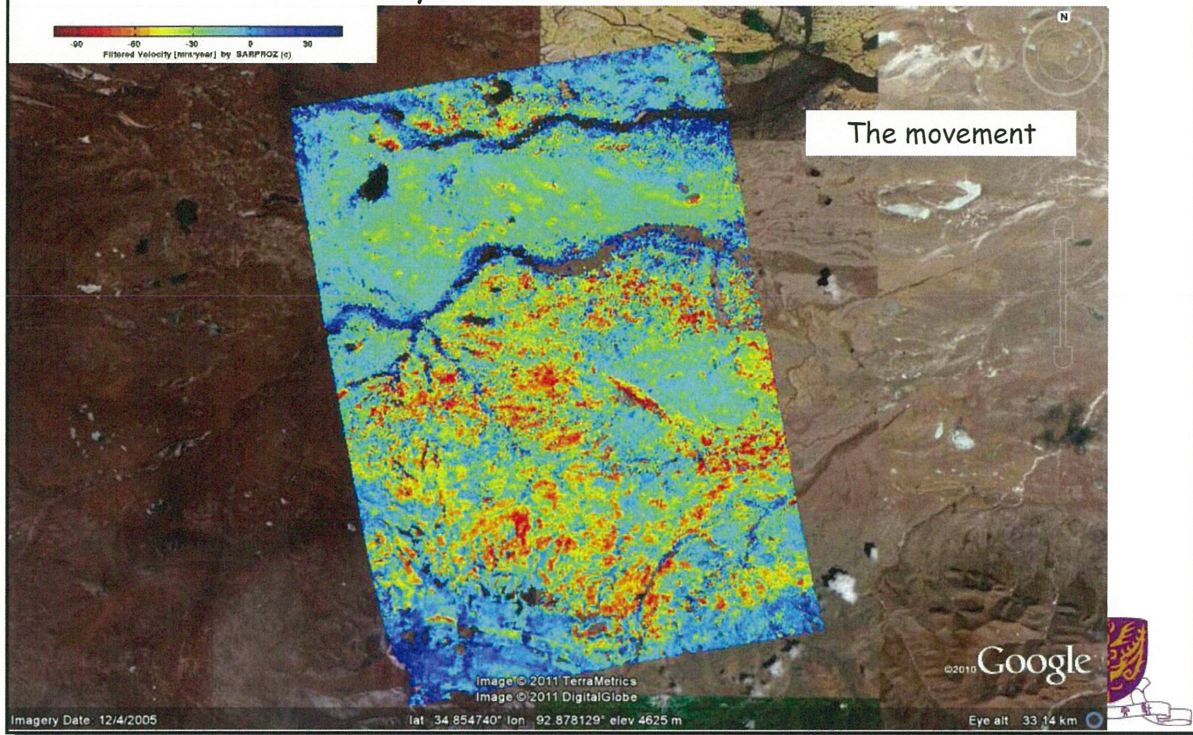
Tianjin full frame, TerraSAR and ALOS data

Height w.r.t DTM

Power lines in TSX PS's
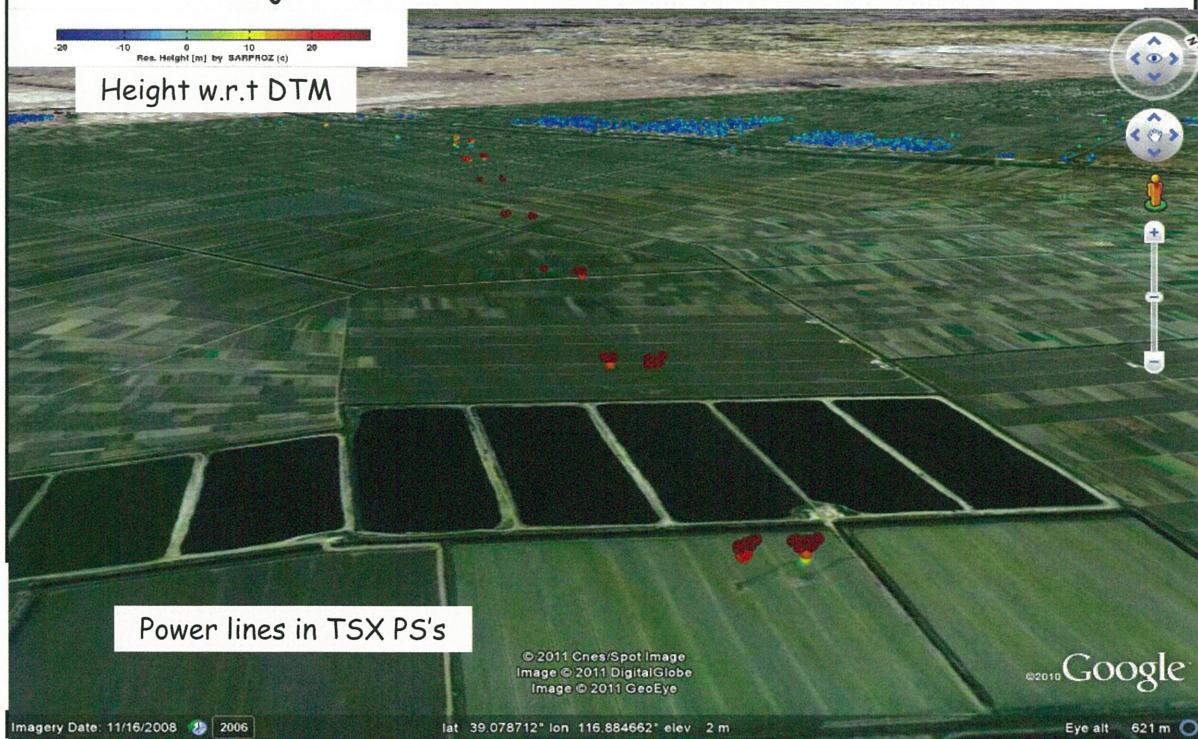
Techniques (5)

Change Detection and "Temporary" PS analysis

Tibet Railway stability monitoring

Monitoring the displacement of corner reflectors with Envisat

Corner reflector deployment in 2008

Software

SAR images

Corner locations on Google Earth

Displacement time history [mm]
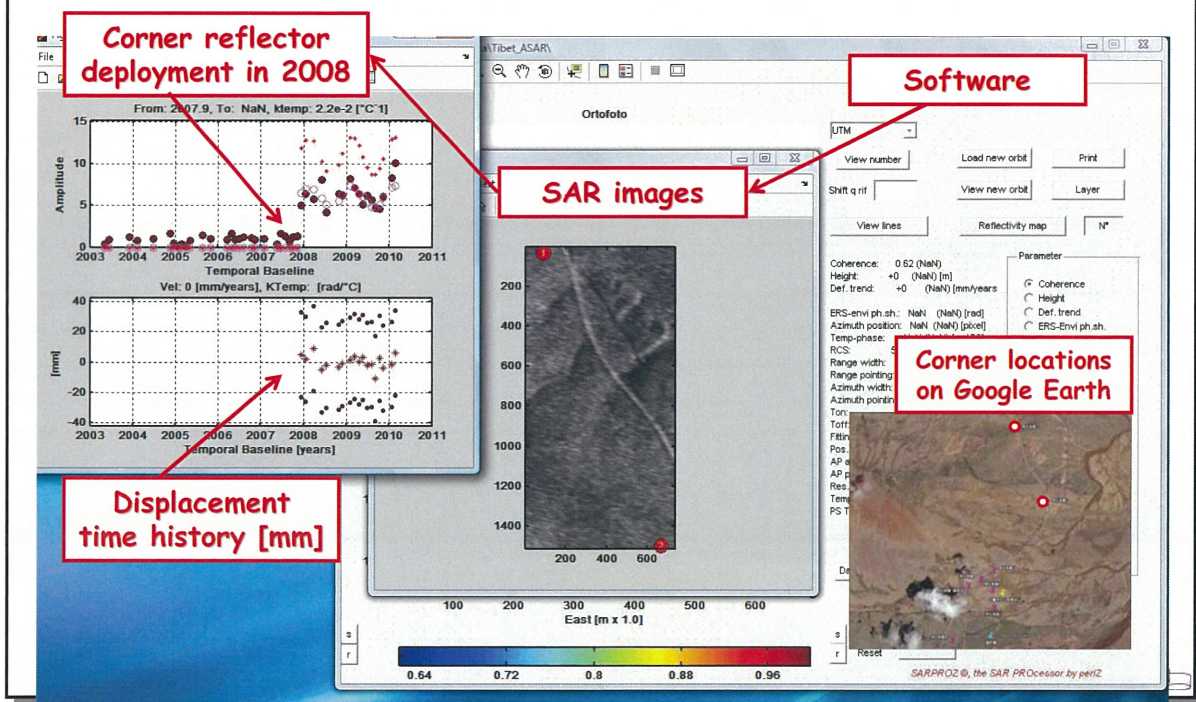
Case study: Hong Kong Government project

Hy(S)Q/007/2011 – Research on SPRST in Ground Settlement Monitoring

Reclaimed

| === Tunnel Alignment | ○ Ventilation Bldg (VB) | —— Study Area Boundary |

Hong Kong with TerraSAR data: study and test of CR's
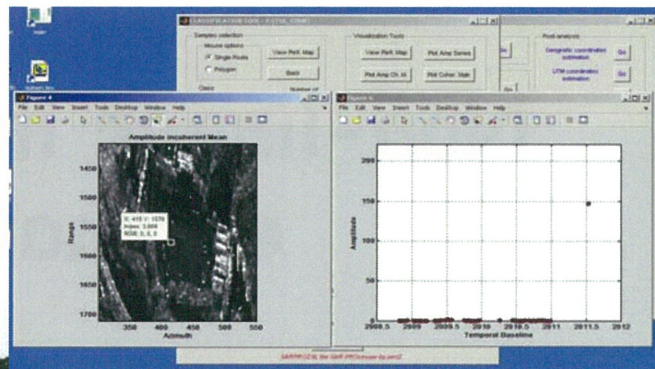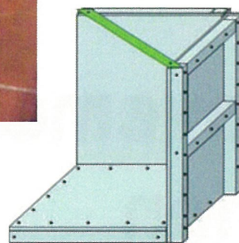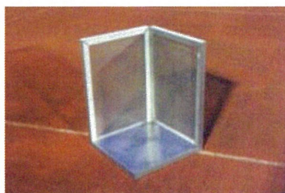
Cheap, light, easy to carry, easy to mount, resistant to HK weather, ...
...and: temporary.

Hong Kong with TerraSAR data: deployment of CR's

CERES, Chiba University   Daniele Perissin   ISEIS-CUHK   31/37

Techniques (5)

Non-linear movements estimation

CERES, Chiba University   Daniele Perissin   ISEIS-CUHK   32/37

PSInSAR applications

Vertical-horizontal motion decomposition

Regular sampling required for non-linear motion reconstruction !!!

Radarsat data

CERES, Chiba University
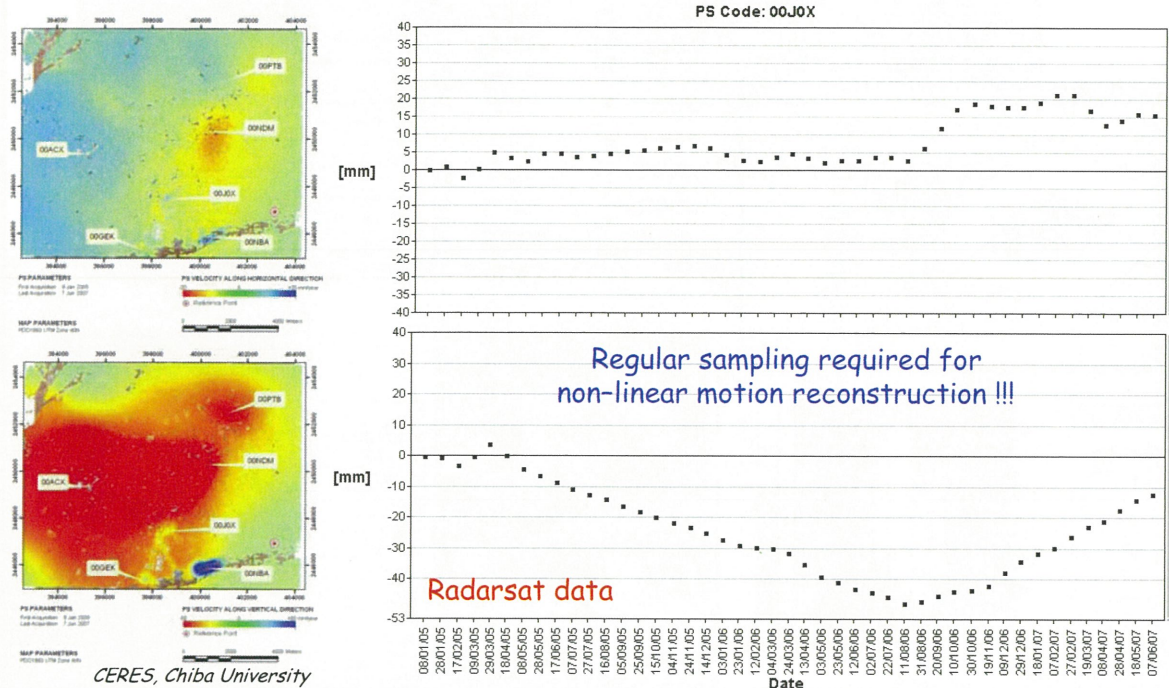
All these techniques (PS, A-PS, Q-PS, T-PS, …) are implemented in a sw:

SARPROZ

The SAR processing tool by PeriZ

http://ihome.cuhk.edu.hk/~b122066/index_files/download.htm

CERES, Chiba University   Daniele Perissin   ISEIS-CUHK   34/37

The SARPROZ interface
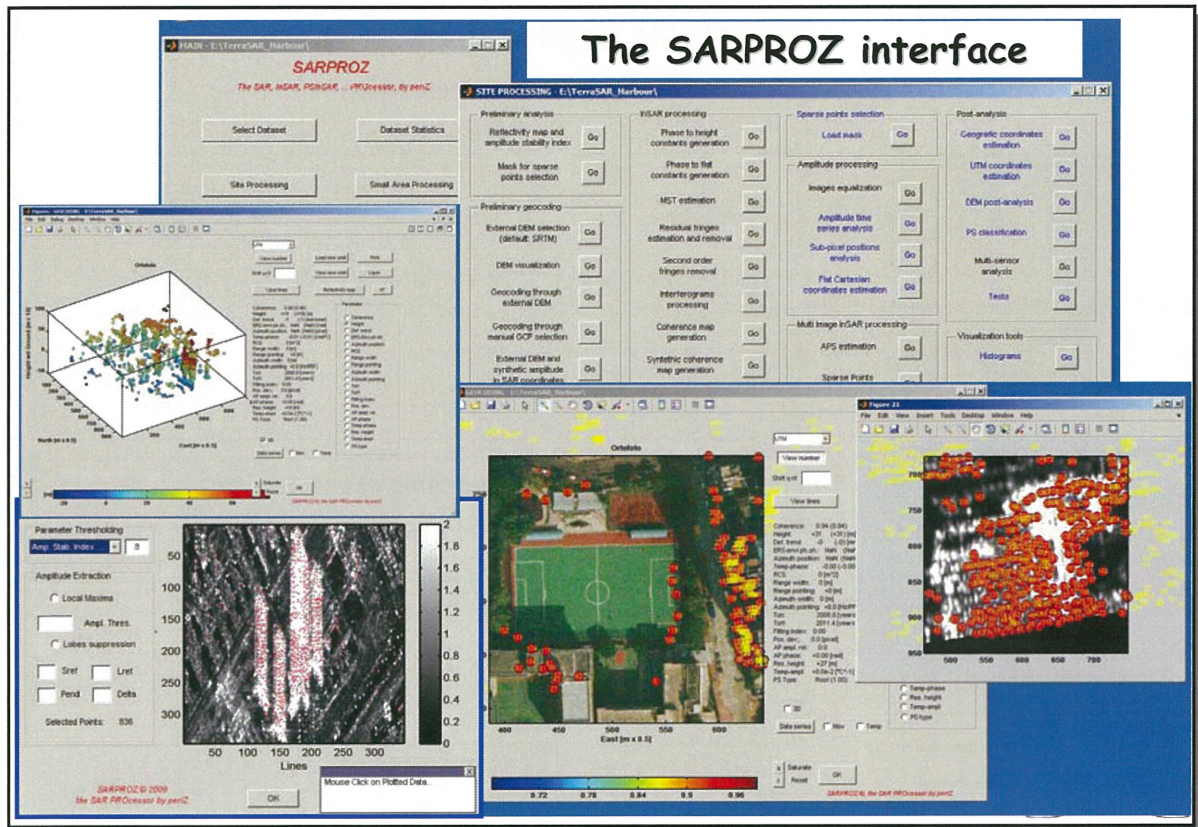
Main characteristics of *SARPROZ*:

- User friendly Graphical **Interface**: no other language knowledge is required for standard uses

- Based on **Matlab**: advanced users can very easily develop their own software extensions. Data and parameters are very easily imported/exported using Matlab.

- It can be compiled and it runs independently from Matlab on **any platform** (Unix, PC, Mac).

- Completely **parallelized**: SARPROZ can run on multiple CPU cores or computer clusters automatically.

http://ihome.cuhk.edu.hk/~b122066/index_files/download.htm

Multi-temporal InSAR processing:
techniques and applications

Conclusions

Multi-temporal InSAR processing is a complex task involving different techniques depending on available data and aim of the analysis.

To be able to solve all cases, high expertise and powerful software tools are needed.

Multi-temporal InSAR has a wide range of applications, here we saw monitoring urban and extra/urban phenomena, like subsidence and settlement due to excavations/land reclamation

Collaborations are very welcome: daniele.perissin@cuhk.edu.hk

Chemistry of stratosphere and mesosphere revealed by ISS/JEM/SMILES for Earth Diagnosis.

Makoto SUZUKI[1], Naohiro Manago[1]

(JAXA/ISAS, Chiba U./CeRES)

Naohiro Manago[1], Chihiro MITSUDA[2], Koji IMAI[3], Hideharu AKIYOSHI[4], Takuki SANO[1], Yoko NAITO[5],
D. Kinnison[6], and Masato SHIOTANI[7]

[1]Institute of Space and Astronautical Science, JAXA
[2]Fujitsu FIP, [3]Tome R&D Inc.
[4]National Institute for Environmental Studies
[5]Department of Geophysics, Kyoto University, [6]NCAR

[7]Research Institute for Sustainable Humanosphere, Kyoto University

---

Passive microwave remote sensing in Japan

- AMSR, AMSR-E have shown excellent performance for remote sensing of SST, sea ice, etc.
- AQUA/AMSR-E had stopped operation last year, but AMSR-2 instrument and GCOM-W satellite is now waiting for launch (it was delayed from Feb. 2012, by the delay of another satellite provider).

- A sub-mm chemistry mission, SMILES had been conducted jointly by JAXA and NICT. It proposed around 1987 originally, and it finally onboard ISS on Sep. 18, 2009. It worked only 6 months, but it demonstrated breakthrough performance at 625, 650 GHz region, Tsys = 340K, using 4 K cooled SIS detector.
  - This is the my 3rd instruments that worked only 6 months.
    - ADEOS-I/ILAS, ADEOS-II/ILAS-II, ISS/JEM/SMILES (this talk)
    - And I suffered another satellite failure, not entering Venus orbit, on Dec. 9, 2010, but it failed. Venus Climate Orbiter, Akatsuki, is now wandering around 0.6-0.7 AU to reach Venus again around 2015/16.

JEM: Japanese Experiment Module

500 kg class 12 Boxes for Remote Sensing etc.
3 tons also available.

HTV, 1st launch Sep. 11, 2009 using Japanese H-IIB rocket.

JEM/SMILES Payload

• Dimension:
   1.85 m x 1 m x 0.8 m
• Weight: < 500 kg
• Mission Life: 1 year
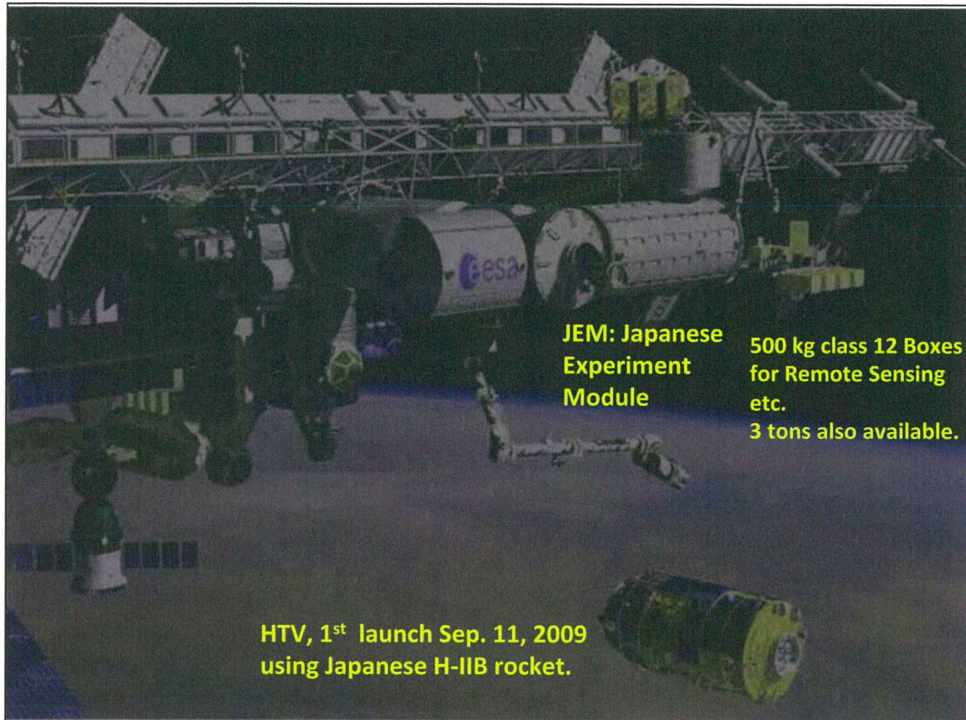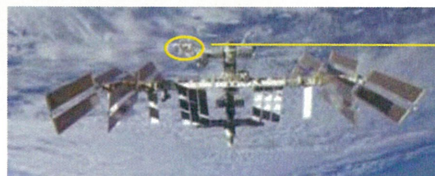
SMILES

The SMILES was carried by the H-IIB with the H-II Transfer Vehicle (HTV) (Sep. 11); the HTV was attached to the ISS (Sep. 18); the SMILES was attached to the JEM (Sep. 25) (All dates in JST)

Aug. 23, 2010   Presentation at Hokkaido U.   4

-- 97 --

JEM/SMILES Mission

(JEM/SMILES: Superconducting Submillimeter-Wave Limb-Emission Sounder designed to be aboard the Japanese Experiment Module on ISS; Collaboration project of JAXA - Japan Aerospace Exploration Agency - and NICT - National Institute of Information and Communications Technology -)

1. Demonstration of superconductive mixer and 4-K mechanical cooler for the submillimeter limb-emission sounding in space

[Mechanical Cooler] Two-stage Stirling and J-T; 20mW @4K, 200mW @20K, 1000mW @100K; Power Consumption: <300 W; Mass: 90 kg

[SIS Mixer]
RF: 640 GHz, IF: 11-13 GHz; Junction: Nb/AlOx/Nb, ~7 kA/cm^2; Fabricated at Nobeyama RO

2. Observation on atmospheric minor constituents in the middle atmosphere

[Standard Products]
- 1 scan : O_3, HCl, ClO, CH_3CN, O_3 isotopes, HOCl, HNO_3
- Multi-scan : HO_2, BrO

[Research Products] UTH, Cirrus Clouds, volcanic SO_2, H_2O_2

Aug. 23, 2010   Presentation at Hokkaido U.   5

SMILES Instrument

625, 650 GHz region, SSB system
4 K cooled, Tsys = 340 K
Two 1.2 GHz bandwidth spectrometers
0.8 MHz spectral resolution.
Comparable or even better than best laboratory instruments.
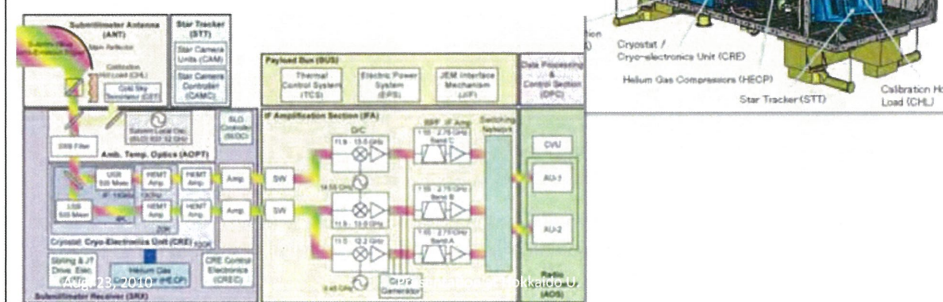
Scientific targets of SMILES

1. **Inorganic Chlorine chemistry**
   - **ClO to HCl ratio**
     (O_3 trend in the US)
   - **HOCl production**
     (O_3 trend in the LS)
   - **Global ClO**
     (background ClO)
2. **Bromine budget** (very short-lived source gas issue)
3. **HO_x budget**

etc.

Simulated SMILES observation performance
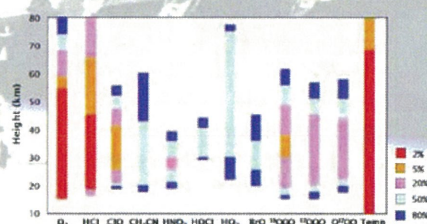
Error estimation for the mid-latitude case based on the single scan measurement

Sep. 27-29, 2010   AURA meeting, M. Suzuki et al   7

Overview of JEM/SMILES Instruments:
SIS Device
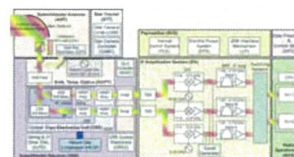
SIS Junction: Nb/AlOx/Nb
Junction Area: ~1 x 1 mm^2
Current Density: 6-7 kA/cm^2
Fabricated at Nobeyama Radio Observatory, JAPAN

500 nm   Nb

AlOx

Nb

50 mm
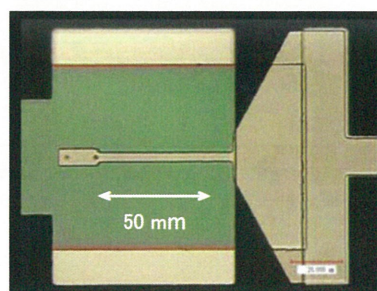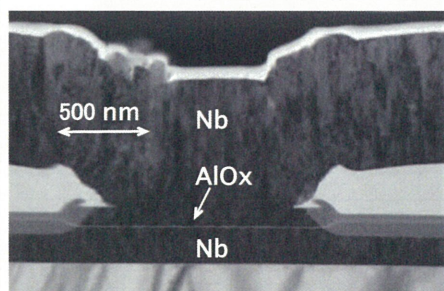
Two Bands among Band A, B, C can be observed.

Band A

band A (091012000062)
2009/10/12 03:22:14, N23.30 E173.83, SZA 55.8 deg at 30km

15.9 km 25.9 km 35.6 km 45.2 km
19.9 km 29.8 km 39.5 km

Band B

band B (091017000060)
2009/10/17 00:53:32, S21.52 W138.83, SZA 57.3 deg at 30km

15.1 km 25.1 km 35.0 km 44.8 km
19.1 km 29.1 km 40.9 km

Band C

band C (091012000062)
2009/10/12 03:22:14, N23.30 E173.83, SZA 55.8 deg at 30 km

15.9 km 25.9 km 35.6 km 45.2 km
19.9 km 29.8 km 39.5 km
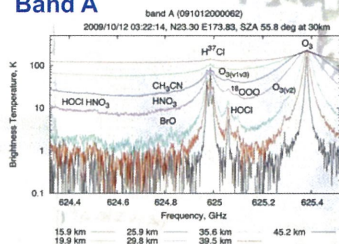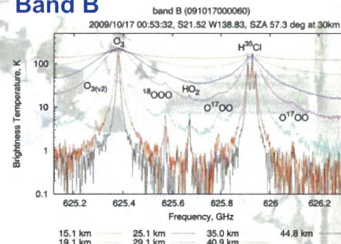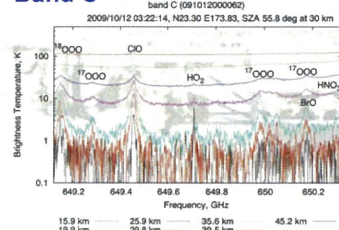
Frequency region has been selected by engineering interest, as high as possible, but 625-626 GHz region is the only frequency to measure HCl below 1 THz.

At 600 GHz troposphere is opaque in limb.

Tsys ~ 350 K, and Noise floor is ~0.4 K, given by

$$NE\Delta T_B = \frac{T_{sys} + T_{Atm}}{\sqrt{\Delta v \cdot \tau}}$$

Sep. 27-29, 2010   AURA meeting, M. Suzuki et al   9

ISS Orbit plane rotates in ~90 days, 45 days for diurnal coverage. It will be good platform for diurnal variation study and solar occultation, such as ISS/SAGE-III (2015 ?).

Actual Local Time Coverage of SMILES in January 2010. Blue: January 1st. Red: not observed.
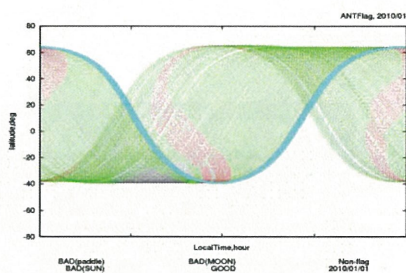
ISS orbit
• Low altitude: 350 km
• Moderate inclination: 51.2°

Sep. 27-29, 2010   AURA meeting, M. Suzuki et al   10

Comparison of SMILES ClO v2.0 with MLS 3.3
MLS coincidence, DSZA < 2°, SMILES ver.2 release candidate.

Coincidence event on Oct. 12, 2009 SMILES, MLS at 50.4°N 130.7°E (the first coincidence in current criteria). SZA= 59.6°

Coincidence Statistics 30S-40S, 161 SMILES vs. **301 MLS profiles**, most coincidence cases in current criteria. < 10% agreement with MLS 3.3 between 22-48 km
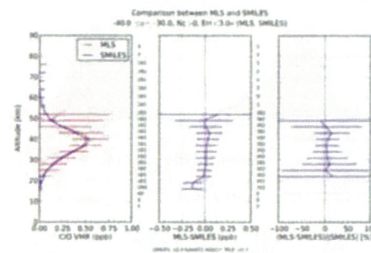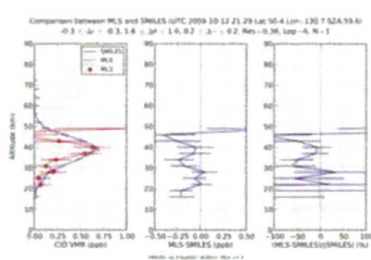
Daytime ClO comparison with NCAR WACCM
Other latitude slightly worth than these examples.

coincidences 0-10N, Oct. - Feb.,
SMILES vs. **WACCM**

coincidences 30-40N, Oct. - Feb.,
SMILES vs. **WACCM**
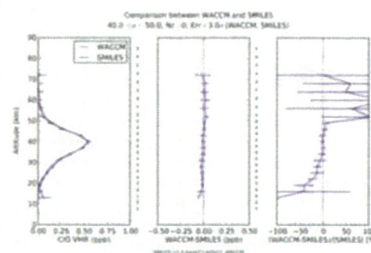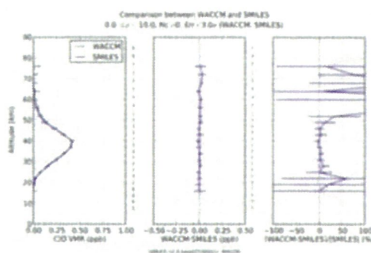
Detection limit of SMILES ClO, 15 ppt at 25 km in single shot, negative bias at 22 km in nighttime
Detection limit changes with pressure.

Daytime (noon) and **Nighttime (midnight) difference at 10N-10S**

Theoretical detection limit and **standard variation of nighttime**. Below 35 km, it should be detection limit.
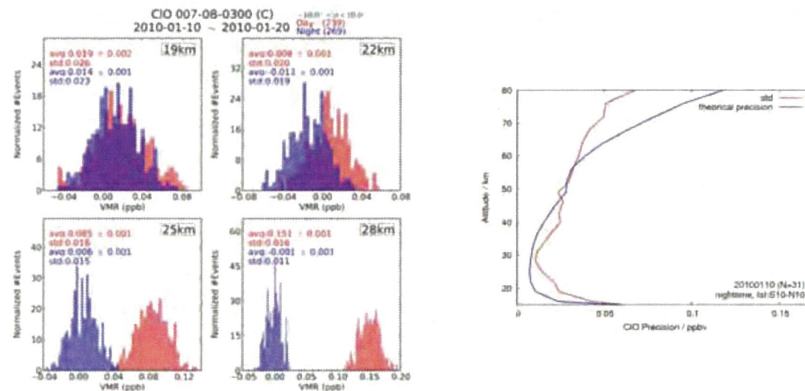
SMILES (+ MIPAS) can provide knowledge of chlorine partitioning at the background atmosphere based upon observations.
2010/10/12, local solar noon (53N-60N) and midnight (23S-33S), ClONO$_2$: MIPAS IMK, day 51N-57N, night 50N-54N

Daytime profiles   **Nighttime profiles**
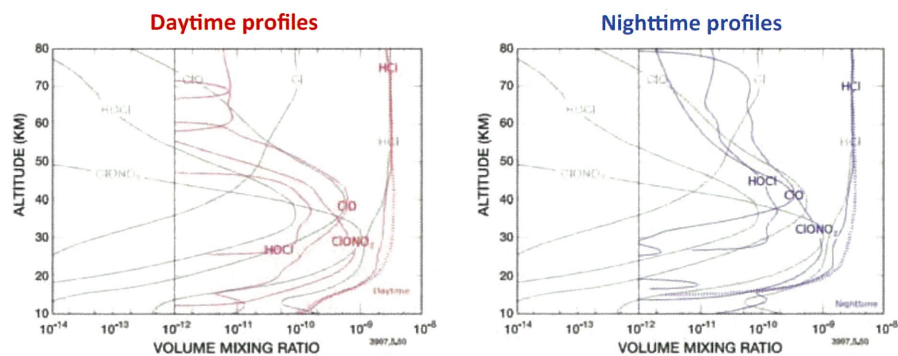
Brasseur and Solomon, pp.373

Fig. 1 HCl (left), ClO (center), and O₃ (right) distribution on Jan. 23, 2010 at the 22 km altitude in the northern hemisphere.
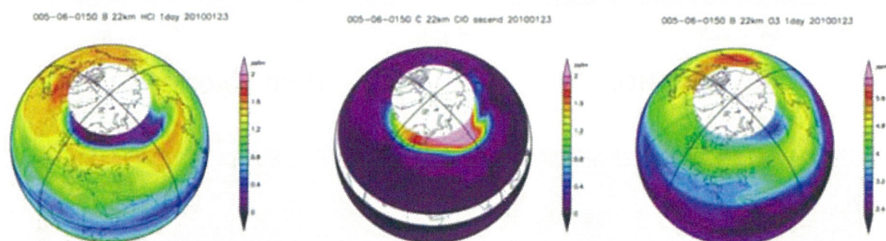
HCl is about 1.6 ppbt at outside polar vortex and it is almost entirely converted to the ClO (1.6 to 2.0 ppbt). O3 destruction has occurred as much as 20% (from 4 ppmv to 3.2 ppmv) after 3 weeks of heterogeneous chemical process.

Fig. 2 (a) shows trajectory of observation points of SMILES (large circles) from 15:23UT to 15:47 in Jan. 23, 2009, and CALIPSO observation points which passed north of Europe. Fig. 2(b) shows SMILES ClO vertical section.
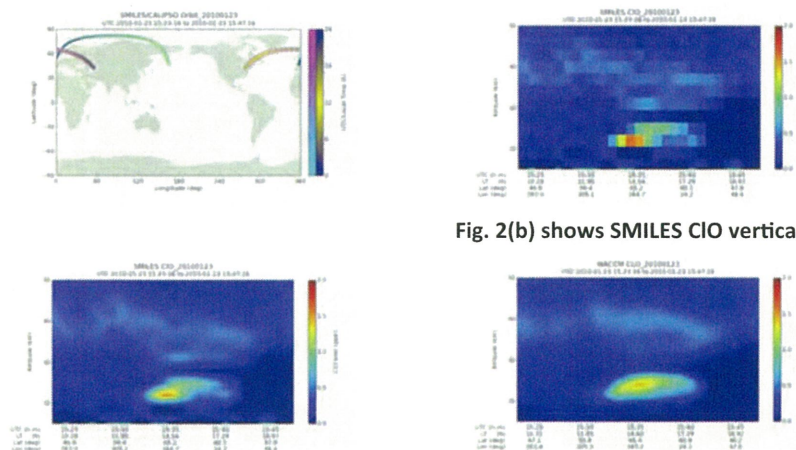
Fig. 2(b) shows SMILES ClO vertical section.

(c) SMILES ClO vertical section interpolated.

(d) SD-WACCM ClO vertical section.
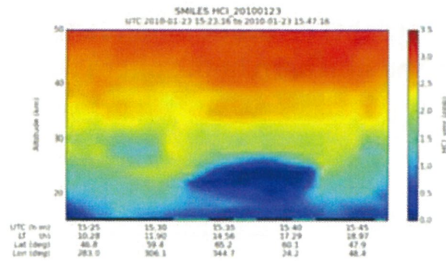
(e) SMILES HCl.
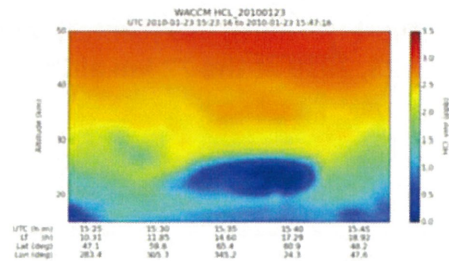
(f) SD-WACCM HCl
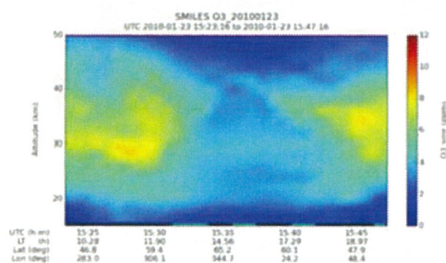
(g) SMILES O$_3$
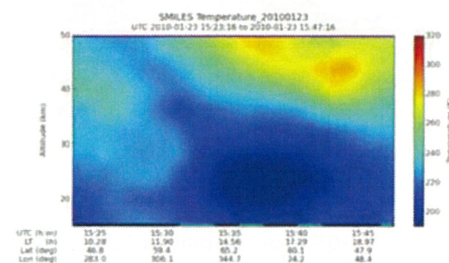
(h) SMILES Temperature

**Checking ClO more thoroughly, Jan 23 at different orbits.
(left) SMILES interpolated, (right) WCCAM interpolated.**
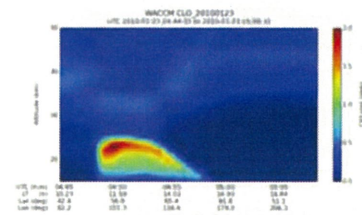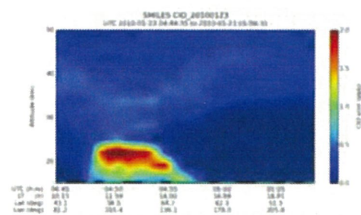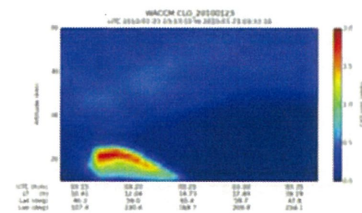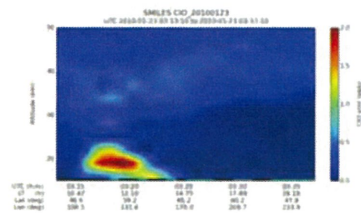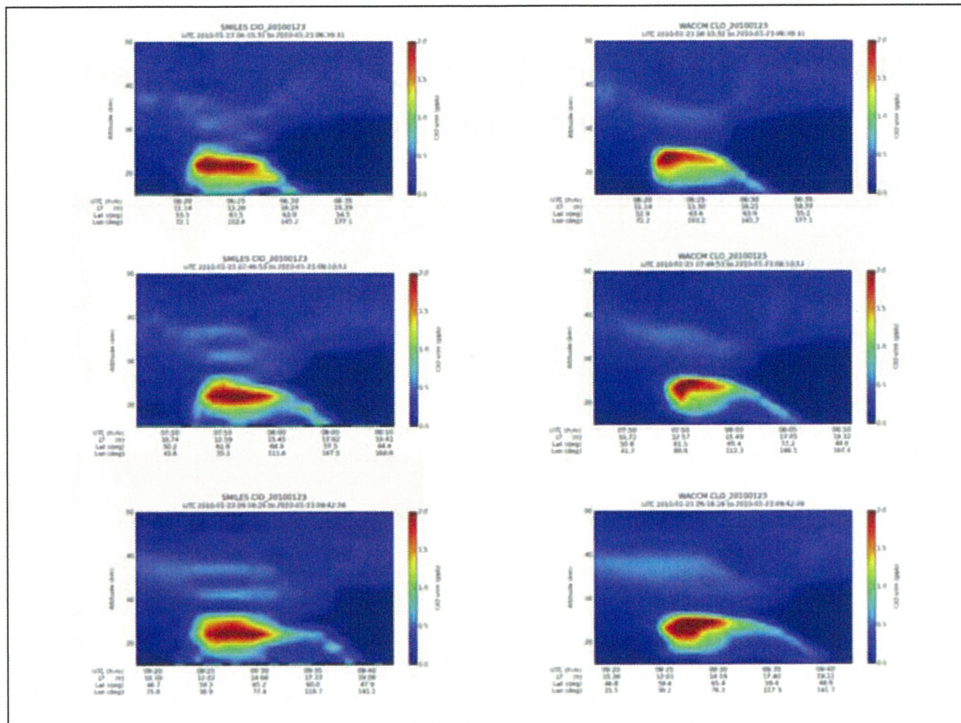
SMILES can measure same location at different local times. Jan. 23rd masurements showed, nighttime CLO decline generally agreed well with WACCM calculation. This suggest current knowledge of (ClO)$_2$ formation rate is acceptable.
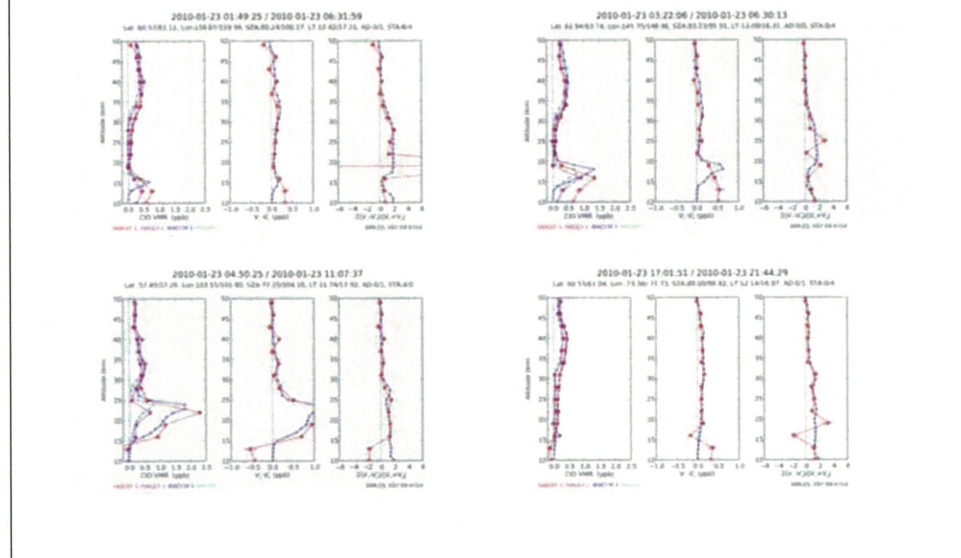
SMILES O₃(Left-Upper), Locations (Right-Upper)
ClO (Left-Lower), HCl (Right-Lower)
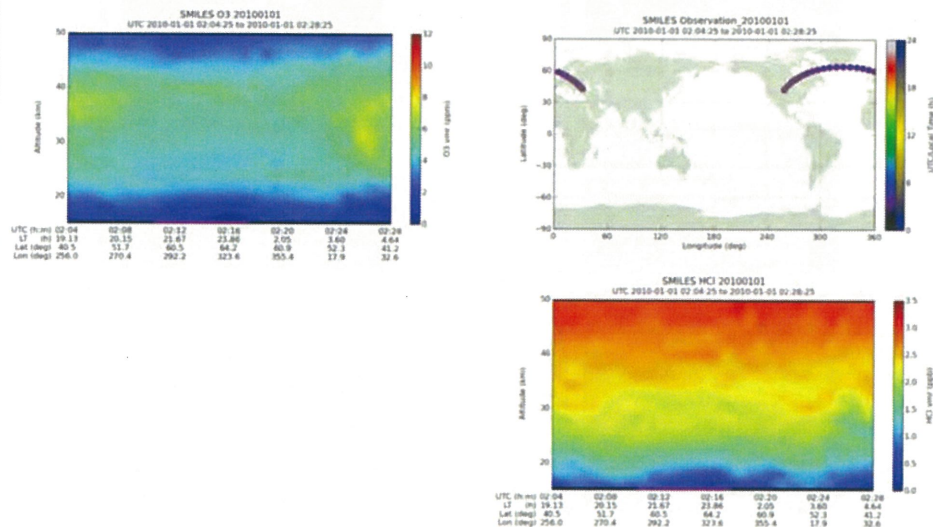
SMILES O3(LeftUpper), ClO(LD),
Locations(RU). CALIPSO (RD)

O3 (AB) 2010-01-01
SMILES: 007-08-0310_new   Altitude: 22.00 km

SMILES SZA 2010-01-01
Ascending
Local Time: 17.22 ± 3.72 (h)

HCl (AB) 2010-01-01
SMILES: 007-08-0310_new   Altitude: 22.00 km
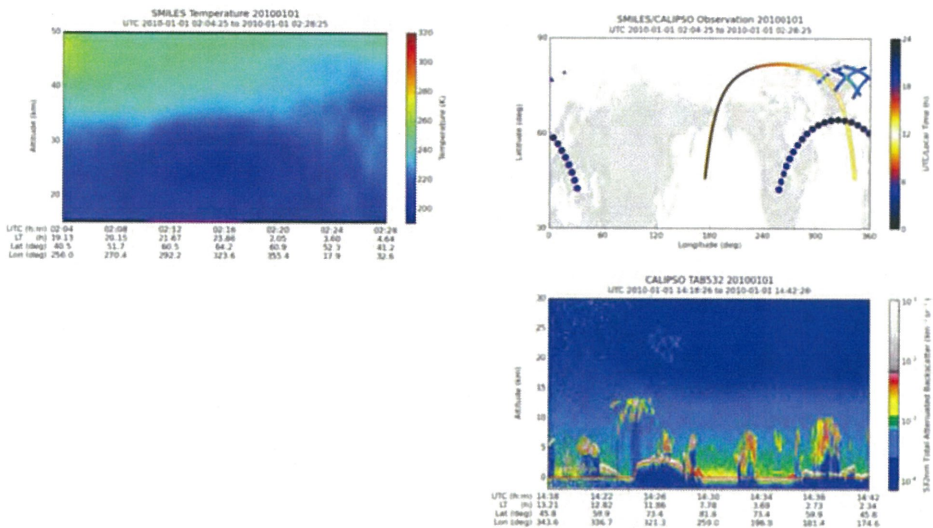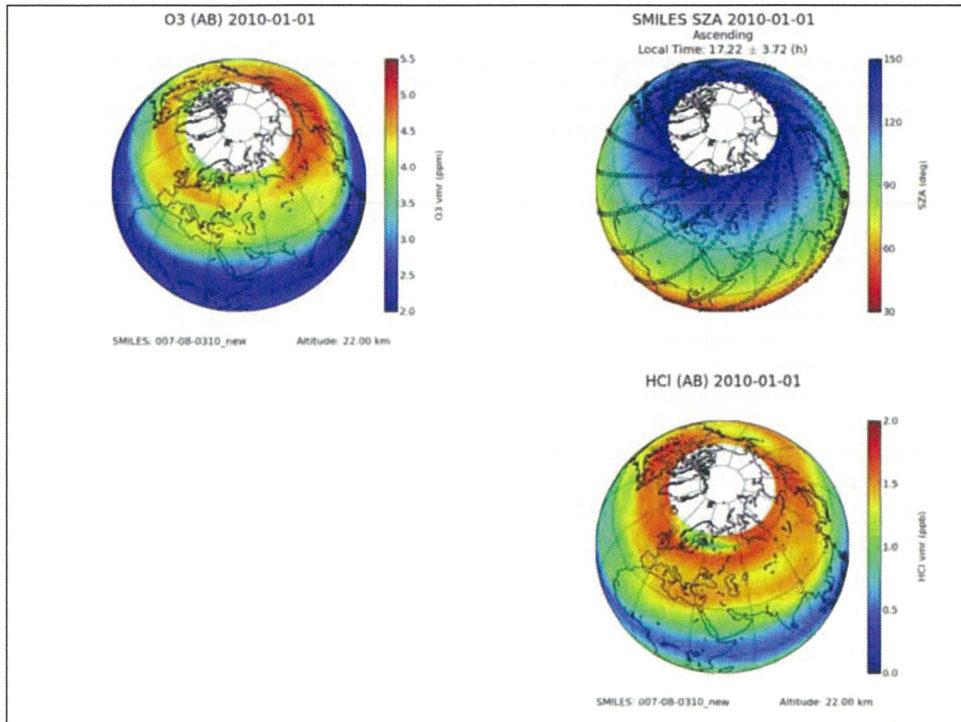
Diurnal variation of O3 in the mesosphere observed by SMILES

SMILES and a model calculation (Vaughan, *Nature*, 1984)
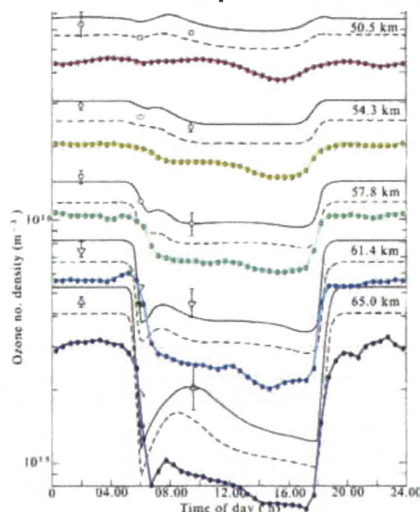
- mesospheric O_3 shows strong diurnal variation, but it was not observed clearly from ground and space.

- Daytime O_3 and HO_2 etc have relations to H_2O, which is now under evaluation. (Clancy et al, JGR 1994)

$$O_3 \propto (k5 \cdot k19)^{1/3}(k7 \cdot J3a)^{-1}(k9 \cdot k10)^{-1/2}[H_2O]^{-1/2} \quad (1)$$

$$HO_2 \propto (k5 \cdot k19)^{-1/2}(k7 \cdot J3a \cdot k9)^{1/2}(k10)^{-1/2}[H_2O]^{1/2} \quad (2)$$

Kovalenko et al (2007) have questioned the reaction rate of $ClO + HO_2 \rightarrow HOCl + O_2$ (JPL206/2011), and it proposed to be nar the value reported by Stimpfle (1979). von Clarmann et al ら(2009) also supported this claiming from MIPAS-B balloon measurements. This could affect Total Ozone Loss at the lower stratosphere significantly. We checked the reaction rate by using steady state relations around [HOCl] at the 30-45 km.

Zonal mean temperature = 249K.
k_1 (nominal)
 $k_1 = 2.7e{-}12 * \exp(+220/T)$
 6.53 x10^{-12} cm^3/molecule/s (JPL2006)
k_1 (upper limit)
 9.66x10^{-12} cm^3/molecule/s
k_1 (lower limit)
 4.41x10^{-12} cm^3/molecule/s
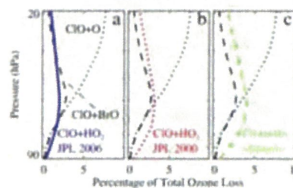
Kovalenko et al (2007) [Balloon and Model] showed better agreement with k1 by Stimpfle et al (1979). von Clarmann et al (2009) also reported same results using ENVISAT/MIPAS.
 $k_1 = 3.3x\ 10^{-11} \exp(-850/T) + 4.5x\ 10^{-12}(T/300)^{3.7}$
 3.34479x 10^{-12} cm3/molecule/s (Stimpfle)

$ClO + HO_2 \rightarrow HOCl + O_2$ (k_1)

At the middle atmosphere 40-50 km, chlorine spices are distributed among HCl, HOCl, and ClO. The chemical balance among these species is controlled by following chemical reactions;

 $ClO + HO_2 \dashrightarrow HOCl + O_2 \ldots k_1$ (1)
 $HOCl + OH \dashrightarrow H_2O + ClO \ldots k_2$ (2)
 $HOCl + h\nu \dashrightarrow OH + Cl \ldots j_3$ (4)
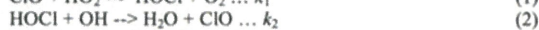
The daytime chemical equilibrium [ClO]/[HOCl] can be simplified at 40-50km, where [OH] is small, as following,

$$\frac{[ClO]}{[HOCl]} \approx \frac{j_1}{k_1[HO_2]}$$ (5)

- SMILES ver. 2.0a, [ClO], [HO2], [HOCl]
- GEOS-5 meteorological data
- j_3: HOCl photolysis is calculated, from cross-section JPL2006, multiple scattering calculation using MODTRAN5 (DISORT, 16 streams).

SMILES観測(ver. 2.0a)に基づくk_1の計算は30, 35, 40 kmにおいてJPL2006を支持している。
Oct. 12, 2009, 57.1±1.8°N, SZA=64.8±1.6°

H (km)	T (K)	k_1 (cm^3/molecules/s)			
		SMILES	WACCM	JPL2006	Stimpfle
30	223.0	5.91E-12	6.87E-12	7.24E-12	2.23E-12
35	228.3	9.75E-12	6.10E-12	7.08E-12	2.44E-12
40	239.8	7.25E-12	5.38E-12	6.76E-12	2.92E-12
45	249.2	3.72E-12	3.70E-12	6.53E-12	3.36E-12

Stratospheric ClO, HO$_2$, and HOCl measurements by SMILES can estimate k (d$_{34}$): ClO + HO$_2$ → HOCl + O$_2$
JPL2011 value: A=2.7E-12, R/E = 220

d_{34} = [HOCl]/[ClO]/[HO2]x{JHOCL + d34[OH] + f35[O]}
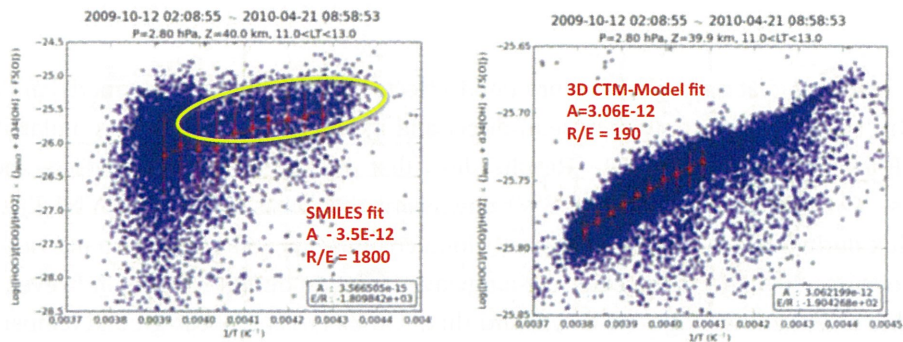
SMILES data fit (left), was not successful but agree with JPL2011 at 250 K.
If we look at only the yellow circle region T<250 K (1/T > 0.004), it may agree with JPL2011.

Summary

- SMILES observed chemistry of 2009-10 Arctic winter with higher sensitivity (~0.015 ppb precision for ClO, better than Aura/MLS ~0.1 ppb), it should make description of chemistry much easy and clear.
- Spatial and temporal features agreed quite well between SMILES and SD-WACCM, in general.
- (ClO)$_2$ formation was tentatively checked through ClO decay during nighttime by comparison with SD-WACCM results, and it looks current knowledge of chemical kinetics is acceptable.
- Chlorine partitioning inside polar vortex can be studied with ClONO$_2$ and other data (from other sensor or model calculations).
- SMILES L2 data (currently ver. 2.1) will be kept updating (to ver. 2.2, 2.3, ...), and ver. 2.1 will be open to general public soon.

Simulation of direct and indirect effects of aerosol on ground radiative fluxes in Chiba City region

Gerry Bagtasa[1,2], Naohiro Manago[1], Naoko Saitoh[1], Hiroaki Kuze[1]

[1]*Center for Environmental Remote Sensing, Chiba University,*
Chiba Inage-ku Yayoi-cho 1-33, 263-8522 Chiba Japan
[2]*Institute of Environmental Science & Meteorology/Natural Sciences Research Institute,*
University of the Philippines, Diliman Quezon City, 1004 Philippines
E-mail: gerrybagtasa@gmail.com

Abstract

There is growing evidence that aerosols have profound effects on radiative and thermodynamic systems of the atmosphere. In this study, the effects (direct, semi-direct and indirect) of aerosols are simulated over Chiba city region using WRF-Chem for the year 2011. Results show that the indirect effect supersede the direct radiative effects of aerosols. Ground-based shortwave (SW) downward flux measurement (SKYNET) shows substantial decrease in SW flux during summer due to increased cloud coverage as compared to an aerosol-free atmosphere. Increased cloud coverage also affects the outgoing longwave radiation during summer, however, it does not seem to have considerable effect on the longwave downward flux. On its effect on near-ground temperature, aerosols in the fine and coarse modes tend to increase and decrease near-ground temperature, respectively.

Keywords : aerosols, direct and indirect effect, radiative flux, simulation, WRF-Chem

1. Introduction

Atmospheric effects of aerosols are one of the major uncertainties in our current understanding of Earth's climate system (IPCC, 2007). Aerosol radiative forcing remains at an uncertainty of -0.5+/-0.4Wm^{-2} while radiative forcing due to greenhouse gases is at 2.63+/-0.26 Wm^{-2} (Forster et. al., 2007). Recently, there is growing evidence that aerosols have profound effects on radiative and thermodynamic systems of the atmosphere (IPCC, 2007). These effects include reduction in solar radiation (direct effect), changes in near surface temperature as well as planetary boundary layer height (semi-direct effect), reduction in cloud droplet size and an increase in cloud droplet number concentration that can lead to changes in cloud albedo and lifetimes (indirect effect) (Isakzen et.al., 2009).

While most aerosol simulation studies focus on past air pollution episodes, only a few deal with the feedback effects of aerosols. For instance, Chapman et. al. (2009) investigated the influence of elevated aerosol sources on summertime aerosol forcing and cloud and aerosol interaction in northeastern America. Zhang et. al. (2010) simulated aerosol-climate feedback effects over the continental USA for January and July of 2001. Goto et. al. (2012) analyzed the effect of aerosol loading on the relationship between SW downward flux, atmospheric optical thickness and single scattering albedo. In this study, we used an online-coupled chemical transport and radiation model (WRF-Chem) to investigate the monthly variation of aerosol direct, semi-direct and indirect effects for the year 2011 in Chiba City region.

2. WRF-Chem Model

Weather Research and Forecast (WRF) (http://www.wrf-model.org) is a mesoscale numerical weather system designed for both operational forecasting and atmospheric research applications with horizontal resolutions ranging from meters to thousands of kilometers. It is a non-hydrostatic model, with several dynamic cores including a fully mass and scalar conserving coordinate version that is widely used in air quality prediction applications. WRF also includes various choices for physical parameterizations to represent atmospheric processes (i.e. microphysics, cloud, radiation, etc.).

The chemistry component of the WRF-Chem (Grell et. al., 2005) is a regional air quality modeling system, which is being continually developed by NOAA (National Oceanic and Atmospheric Administration of USA) and several other research institutes

(http://ruc.noaa.gov/wrf/WG11/). The model treats the processes of transport (advective, convective and diffusive), wet and dry deposition, chemical transformation, emission, photolysis, aerosol chemistry and dynamics, etc. Detailed description of the model is found elsewhere (Grell et. al., 2005). In the past, chemical transport models treated the meteorological and chemical processes separately. Typically the meteorological model was first considered, after which a chemical model is supplied. WRF-Chem is fully consistent with the meteorological component, having the same transport scheme, same time steps, same horizontal and vertical grids and same physical schemes for sub-grid scale transport. This enables users to see the feedback mechanisms between chemistry, radiation, cloud and climate.

3. Method

In this study, we simulated the atmosphere over Chiba City area with and without the existence of aerosols. The effects of these 2 conditions on the overall state of the atmosphere are analyzed and contrasted. Moreover, some observed radiative and meteorological parameters are compared to the simulated atmosphere. These parameters include the shortwave SW and longwave LW downward flux observations, outgoing longwave radiation (OLR), cloud cover and near-surface temperature.

3.1 Observational data

To assess the radiative effects of aerosol, SW and LW downward flux observations by SKYNET (http://atmos.cr.chiba-u.ac.jp/index.html) in Chiba was used. The observation sites of SKYNET are located mainly in East Asia from Mongolia to Thailand as well as in Japan. Observation sites include such instruments as skyradiometer, pyranometer, pyrgeometer, etc. The data observed at each site are collected into a site server and then transfered using an internet for super sites and sent by off-line transportation for other sites. These data are archived into a SKYNET server in Chiba University and then open to the public. Suspended particulate matter (SPM) concentrations are collected from the Atmospheric Environmental Regional Observation System (AEROS) which covers the whole of Japan (http://soramame.taiki.go.jp/). AEROS has 124 sites all over Chiba prefecture and data can be freely downloaded from their website. Meteorological observations used in this study are from the Japan Meteorological Agency's (JMA) Automated Meteorological Data Acquisition System (AMeDAS). AMeDAS is a surface observation network used for gathering regional weather data throughout Japan.

3.2 Domain configuration and Initial and boundary condition

The simulation domain for this study extends from 29.45^0N to 46.18^0N and 126.52^0E to 148.48^0E, covering the main islands of Japan (i.e. Honshu, Kyushu, Hokkaido and Shikoku; excluding Okinawa). The model run has a horizontal grid spacing resolution of 22 km. The meteorological initial and boundary conditions are from the National Center for Environmental Prediction (NCEP) Final Operational Model Global Tropospheric Analyses (FNL) data, available every 6 hours at 1^0x1^0 grid spacing resolution (http://dss.ucar.edu/datasets/ds083.2/). Anthropogenic emissions for gaseous species and aerosols were from the global emission inventory data for the year 2005 compiled and distributed by the Database for Global Atmospheric Research (EDGAR) system (http://www.mnp.nl/edgar) and Reanalysis of tropospheric chemical composition (RETRO) (http://retro.enes.org/index.shtml).

3.3 WRF-Chem Model Configuration

Table 1 summarizes the configuration used in the simulation.

Table 1: WRF-Chem configuration options

Process	WRF-Chem Options
Microphysics scheme	Lin et. al.
Longwave radiation	RRTM scheme
Shortwave radiation	Goddard
Surface layer	Monin-Obukhov
Land surface	Noah Land Surface Model
Boundary layer	Yonsei University scheme
Cumulus parameterizations	Grell 3D
Aerosol chemistry	MADE/SORGAM (Tri-modal)

4. Results and Discussion

Atmosphere over the Chiba City area was simulated with the following conditions: (1) aerosol-free atmosphere hereon denoted by "noChem" and (2) aerosol including gas chemistry, referred to as "wChem", as calculated using the global emission inventories RETRO and EDGAR, including sea-salt, DMS and dust aerosols. Fig. 1 shows the daily-averaged downward SW Flux from January 1 to December 31 of 2011.
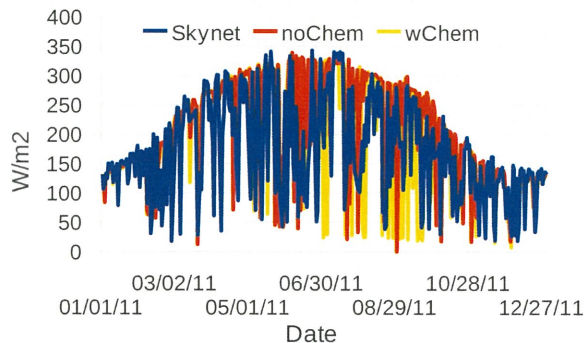
Fig. 1 Observed and simulated daily downward SW Flux variation for the year 2011.
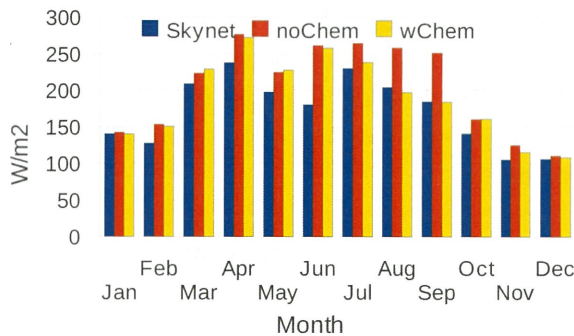
Fig. 2 Observed and simulated monthly-averaged downward SW Flux for the year 2011.

Figure 2 shows the monthly-averaged downward SW Flux for the year 2011. The graph shows a consistent over-estimation bias of the WRF-Chem model in estimating ground SW flux as compared to observations of SKYNET. However, for the months of August and September, there was an apparent difference between noChem and wChem simulations, where aerosol-free condition simulation shows larger calculated values of downward SW flux. This apparent difference is not seen in fig. 3, which is the monthly-averaged downward LW flux for the same year.
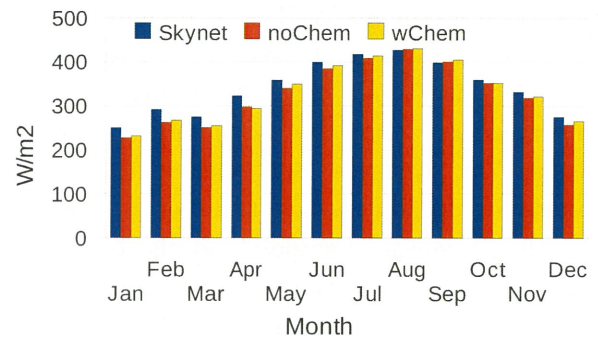
Fig. 3 Observed and simulated monthly-averaged downward LW Flux for the year 2011.
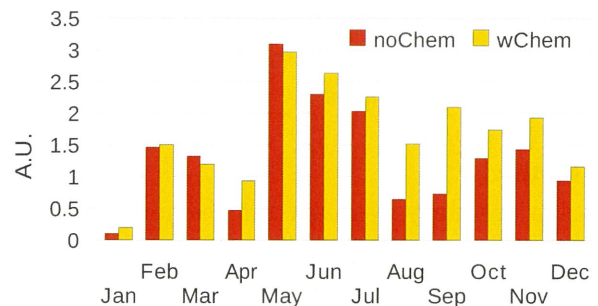
Fig. 4 Simulated monthly-averaged cloud cover over Chiba City area for the year 2011

Figure 4 shows the simulated monthly cloud cover over Chiba city area. Here, it is apparent that simulated cloud cover for the aerosol-loaded (wChem) atmosphere is more than two times higher than the aerosol-free (noChem) simulation. This resulted to a lower SW flux for the aerosol-free atmospheric simulation. However, the underestimation of the aerosol-free condition has no apparent effect on the downward LW flux as seen in Fig. 3.

Although SKYNET has no OLR, simulated OLR for aerosol-free and aerosol-loaded atmosphere as shown in fig. 5 also shows differences in their values for the months of August and September. This time, simulated OLR is higher for the noChem run. This is still due to the higher cloud cover for the 2 summer months resulting from the existence of aerosols in the atmosphere.
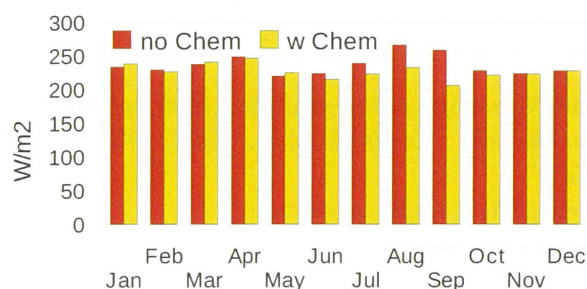
Fig. 5 Simulated monthly-averaged outgoing longwave radiation (OLR)

Fig. 6 shows the average observation and simulation of near-surface temperature from AMeDAS. The WRF has an apparent underestimation bias in estimating near-ground temperatures except for the months of August and September. For the wChem simulation run, however, temperature tends to be higher, and closer to actual observation, than the noChem run. Aerosols tend to increase near-ground temperature but was compensated with higher cloud cover during the months of August and September.
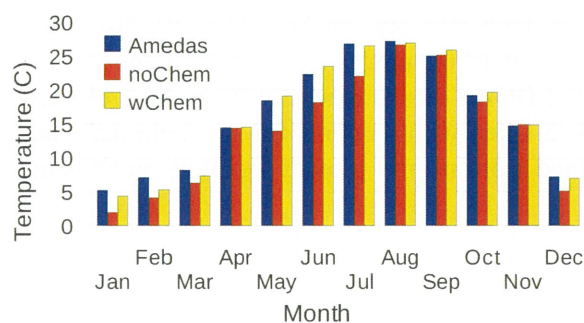
Fig. 6 Observed and simulated monthly-averaged near surface temperature in Chiba City.

5. Conclusion

Simulation of aerosol-free (noChem) and aerosol-loaded (wChem) atmospheres over Chiba City area was done to quantify the effects (direct and indirect) of atmospheric aerosols. Comparison between observed and simulated SW flux showed large deviation for the aerosol-free condition particularly for the months of August and September. This is also the case for the OLR. This can be attributed to the underestimation of cloud cover for an aerosol-free atmosphere. Moreover, existence of aerosols tends to increase near-surface temperature as shown by the simulation, though there is not much difference in terms of near-surface temperature for

the months of August and September due to the higher cloud cover that compensated supposed increase of temperature from the wChem simulation run. Separate wChem simulations with only fine aerosols and fine plus coarse aerosols showed that coarse aerosols slightly reduce near ground temperature.

References
1) IPCC, 2007. The Physical Science Basis. Contribution of Working Group I to the Fourth Assessment Report of the Intergovernmental Panel on Climate Change. Cambridge University Press, Cambridge, United Kingdom and New York, NY, USA.

2) Forster, P., Ramaswamy, V., Artaxo, P., Berntsen, T., Betts, R., Fahey, D.W., Haywood, J., Lean, J., Lowe, D.C., Myhre, G., Nganga, J., Prinn, R., Raga, G., Schulz, M., Van Dorland, R., 2007. Changes in atmospheric constituents and in radiative forcing. In: Solomon, S., Qin, D., Manning, M., Chen, Z., Marquis, M., Averyt, K.B., Tignor, M., Miller, H.L. (Eds.), Climate Change 2007: The Physical Science Basis. Contribution of Working Group I to the Fourth Assessment Report of the Intergovernmental Panel on Climate Change. Cambridge University Press, Cambridge, United Kingdom and New York, NY, USA.

3) Isaksen, I.S.A., C. Granier, G. Myhre, T.K. Berntsen, S.B. Dalsøren, M. Gauss, Z. Klimont, R. Benestad , P. Bousquet, W. Collins, T. Cox, V. Eyring, D. Fowler, S. Fuzzi, P. Jockel, P. Laj, U. Lohmann, M. Maione, P. Monks, A.S.H. Prevot, F. Raes, A. Richter, B. Rognerud, M. Schulz, D. Shindell, D.S. Stevenson, T. Storelvmo, W.-C. Wang, M. van Weele, M. Wild, D. Wuebbles. Atmospheric composition change: Climate–Chemistry interactions . Atm. Environment 43 (2009) 5138–5192

4) Chapman, E. G., W. I. Gustafson Jr., R. C. Easter, J. C. Barnard, S. J. Ghan, M. S. Pekour, and J. D. Fast . Coupling aerosol-cloud-radiative processes in the WRF-Chem model: Investigating the radiative impact of elevated point sources . Atmos. Chem. Phys., 9, 945–964, 2009

5) Zhang, Y., X.-Y. Wen , C.J. Jang . Simulating chemistry-aerosol-cloud-radiation-climate feedbacks over the continental U.S. using the online-coupled Weather Research Forecasting Model with chemistry (WRF/Chem). Atmospheric Environment 44 (2010) 3568-3582

6) Goto, D., Shuhei Kanazawa, Teruyuki Nakajima, Toshihiko Takemura. Evaluation of a relationship between aerosols and surface downward shortwave flux through an integrative analysis of modeling and observation . Atmospheric Environment (2012) in press

7) Grell, G.A., S.E. Peckham, R. Schmitz, S.A. McKeen, G. Frost, W.C. Skamarock, B. Eder. Fully coupled online chemistry within the WRF model Atmospheric Environment, 39 (2005), pp. 6957–6975

Direct sunlight-DOAS measurement of aerosol and NO₂ using a non-scanning fiber sensor

Ilham Alimuddin,[1] Tomoaki Tanaka,[2] Hiroshi Hara,[2] Yusaku Mabuchi,[1] Naohiro Manago,[1] Tatsuya Yokota,[2] and Hiroaki Kuze[1]

[1]*Centre for Environmental Remote Sensing (CEReS), Chiba University,*
[2]*National Institute for Environmental Studies*
E-mail: ialimuddin@graduate.chiba-u.jp

Abstract

The technique called Differential Optical Absorption Spectroscopy (DOAS) is useful for optical remote sensing, enabling measurement of atmospheric trace species over a long distance of a few kilometers [1]. The DOAS method based on a intense light source such as a xenon lamp emitting visible radiation is quite suitable for urban air pollution studies, since both nitrogen dioxide (NO₂) and aerosol, the most important pollutants originated from human activities, can be directly measured using a near horizontal light path in the lower troposphere. In contrast to such active DOAS approach, the use of direct solar radiation can possibly be used for the retrieval of the same air pollution species. In this study, we describe a non-scanning, fiber-based sensor for monitoring the sunlight. Three independent optical fibers are directed toward slightly different azimuthal directions along the ecliptic, receiving the sunlight during several hours around noon. The ends of the fibers are bundled together at the surface of a diffuser plate. The scattered light from the plate is collected with a lens, and coupled to another fiber that, in turn, is connected to a high resolution spectrometer (USB 2000+). This spectrometer can transmit the data in every 100 ms to a PC for implementing the spectral analysis.

The measurement was carried out on three, nearly cloud-free days on 11-13 January 2012. The spectral features in the wavelength range between 400 and 700 nm can be used for the aerosol retrieval, whereas that between 400 and 450 nm for the DOAS measurement of NO₂. The resulting column values are compared with the simultaneous data taken with a collocated sunphotometer and CEReS DOAS spectrometer [1]. Also, the data obtained from nearby ground sampling stations are taken from AEROS database.

Keywords : MAX DOAS, fiber sensor, aerosol, *NO₂*

1. Introduction

In recent years, the atmospheric pollution in Japan has been improved as a whole, as compared with situations a couple of decades ago. Nevertheless, occurrence of air pollution exceeding the environmental standards is still seen in places such as urban roadside and factory areas. Therefore, efforts are required for monitoring anthropogenic air pollution, especially the combustion products such as nitrogen oxides and aerosol particles, also known as suspended particulate matter (SPM). The determination of total (column) amount of such air pollutants can be implemented via optical measurement, in which the spectral intensity is compared before and after the extinction (i.e. the sum of scattering absorption) (1). In this study, we experiment the DOAS method to measure this.

2. Data and Methodology

Raw data is basically retrieved from the spectrum capturing devices such as spectrometer. The design of the spectrometer and how it is supported by other devices in capturing the signal that differentiate DOAS method one from another. In terms of light source there 2 types of DOAS, active is when the light source is an artificial light such as Xenon lamp, while passive DOAS only relies the source from the direct and scattered spectrum of the sun. Pulsed or Long Path DOAS is an example of active DOAS and Multi Axis DOAS is passive, Fig. 1. The direct sun-light DOAS is also categorized as passive and considered low cost as it only uses 400um optical fibers. In our laboratory we experiment all these types of DOAS with the path shown in Figure 1.
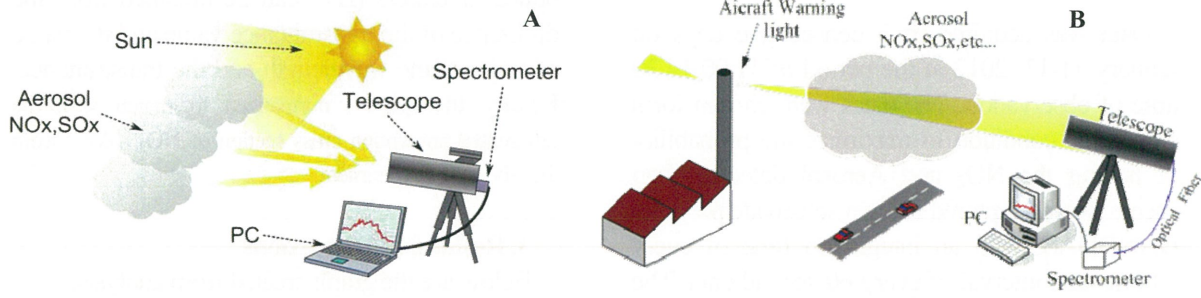
Figure 1. Types of DOAS used in Chiba University measurement. A. LP DOAS B. MAX DOAS

Figure 2. The direct sunlight DOAS configuration with USB2000+ Spectrometer.

The Direct Sunlight DOAS method is similar to MAX DOAS technique (2). It uses three independent optical fibers are directed toward slightly different azimuthal directions along the ecliptic, receiving the sunlight during several hours around noon. The ends of the fibers are bundled together at the surface of a diffuser plate. The scattered light from the plate is collected with a lens, and coupled to another fiber that, in turn, is connected to a high resolution spectrometer (USB 2000+).

The analysis of the DOAS spectra is based on the Beer–Lambert's law expressed as:

$$I(\lambda) = kI_0(\lambda)e^{-L\sigma(\lambda)n} \quad (1)$$

where $I(\lambda)$ is the measured intensity, k is the system constant, $I_0(\lambda)$ is the unattenuated reference intensity, L is the path length, $\sigma(\lambda)$ the wavelength-dependent absorption cross section, and n is the number density of the species averaged over the path length. The dimensionless quantity $L\sigma(\lambda)n$ represents the optical thickness, denoted as τ. Below we describe the algorithm developed for the retrieval of NO2 concentration and the aerosol optical thickness. After the background subtraction, the observed light intensity $I_{obs}(\lambda)$ can be expressed as:

$$I(\lambda) = k\, Iref(\lambda)\, Tg(\lambda)\, Tm(\lambda)\, Ta(\lambda) \quad (2)$$
Where

$I(\lambda)$: the observed spectrum
K : Apparatus constant
$Iref(\lambda)$: reference spectrum
$Tg(\lambda)$: NO2 Transmittance
$Tm(\lambda)$:moleculetransmittance
$Ta(\lambda)$: aerosol transmittance

From the formula above we can derive equations,

$$\tau m = 0.00535\, \lambda^{-(3.916+0.074\,\lambda+0.05/\lambda)} \quad (\lambda \text{ in } \mu m) \quad (3)$$
$$\tau a = B\, \lambda^{-A} \quad (\lambda \text{ in } \mu m)$$
$$T = exp(-\tau) \quad (4)$$
$$I'(\lambda) = I(\lambda)\,/\,Iref(\lambda)Tm(\lambda) = kTg(\lambda)Ta(\lambda)$$
$$I_0'(\lambda) = kTg(\lambda)$$
$$Tg(\lambda) = I'(\lambda)\,/\,I_0'(\lambda)$$
$$\tau g = -ln[I'(\lambda)\,/\,I_0'(\lambda)] = ln[I_0'(\lambda)\,/\,I'(\lambda)]$$
$$\tau g = \sigma(\lambda)NL \quad (5)$$

with this equation we can obtain the gas column density (3).

Data was acquired in 3 consecutive days on January 11-13, 2012 at the period of 11.00-14.30 time of observation. The dates were chosen for a cloud free condition to maximize the probability of having the NO₂ and Aerosol detected. Sun spectrum was captured using a self-made program, DANDOAS, with an integration time of every 100 ms and interval of every 60 second data. The fibers were facing the directions from 180-185 degrees.

Below is the graph showing the raw data taken on 3 different dates, Fig 3. And data taken on 2012-01-11-11.00 compared with the spectrum of the sun at the Top of Atmosphere (TOA) from 400-1000 nm wavelength and the standard air mass, AM 1.5.
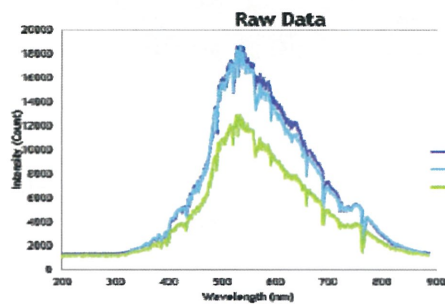
Fig. 3 Raw data measured at 3 different dates at the same acquisition time
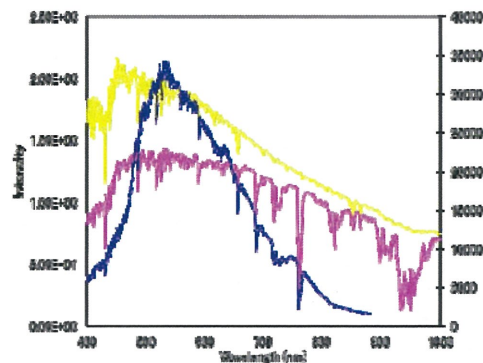
Fig. 4. Raw data (blue) compared with AM1.5 (pink) and sun spectrum of the Top Of Atmosphere (TOA) (yellow) on the wavelength of 400-1000 nm.

The observation intensity data of 400-450 nm after being normalized were compared with the spectrum of TOA at the same wavelength to obtain the transmittance value. The differential

optical thickness ($\Delta\tau$) can be obtained from the difference of the transmittance value and the value of slope of the wavelength and the transmittance. Finally the ($\Delta\tau$) normalized to match with the differential absorption cross section of NO₂ ($\Delta\sigma$) from the laboratory experiment.

3. Result and Discussions

Below are the graph created from analysis.
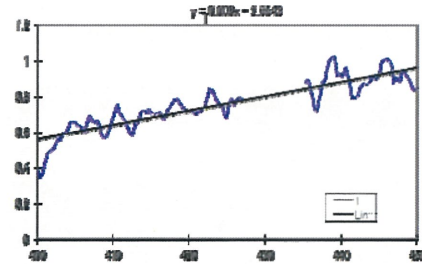
Fig. 5. The slope created from the transmittance value for each observed wavelength 400-450 nm.

On the graph it is noted that the transmittance value for 428-435 nm wavelength are missing due to the inconsistencies of the measurement after the spectral matching, Figure 6..
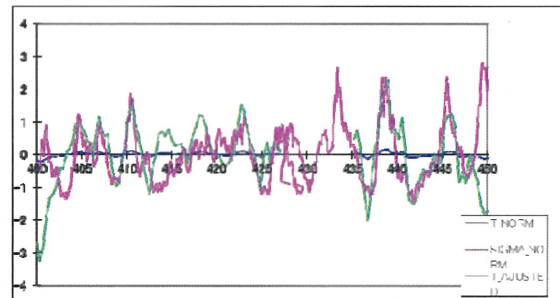
Fig. 6. Spectral matching of the $\Delta\tau$ and $\Delta\sigma$.
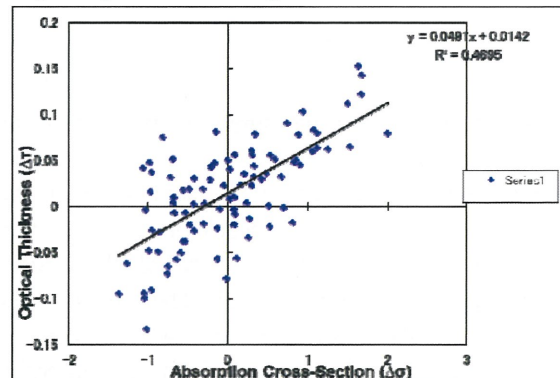
Fig. 7. Scatter plot of $\Delta\tau$ and $\Delta\sigma$.

From the differential optical thickness ($\Delta\tau$) normalized value and the differential absorption cross section ($\Delta\sigma$) normalized value, a scatter plot was created to obtain the value of the NO_2 gas column density, Fig 6. Of the scatter plot, the slope is $y = 0.0491x + 0.0142$ indicates strong linear relationship while the R^2 value is less than 0.5 indicates the relative column density is weak (4).

We also compare the result with other measurement conducted within local area of DOAS system and ground measurement of AEROS soramame data.
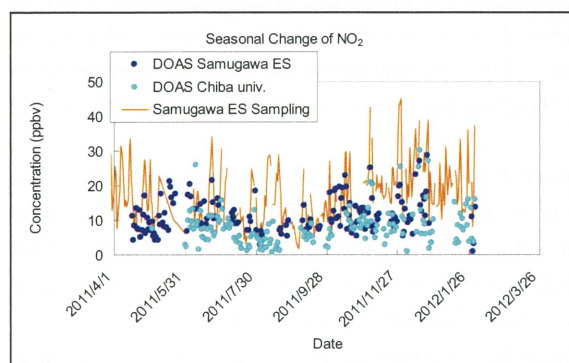
Fig. 8. Measurement of local DOAS system.

When compared to that observed by DOAS and Chiba University (DOAS Chiba univ.), there is a high value on the average degree of 5ppbv which is better results of DOAS measurement in Samukawa Elementary School Ground Station (3). It is obvious changes were seen at high concentrations of NO_2 in the summer becomes low in concentration compared to the winter season.

4.Conclusion and Further works

DOAS technique has been proven to be reliable in retrieving trace gas concentration and particulate matter and for preliminary result, using DOAS technique direct to sunlight without scanning devices enable the efficiency and low cost devices in measuring pollutant concentration in the certain atmospheric column in any given condition.

Further work will be carried out in analyzing the data and compared with other measurement result.

Acknowledgement

References

1) Kenji Kuriyama , Yasuto Kaba, Yotsumi Yoshii, Syuji Miyazawa, Naohiro Manago, Ippei Harada, Hiroaki Kuze, Pulsed differential optical absorption spectroscopy applied to air pollution measurement in urban troposphere, Journal of Quantitative Spectroscopy & Radiative Transfer 112, 277-284 (2011).

2) G. Honninger, C. von Friedeburg, U. Platt, Multi axis differential optical absorption spectroscopy (MAX-DOAS), Atmos. Chem. Phys., 4, 231-254 (2004).

3) Kenji Kuriyama, Yasuto Kaba, Hayato Saitoh, Bannu, Naohiro Manago, Yohei Harayama, Kohei Osa, Masaya Yamamoto, Hiroaki Kuze, Visible and near-infrared differential optical absorption spectroscopy (DOAS) for the measurement of nitrogen dioxide, carbon dioxide and water vapor, International Journal of Technology , 2, 94-101(2011).

4) Naohiro Manago, Shuji Miyazawa, Bannu, Hiroaki Kuze, Seasonal variation of tropospheric aerosol properties by direct and scattered solar radiation spectroscopy, Journal of Quantitative Spectroscopy and Radiative Transfer, 112, 285-291 (2011).

Monitoring Land Subsidence of The City of Makassar using JERS-1 SAR data

Ilham Alimuddin[1,2], Luhur Bayuaji[1], Josaphat Tetuko Sri Sumantyo[1,] Hiroaki Kuze[1]

[1]*Centre for Environmental Remote Sensing (CEReS), Chiba University,*
[2]*Department of Geology, Faculty of Engineering, Hasanuddin University, Indonesia*
E-mail: ialimuddin@graduate.chiba-u.jp

Abstract

Most of the land subsidence events in large cities are associated with the withdrawal of large amounts of groundwater from an aquifer. Such events have occurred in a number of cities in the world due to the groundwater extraction required for development and modernization. Cities in Indonesia have experienced the same phenomena because of the excessive use of groundwater, resulting in the subsidence of the watertable. Study on land subsidence in Jakarta, the capital of Indonesia, was initiated in 1970s using various methods including the latest method based on ground positioning system (GPS) and differential interferometric synthetic aperture radar (DInSAR). Other cities such as Semarang, Surabaya, and Bandung have also been investigated using similar approaches.

The target area of the present study is the city of Makassar, the capital city of South Sulawesi province. The population of the city has increased to 1.2 million in 2010 from the value of 0.94 million in 1990, causing the increased use of both land surface and ground water. Here the DInSAR analysis is conducted on the JERS-1 SAR data acquired during a six year period of 1993-1998. For field recognition, we make use of the QuickBird high resolution optical data, as well as the observation result from a recent field campaign performed in 2009.

The result has indicated that the western part of Makassar has subsided by 10-15 cm during the period of JERS-1 SAR data acquisition. It is known that this part of the city used to be coastal areas and has been reclaimed after around the year 2000. Other than the ground water extraction, the land on the northern part of the city has also subsided due presumably to the load of warehouse and housing constructions. The DInSAR result is in line with the field observation where some houses were levelled down from the initial surrounding and load of construction was clearly observed on some sites.

Keywords : Land subsidence, DInSAR, JERS-1 SAR, Quickbird, Makassar

1. Introduction

The earliest study on city subsidence in Indonesia is the city of Jakarta [1,2], capital of Indonesia has been initiated since 1970s using various method of measurement with the latest method using this differential interferometric synthetic aperture radar (DInSAR). Other cities have been investigated using this technique as well including Semarang [3], Surabaya and the latest one Bandung [4]. Other big cities are waiting for further research with this technique such as Makassar, Medan and Denpasar. This paper describes the development of measuring the dimension of land subsidence phenomena that has occurred in the city of Makassar.

The city of Makassar as the capital of South Sulawesi Province is the 4th largest city in Indonesia, considered to be the gateway of Indonesia from the eastern part. Situated at the southwest part of Sulawesi Island, Makassar city covers an area of 175.77 km2 divided into 14 sub districts. Makassar city lies on the geographic coordinate of 119°18'27,97"-119°32'31,03" East Longitude and 5°00'30,18" -5°14'6,49" South Latitude. The landform is relatively flat, classified as alluvial plain and topography level from 0- 21 meter above the sea level, Figure 1. Geologically, the city is covered by 3 types of formation, Camba Volcanic Formation, Baturape Volcanic formation which mainly consist of fine sediment clastic of volcanic eruptive rocks but mostly eroded and alluvium formation deposit as recent weathered material. In general, we can find 3 types of rock units, basalt, tuff and breccia which derivated from the volcanic origins and sediment deposit like fine to coarse sand. The population of the city has increased to 1.2 million in 2010 from the figure of 0.94 million in 1990, causing the increased use of both land surface and ground water. The rapid urbanization has made Makassar as center for economic development in eastern part of Indonesia.

Based on the statistic data of Makassar City, population has been increasing due to the development and

modernisations that create urbanisation. Makassar as the capital city of the South Sulawesi Province is the target of urbanization. Hence the situation will continuously grow alongside the needs for the people for development to have a better life. As the number of population increase, industries has been triggered to provide new open areas for business, construction and this situation demand spaces. When the government is not able to be pushed in the rural area, the spaces in the city will eventually decrease for particular landuse creating land degradation and could generate land subsidence in the future due to the extraction of water well in the surrounding areas. This has been suspected as the cause of the subsidence of the city land phenomena.
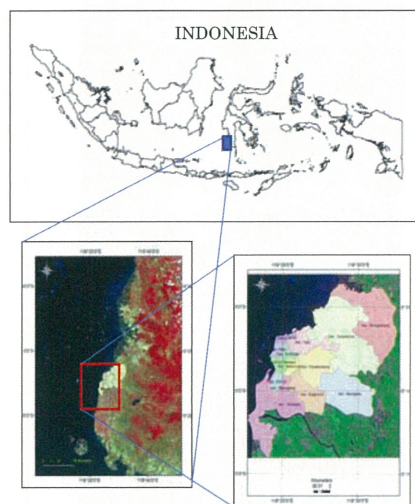
Figure 1. Study area of Makassar City Land Subsidence with the 14 subdistricts.

2. Data and Methodology

This research utilized 8 scenes of JERS-1 SAR images of level 0 covers a swath area of 75 km^2 in descending modes with 35.5 degree of incident angle, but the area focused for the subsidence study is only 175.77 km^2. The subsidence analysis is also supported with optical image data, SPOT 4 acquired 2007 and ALOS AVNIR 2 acquired on June 21 2008. Field campaign was conducted in September 2009 and January 2011 with each measurement was taken by handheld Global Positioning System (GPS). For site validation other than the field check we also used high resolutionof IKONOS images acquired in 2009 and for ground sampling validation of Quickbird acquired on May 6, 2007. All supporting data are georeferenced UTM and WGS 1984 GIS platform.
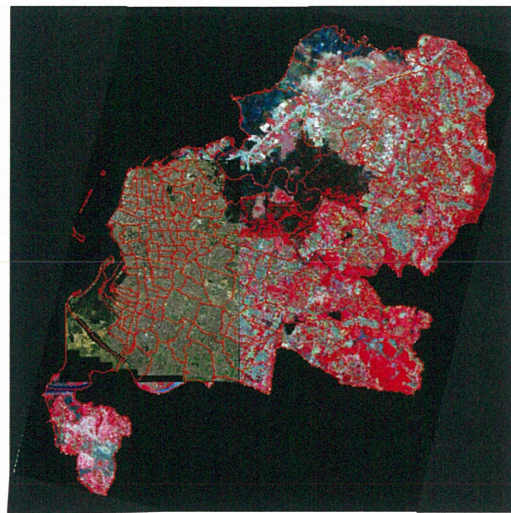
Figure 2.Quickbird and AVNIR2 image of the coverage area.
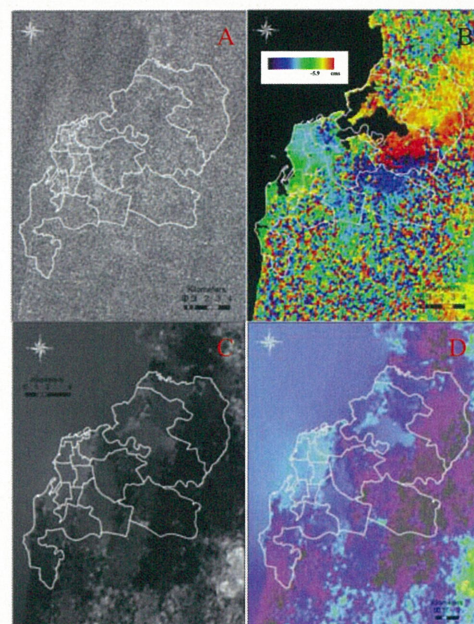
Figure 3. DInSAR Processing images of Makassar City. A.Coherence image of 1995/1996. B. DInSAR Image pair of 1995/1996 images C. SAR, real image D. Deformation Image.

Differential Interferometric Synthetic Aperture Radar (DInSAR) were performed using SIGMASAR software developed by JAXA (Dr. Shimada) combined with ENVI and ARC GIS in creating the GIS analysis. The DInSAR processing uses 2 pass interferometry with 2 pairs of SLC images were processed to create interferogram. The differential interferogram furtherly flattened and unwrapped to obtain the deformation map of the subsidence area
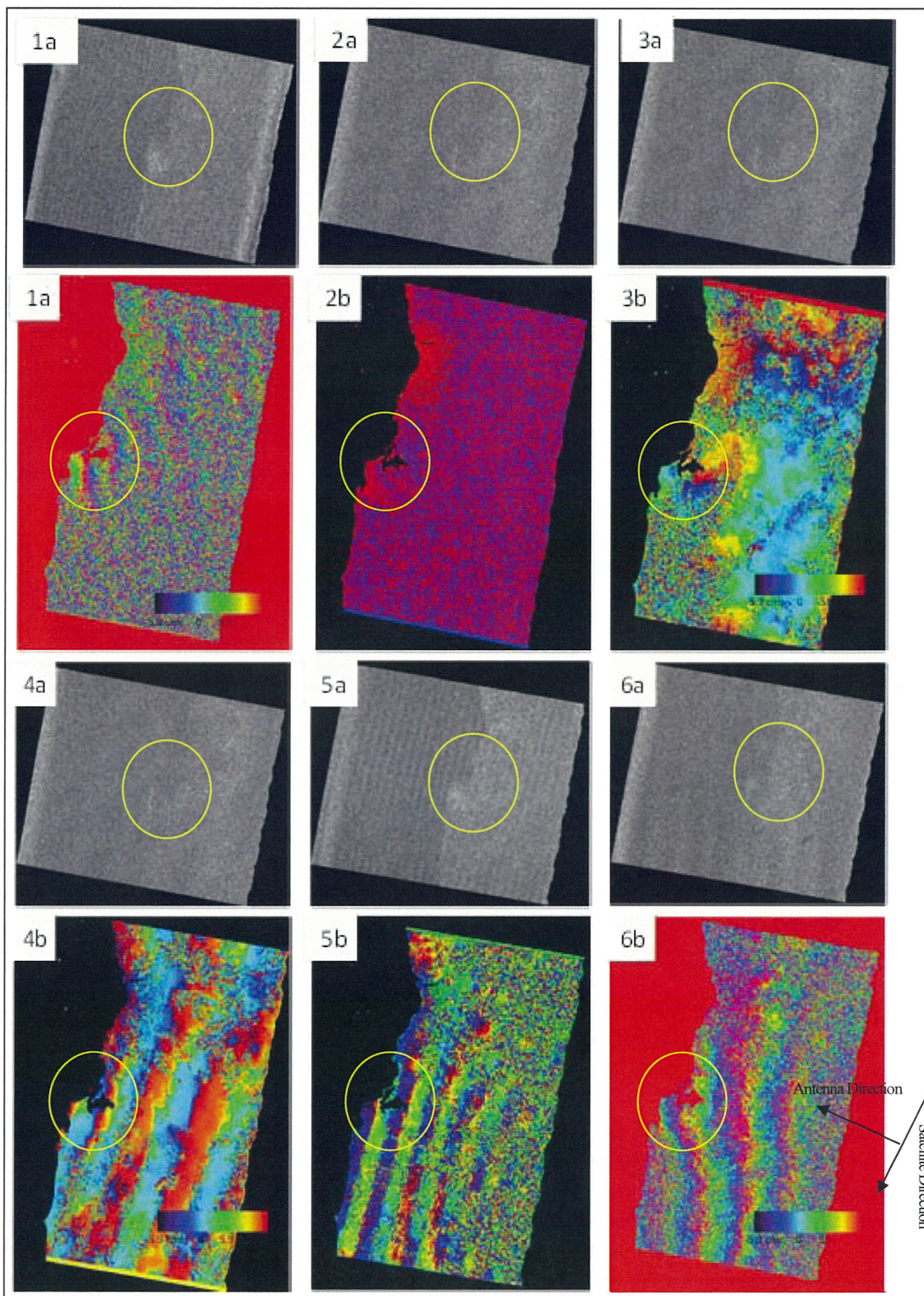
Figure 4. DInSAR processing images a. Coherence images b. DInSAR images Pair of 1993/1994, 2. Pair of 1994/1995, 3. Pair of 1995/1996, 4. Pair of 1996/1997, 5. Pair of 1997/1998. 6. Pair of 1998/1998. Later image is master and earlier image is slave. Yellow outline is the approximate coverage of Makassar City.

3. Result and Discussions

We have shown that the application of DInSAR technique using JERS-1 data can reveal subsidence conditions in the study area. Mostly the subsidence occurred in the northern part of Makassar city during the time interval studied here, though the population density in northern part is lowest among the entire city regions. Industrial district, reclamation area, trading center area, international airport and the seaport are built in this region. The center of the subsidence with the subsidence-affected coverage area can also be estimated easily. It has been found that the subsidence occurred in separated regions with different land usage. Nevertheless, the ground survey has indicated that high human activity exists in every point of subsidence.

Various human activities such as ground water pumping and construction working should have affected the local subsidence phenomena in Makassar, as in the case of other large-scale cities [5]. The main cause of subsidence in Makassar has not been revealed because of the complex feature of the phenomena. However, the result of the present study strongly suggests that the human activity and land use alteration are influencing the geomorphological changes in this city.
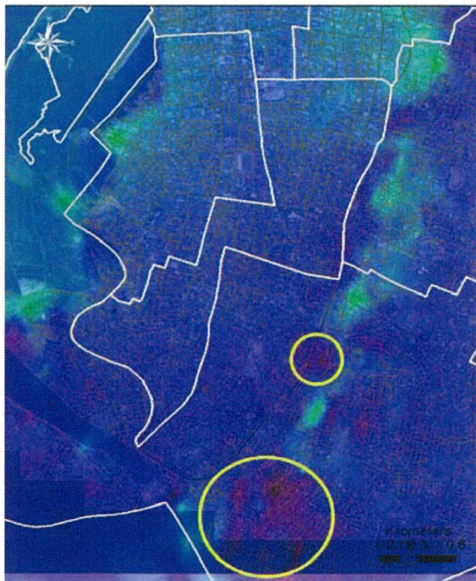
Figure 5. Focus on deformation image of Tamalate and surrounding overlaid with Quickbird image acquired on 20070506. The yellow circle line indicates subsidence.
Field campaign conducted in September 2009 revealed some locations that indicate the incidence of land subsidence and the fact that some parts of the city are having load of building construction that make the city experience of slight movement of its earth surface.

New building construction of warehouses can be seen in picture P1 taken in the area of Tallo, New housing and modern apartment as well as community business complex in P2. Evidence of subsidence can be seen from P4 in Paotere, P5 in Panakkukang, P6 in Mariso and P7 in Tamalate. On of the main road, the soil load can be a thickness of 15-20 centimetres.

Figure 6. Field survey indicates a subsidence.

4. Conclusion

DInSAR method is used to estimate subsidence phenomena which has been derived and applied in this study. Continuous information of subsidence area will be useful for urban maintenance and urban development field, as one important factor for planning and construction works. So far, only few subsidence-related studies have been carried out using SAR data over urban area. We have tried to apply JERS-1 SAR although not all pairs can give good coherence due to the baseline and atmospheric aspects.

Makassar City has been experiencing land subsidence in certain areas as well land piling specially in the area where new building construction complex. We have successfully implemented the DInSAR processing technique in measuring the dimension of the land subsidence. The incidences in some areas show evidence of from 10-15 cm of subsidence. Shown by field observation conforming the DInSAR images.

References

1) Bayuaji, L, Sri Sumantyo, J.T., and Kuze,H., ALOS PALSAR D-InSAR for land subsidence mapping in Jakarta, Indonesia. *Canadian. J. Remote Sensing*, Vol. 36, No. 1, pp. 1–8, 2010.

2) Abidin, H.Z., Andreas, H., Gumilar, I., Gamal, M., Fukuda, Y., Pohan, Y.E. and Deguchi, T., Land subsidence of Jakarta (Indonesia) and its relation with urban development, *Nat Hazards*, 59:1753–1771. 2011.

3) Marfai, M. and King, L., Monitoring land subsidence in Semarang, Indonesia. *Environmental Geology*, 53, pp. 651-659. 2007.

4) Sri Sumantyo, J. T., Shimada, M., Mathieu, P.P., and Abidin, H.Z., Long-Term Consecutive DInSAR for Volume Change Estimation of Land Deformation. *IEEE Transactions on Geoscience and Remote Sensing*, Vol. 50, No. 1, pp. 259 - 270, 2012.

UAVSAR Processing System with Virtex-6 FPGA Board

Kazuteru Namba[1], Takuma Kusama[1], Koshi Oishi[1], Kei Iizuka[1],
Hideo Ito[1], Josaphat Tetuko Sri Sumantyo[2]

[1]*Graduate School of Advanced Integration Science Chiba University, namba@ieee.org*
[2]*Center for Environmental Remote Sensing (CEReS) Chiba University, jtetukoss@faculty.chiba-u.jp*
1-33 Yayoi-cho Inage-ku Chiba-shi Chiba, 263-8522 Japan

Abstract

Synthetic Aperture Radar (SAR) is a class of multipurpose sensors, which can operate in all-weather and day-night time. Circular Polarization SAR (CP-SAR) is less subject to the ionosphere of the earth, and thus it is expected to improve accuracy of observation. We are requested to reduce the size of SAR image data by making on-board SAR image processing on a flight platform. From such a viewpoint, an on-board SAR image processing system is developed for the unmanned aerial vehicle (UAV) with the CP-SAR.

This paper shows an on-board SAR image processing system on an UAV. This radar system is required semi-real-time observation. The proposed system is composed of two FPGA evaluation boards and a PC. One board makes SAR image processing using Range-Doppler-Algorithm (RDA). The other board and the PC has Intel Atom processor and a Solid State Drive (SSD) are used to store data. The proposed system processes a SAR image in 32 seconds or less at a guess. This indicates that the proposed system is applicable to an on-board SAR image processing system on an UAV making semi-real-time observation.

Keywords : CP-SAR, SAR image processing, on-board processing, FPGA

1. Introduction

Synthetic Aperture Radar (SAR) is a class of multipurpose sensors that can operate in all-weather and day-night time. The SAR is available for various purposes such as observing real-time information of ocean waves and monitoring the area of forest [1]. Data observed by radar on aerial platforms such as satellites and aircrafts are processed and delivered to the earth. To use it for disaster management, we have to process and deliver them at high speed. By processing observed raw data at an on-board SAR image processing system, we can reduce the size of data. As a result, we can reduce the communication time between the platforms and the ground, and the required size of storage system in the platforms.

Circular Polarization SAR [2] (CP-SAR: Circularly Polarized SAR) is the world's first SAR that utilizes the circularly polarization. The CP-SAR is less subject to the ionosphere of the earth compared to the traditional radar using horizontal and vertically polarized waves, and thus it is expected to improve accuracy of observation. From this, the Center for Environmental Remote Sensing (CEReS) is developing a micro-satellite carrying CP-SAR. For a preparatory experiment, the CEReS plans to fly Unmanned Aerial Vehicles (UAVs) equipped with CP-SAR. This paper presents an on-board SAR image processing system on UAV

for the preparatory experiment. The proposed system is composed of two FPGA evaluation boards and a PC. One board processes SAR image. This board contains a Xilinx Virtex-6 FPGA (XC6VLX240T-1FFG1156) and a 2 GB DDR3 DRAM. The proposed image processing system has only one 2 GB DRAM, though it processes SAR image data with the size of 6,144 x 19,904 pixels. This fact enables us to process SAR image with only one evaluation board and thus it makes the construction cost for the proposed system low. The other board contains Xilinx Spartan-6 FPGA (XC6SLX45TFGG484), and the PC has Intel Atom processor and a Solid State Drive (SSD). They are used to store data processed by Virtex-6 FPGA.

2. Preliminary
2.1 UAV

Figure.1 shows a picture of the UAV that the CEReS will use the preparatory experiment. This UAV is of 4.75 m length and with 6.00 m wingspan. It is 0.51 m tall. The flight altitude is 3 − 4 km in plan. The main apparatus carried on UAV is CP-SAR antennas, an antenna control system, a flight control system, and SAR image processing system described in this paper. The UAV has no image data downlink system and has a SSD storing the processed pictures. The stored data will be observed after landing.

Fig. 1　UAV used in preparatory experiment

Fig. 2　SAR image processing algorithm

2.2 SAR image processing

Raw image data obtained from CP-SAR requires two-dimensional data processing, range compression for range direction (direction of the microwave radiation) and azimuth compression for azimuth direction (traveling direction of the platform), just like data from traditional SARs. To process image data, the proposed system uses Range-Doppler-Algorithm (RDA), shown in Figure 2 [3]. This algorithm uses two reference data, range and azimuth reference data, obtained beforehand and processed with FFT. We can obtain the processed image from the raw image performing the following operations: First, the raw data are processed with FFT in the range direction, and it is converted from the time domain into the frequency range. Subsequently, in range compression, data are convoluted with (multiplied by) the range reference data. Next, it is processed with FFT in the azimuth direction. To prevent image resolution reducing, the Secondary Range Compression (SRC) is performed. After SRC, data are processed with IFFT in the range direction. Next, we perform Range Cell Migration Correction (RCMC), which corrects errors caused by migration of the UAV. Next, data are convoluted with the azimuth reference data. Finally, we process data with IFFT in the azimuth direction, and then we obtain the processed SAR image.

3. Proposed SAR image processing system

Figure 3 illustrates the outline of the proposed SAR image processing system. The proposed system contains a Xilinx ML605 evaluation board with Xilinx Virtex-6 FPGA. All operations for SAR image processing shown in the previous section (Figure 1) are performed on this board. In the proposed system, processed data are stored in SSD and they will be observed after landing of UAV. Unlike traditional hard disk drive (HDD), SSD features high shock resistance and thus it is available for the preparation experiment on UAV. To transfer processed data from the ML605 board to the SSD at a low cost, we use a Xilinx SP605 evaluation board with Xilinx Spartan-6 FPGA and a Windows 7 PC with Intel Atom processor. First, processed data are sent to SP605 via Rocket IO [4], and next, they are sent to PC through PCI-Express bus. Finally, the PC stores the data into SSD.
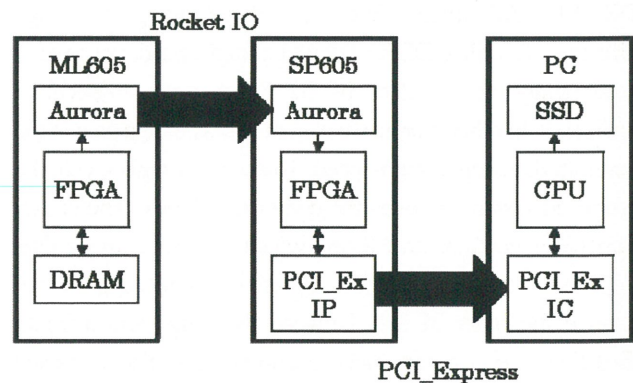
Fig. 3　Outline of proposed system

Figure 4 shows the block diagram of the proposed SAR image processing system, implemented on ML605. The FPGA contains four blocks, a calculation block, an FFT block, a corner turn block and a DRAM controller. The FFT block is much larger than the other three blocks. As shown in
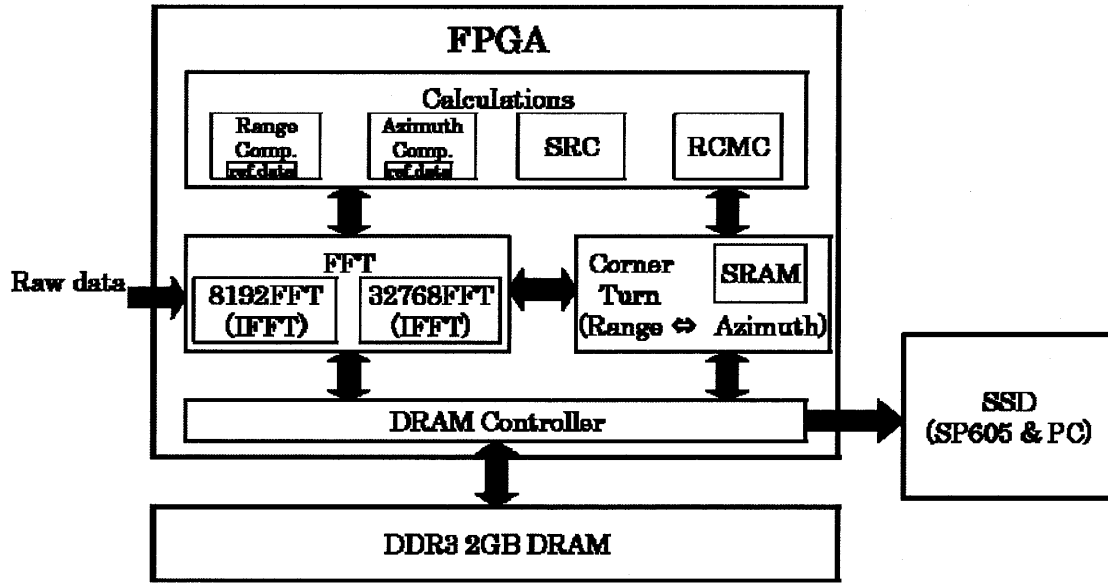
Fig. 4   Block diagram of proposed SAR image processing system

Figure 2, the algorithm contains six times of FFT processing. However, to implement this algorithm in one ML605 board, the proposed system has only two FFT circuits, 8,192-point FFT and 32,768-point FFT circuits. The 8,192 (32,768) point FFT circuit makes both FFT and IFFT processing in the range (azimuth) direction for both the processed SAR image and the reference data. The other calculations, i.e. range and azimuth compression, SRC and RCMC, are made in the calculation block. The range and azimuth compressors have SRAM for storing reference data. The proposed system has one 2 GB DDR3 DRAM controlled by the DRAM controller on the FPGA. The DRAM can keep only one SAR image data with the size of 8,192 x 32,768. In the DRAM, SAR image data are ordered along the range direction. To utilize DDR3 DRAM at high speed, we have to sequentially access data of 32 bytes with consecutive addresses. In other words, we cannot access image data in the azimuth direction at high-speed. To access at high-speed, the proposed system contains the corner turn block. The corner turn block contains an SRAM which can store image data with the size of 32 x 32,768. By using this SRAM, we can change the order of data between the range and azimuth directions, i.e. we can make a corner turn. The proposed system processes the SAR image as follows:

I.   Process raw data in the range direction with the range FFT.

II.   Convolute the data with the range reference data in the range compressor.

III.   Send the data into the SRAM of the corner turn block and make a corner turn.

IV.   Store the data in the azimuth direction into the DDR3 DRAM through the DRAM controller.

V.   Load the data from the DRAM, and process it with the azimuth FFT.

VI.   Process the data with the SRC.

VII.   Copy the data into the SRAM in the corner turn block.

VIII.   Store data in the range direction into the DRAM.

IX.   Load the data from the DRAM, and process it with the range IFFT.

X.   Process the data with the RCMC.

XI.   Copy the data into the corner turn block, and store the data in the azimuth direction into the DRAM.

XII.   Load the data along the azimuth direction into the azimuth compressor, and then convolute the data with the azimuth reference data.

XIII.   Process the data with the azimuth IFFT.

XIV.   Copy the data into the corner turn block.

XV.   Output the data to the SSD in the range direction.

4. Evaluation

For every SAR image with the size of 6,144 x 19,904, the SAR image processing time required for our near-real-time observation system is 60 seconds [3]. This evaluation shows that the proposed system satisfies this requirement. Table 1 shows the evaluation result. In the evaluation, the operation clock frequencies of the FPGA and DDR3 DRAM are 200 and 800 MHz, respectively. The FFT calculation time was

4.74 second. The time for the other calculation was not measured because some calculations used on our UAV were not fixed. However, it was estimated at shorter than the FFT calculation time. The communication time between ML605 and SP605 was 5.70 second, and that between SP605 and SSD was 16.20 second. These operations are made in a sequential fashion. In sum, the total operation time is 31.38 second or shorter for every SAR image, which satisfies the requirement. The table 2 shows the comparison result with the existing SAR image processing systems [4,5]. The operation time of the existing system [4] is longer than that of the proposed system because it uses five older FPGA boards with Virtex-5, which brings about long communication time between FPGA boards. The operation time of [4] is much longer, because its operation differs from those of the proposed system and the existing one [4]. In fact, the system [5] makes some corrections which are not made in the proposed system and [4]. Thus, we cannot make a simple comparison with [5] using the table 2.

Table1. Operation time for proposed system

Operation		Time (second)
SAR image processing	FFT	4.74
	Other	4.74 or shorter
ML605 to SP605		5.70
SP605 to SSD		16.20
Total		31.38 or shorter

Table2. Comparison with existing systems

	[4]	[5]	Proposed system
Total time (second)	50	180 or shorter	31.38 or shorter

4. Conclusion

This paper presented a low-cost UAV on-board SAR image processing system, which uses FPGA evaluation boards ML605, SP605, and a PC with an SSD. The operation time of the proposed system is shorter than 31.38 second, which satisfies the requirement for near-real-time observation systems. In this work, some parts of the proposed system have not been completed while major parts have already been implemented. Future works include the development and evaluation of the completed system.

References

1) Kazuo OUCHI, "Principles of Synthetic Aperture Radar for Remote Sensing," Tokyo Denki University Press, 2004 (In Japanese).

2) Josaphat Tetuko SRI SUMANTYO, "Development of Circularly Polarized Synthetic Aperture Radar (CP-SAR) Onboard Small Satellite," PIERS 2011 Progress in Electromagnetics Research Symposium, 2011.

3) ERSDAC, "Description of SAR Image Processing Algolithum," 2005, available from <http://www.palsar.ersdac.or.jp/> (In Japanese)

4) Toshiki HIRATA, Kazuteru NAMBA, Hideo ITO, Josaphat Tetuko SRI SUMANTYO "CP-SAR Image Processing System using FPGA," IEICE Technical Report, FIIS, 2010 (In Japanese).

5) Yunling Lou, Scott Hensley, Charles Le, Delwyn Moller, "On-Board Processor for Direct Distribution of Change Detection Data Products," Radar Conference, pp.33-37, 2004.

Measurement of trace gases in the lower troposphere using visible and near-infrared light sources

Kenji Kuriyama, Hayato Saito, Yusaku Mabuchi, Naohiro Manago, Ippei Harada, Hiroaki Kuze

CEReS, Chiba University, tskmasu@graduate.chiba-u.jp

Abstract

We have developed spectroscopic methods for continuous monitoring trace species in the lower atmosphere. Such kind of approach based on in-situ, long path length measurement is complementary to the conventional methods based on air sampling. First, differential optical absorption spectroscopy (DOAS) has been applied to simultaneously monitor aerosol and nitrogen dioxide, both being the most important air pollutants in the urban atmosphere. A pulsed xenon lamp equipped on a tall smokestack has been exploited as a light source of the DOAS measurement with an optical path length of 5.5 km. By analyzing the DOAS data with ancillary data from ground sampling, sunphotometer as well as weather data, aerosol behavior characteristic of the Chiba area has been revealed in relation to the regional wind system. Second, the long-path measurement using infrared light sources has demonstrated the capability of measuring atmospheric concentration of carbon dioxide, one of the most important greenhouse gases.

Keywords : Differential Optical Absorption Spectroscopy (DOAS), Air pollution, Aerosol, Molecular absorption, Trace gas species

1. Introduction

The air pollution in Chiba city, which is located along the coast of the Tokyo Bay, exhibits complicated behavior influenced by both local sources such as heavy traffic and industrial complexes and advection from the larger Tokyo metropolitan area. The dominance of southwesterly winds in summer generally causes high humidity from the bay area, whereas that of north to northwesterly winds in winter results in high level air pollution in conjunction with the formation of nocturnal inversion layer [1] . Here we employ the long-term differential optical absorption spectroscopy (DOAS) data taken with an optical path of 5.5 km that connects the observation setup at CEReS and a 130 m tall smokestack of a garbage incinerator operated by the city government. Also the data provided from a collateral sunphotometer and nearby ground sampling stations are employed to elucidate the behavior of major pollution species, aerosol (suspended particulate matter, SPM) and NO_2. Since the DOAS data can be obtained every 5 min, it provides much higher temporal resolution than the ground sampling data, which are produced on hourly basis.

The analysis has indicated that both coarse particles (such as sea salt) and fine particles (such as sulfates) are transported by sea breeze from the southwestern part of the city, where industrial complexes are located along the Tokyo Bay. Since our observation path is severely affected by traffic exhaust from major highways, a significant level of air pollution sometimes takes place depending on the sea/land wind conditions and the development of inversion layer. It has been observed that especially in winter, radiative cooling and weak wind conditions often result in considerable accumulation of pollutants.

Similar long-path optical absorption can also be applied to the monitoring of carbon dioxide (CO_2), the most important greenhouse gases of anthropogenic origins. As a counter-measure for increasing CO_2 concentrations, reliable and less costly approach that enables the in-situ measurement of CO_2 and other greenhouse gases are becoming more and more important. The Greenhouse gases Observing SATellite (GOSAT) was launched on January 23, 2009 by JAXA and NIES (http://www.jaxa.jp/projects/sat/gosat/index). The data for CO_2 column amount retrieved by a ground-based Fourier transform spectrometer (FTS) are useful for the validation of satellite data (Bosch et al., 2006). A network of FTS's has been established by NIES on a global scale (Total Carbon Observing Network : TCCON, https://TCCON- wiki.caltech. edu/) [3] The column amounts of both CO_2 and CH_4 (XCO_2 and XCH_4) from TCCON are calibrated to the concentration scale of WHO with the help of airborne sampling data of these trace gas species [4]. In our approach, on the other

hand, the absorption spectra of both CO_2 and water vapor have been measured along an optical path length of 6.2 km by means of DOAS approach using a halogen lamp and a super luminescent diode (SLD). Conventionally the CO_2 concentration measurement has been undertaken using sampling methods, giving precise but very local concentration of this greenhouse gas species. In contrast, the present method is able to provide data averaged over a long path length, thus better representing the regional concentration. Although the present effective resolution of approximately 8 nm is still insufficient for resolving each rovibrational transition in the 1.6 μm band, further improvement of the detection system will enable the concentration measurement with the accuracy of a few ppm.

2. Instruments

Pulsed flashlights equipped at tall constructions, called aviation obstruction lights, have successfully employed as light sources for the DOAS measurements of NO_2, the most important air pollution species in urban areas [5]. Also, this approach makes it possible to monitor the quantity of aerosol, or suspended particulate matter (SPM). Conventionally aerosol measurements have been carried out by means or ground sampling or sunphotometer, giving data that represent local atmosphere or column amount, or aerosol optical thickness (AOT), toward the solar direction. Thus, the DOAS measurement based on nearly horizontal light path near the ground level provides complementary information as compared with these existing approaches. Both the DOAS and sunphotometer measurements can yield the information on the wavelength dependence of aerosol scattering or extinction, in the form of Angstrom exponent. Here we make interpretation of the DOAS data in comparison with the data from ground sampling and sunphotometer measurements, as well as meteorological data such as wind speed and wind direction. The DOAS instrument, located at CEReS with a height of about 25 m above ground (45 m ASL), is composed of an astronomical telescope and a compact CCD spectrometer connected to a PC. The light source at the top of a 130-m tall incinerator stack (160 m ASL) is a xenon flashlight, giving short (0.5 ms), intense (2×10^5 cd) pulses every 1.5 s. Both NO_2 and aerosol quantities are obtained along the 5.5 km light path.

For CO_2 measurement, we employ both a halogen lamp (Ushio, JCS1000WBGX) and a super luminescent diode (DenseLight, CS5403A) as light sources. A 10-cm diameter telescope is used to collimate the light beam from either of these sources. The detection is attained with an InGaAs photodiode array (Hamamatsu, C9914GB) with a nominal resolution of 8 nm. In order to increase the resolution, and hence the sensitivity of the CO_2 detection, we have also constructed a home-made high-resolution spectrometer for the detection of CO_2 absorption band at 1.6 μm wavelength. Briefly, the spectrometer is equipped with a reflective, blazed grating for the use in the near-infrared region, and two cylindrical lenses are employed for coupling the diffracted light onto the array detector (Hamamatsu, G10768-1024D), resulting in a better resolution of 0.1-0.3 nm/pixel.

3. Results and discussion

3.1 Continuous monitoring of air pollution using DOAS

Here we describe the DOAS data in winter, since higher level of air pollution often takes place during the cold season because of the stable and dry weather conditions. Figure 1 shows the DOAS NO_2 data between 9-10 December 2009 observed at CEReS in comparison with the nearly collateral ground sampling data observed at the Miyanogi station. Since the xenon flashlight is operated only during the daytime, only the sampling data are shown during the nighttime. On 9 December, northwestern wind (land breeze) around 1 m/s speed was observed, while during the subsequent night, wind was nearly nonexistent. Consequently, relatively high concentration of NO_2 (30- 40 ppb) was observed until the morning of 10 December, presumably ascribable to the traffic exhaust. After 6 JST, the increase of both the atmospheric boundary height and wind speed (up to 3 m/s) resulted in the reduced concentration of NO_2 (ca. 15 ppb), representing the diffusion of the pollutants.

Figure 2 shows the aerosol parameters (extinction coefficient, AOT, and Angstrom exponent) in relation to the wind data on 22 February 2009. Relatively smaller values of the Angstrom exponent (α_{ang}) indicate the dominance of coarse particles, mostly due to sea salt particles from the Tokyo Bay. Relatively larger values, on the other hand, suggest that aerosol is from land sources composed of fine particles originating from NO_2 and H_2SO_4. After around 15 JST on 22 February 2001, strong wind from the WSW direction was observed, and as a result, the advection of sea salt particles resulted in the decreased value of α_{ang}.

3.2 Near-infrared, long-path monitoring of CO_2 concentration

Figure 3 shows the absorption spectra of CO_2 and water vapor observed over the atmospheric path length of 6.2 km (30 July 2009). Broad water band are seen in the wavelength regions of 1250-1550 nm and 1750-1975 nm, whereas two CO_2 bands are observed around 1600 nm and 2000 nm. Figure 4
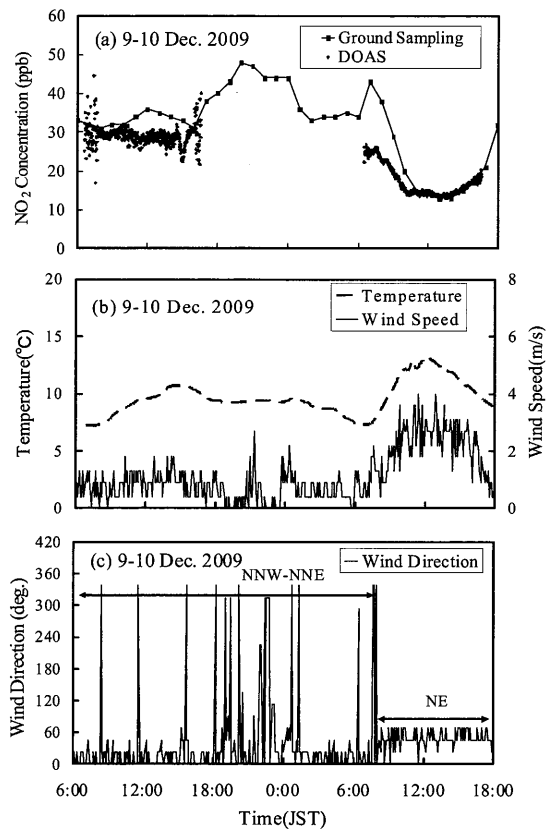
Fig.1 Temporal change of NO₂ concentration comparison between the DOAS and ground observation results , and temperature and wind speed changes during 9-10 December 2009.

Fig.2 Change of aerosol type on 22 February 2009. Panels show the temporal changes of (a) SPM concentration and aerosol extinction coefficient, (b) Angstrom exponent, AOT, and wind speed, and (c) temperature and wind direction.

shows the band in 1950-2050 nm in an expanded scale. Since it is known that the spectrum of the halogen lamp is relatively smooth, the laboratory observed spectrum can be used as a reference (I_0) with appropriate scaling. The transmittance after the absorption $(T = I / I_0)$ can be calculated in this way. As illustrated in Fig. 5, the fitting between the observed (blue) and simulation (red) curves yields the CO_2 concentration of 350 ppm. Here, the simulation has been performed with the MODTRAN radiative transfer code, with an optical resolution of 7.0 nm.

The atmospheric measurement has indicated that a better resolution of the detection system is needed in order to attain better accuracy in CO_2 concentration values from the optical long-path measurement. For this purpose, we have conducted a laboratory experiment in which a super-luminescent diode (SLD) and an InGaAs photodiode array. With a homemade grating spectrometer, the absorption has been obtained in the wavelength region of 1570-1590 nm (Fig. 6). Here the CO_2 absorption is observed with a 1.5-m

long cell filled with 1 atm CO_2 gas. For comparison, laser lines emitted from a narrow-band external cavity diode laser (ECDL) are also shown with a simulated curve based on the HITRAN molecular absorption database. Although very similar absorption features are observed in Fig. 6, the observed absorbance indicates that the effective resolution attained with the experiment has been less than 0.5 nm. Further improvement of the spectrometer is undertaken for realizing better resolution, and hence better detection sensitivity of CO_2 in the real atmospheric experiment.

4. Summary

Since the DOAS data can be obtained in every 5 min, the resultant temporal resolution is much higher than that obtained from the ground sampling that provides air pollution data based on accumulation period of 1 h. We have considered the mechanism of the severe air pollution that often takes place in association with the development of the nocturnal boundary layer by combining the DOAS,
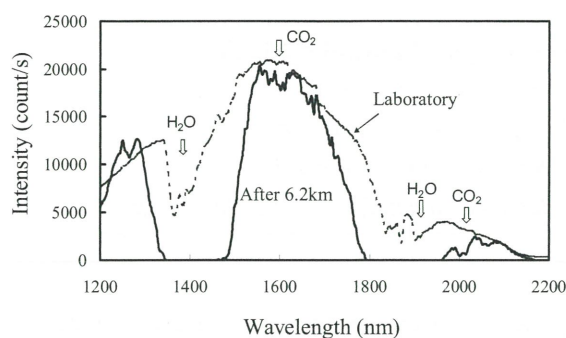
Fig. 3 Molecular absorption spectra observed in the atmospheric measurement over a path length of 6 .2 km
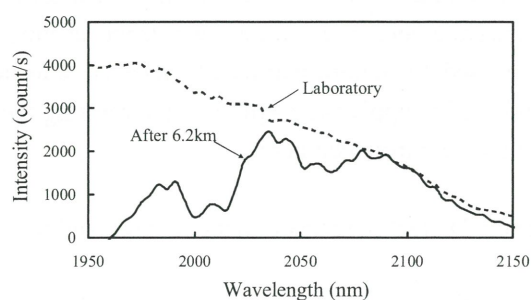
Fig.4 Determination of CO_2 concentration: comparison of the laboratory and atmospheric spectra

Fig. 5 Determination of CO_2 concentration: MODTRAN4 simulation was conducted with Atmosphere=Mid-Latitude Winter, Aerosol=Urban, P_0=1014.7 hPa, T_0=26.1 degC, RH =74.6%, RAT=1.30, VIS=20.0 km, L = 6.216 km, CO_2 =350.4 ppmv, and FWHM = 7.0 nm.
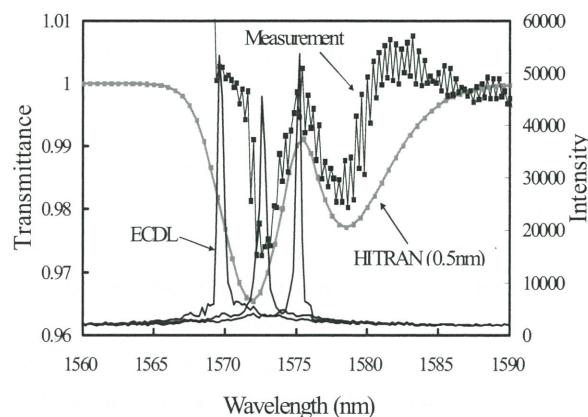
Fig. 6 Laboratory absorption spectrum of CO_2 observed with the homemade spectrometer, with an absorption path length of 1.5 m and CO_2 pressure of 1 atm. For comparison, the atmospheric absorption over a path length is simulated with the HITRAN database .

sunphotometer, and meteorological data.

Conventionally the CO_2 concentration in the atmosphere has been measured as a column amount from in-situ sampling based on ground and/or airborne measurements. In the present paper, we have demonstrated that the capability of the atmospheric long-path measurement for monitoring the concentration of CO_2 and water vapor by utilizing infrared light propagation over a distance of 6.2 km. Such an approach will be useful for carbon fixation studies related to agriculture and forestry, as well as monitoring CO_2 emissions from factories, power plants, and other types emission sources.

References

[1] S. Fukagawa, H. Kuze, G. Bagtasa, S. Naito, M. Yabuki, T. Takamura, N. Takeuchi, Characterization of seasonal variation of tropospheric aerosols in Chiba, Japan, Atmos. Environ, 40, 2160-2168, 2006.

[2] H. Bosch et al, Space-based near-infrared CO_2 measurements: Testing the Orbiting Carbon Observatory retrieval algorithm and validation concept using SCIAMACHY observations over Park Falls, Wisconsin, J. Geophys. Res. 11, D233302, 2006.

[3] O. Uchino, N. Kikuchi, T. Sakai, I. Morino, Y. Yoshida, T. Nagai, A. Shimizu, T. Shibata A.Yamazaki, A. Uchiyama, S. Oshchepkov, A. Bril, T. Yokota, Influence of aerosols and thin cirrus clouds on the GOSAT-observed CO_2: a case study over Tsukuba, Atmos. Chem. Phys. Discus. 11, 29883-29914, 2011.

[4] D. Wunch et al., Calibration of the Total Carbon Column Observing Network using aircraft profile data, Atmos. Meas. Tech., 3, 1351-1362, 2010.

[5] Y. Yoshii, H. Kuze, N. Takeuchi, Long-path measurement of atmospheric NO_2 with an aviation obstruction flashlight and a charge coupled device spectrometer, Appl. Opt., 42 (21), 4362-4368, 2003.

Determination of Dielectric Constants using Reflection Coefficient Measurement and its Application to Snow and Ice Monitoring

Kohei Osa[1], Josaphat Tetuko Sri Sumantyo[2], Fumihiko Nishio[2]

[1]*Weathernews Inc.,*

1-3Nakase Mihama-ku chiba-shi (Japan), k-osa@wni.com,

[2]*Center for Environmental Remote Sensing, Chiba University,*

1-33 Yayoi-cho Inage-ku chiba-shi (Japan), {jtetukoss, fnishio}@faculty.chiba-u.jp

Abstract

The purpose of our research is to investigate and clarify the microwave response from snow and ice on a flat surface and to develop the measurement methods based on these results. The authors attempt to apply those methods to development of microwave sensor for road-surface condition monitoring of winter road maintenance operation, and to ground truth of SAR observations on a sea ice and a snow field. In this paper, a determination method of dielectric constants using reflection coefficients measurement with oblique incidence is introduced. This method is based on free space technique which is often used for determination of dielectric constants of various materials. The authors have conducted experiments and tried to apply the method to determining dielectric constants of snow and ice. And some results of those experiments are introduced here.

Keywords : Microwave remote sensing, Winter road maintenance, Dielectric measurement of snow and ice

1. Introduction

Every material has a unique set of electrical characteristics that depends on its dielectric properties. Complex dielectric constant defined by ε_r ($= \varepsilon' - j\,\varepsilon''$) is one of the important parameters which expresses electric properties of dielectric media. Snow and Ice are also dielectric media in microwave range. Dielectric properties of snow have been reported with many experiments so far, and the empirical models for dry snow and wet snow have been proposed. For example, dielectric constant can be expressed as a function of the physical parameters of snow, density, liquid water content, etc. Based on the results of measurement of the dielectric constants, the physical parameters of snow can be estimated by using those relations and the condition of snow can be estimated consequently. Therefore, it is very important for microwave remote sensing research on snow and ice to investigate the dielectric properties and accurate measurements of dielectric constants are required.

The purpose of our research is to investigate and clarify the microwave response from snow and ice on a flat surface and to develop the measurement methods based on these results. The authors attempt to apply those methods to development of microwave sensor for road-surface condition monitoring of winter road maintenance operation, and to ground truth method on dielectric properties of a sea ice and a snow field.

In this paper, a determination method of dielectric constants using reflection coefficients measurement with oblique incidence is introduced. This method is based on free space technique which is often used for determination of dielectric constants of various materials. The authors have conducted experiments and tried to apply the method to determining dielectric constants of snow and ice. And some results of those experiments are introduced here.

2. Dielectric properties of snow and ice

Snow and Ice are dielectric media in microwave range. Complex dielectric constant defined by ε_r ($= \varepsilon' - j\,\varepsilon''$) is a important parameter which expresses electric properties of dielectric media.

It is well known that the real part value of ice is around three and the imaginary is 10^{-3} at microwave ranges [1]. Snow is a mixture of ice particles and air voids. Dielectric properties of snow have been reported with many experiments so far. Hallikainen and Ulaby et al proposed the empirical models for dry snow and wet snow [2][3]. Dielectric constant ε_r can be expressed as a function of the physical parameters of snow, i.e. density and liquid water content. Based on the results of measurement of ε_r, the physical parameters of snow can be estimated by using those relations and the condition of snow can be estimated consequently.

Dielectric constant of snow (empirical model):
Dry Snow [3]:

$$\varepsilon_r = \varepsilon' = 1.0 + 1.9\rho_{ds} \qquad (\rho_{ds} \leq 0.5[\text{g/cm}^3]) \qquad (1a)$$

$$\varepsilon_r = \varepsilon' = 0.51 + 2.88\rho_{ds} \qquad (\rho_{ds} \geq 0.5[\text{g/cm}^3]) \qquad (1b)$$

where, ρ_s is density of dry snow.
Wet Snow [3]:

$$\varepsilon' = 1.0 + 1.83\rho_s + 0.02\, m_v^{1.015} + \frac{0.073\, m_v^{1.31}}{1 + (f/f_0)^2} \qquad (2a)$$

$$\varepsilon'' = \frac{0.073\,(f/f_0)\, m_v^{1.31}}{1 + (f/f_0)^2} \qquad (2b)$$

where ρ_s is density of dry snow, m_v is liquid water content of snow, f is a frequency of incident wave and f_0 is the relaxation frequency of water.

3. Methodology

The measurement processes are 1) a measurement of reflection responses from specimens, 2) a calculation of reflection coefficients and 3) an estimation of dielectric constants. The outline of the processes is shown in Fig.1.

3.1. Measurement of reflection responses

Magnitude and phase of reflection responses from a specimen are measured with a vector network analyzer (VNA). These measured responses are expressed in S-parameters $S_{11}(\omega)$ in frequency domain. A continuous wave of angular frequency ω is generated with VNA and radiated from an antenna system. The reflected wave from the specimen is received by the antenna and measured as reflection response with the VNA.

3.2. Calibration of reflection coefficients

Because of reflections due to connectors, horn antenna and lens and losses due to cables and so on, the measured S-parameters includes these responses and is different from the actual reflection response of the specimen as following equation. Therefore, it is necessary to remove the residual responses and calibrate the measured values.

3.3. Estimation of dielectric constants

3.3.1. Inverse problem on dielectric constants

Reflection of incident wave occurs at the surface of dielectric medium because of electromagnetic discontinuity. R_1, the reflection coefficient at the boundary, is expressed by Z_0, Z_1, impedances of air and the medium.

$$R_1 \equiv \frac{Z_1 - Z_0}{Z_1 + Z_0} = \frac{1 - \sqrt{\varepsilon_1}}{1 + \sqrt{\varepsilon_1}} \qquad (3)$$

In case of a dielectric medium, which has planer

surface and infinite depth (Fig.2), R_1 can be determined by Γ, a ratio of electric field of the incident wave and reflected wave.

$$\Gamma(\omega) \equiv \frac{E_{reflected}}{E_{incident}} = R_1 = \frac{1 - \sqrt{\varepsilon_1}}{1 + \sqrt{\varepsilon_1}} \qquad (4)$$

Based on the results of measurement of Γ, ε_1 can be estimated by solving the inverse problem.

3.3.2. Layered dielectric medium model (oblique incidence)

Assuming that snow and/or ice on a road surface and road itself compose layered dielectric medium, which has two layers of different media, we measure the dielectric constants of those media. The illustration of the layered dielectric medium model is shown in Fig.3, where θ_0 is a incident angle. Using a continuous wave of angular frequency $\omega (= 2\pi f)$, or frequency f, incident obliquely on the surface of the medium, microwave measurements are made and reflection coefficient $\Gamma(\omega)$ at the surface of the model is expressed by Eq..(5).

$$\Gamma(\omega) = R_1 + (1 + R_1)\frac{R_2\, e^{-2\gamma_1 d_1}}{1 - (-R_1)R_2 e^{-2\gamma_1 d_1}}(1 + (-R_1))$$
$$= \frac{R_1 + R_2 e^{-2\gamma_1 d_1}}{1 + R_1 R_2 e^{-2\gamma_1 d_1}} \qquad (5)$$

where γ_1 is a propagation constant in layer 1 perpendicular to boundary 1. c is light speed. θ_0 is incidence angle. γ_1 is expressed by Eq..(6). R_1, R_2 are reflection coefficients at boundary 1 and 2 respectively, which are expressed by Eq.(7a), (7b) for TE wave, by Eq.(8a), (8b) for TM wave.

$$\gamma_1 = j\frac{\omega}{c}\sqrt{\varepsilon_1 - \sin^2\theta_0} \qquad (6)$$

for TE wave (H polarization):

$$R_{1H} = \frac{\cos\theta_0 - \sqrt{\varepsilon_1 - \sin^2\theta_0}}{\cos\theta_0 + \sqrt{\varepsilon_1 - \sin^2\theta_0}} \qquad (7a)$$

$$R_{2H} = \frac{\sqrt{\varepsilon_1 - \sin^2\theta_0} - \sqrt{\varepsilon_2 - \sin^2\theta_0}}{\sqrt{\varepsilon_1 - \sin^2\theta_0} + \sqrt{\varepsilon_2 - \sin^2\theta_0}} \qquad (7b)$$

for TM wave (V polarization):

$$R_{1V} = \frac{\sqrt{\varepsilon_1 - \sin^2\theta_0} - \varepsilon_1 \cos\theta_0}{\sqrt{\varepsilon_1 - \sin^2\theta_0} + \varepsilon_1 \cos\theta_0} \qquad (8a)$$

$$R_{2V} = \frac{\varepsilon_1\sqrt{\varepsilon_2 - \sin^2\theta_0} - \varepsilon_2\sqrt{\varepsilon_1 - \sin^2\theta_0}}{\varepsilon_1\sqrt{\varepsilon_2 - \sin^2\theta_0} + \varepsilon_2\sqrt{\varepsilon_1 - \sin^2\theta_0}} \qquad (8b)$$

4. Experiments

4.1. Measurement System

An illustration of the measurement system is shown in Fig.4. This system consists of a compact VNA, Anritsu MS2036A, and an antenna system. The antenna system consists of horn antennas and dielectric lenses, which are

set up on a movable frame. Continuous waves generated with the VNA are radiated form the antenna system and incident oblique on the surface of a specimen. Reflected waves are received with the antenna system at the opposite side, and the reflection responses are measured with the VNA.

4.2. Measurement result of artificial snow

i) Specimen: To investigate the microwave response to snow, dielectric measurements for artificial snow were conducted on 20th thru 23rd July 2010 at the Snow and Ice Research Center (Shinjo, Yamagata), NIED. The measurements of artificial dry snow were made in the 4 to 6 GHz range with the incident angles of every 10 degree from 40 to 70 degree. The physical parameters of the specimens are shown in Table 1.

Table.1. Material of specimen.

No	Material of specimen		density [g/cm^3]	thickness [mm]	Temp [deg C]
	Layer1	Layer2	Layer 1	Layer 1	Layer 1
1	Snow	(EPS)	0.34	50	-2.4
2	Snow	(EPS)	0.34	20	-2.4

(EPS: expanded polystyrene foam)

ii) Measurement result: The measurement results of frequency variation of magnitude of reflection coefficients are shown in Fig.5. And estimation results for each specimen are shown in Table 2. Dielectric constants of dry snow can be calculated by the empirical model (Eq..(1)). Substituting the density of the specimen 0.34 g/cm^3, we get the dielectric constant, 1.646. The measurement value of 1.67 and 1.61 agrees well with this value.

Table.2. Measurement result.

No.	Material of specimen		Dielectric constant (real part)		Thickness [mm]
	Layer1	Layer2	Layer 1	Layer 2	Layer 1
1	Snow	(EPS)	1.67	(1)	50.4
2	Snow	(EPS)	1.61	(1)	18.1

(EPS: expanded polystyrene foam)

iii) Angular variations of reflection coefficients: The angular variations of the magnitudes of Γ of V-pol. And H-pol. at 5GHz are shown in Fig.6 7 for specimen No.1 respectively. Furthermore the ratios of Γ of V-pol. by H-pol. at 5GHz are shown in Fig.8 for specimen No.1. From the angular variations of Γ of V-pol., the

Brewstar angles θ_B described by Eq.(9) can be read. But also the angular variations of the Γ ratio can show the angle more clearly.

$$\tan\theta_B = \sqrt{\varepsilon_1} \qquad (9)$$

5. Conclusion

The microwave measurement method of dielectric constants in order to detect snow and ice on a road surface were presented. Some examples of measurements for artificial snow using free space method were introduced. The results show reasonable estimations of the dielectric constants, and they indicate that the method could be utilized for detecting snow and ice on a road surface. Furthermore angular variations of reflection coefficients are shown and the Brewstar angles can be read from them. These results indicate that the angular variations of reflection coefficients with the Brewstar angles can be used to estimate dielectric constants.

However, it cannot be said that we have enough data to develop the sensor system, various cases should be examined. The authors continue to conduct measurements in order to investigate efficiency of the method and grasp the problem for practical use.

Reference

[1] S. Evans, "Dielectric properties of ice and snow-A review", J..Glaciol., vol. 5, pp. 773-792, 1965.

[2] Martti T. Hallikainen et al, "Dielectric Properties of Snow in the 3 to 37 GHz Range", Antennas and propagation, vol. AP-34. No. 11, pp.1329-1340, 1986.

[3] Ulaby, F.T. et al, "Microwave Remote Sensing: Active and Passive vol. III", pp.2062-2071, 1986.

[4] Osam Hashimoto, "Measurement Techniques for Microwave and Millimeter-Wave", pp.12-16, Realize Inc., 1998.

[5] Kohei Osa et al, ""An Application of Microwave Measurement for Complex Dielectric Constants to Detecting Snow and Ice on Road surface", IEICE Trans. Commun., Vol.E94-B, No.11, pp.2987-2990, 2011.
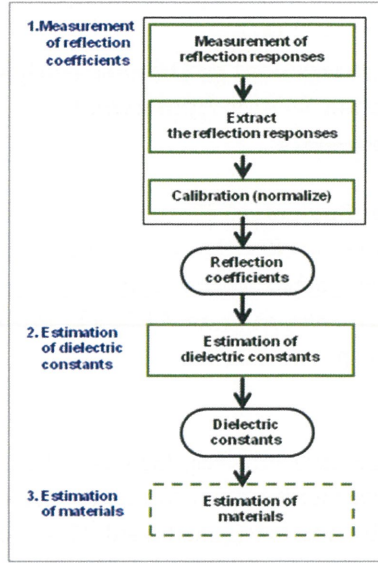
Fig. 1 Measurement process.
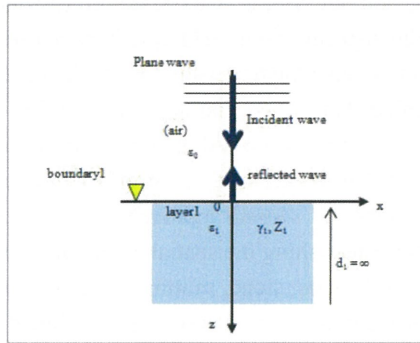
Fig. 2 Reflection at surface of a dielectric medium.
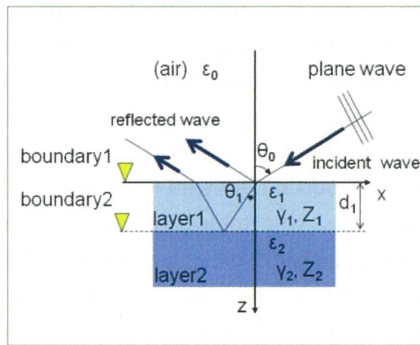
Fig. 3 Theoretical model.
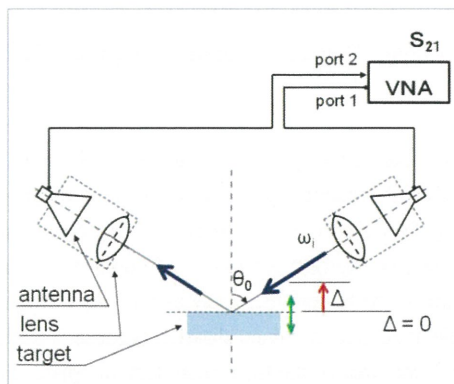
Fig. 4 Measurement system.
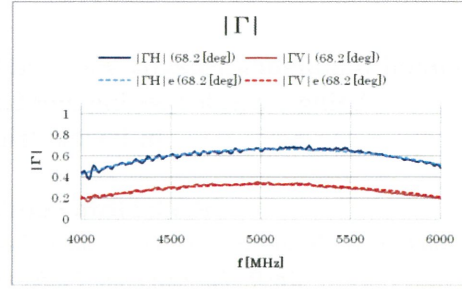
Fig. 5 Measurement result; frequency variation of magnitude of reflection coefficients (d1=50[mm]).
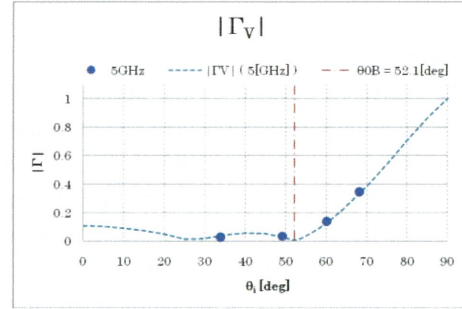
Fig. 6 Angular variation of magnitude of reflection coefficients at 5GHz of V-pol. (d1=50[mm]).
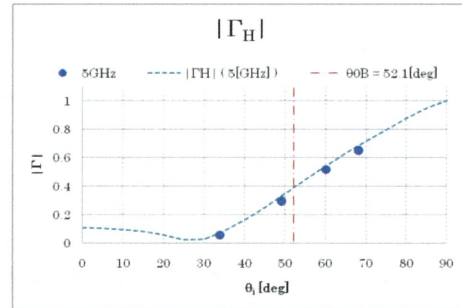
Fig. 7 Angular variation of magnitude of reflection coefficients at 5GHz of H-pol. (d1=50[mm]).
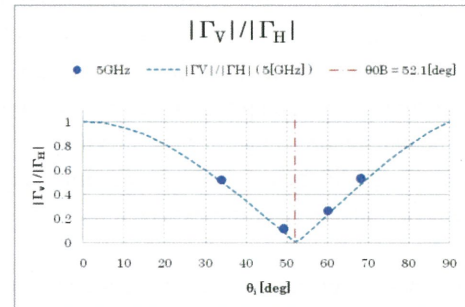
Fig. 8 Angular variation of reflection coefficients ratio of V-pol. by H-pol. at 5GHz. (d1=50[mm]).

Tsunami Inundation Hazard Map and Evacuation Route Assessment as Disaster Mitigation Using Remote Sensing and Geographic Information System Application in Parangtritis Coastal Area, Indonesia

Ratih Fitria Putri[1], Josaphat Tetuko Sri Sumantyo[2]

[1]*Microwave Remote Sensing Laboratory, Center for Environmental Remote Sensing Chiba University1-33, Yayoi-cho, Inage-ku, Chiba-shi, 263-8522 Japan, ratih_nabila@yahoo.co.id*

[2] *Center for Environmental Remote Sensing Chiba University1-33, Yayoi-cho, Inage-ku, Chiba-shi, 263-8522 Japan,* jtetukoss@faculty,chiba-u.jp

Abstract

Parangtritis is located on the coastal area of Bantul District, Yogyakarta Province, Indonesia. This area is considered as high vulnerable area due to tsunami. The coastal area of Parangtritis has multi-land use purposes, as tourism, residential, and agricultural areas which leading to the vulnerable area to tsunami hazard. This research is aimed at analyzing the tsunami hazard impact and making risk disaster mitigation of this hazard. This research uses four scenarios of direction, i.e. wave from west, south-west south, and south east. This research also uses 6 scenarios of run-up, i.e. 5 m, 10 m, 15 m, 20 m, 25 m, and 30 m. The superimposed technique between hazard model, agricultural and non agricultural land use map will be carried out to have the understanding of the potential impact of tsunami to agricultural land production. The research revealed that the coastal area of Bantul is very vulnerable to tsunami hazard. Tsunami is a natural phenomenon which cannot be prevented; however, this does not imply that no one should live in coastal areas. It is very important to maximize the mitigation effort in order to minimize the negative impact from the natural disaster. A remotely sensed approach in combination with the Geographic Information System (GIS) might be more useful for establishing the spatial extent of potential hazard inundation. Digital Image Processing methods used to produce hill shade, slope, minimum and maximum curvature maps based on SRTM DEM contribute to the detection of morphologic traces. These maps combined with Landsat ETM and seismo-tectonic data in a GIS database allow the delineation of coastal regions can be useful for Tsunami analysis. This paper reports the results of an assessment of the impact of tsunami inundation for a coastal segment of Parangtritis. This study has been undertaken for three reasons: (1) the Parangtritis coastal area is one of the most vulnerable areas due to tsunami and has been identified as an area at risk from future tsunami occurrence; (2) this research will predict and make tsunami inundation hazard scenario simulation in research area; (3) Furthermore, to our knowledge, coastal land-use planning in general fail to considered the potential role of the extreme hazard facing on the coastal area. Bantul Local government cooperation with Yogyakarta Central Government has been install siren systems in Parangtritis area where the vulnerable area of tsunami. An emergency evacuation place on the way to a hill top is effective for saving lives. In case of tsunami at midnight, it will be much more dangerous for the villagers to evacuate, because of the complete darkness without electricity, so indications to let them know the evacuation route should be considered. For successful evacuation, therefore higher evacuation places than the expected tsunami should be set in and/or near residential areas.

Keywords: Tsunami Inundation Hazard Scenario, Evacuation Route, Disater Mitigation, Remote Sensing, Geographic Information System.

1. Introduction

Human lives in present day are very vulnerable faced with natural disaster. The disaster happen because of the natural processes both of endogenic (earthquake, volcanic eruption, tsunami) and exogenic processes (flood, landslide, drought, or meteoric). Increasing number of people and the unpredictable disaster has made higher risk in term of losses.

Nowadays the development in Remote Sensing and Geographic Information System can use for reducing and monitoring the disaster. For this reason, well prepared of the disaster risk management are requires in order to minimize disaster impact to human life. Indonesia is one of the most vulnerable areas due to natural disaster, because it is closed to the collision area of the three main tectonic plates in the

world. As the result, this area is very susceptible to the endogen activity and others natural disaster risk.

Table 1 described tsunami record in Indonesia. Tsunami Aceh occurred in 2004 that caused by big earthquake (9.1 in Scale Richter) and recorded as the biggest earthquake since 1900[1]. In the year of 2006, the tsunami happens in the southern part of West Java which shifted to the east. The effect is all the southern part of coastal zone in Java was affected by tsunami.

Table.1. Tsunami Record in Indonesia

Year	Magnitude	Victims (Dead/Injured)	Location
1883	Volcano	36000	Krakatau
1961	-	2/6	NTT, Flores Tengah
1964	-	110/479	Sumatera
1965	7.5	71 Dead	Maluku, Seram, dan Sanana
1967	5.8	58/100	Tinambung (South Sulawesi)
1968	7.4	392 Dead	Tambo (Center Sulawesi)
1969	6.9	64/97	Majene (South Sulawesi)
1977	-	316 Dead	NTB dan P. Sumbawa
1977	8	2/25	NTT, Flores, and P. Atauro
1979	-	27/200	NTB, Sumbawa, Bali, and Lombok
1982	-	13/400	NTT, Larantuka
1987	-	83/108	NTT, East Flores, and P. Pantar
1989	-	7 Dead	NTT and P. Alor
1992	7.5	1952/2126	NTT, Flores, P. Babi
1994	7.8	38/400	Banyuwangi (East Java)
1996	8	3/63	Palu (Center Sulawesi)
1996	8	107 Dead	P. Biak (Irian Jaya)
1998	-	34 Dead	Tabuna Maliabu (Maluku)
2000	-	4 Dead	Banggai, Center Sulawesi
2004	9.1	>200000	NAD and Nort Sumatera
2005	-	-	P. Nias
2006	7.7	665	South Java

*Source: Diposaptono & Budiman,2006[2]

Java Island due to tectonic setting is very vulnerable occurred by Tsunami disaster. According to the catalogue for tsunamis in the Indian Ocean, which includes about tsunamis, 80% of the tsunamis are from Sunda arc region, where on an average, tsunamis are generated once in three years with different scale events[3]. Figure 1 shows the study area. Parangtritis have highly vulnerable of tsunami hazard, it caused many buildings in the coastal area of only a few meters from the coastline and the area is relatively flat. Parangtritis area located on the South Coast of Java subduction zone directly facing the Indo-Australian Plate and Eurasian Plate.

Fig. 1. Study Area

A remotely sensed approach in combination with the Geographic Information System (GIS) might be more useful for establishing the spatial extent of potential hazard inundation as well as to calculate the spatial agricultural damage over large areas[4]. Remote Sensing Approaches for coastal morphology were developing rapidly in the last 2 years. Based on the Landsat ETM and DEM data derived by SRTM of the coastal area produced spatial information in order to represent the coastal morphology.

2. Methods

The inundation zone due to tsunami would be determined using the predicted water depth scenario. This study intends to identify the inundation zone of the hypothetical water depth scenario and quantify the impact of the inundation to agricultural land and non agricultural land. Unfortunately, we exclude the physical mechanisms or hydrodynamic characteristics of tsunami during generation, propagation, or inundation. The formulation of Tsunami inundation wave simulation as below:

The relationship between the height of the tsunami, the coefficient of roughness, and distance towards land was formulated as follows:

$$X_{max} = \frac{0.06 \, H_0^{4/3}}{n^2} \qquad (1)$$

Where:

X_{maks} = Maximum distance the tsunami on land from the shoreline;

H_0 = Height of waves at the shoreline;

n = Roughness coefficient (0.015 to 0.07)

To follow the condition of the surface which has a surface height variation, equation 2 is modified by by entering a determining factor as to lose altitude slopes of the tsunami as shown in the following equation formulated by

Berryman[5].

$$H_{loss} = \left(\frac{16,7 \cdot n^2}{H_0^{\frac{1}{3}}} \right) + 0,5 \cdot \sin S \tag{2}$$

Where:

H_{loss} = Losing altitude for the 1 m distance tsunami propagation

N = Roughness coefficient

H_0 = Initial height of the tsunami on the coastline

S = Slope Surface

S = slope surface Z

$$u = \sqrt{2g \cdot h} \tag{3}$$

Where:

u = Wave Velocity

g = Gravitation Velocity

h = Depth

Equation 3 shows that the velocity is proportional to the height of the tsunami inundation. Tsunami on Parangtritis area is simulated by made a model with few scenarios; 5 m, 10 m, 15 m, 20 m, 25 m and 30 m with different direction wave (West, South and South-West wave direction). Those variations were to represent the scenarios that possible happen on south coast of Java, on field measurement reported that along the south coast of Java between Batukaras and Baron the measured run up heights (RU) ranged from less than 1 m to 15, 7 m. Modelling of inundation areas are based on surface roughness coefficient, wave direction, wave height variation, and slope (slope) area of research. The parameters are then used to calculate the landward inundation. Propagation calculations per pixel that passes through the use of certain land and a certain slope, the reduction in height of the tsunami can be detected. Figure 4 shows flowchart research design.
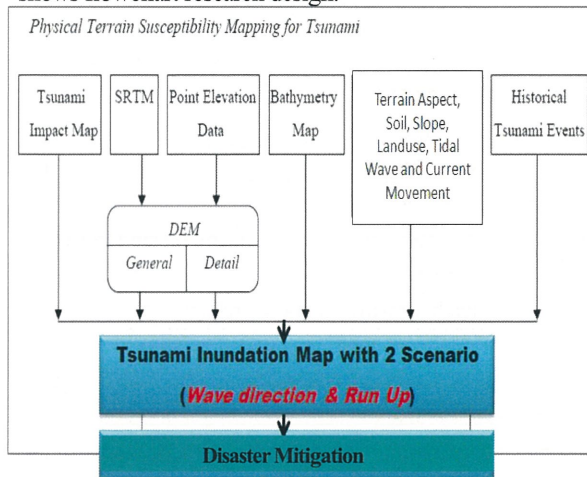
Fig. 4. Flowchart Research Design

3. Results and Discussion

Tsunami Inundation Hazard Scenario Simulation Map

Based on inundation simulation results of the tsunami on the mainland can be seen that the direction of arrival of waves in the stagnant area of influence. At the height of the waves 30 meters inundated the most extensive area occurs when the wave coming from the southwest or an angle almost perpendicular to the coastline with inundation area is 419,144 hectares. Area inundated by the smallest occur if the direction of incoming waves from the southeast scenario. If the waves coming from the south it will inundate an area of 3,038 hectares of rice fields. The most extensive inundation occurs when the wave came from the southwest that is 18,209 hectares. When the tsunami came with run up scenario 5 meters then the whole model shows that there are no fields are flooded. Spatial distribution on a variety of tsunami wave height and direction is presented in Figure 5a, 5b, 5c and 5d shows tsunami inundation hazard map. Tsunami inundation zone for 20 meters scenario has 129.250 hectares (west wave direction); 337.960 hectares (southwest wave direction); 319.125 hectares (south wave direction); and 197.976 hectares (southeast wave direction).
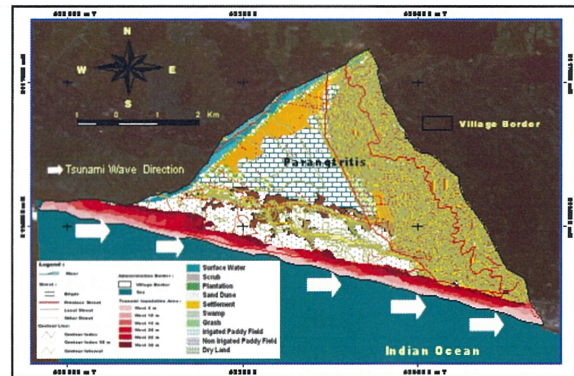
Fig. 5a. Tsunami Inundation Hazard Map with uthwest Direction Wave Simulation
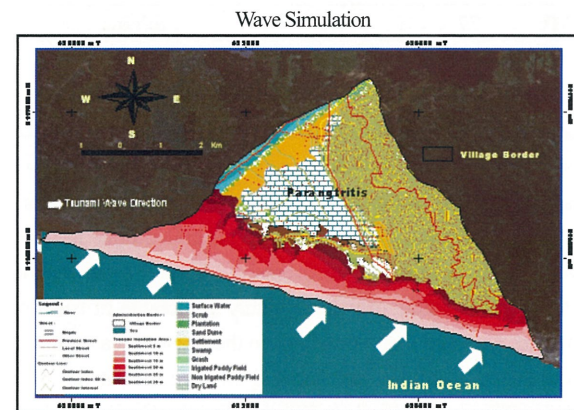
Fig. 5b. Tsunami Inundation Hazard Map with Southwest Direction Wave Simulation
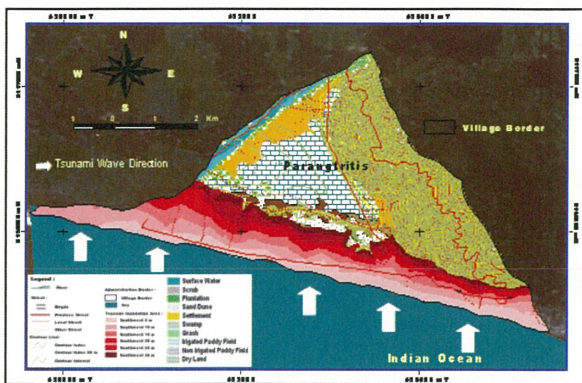
Fig. 5c. Tsunami Inundation Hazard Map with South Direction Wave
Simulation
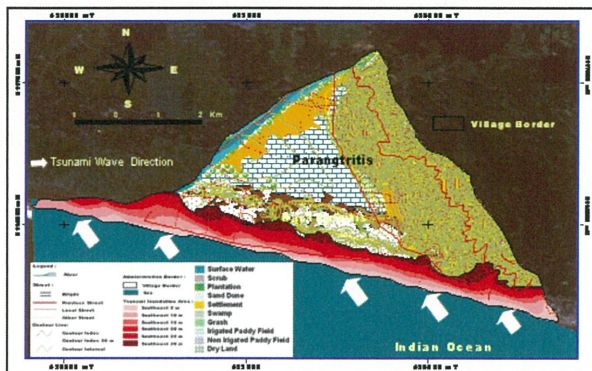
Fig. 5d. Tsunami Inundation Hazard Map with Southeast Direction
Wave Simulation

Evacuation Route as Tsunami Disaster Mitigation

An emergency evacuation place on the way to a hill top is effective for saving lives. There are two alternative paths disaster evacuation for this area, evacuation path to the Yogyakarta city and evacuation path to the mountain area on the east side of area which is the more save zone from the tsunami disaster. The city area can be reach by the road way. Meanwhile the mountain side can be reach by road way and the footpath which is well known by local people. Figure 6 shows evacuation route of tsunami inundation.

Tsunami inundation impact of Parangtiritis coastal area will be needed special safety handling and supervising for holiday and special events due to the high tourist visitors come, can be in thousands visitors on these days. Every visitor has difference preference on the place along the beach but based on this research, area that within around SAR post, this area more density than others. For hazard zone tsunami can be concluded that only when the height 10 m the very danger situation came that threat all the houses and population on that area
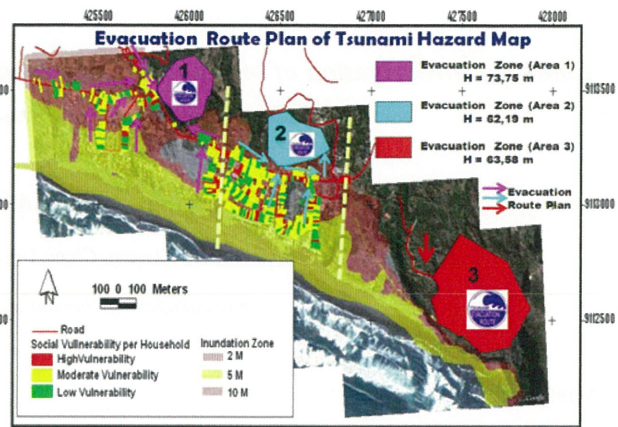
Fig. 6. Evacuation Route Plan of Tsunami Hazard Map as Disaster
Management Planning

4. Summary

Tsunami is a natural phenomenon which cannot be prevented; however, this does not imply that no one should live in coastal areas. It's very important to maximize the mitigation effort in order to minimize the negative impact from the natural disaster. Both government and local people have to sit together, discussing one thing how the standard operation procedure when if the tsunami happen, and how it could be done or government could provide nearest evacuation zone. The result of our study may have important implications for many different stakeholders to make coastal zone in Parangtritis coastal area.

Acknowledgemment

References

1) http://www.ngdc.noaa.gov; spatial data source of tsunami events database, 27 July 2006.
2) Diposaptono, S. and Budiman. *Tsunami*. Bogor, Penerbit Buku Ilmiah Populer, 2006.
3) Rastogi, B.K. and R.K. Jaiswal, A catalog of tsunamis in the Indian Ocean, Science of Tsunami Hazards, 25(3), 128-143 pp, 2006.
4) Berryman, K. *Review of Tsunami Hazard and Risk in New Zealand.* New Zealand: Institute of Geological and Nuclear Science, 2006.
5) Handriani, M. Aplikasi Citra Ikonos Untuk Kajian Perubahan Pantai di Wilayah Ulee Lheue dan Lhok Nga Propinsi Nangroe Aceh Darussalam Pra dan Pasca Tsunami Tahun 2004. *Thesis*. IPB, Bogor, 2006.

Continous investigation of Metropolitan city land deformation by DInSAR technique on L, C and X-band SAR data, case study: Jakarta city, Indonesia

Luhur Bayuaji[1], Bambang Setiadi[1] and Josaphat Tetuko Sri Sumantyo[1]

[1]*Center for Environmental Remote Sensing, Chiba University 1-33 Yayoi-cho, Inage-ku, Chiba, 263-8522 Japan,*

{bayuaji@restaff., bambang@, jtetukoss@faculty.}chiba-u.jp

Abstract

Jakarta, the capital city of Indonesia, has been suffered from land deformation that causes of the damage of properties, public facilities and flood during rainy season. The geologycal structure in Jakarta Area is mostly Alluvial in the northern part. The enermous use of ground water is estimated as the cause of the land deformation. In this study, we apply DInSAR technique on L, C and X-band SAR data to monitor land deformation between 2007 and 2011, continuously. This study exposed the ability of L, C and X-band to analyze land deformation in urban area. The result showed the deformation occurred on several places in nothern part of Jakarta.

Keywords: InSAR, DInSAR, Subsidence, Jakarta

1. Introduction

Differential synthetic aperture radar interferometry (DInSAR) is a technique useful for accurately detecting the ground displacement or land deformation in the antenna line-of-sight (slant-range) direction using synthetic aperture radar (SAR) data taken at two separate acquisition times [1, 2]. The D-InSAR method is complementary to ground-based methods such as levelling and global positioning system (GPS) measurements, yielding information in a wide coverage area even when the area is inaccessible [3].

The area studied in the present work is Jakarta, the capital city of Indonesia. The interferograms, from L, C and X-Band, were used to investigate the land deformation on the study area during 2007 and 2011. Some data from L and C-Band was overlapped in time line. This study will hghlight the specific characteristic of each frequency band in term of accuracy, error noise and decolleration that accure considering different sensor characteristic usage.

2. Study Area

Jakarta is located between 106°33'00"-107°00'00"E longitude and 5°48'30"-6°24'00"S latitude, in the northern part of West Java province. The area is relatively flat: in the northern and central part, topographical slopes range between 0°-2° and in the southern part, they are up to 5°. The altitude of the southernmost area is about 50 m above sea level and the other areas are lower (Figure 1A).

Figure 1B shows the geological information of the study area, which is mostly dominated by alluvial deposit. There are 13 natural and artificial (for supplying public water) rivers flowing through the city. It has humid tropical climate with annual rainfall varying between 1500-2500 mm and is influenced by the monsoons. The nighttime population is around 8 million, which increases to 11 million during business hours since many people commute from satellite cities of Jakarta. The population (residence) density in the five districts was between 9,600-23,000 people km-2 as of the year 2000, while the most recent statistics in 2009 indicates that the values are between 12,000-19,000 people km-2 [4].

The occurrence of land subsidence in Jakarta was recognized by a Dutch surveyor as early as 1926 [5]. Scientific investigations started in 1978,

and continuous investigation using leveling measurement was conducted during 1982-1999 [6]. The measurement using GPS was also undertaken during 1997-2005 [7]: however, its extension to a long-time and wide-area measurement would impose considerable effort and cost.

In this study we would like to investigate land subsidence by applying DInSAR technique on three different wavelength satellite data between 2007 and 2011.

3. L, C and X-Band SAR data set

3.1. L-Band Interferometry: ALOS

The L-Band ALOS PALSAR intrument has been applied to many susidence studies [8, 9]. In this study, ALOS has the longest wacelength (23.6 cm) and has the advantage of deeper prenetration of vegetated areas that contribute to reduce the temporal decorrelation.

We analyzed the subsidence using four images between 2007 and 2009, that construced into three pairs. All the images have been acquired from ascending orbits. The topographic-phase component was removed using 90-m DEM obtained from the Shuttle Radar Topography Mission (SRTM) version 4.1 that has been processed with hole-filled algorithm.

3.2. C-Band Interferometry: Envisat

The C-Band Envisat Advanced SAR (ASAR) sensor has been on operation mode since 2002 and has been used in may subsidence analysis [10, 11]. The wavelength is about 5.6 cm that give a temporal decorrelation over vegetation area compared to L-Band data of ALOS PALSAR. We exploited five images between 2007 and 2009 with ascending orbit. Four pairs have been constructed and have overlapped with ALOS PALSAR data interferometry.
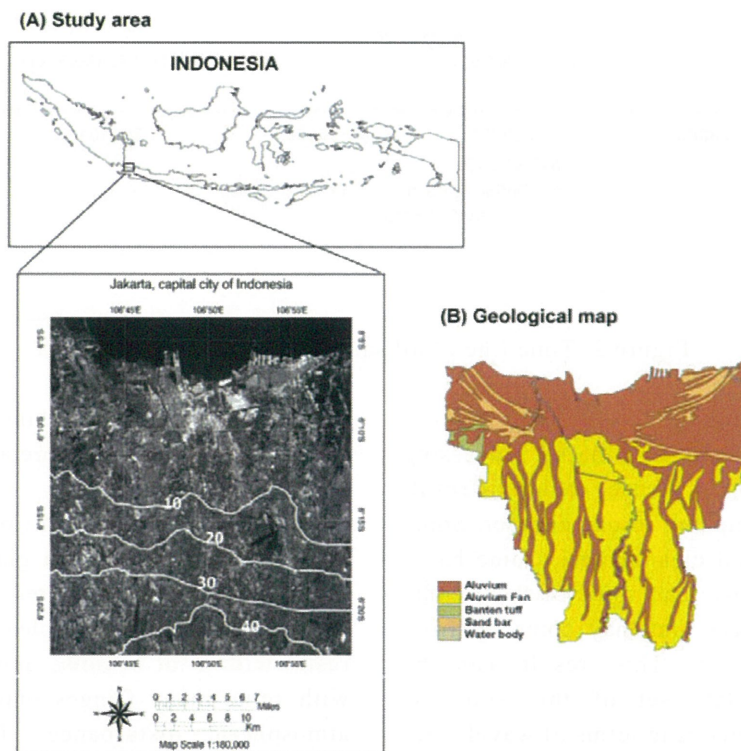
Figure 1. (A) Jakarta city map (B) Jakarta city geological map

3.3. X-Band Interferometry: TERRASAR-X

The ability of TERRASAR-X data to analyze subsidence in urban area has been proved in [12]. In this study, even though the TERRASAR-X has the shortest wavelength (3.1 cm), it has the highest spatial resolution compared to other data and become its advantage.

The TERRASAR-X data is the only data that has

descending orbit in this study. We processed one pair of TERRASAR-X data between 2010 and 2011. This is the newest available data in this study

The timeline of obtained SAR for all satellites can be found in figure 2, while in Table 1, we report their pair, spatial baseline and temporal baseline

Tabel 1. List of Interferogram pairs along with spatial and temporal baseline

Satellite	Pair Number	Pair Combination		Perpendicular Baseline (m)	Temporal Baseline (week)
		Master	Slave		
ALOS	1	20070131	20080203	220	52
	2	20080203	20081105	840	39
	3	20081105	20090205	380	13
ENVISAT	1	20070210	20080719	124	75
	2	20080719	20080927	154	10
	3	20080927	20081206	15	10
	4	20081206	20090912	188	40
TERRASAR-X	1	20100809	20110613	110	44
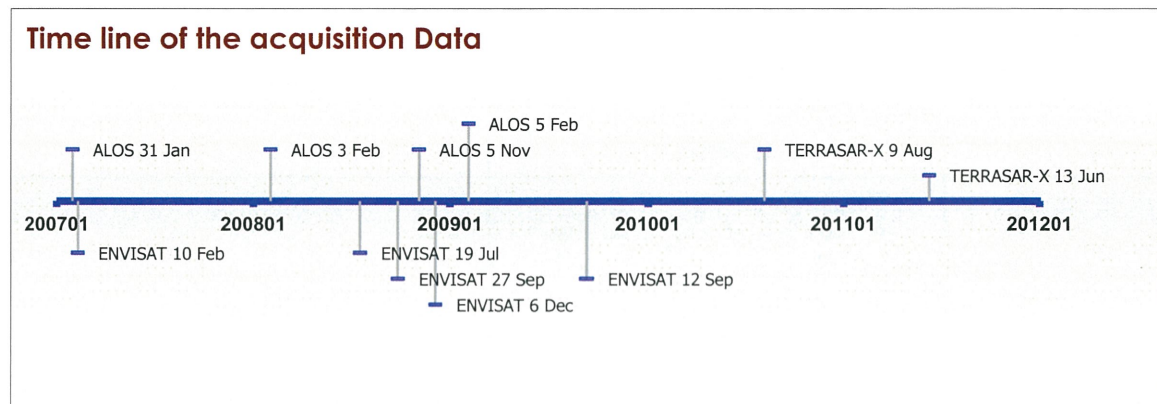
Figure 2. Time line of all satellite acquisition SAR data

4. Result and Discussion

Figure 3 shows the result of DInSAR processing for every data pairs. At a glance, each pair result has less similarity compared to one another. Some of them gives good and clear fringes, some has a result with a lot of noise and some of them come with some many fringes that may come up from atmospheric disturbance. This result can be accepted since the data set of this study is particularly inhomogeneous in terms of wavelength, spatial resolution, three different acquisition geometries and temporal decorrelation.

Giving a side of less similarity result, the subsidence on the northern part of Jakarta can be easily recognized. The subsidence occurrence in this area can be expected since this area formed on alluvial geological structure as seen in Figure 1B.

5. Result and Discussion

Figure 3 shows the result of DInSAR processing for every data pairs. At a glance, each pair result has less similarity compared to one another. Some of them gives good and clear fringes, some has a result with a lot of noise and some of them come with some many fringes that may come up from atmospheric disturbance. This result can be accepted since the data set of this study is particularly inhomogeneous in terms of wavelength, spatial resolution, three different acquisition geometries and temporal decorrelation.

Figure 3. DInSAR result of all interferogram pairs. (A-C) Interferogram pair of ALOS PALSAR data for 20070131-20080203, 20080203-20081105 and 20081105-20090205, respectively (D) Interferogram of 20100809-20110613 TERRASAR-X pair (E-H) Interferogram pair of ENVISAT-ASAR data for 20070210-20080719, 20080719-20090927, 20080927-20081206 and 20081206-20090912, respectively.

Giving a side of less similarity result, the subsidence on the northern part of Jakarta can be easily recognized. The subsidence occurrence in this area can be expected since this area formed on alluvial geological structure as seen in Figure 1B.

The discussion will go deeper to the subset area that fringes constantly appear in each pair of interferogram data. The subset area location can be seen on rectangle area of Figure 3(A), hereafter called Cengkareng area.

The Cengkareng area is a newly developed residence area with more than 300 hundred households living over this area. The cause of subsidence was predicted as the result of ground water extraction, the building construction load and human activity over this area.

The DInSAR result of Cengkareng area shown in Figure 4. The land subsidence is getting worse as the temporal baseline increased. It gives the indication that the subsidence continuously occur in this area. The maximum subsidence for ALOS PALSAR pair was about 1.5 fringes and corresponds to 17.7 cm. As for ENVISAT ASAR pair, the maximum detected subsidence was about 8 fringes and correspond to 22.4 cm. Unfortunately, Cengkareng area cannot be covered on TERRASAR-X pair data as seen on figure 4 (D), but the available DInSAR result shows 8 fringes and correspond to 12 cm. The maximum estimated subsidence for each pairs shown in Table 2
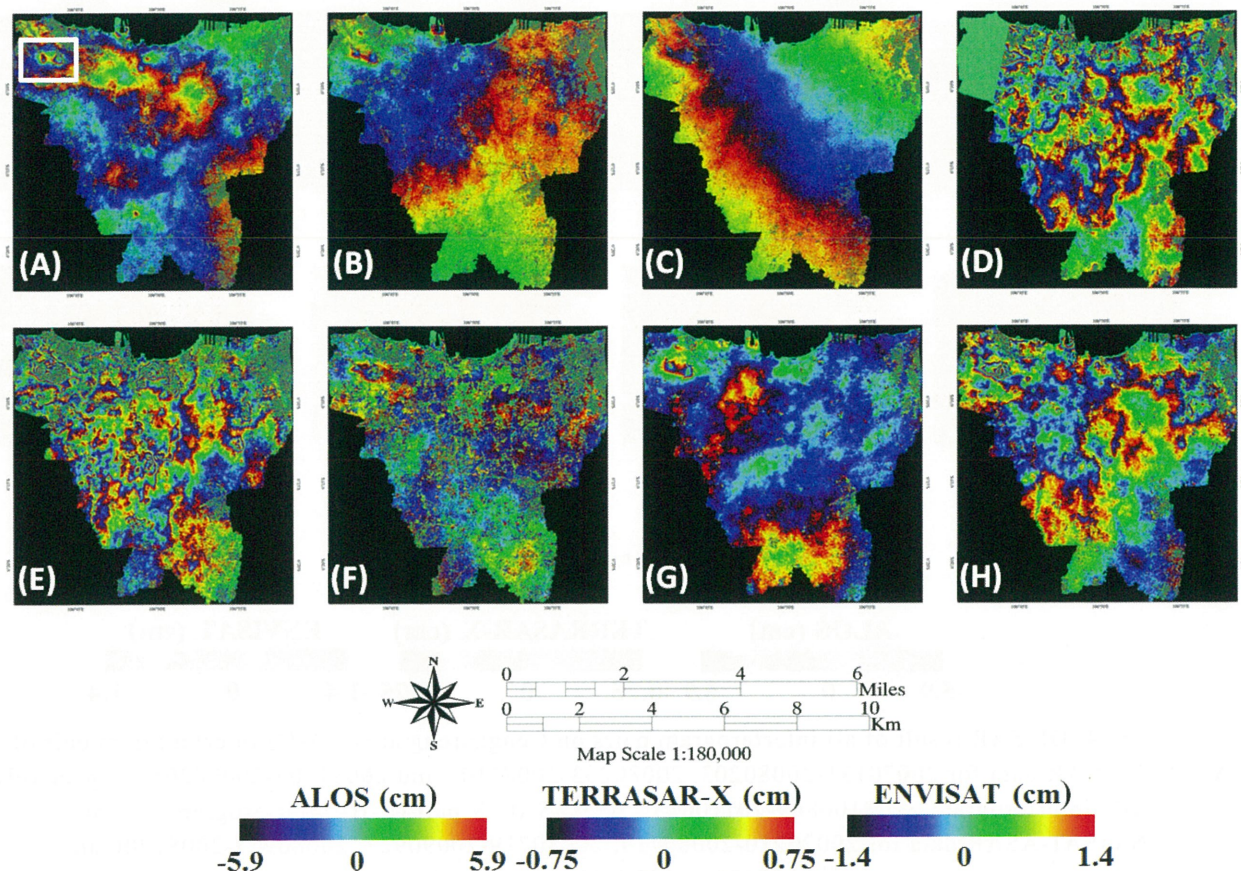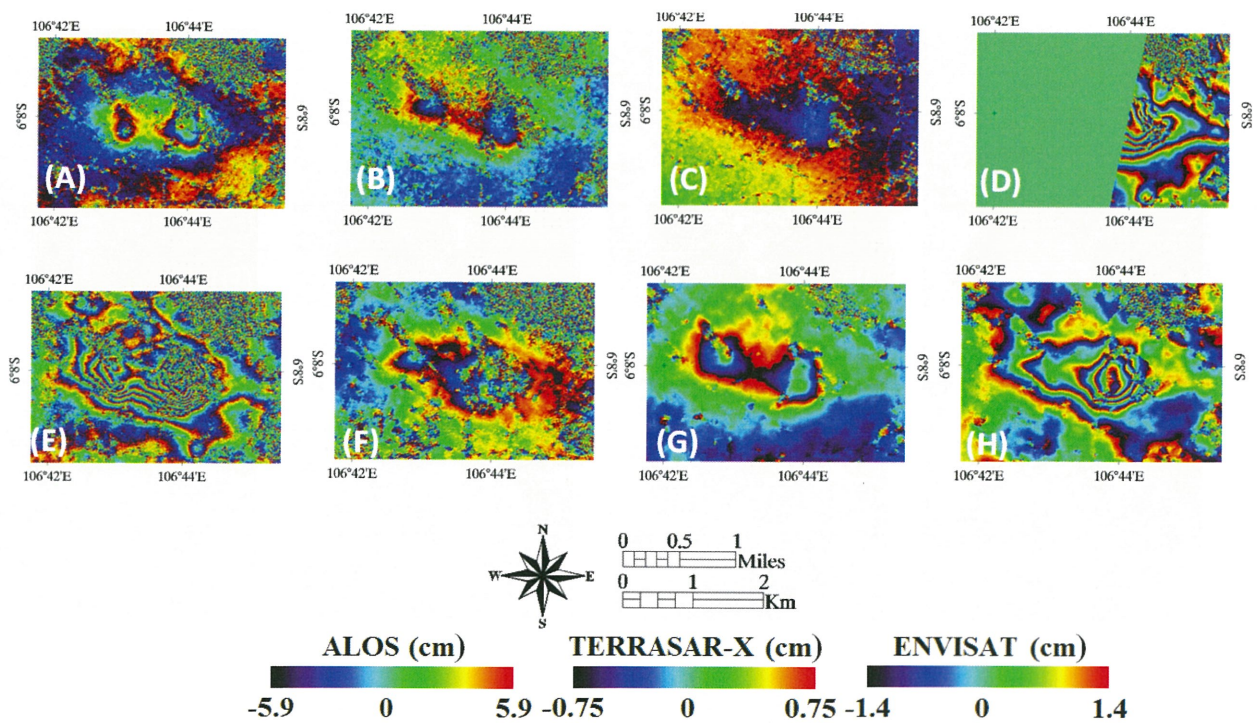
Figure 4. DInSAR result of all interferogram pairs on Cengkareng area. (A-C) Interferogram pair of ALOS PALSAR data for 20070131-20080203, 20080203-20081105 and 20081105-20090205, respectively (D) Interferogram of 20100809-20110613 TERRASAR-X pair (E-H) Interferogram pair of ENVISAT-ASAR data for 20070210-20080719, 20080719-20090927, 20080927-20081206 and 20081206-20090912, respectively.

The comparison between three pairs of DInSAR result, ALOS PALSAR pair on 20080203-20081105, ENVISAR ASAR pair on 20081206-20090912 and TERRASAR-X pair, gives similar subsidence estimation in term of same temporal baseline (about 40 weeks). The subsidence estimation for ALOS, ENVISAT and TERRASAR-X result was 11.8 cm, 12.6 cm and 12 cm, respectively, with the condition of incomplete DInSAR result of TERRASAR-X.

Three different satellite images showed the agreement in term of similar temporal baseline.

Table 2. Estimated maximum subsidence and subsidence rate of each pair

Satellite	Pair Number	Pair Combination		Estimated maximum subsidence (cm)	Subsidence rate (cm/year)
		Master	Slave		
ALOS	1	20070131	20080203	17.7	18.38
	2	20080203	20081105	11.8	16.34
	3	20081105	20090205	5.9	24.51
ENVISAT	1	20070210	20080719	22.4	16.13
	2	20080719	20080927	2.8	15.12
	3	20080927	20081206	4.2	22.68
	4	20081206	20090912	12.6	17.01
TERRASAR-X	1	20100809	20110613	12	14.73

6. Conclusion

In this study, the ability of three different wavelength satellite data has been investigated to detect monitor land subsidence over urban area. Despite of inhomogeneous data set, the result showed the agreement for Cengkareng area. From an applicative perspective, it gives the possibility to monitor the subsidence of urban area by using inhomogeneous data set.

In order to improve the analysis, the transformation to common geometry of one satellite will be conducted in the future.

7. Acknowledgement

8. References

[1] S. Stramondo, C. Bignami, M. Chini, N. Pierdicca and A. Tertulliani, "Satellite radar and optical remote sensing for earthquake damage detection: Results from different case studies", International Journal of Remote Sensing, vol.27, no.20, pp. 4433 - 4447 2006.

[2] D. M. Tralli, R. G. Blom, V. Zlotnicki, A. Donnellan and D. L. Evans, "Satellite remote sensing of earthquake, volcano, flood, landslide and coastal inundation hazards", ISPRS Journal of Photogrammetry and Remote Sensing, vol.59, no.4, pp. 185-198 2005.

[3] D. Raucoules, C. Colesanti and C. Carnec, "Use of sar interferometry for detecting and assessing ground subsidence", Comptes Rendus Geosciences, vol.339, no.5, pp. 289-302 2007.

[4] Dinas Kependudukan dan Pencatatan Sipil Provinsi DKI Jakarta, "Kepadatan penduduk per wilayah kotamadya", Jakarta province government, Jakarta, 2009.

[5] H. Z. Abidin, H. Andreas, M. Gamal, R. Djaja, C. Subarya, K. Hirose, Y. Maruyama, D. Murdohardono and H. Rajiyowiryono, "Monitoring land subsidence of jakarta (indonesia) using leveling, gps survey and insar techniques", International Association of Geodesy Symposia, vol.128, pp. 561-566, 09 June 2005.

[6] R. Djaja, J. Rais, H. Z. Abidin and W. Kuntjoro, "The land subsidence of jakarta metropolitan area", in Proceedings of 3rd FIG Regional Conference for Asia and the Pacific, pp. 14, Jakarta, Indonesia, 2004.

[7] H. Z. Abidin, H. Andreas, R. Djaja, D. Darmawan and M. Gamal, "Land subsidence characteristics of jakarta between 1997 and 2005, as estimated using gps surveys", GPS Solutions, vol.12, no.1, pp. 23-32, 20 March 2007.

[8] T. Onuma and S. Ohkawa, "Detection of surface deformation related with co2 injection by dinsar at in salah, algeria", Energy Procedia, vol.1, no.1, pp. 2177-2184 2009.

[9] Y. Wang and T. R. Allen, "Estuarine shoreline change detection using japanese alos palsar hh and jers-1 l-hh sar data in the albemarle-pamlico sounds, north carolina, USA", International Journal of Remote Sensing, vol.29, no.15, pp. 4429 - 4442 2008.

[10] A. I. Calderhead, A. Martel, P. J. Alasset, A. Rivera and J. Garfias, "Land subsidence induced by groundwater pumping, monitored by d-insar and field data in the toluca valley, mexico", Canadian Journal of Remote Sensing, vol.36, no.1, pp. 9-23, 2010/02/01 2010.

[11] F. Jinghui, G. Xiaofang, G. Huadong, H. Zhengmin, G. Daqing and L. Shengwei, "Mapping subsidence in tianjin area using asar images based on ps technique", in Geoscience and Remote Sensing Symposium, 2007. IGARSS 2007. IEEE International, pp. 2975-2978, 2007.

[12] G. Herrera, R. Tomás, D. Monells, G. Centolanza, J. J. Mallorquí, F. Vicente, V. D. Navarro, J. M. Lopez-Sanchez, M. Sanabria, M. Cano and J. Mulas, "Analysis of subsidence using terrasar-x data: Murcia case study", Engineering Geology, vol.116, no.3-4, pp. 284-295 2010.

Design of a Broadband Antenna for CP-SAR Installed on Unmanned Aerial Vehicle

Yohandri[1,2], J. T. Sri Sumantyo[1], and Hiroaki Kuze[1]

[1]*Microwave Remote Sensing Laboratory, Center for Environmental Remote Sensing, Chiba University, 1-33, Yayoi, Inage, Chiba 263-8522 Japan*

[2]*Physics Department, State University of Padang, Kampus UNP Jln. Prof. Hamka Air Tawar, Padang, West Sumatera, 25131 Indonesia, andri_unp@yahoo.com*

Abstract

A broadband antenna for circularly polarized synthetic aperture radar (CP-SAR) sensor has been designed. This L-band sensor is projected to reduce the Faraday rotation effect and generate the axial ratio image (ARI), which is a new data that expectantly will reveal unique various backscattering characteristics. The sensor will be installed onboard unmanned aerial vehicle (UAV) which will be aimed for fundamental research and applications. To satisfy the requirements of the CP-SAR system onboard UAV, a new broadband microstrip antenna design is presented in this paper. The finite-element method is employed for optimizing the design and achieving a good circular polarization at the center frequency of 1.27 GHz. The broadband axial ratio bandwidth and reasonable gain indicate that this antenna is promising for the CP-SAR sensor. This research will contribute to the field of radar for remote-sensing technology.

Keywords: Synthetic aperture radar, Circular polarization, Broadband antenna

1. Introduction

The role of Synthetic Aperture Radar (SAR) is critical in currently remote-sensing applications due to ability penetrate the cloud, operate in all-weather condition at night and day time. Various applications of SAR data can be found in many areas such as for determination land subsidence [1], volume change estimation of land deformation [2] and, etc.. However, the today SAR with linear polarization has limited information data, which consists of amplitude and phase. To obtain a more thorough measurement data, a SAR sensor with more information will be contributed. Hence, we propose the new SAR system called Circularly Polarized Synthetic Aperture Radar (CP-SAR).

A CP-SAR sensor is projected to generate the axial ratio image, which is a new data that expectantly will reveal unique various backscattering characteristics. In other hands, the CP-SAR sensor also can be applied to reduce the Faraday rotation effect occurring in linear polarization when propagates through the ionosphere [3-5]. The L-band (1.27 GHz) CP-SAR sensor will be installed on an unmanned aerial vehicle (UAV). In UAV experiment, the microwave signal from UAV platform is transmitted by either the left-hand or right-hand circularly polarized (LHCP or RHCP) antenna. The backscattering signal from the target is captured by both the LHCP and RHCP antennas to generate the axial ratio image (see Figure 1). The CP-SAR parameters,

including size, weight, power consumption, etc. have been thoroughly considered to achieve the CP-SAR measurement while maintaining the aerodynamic stability of the UAV system. This sensor is intended for several targets such as land cover and snow cover mapping, oceanography, and disaster monitoring.

To realize this CP-SAR sensor, the link budget calculation of the system has been done in the Microwave Remote Sensing Laboratory (MRSL), Chiba University. The key parameters of the system are presented as listed in Table 1. Based on these parameters, the CP-SAR system and a circularly polarized (CP) antenna are designed.

In previous research, a number of CP microstrip antennas for CP-SAR have been developed [6-10]. Nonetheless, the axial ratio bandwidth of these antennas is quite narrow ($\leq$ 1%). In CP-SAR system onboard UAV, the broadband axial ratio antenna is required to maintain the fine resolutions of the sensor. Therefore, the purpose of the present paper is to describe the design of a broadband CP microstrip antenna for CP-SAR installed on UAV.

2. CP-SAR Sensor System and UAV

Generally, the major parts of the sensor system are composed of a transmitter (Tx), a receiver (Rx) and antennas as shown in Figure 2. The transmitter sub-system consists of a chirp generator, band - pass filters (BPF), an up-converter, a

Table 1 The key antenna parameters for CP-SAR sensor onboard UAV[11].

Parameters	Specification
Frequency center (GHz)	1.27
Pulse Bandwidth (MHz)	233.31
Axial ratio (dB)	≤3
Antenna efficiency	>80%
Antenna gain (dBic)	14.32
Azimuth beamwidth	6.77°
Elevation beamwidth	3.57° - 31.02°
Antenna size (m)	1.5 x 0.4
Polarization (Tx/Rx)	RHCP + LHCP
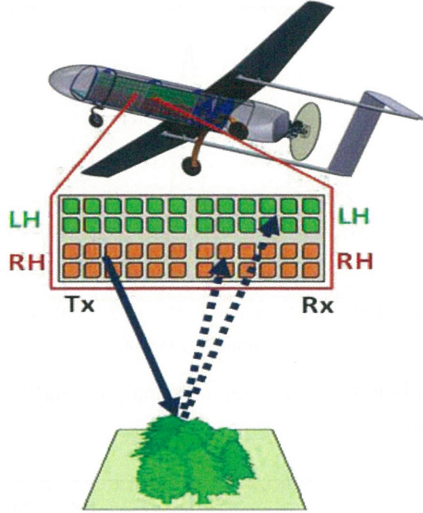
Fig. 1 Transmitting and receiving signal on UAV.
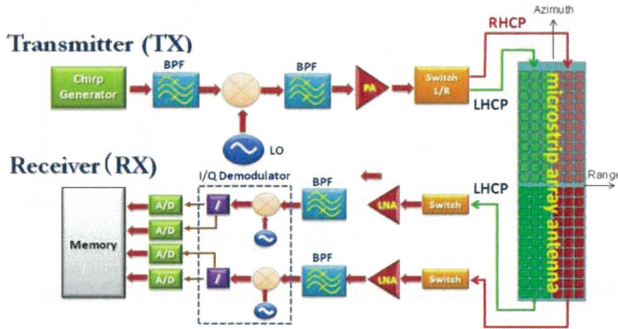
Fig. 2 Design of CP-SAR sensor system.

power amplifier (PA), a local oscillator (LO), and a switch that chooses either the LHCP or RHCP transmitted from the UAV platform. Thus, the receiver sub-system is capable of processing both the LHCP and RHCP signals simultaneously. Major components of the receiver subsystem are a low-noise amplifier (LNA), two BPFs, two I/Q demodulators, 4 channel analog to digital converters (ADCs) and a data recorder (memory).
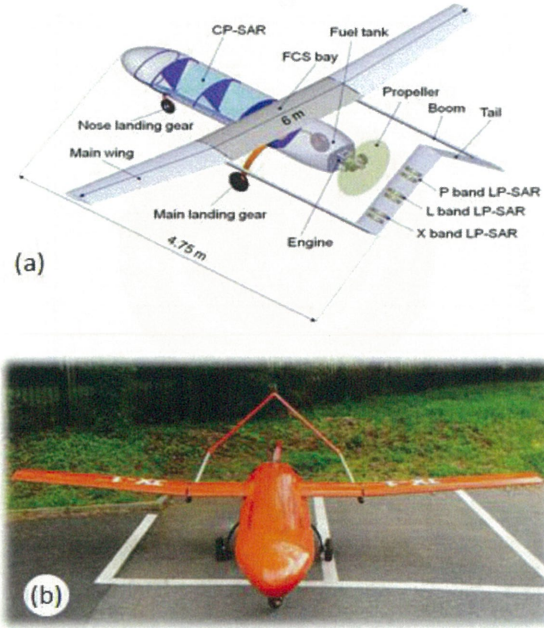
Fig. 3 Unmanned aerial vehicle: (a) Profile of UAV, and (b) Photograph.

Table 2 General specification of the UAV.

| Parameters	Specification
Payload (kg)	20-25
Endurance (hrs)	4-6
Altitude (m)	1000-4000
Speed (km/h)	100-120

The UAV platform has 4.75 m main body length and 6 m wingspan, with a maximum payload of 25 kg. General specifications of the UAV are described in Table 2. The profile and photograph of UAV are shown in Figures 3(b) and 3(c), respectively.

3. Antenna Geometry Design

The geometry of the proposed antenna is shown in Figure 4, where Figure 4(a) gives the top and side view structure, and 4(b) show the 3D view of the antenna structure. The circular microstrip antenna is designed on two layers substrate (NPC-H220A, Nippon Pillar) having a permittivity $\varepsilon_r = 2.17$ and a loss tangent $\delta = 0.0005$. In addition, to obtain a broadband antenna, a Wilkinson power divider is implemented on the feed structure.

The proposed antenna is optimized using Ansoft High Frequency Structure Simulator (HFSS). Based on the simulated result, the optimum geometry parameters of the antenna are the following: $L = 148$ mm, $W = 124$ mm, $h = 1.60$ mm, $W_f = 4.70$ mm, $L_f = 40.0$ mm, $R = 46.0$ mm, $R_f = 25.7$ mm, and $d = 17.7$ mm.
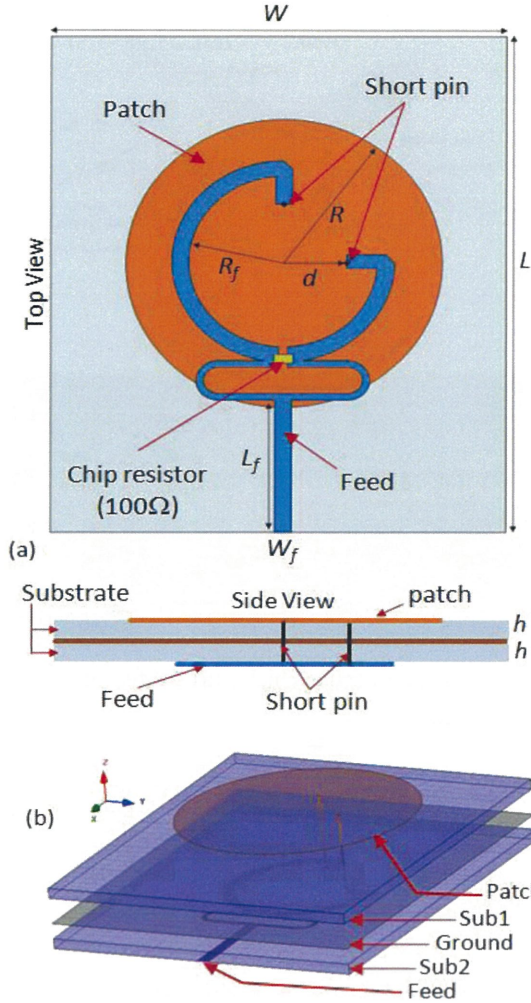
Fig. 4 Geometry design of the proposed antenna: (a) Top and side view, and (b) 3D view.
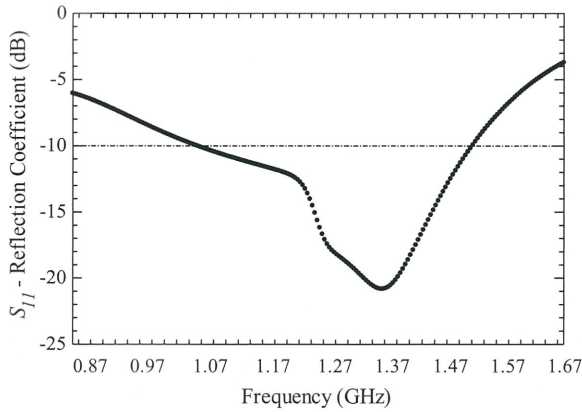
Fig. 5 Reflection coefficient plotted as a function of frequency.

4. Simulation Results and Discussion

Figures 5 to 10 shows the reflection coefficient (S_{11}), axial ratio (AR), gain (G), and radiation pattern of the antenna. The broadband CP antenna characteristic can be achieved as shown in Fig. 5 and Fig. 6.
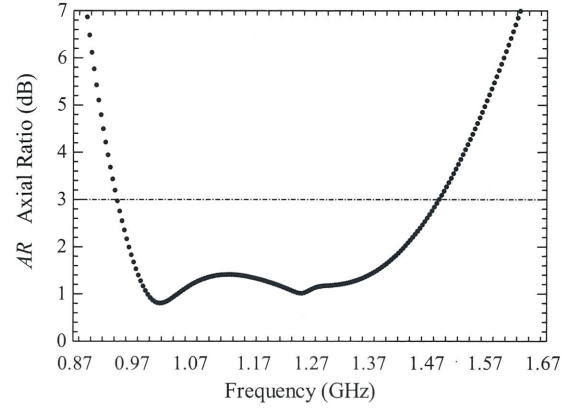
Fig. 6 Axial ratio (AR) plotted as a function of frequency.
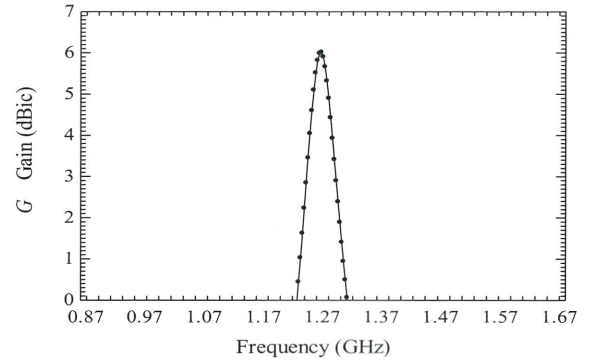
Fig. 7 Relationship between antenna gain and frequency at θ angle $= 0°$.
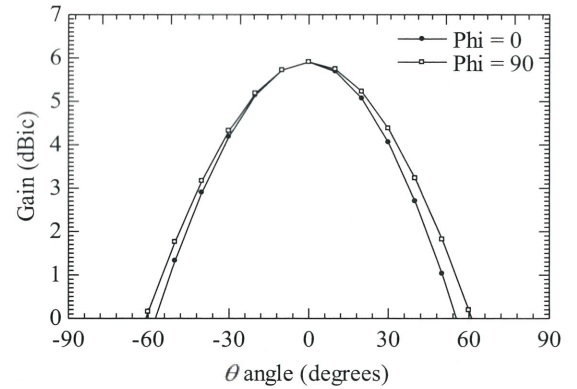
Fig. 8 Radiation pattern of the antenna at $f = 1.27$ GHz.
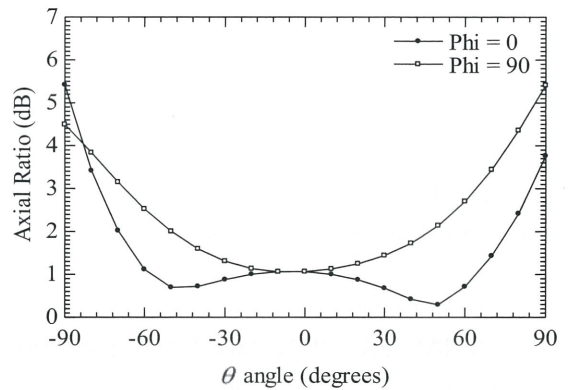
Fig. 9 Axial ratio plotted as a function of theta angle.
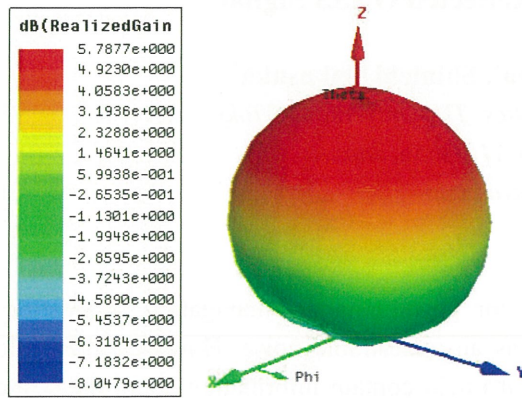
Fig. 10 A 3D beampattern of the antenna at f = 1.27 GHz.

4. Summary

The design of a broadband antenna for CP-SAR sensor onboard an unmanned aerial vehicle has been presented in this paper. The good CP performance has been attained over a 3-dB axial ratio bandwidth of around 540 MHz (42.5%), with fairly high gain of about 6.02 dBic in the operating band (1.27 GHz). In general, the simulated result performance in terms of return losses, axial ratio, and radiation patterns, mostly satisfy the requirements for the CP-SAR sensor onboard UAV. In the future work, the fabrication and array configuration of the broadband antenna will be realized and installed onboard UAV.

Acknowledgements

References

1) Luhur Bayuaji, J.T. Sri Sumantyo, and Hiroaki Kuze, "ALOS/PALSAR D-InSAR for land subsidence mapping in Jakarta city, Indonesia," *The Canadian Journal of Remote Sensing*, Vol. 36, No. 1, pp. 1-8, February 2010.

2) J. T. Sri Sumantyo, M. Shimada, P.P. Mathieu, and H.Z. Abidin, "Long-term Consecutive DInSAR for Volume Change Estimation of Land Deformation," *IEEE Transactions on Geoscience and Remote Sensing*, Vol. 50, No. 1, pp. 259 - 270, January 2012.

3) Maini AK, and Agrawal V. *Satellite technology: principles and applications*. England: John Wiley, 2007.

4) Le Vine DM, Jacob SD, Dinnat EP, de Matthaeis P, Abraham S., "The influence of antenna pattern on Faraday rotation in remote sensing at L-band," *IEEE Trans on Geoscience and Remote Sensing* 2007:45:2737-2746.

5) Rignot EJM. "Effect of Faraday rotation on L-band interferometric and polarimetric synthetic-aperture radar data," *IEEE Trans Geoscience and Remote Sensing* 2000:38:383-390.

6) Yohandri, J.T. Sri Sumantyo, and Hiroaki Kuze, "A new triple proximity-fed circularly polarized microstrip antenna," *AEU - International Journal of Electronics and Communications* doi:10.1016/ j.aeue.2011.09.008.

7) Yohandri, V. Wissan, I. Firmansyah, P. Rizki Akbar, J.T. Sri Sumantyo, and H. Kuze, "Development of Circularly Polarized Array Antenna for Synthetic Aperture Radar Sensor Installed on UAV," *Progress in Electromagnetics Research C*, Vol. 19, pp. 119-133, January 2011.

8) Merna Baharuddin, Victor Wissan, J. T. Sri Sumantyo, and Hiroaki Kuze, "Elliptical microstrip antenna for circularly polarized synthetic aperture radar," *International Journal of Electronics and Communications (IJEC)*, Vol. 65, No. 1, pp. 62-67, January 2011.

9) M. Baharuddin, V. Wissan, J.T. Sri Sumantyo, and Hiroaki Kuze, "Development of an elliptical annular ring microstrip antenna with sine wave periphery," *Progress in Electromagnetics Research C*, Vol. 12, pp.27-36, January 2010.

10) M. Baharuddin, V. Wissan, J.T. Sri Sumantyo, and Hiroaki Kuze, "Equilateral Triangular Microstrip Antenna for Circularly-polarized Synthetic Aperture Radar," *Progress in Electromagnetics Research C*, Vol. 8, pp. 107-120, June 2009.

11) Rizki Akbar, P., J.T. Sri Sumantyo, and Hiroaki Kuze, "CP-SAR UAV development," *International Archives of The Photogrammetry, Remote Sensing And Spatial Information Science*, Vol. XXXVIII, Part 8, Kyoto Japan, 203-208, 2010.

SAR Imaging Technology using Reflected GNSS Signal

Yoshinori Mikawa[1], Takuji Ebinuma[1], Shinichi Nakasuka[1]
[1]*Department of Aeronautics and Astronautics, The University of Tokyo*
7-3-1 Hongo, Bunkyo-ku, Tokyo, 113-8656, Japan
mikawa@space.t.u-tokyo.ac.jp

Abstract

Global Navigation Satellite System (GNSS) is usually used for positioning and navigation application and reflected GNSS signal is called "multi-path" and considered as an undesirable noise. However, this reflected signal can be utilized for remote sensing applications because it might contain information about the scattering surface of the Earth. In this paper, the concept of remote sensing technology using reflected GNSS signal is introduced and a method to reconstruct imagery with the aperture synthesis technique is discussed.

Keywords : GNSS, Bi-static Radar, Aperture Synthesis

1. Introduction

Global Navigation Satellite System (GNSS) is one of the most successful space technologies and we can receive the signal of GNSS anytime and anywhere on the Earth which is not only achieved directly from GNSS satellites but also reflected and scattered by the Earth's surface. The GNSS Signal is usually utilized to identify the location and motion of the user for some navigation applications and on the other hand, the reflected signal is called *multi-path* which is considered as an undesirable noise source and deteriorates the accuracy of navigation. However, the reflected signal has a potential to be utilized for many kinds of remote sensing applications because meaningful information about the scattering surface can be obtained through this reflected signal.

The configuration of this concept is considered as bi-static but actually our configuration is called *the space-surface bi-static geometry* because a transmitter is usually non-cooperative one such as GPS satellite and is very far away from the Earth but on the other hand, a receiver platform would be an Unmanned Aerial Vehicle (UAV) which flies near the Earth's surface. This asymmetry in its geometry is the difference from normal bi-static configuration and would be the key to construct the imaging algorithm using GNSS signal. This space-surface bi-static configuration has several advantages against the conventional bi-static configurations and the biggest advantage is its high availability. We can receive the signal all the time wherever we are due to the GNSS constellation. In addition, GNSS is usually maintained to keep its navigation accuracy and we benefit from it in that we can utilize this high quality signal without preparing our own transmitter. This also makes the whole system simpler because all we have to develop is the devices for receiving.

This concept has several disadvantages and problems to be solved as well. Weak signal strength is on the top of the list and for example, the signal strength of GPS signal on the Earth's surface is about -160dBW and that of the scattered signal is even weaker. The development of the imaging algorithm for the aperture synthesis comes following and the conventional stop-and-go model is not suitable for the configuration where GNSS satellite is available as a non-cooperative transmitter because much longer stop-time is necessary due to the long propagation distance and the correlation process with the reference signal, which influences the azimuth sampling frequency and eventually the matched filter in the slow-time domain. This limitation on the azimuth sampling frequency might result in the azimuth ambiguity in the slow-time frequency domain. We discuss a method to simulate the space-surface bi-static configuration by considering actual signal spectrum and property of GPS CDMA signal in this paper.

2. Method

In general processing of SAR imagery, a geometry model called "stop-and-go" model is utilized to describe the echo signal. This model assumes that

geometry including SAR platform and target points is *stationary* between transmission and reception of signal because the speed of signal is much faster than that of SAR platform. However, this model is not suitable for SAR geometry using reflected GNSS signal because the signal propagation time is quite longer compared to conventional mono-static SAR geometry and it takes about 70 milliseconds in general. Such a long stop time would affect the sampling frequency in the slow time domain and eventually the bandwidth of sampled Doppler frequency would get quite narrower.

Fortunately, GNSS signal is not a pulse signal but a continuous signal and we can receive anytime once the receiving window is open. From here, we discuss using C/A code signal on L1 carrier of GPS. Due to this property of GPS signal, we don't have to wait for the echo signal using conventional stop-and-go model but all we have to do for reception is just to open window. The slow time sampling frequency depends on the signal correlation process and in this case, 1 millisecond is necessary for C/A code correlation. The problem which occurs when this modified geometry is utilized is definition of signal delay. The reason why the geometry *is assumed* to be stationary during waiting and receiving echo signals is to align the time corresponding to zero delay among slow time sample bins, that is:

$$t_d(t) = \frac{R_R(t) + R_T(t)}{c} \qquad \text{... (1)}$$

R_R: distance between receiving platform and target point

R_T: distance between transmitting platform and target point

in mono-static case, $R_T = R_R$

t: slow time sample bin

On the other hand, the modified delay is described using continuous signal as below:

$$t_d(t) = \frac{R_R(t) + R_T(t - t_d)}{c} \qquad \text{... (2)}$$

R_R: distance between receiving platform and target point

R_T: distance between transmitting platform and target point

t: slow time sample bin

The geometry is no longer stationary between transmission and reception of signal and (2) equation should be solved using iteration calculation. What

matters most from the point of view of SAR imaging process is how this delay *appears* in the imaging space which is described using slow time and fast time. This problem can be solved using the GPS time synchronization process. GPS signal is encoded with a kind of PRN (Pseudo Random Noise) code and this PRN code is utilized to determine the GPS time. In the case of C/A code, the whole timespan of code is accurately 1 millisecond and synchronized with GPS time to a precision of 1 millisecond. This property is very helpful for users to synchronize their clock to GPS time. Once the reference signal is selected appropriately, the delay appears in the imaging space with the ambiguity of 1 millisecond as follows:

$$t_d = N \times 1ms + Frac \qquad \text{... (3)}$$

N: ambiguity of 1 millisecond

1 millisecond corresponds to 300 kilometers and it would be enough for imaging because the range swath of imaging region might be less than 300 kilometers. On the other hand, the geometry is assumed to be stationary during this 1 millisecond in this modified model because the change of geometry during this 1 millisecond is not critical compared to the resolution of C/A code. Chip duration of C/A code is about 1 microsecond which corresponds to 300 meters but the change of geometry during 1 millisecond might be less than several meters. It is clear that this small difference does not affect the result of aperture synthesis.

The reflected signal of GPS signal is described as below:

$$s_r(t, \tau) = \sigma\sqrt{2P}x(t + \tau - t_d)cos(2\pi(f_c + f_d)(t + \tau - t_d))$$
$$\text{... (4)}$$

t: slow time sample bin

τ: fast time sample bin

t_d: delay which is defined from (2)

f_d: Doppler frequency

$x(t)$: C/A code function

Doppler shift due to the motion of GPS satellite works as constant bias in the frequency domain because the line of sight vector between GPS satellite and target point is assumed to be constant during aperture synthesis integration time and can be removed easily. Therefore, Doppler shift due to the motion of

receiving platform is only considered in the following discussion.

3. Simulation and Result

Simulation parameters are defined as follows:
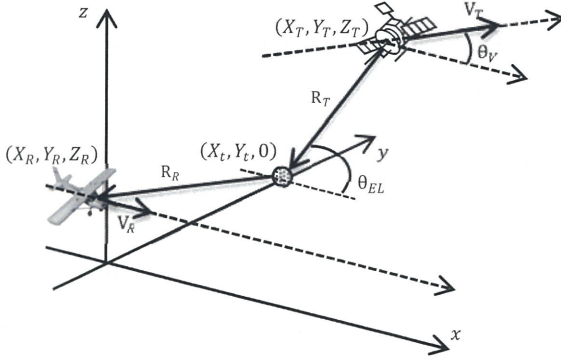

Fig. 1 Geometry in simulation

Table 1 Parameters in simulation

Parameter	Value	Note
Mean R_T	20,000 [km]	@ t = 0
θ_{EL}	30 [deg]	
θ_V	30 [deg]	
V_T	3000 [m/s]	
V_R	100 [m/s]	
Z_R	577 [m]	
X_t, Y_t	0, 1000.0 [m]	
θ_{beam}	0.1 [rad]	Beam width
$B_{C/A}$	2.0 [MHz]	Band width
f_c	1.5 [GHz]	Carrier Freq.

The range migration in this geometry is quite different from that of conventional mono-static geometry because the range between GPS satellite and target is assumed to a linear function.
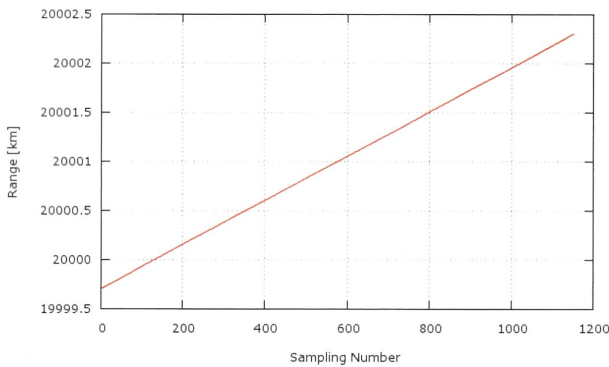

Fig. 2 Range Migration in simulation

The replica code derives from the signal which has no delay and no Doppler shift. After range compression using this reference signal, the range migration correction is processed. This interpolation process utilizes the delay history in the slow time domain and this delay history can be calculated using the position of GPS satellite and user's receiving platform. This means that the positioning should be established using direct signal of L1 during the aperture synthesis integration time. Azimuth compression process follows and finally the PSF (Point Spread Function) can be obtained in the imaging space.

As shown in the figure below, the PSF of target point is successfully obtained. In the fast time domain, we can see clear auto-correlation peak of C/A code and its width in range is 2 chips of C/A code. The resolution in the fast time domain is defined as 1 chip if the resolution is defined with Sparrow's criterion. Due to the auto-correlation property of C/A code, no other peak is seen in the fast time domain. Compared to the resolution in the slow time domain, the resolution in the fast time domain is rather worse because of the chip duration of C/A code which corresponds to 300 meters. This is to be improved using the signal which has wider bandwidth such as L5 signal of GPS or E5 signal of Galileo.
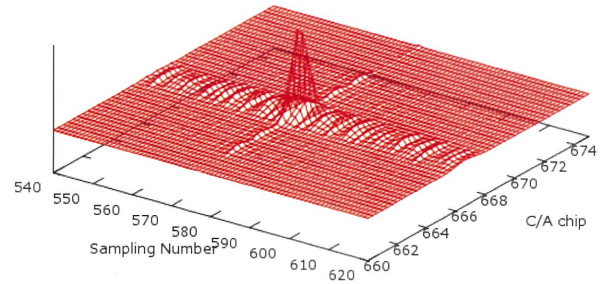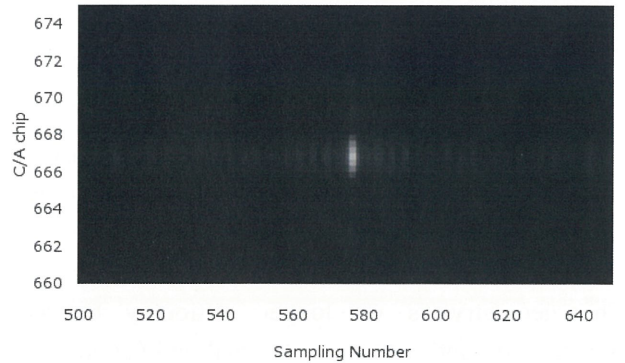

Fig. 3 Reconstructed PSF of target point

Fig. 4 Colormap: Reconstructed PSF of target point

4. Conclusion

We proposed the modified stop-and-go model which can be applied into the space-surface geometry. The PSF of target point was successfully reconstructed using this model and the signal property of C/A code of GPS signal.

5. Future Work

As mentioned before, the next step is to improve the range resolution using GPS L5 signal property whose bandwidth is ten times wider than that of L1 C/A code. Besides that, the aperture synthesis algorithm should be modified in order to process whole target region because all the target points have different range migration history in this space-surface geometry. The Doppler phase profile also should be examined in great detail to establish an imaging algorithm which can deal with many target points at once.

6. Acknowledgement

7. Reference

1) Mikhail Cherniakov et al.:Space-Surface Bistatic SAR Image Formation Algorithms, *IEEE Transactions on geoscience and remote sensing*, **47** (2009), pp.1827-1843.

2) Mikhail Cherniakov et al.: Signal detectability in SS-BSAR with GNSS non-cooperative transmitter, *IEEE Proceedings on Radar, Sonar and Navigation*, **152** (2005), pp.124-132

3) M. Usman el at.:Acquisition of Reflected GPS Signals for Remote Sensing Applications, *ICAST 2008, 2nd International Conference on Advances in Space Technologies*, (2008), pp.131-136

4) M. Usman et al.: A Remote Imaging System Based on Reflected GPS Signals, *2006 International Conference on Advances in Space Technologies*, (2006), pp. 173-178

5) Mehrdad Soumehkh et al.:Bistatic Synthetic Aperture Radar Inversion with Application in Dynamic Object Imaging, *ICASSP-91., 1991 International Conference on Acoustics, Speech, and Signal Processing*, **39** (1991), pp. 2577-2580

Assessment of scene changes in multi-sensor and multi-temporal fusion images of very high resolution satellite imagery

Yuhendra[1,2], Ilham Alimuddin[1], Joshapat Tetuko Sri Sumanyto[1], Hiroaki Kuze[1]

[1]*Center for Environmental Remote Sensing (CEReS), Chiba University, Japan*
[2]*Department of Informatics, Faculty of Engineering, Padang Institute of Technology, Indonesia*
E-mail: yuhendra@graduate.chiba-u.jp

Abstract

Image fusion and subsequent scene analysis are important for studying Earth surface conditions from remotely sensed imagery. The fusion of the same scene using satellite data taken with different sensors or acquisition times is known as multi-sensor or multi-temporal fusion, respectively. The purpose of this study is to investigate the effects of the multi-sensor, multi-temporal fusion process when a pan-sharpened scene is produced from low spatial resolution multispectral (MS) images and a high spatial resolution panchromatic (PAN) image. It is found that the component substitution (CS) fusion method provides better performance than the multi-resolution analysis (MRA) scheme. Quantitative analysis shows that the CS-based method gives a better result in terms of spatial quality (sharpness), whereas the MRA-based method yields better spectral quality, i.e., better color fidelity to the original MS images.

Keywords : Multi-sensor, Multi-temporal fusion, Component substitution, Multi-resolution analysis

1. Introduction

Following the rapid advance of new and greatly improved remote sensing (RS) sensor systems, various kinds of remote sensing data have been acquired and applied to a number of interdisciplinary Earth observation studies. The combination of low spatial resolution multispectral (MS) and high spatial resolution panchromatic (PAN) imaging sensors is usually used for change detection studies, each one having its own specific advantage (Chibani, 2007). Nowadays various operating sensors that can produce very high resolution (VHR) imagery (WorldView, QuicBird, GeoEye, and Orbview, etc.) are employed for purposes including image sharpening, land classification, change detection, and object identification (Zeng, 2010). In order to enhance the applicability of such image analysis based on remote sensing data, it is useful to consider image fusion of the same scene taken at different acquisition times with the same or different sensors.

Since multi-sensor, multi-temporal, multi-resolution and multi-parameter image data are available from operational Earth observation satellites, possibly a more complete view of observed objects can be obtained through the fusion technique (Zhu and Tateishi, 2006). Studies of fusing multiple images provided by heterogeneous image sensors have been proposed in many literatures with different methodologies, context and purposes (Yuhendra et.al., 2012). The objective of this study is to analyze and assess the scene changes given to multi-temporal images by comparing two different algorithms of multi-resolution analysis (MRA) and component substitution (CS).

2. Study area and satellite imagery

2.1 Study area

The study area for this work is located in the downtown of San Francisco, California, with geographical coordinates of 122°23'1.08"W and 37°42'38.81"N. As shown in Fig. 1, the scene includes significant stretches of the Pacific Ocean and San Francisco Bay within its boundaries (Figure 1).

2.2 Satellite images

For this work, two optical images acquired by QuickBird (QB) and WorldView-2 (WV) on 11 November 2007 and 9 October 2011, respectively, were used for investigating the performance of multi-sensor, multi-temporal fusion. The characteristics of both images are summarized in Table 1.
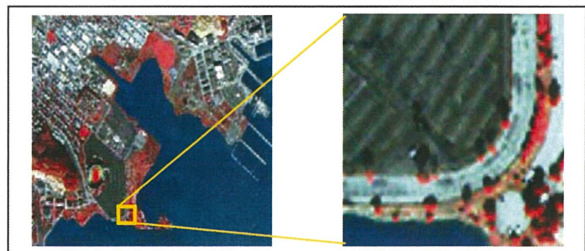

Fig. 1 Study area in downtown San Francisco, US.

2.3. Spectral response of sensors

Significant spectral distortion in the fusion product image can occur due mainly to the wavelength extension of the new satellite PAN sensors. Table 2 shows the wavelength range and spatial resolution of different PAN sensors. In image fusion techniques, it is important to properly include the sensor spectral response information (Otazu, et al., 2005).

3. Methods

3.1 Pre-processing

Since the images used in this study were from two different sensors, several pre-processing steps are needed. From the original WV and QB, a total of 56 and 4 bands color combinations are produced and analyzed using the optimum index factor (OIF). The highest value of average OIF has been obtained for the band combination 3-5-7 and 2-3-4, both for WV and QB. The pixel size of WV PAN (0.5 m) is greater than that for QB PAN (0.6 m). Thus, in order to minimize the spectral difference, WV MS, QB MS and QB PAN image are used, after being re-sampled at 0.5 m using cubic convolution. Then, image registration is implemented by means of the rational polynomial coefficient with nearest neighbor transformation for attaining a good registration with the root-mean-square (RMS) error of 0.75 pixel value for all the ground control points (GCPs).
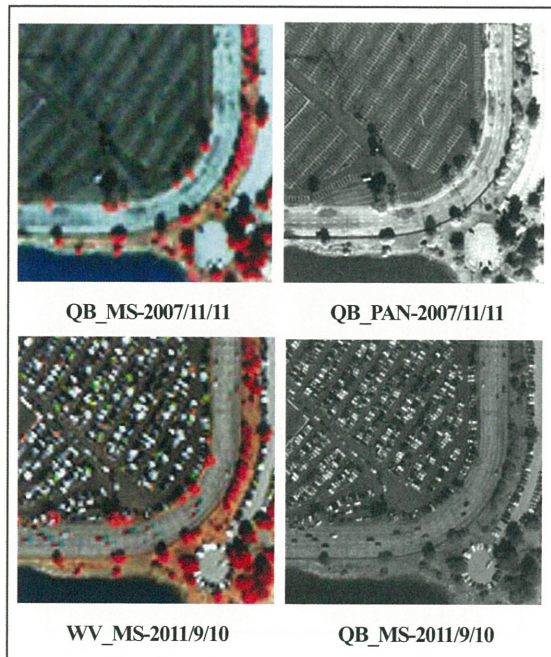

QB_MS-2007/11/11   **QB_PAN-2007/11/11**

WV_MS-2011/9/10   **QB_MS-2011/9/10**

Fig. 2 Multi-temporal optical images of QB and WV.

Table 1. Characteristics of VHR optical sensors.

Sensor	Band Name	Wavelength (μm)	Resolution (m)	Date Acquisition
QB	B1(Blue)	0.45-0.52	2.44-2.88	11 Nov. 2007 / 9 Oct. 2011
	B2(Green)	0.52-0.60		
	B3(Red)	0.63-0.69		
	B4(NIR)	0.76-0.90		
	PAN	0.45-0.90	61 -72 cm	
WV-2	B1(NIR1)	0.77-0.89	2.07	
	B2(Red)	0.63-0.69		
	B3(Green)	0.51-0.58		
	B4(Blue)	0.45-0.51		
	B5(R.Edge)	0.70-0.74	52 cm	
	B6(Yellow)	0.58-0.62		
	B7(Coastal)	0.40-0.45		
	B8(NIR2)	0.45-0.48		
	PAN	0.45-0.80		

Table 2. Spectral range of different PAN sensors.

Sensor	Wavelength range (μm) PAN	Spatial resolution (m)
GeoEye-1	0.45 – 0.80	0.5
QuickBird	0.45 – 0.90	0.7
Ikonos-2	0.45 – 0.90	1.0
WorldView-2	0.45 – 0.80	0.46
Spot 5	0.48 – 0.71	5
EO1(ALI)	0.48 – 0.69	10
ALOS	0.52 – 0.77	2.5

3.2 Pan-sharpening Techniques

Two main approaches of pan-sharpening, namely MRA and CS, are compared in the present analysis. Multi-resolution analysis (MRA) is an approach based on fast Fourier transform (FFT)-enhanced intensity-hue- saturation (IHS) transformation (Figure 3). Since this methods is capable of preserving the spectral characteristic, generally it is suitable for image analysis purposes (Ling, et.al, 2007; Ehler, et.al., 2010; Yuhendra, et.al, 2012). Another approach is the one based on component substitution (CS), a form of Gram-Schmidt transformation. The CS method performs fusion through MS transformation without any filtering operation of the PAN image. The re-sampled multispectral images are transformed from the RGB to IHS color space to obtain the intensity (I), hue (H), and saturation (S) components, and low-pass filtering (LPF) is applied to the intensity component. After high-pass filtering (HPF), the

PAN image is added to the low-pass filtered intensity component by means of inverse FFT (FFT^{-1}). Finally, inverse IHS transformation (IHS^{-1}) is performed on the IHS image to create the fused image.
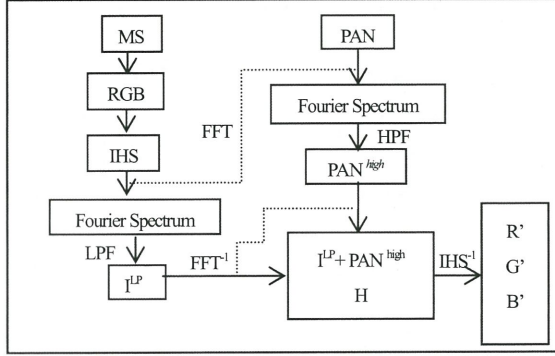

Fig. 3 MRA fusion using FFT-Enhanced IHS

3.3 Multi-temporal analysis

For analyzing information from multi-temporal observations, the following combinations are employed here: (1) both PAN and MS images of November 2007 (QB_PAN_MS), (2) PAN of November 2007 and MS of October 2011 (QB_PAN, WV_MS), (3) both PAN and MS images of October 2011 (WV_PAN_MS), and (4) PAN of October 2007 and MS of November 2011 (WV_PAN,QB_MS). For each of these choices, both MRA and CS pan-sharpening methods are applied.

In order to quantitatively evaluate scene changes from the resulting fusion images, comparison is made for the image quality in terms of quality indexes such as root mean square error (RMSE), relative average spectral error (RASE), and relative dimensionless global error in synthesis (ERGAS), These indexes have been given by (Deshmukh and Bhosale, 2010 ; Li *et al.*, 2010).

$$RMSE(B_i) = Bias^2(B_i) + STD^2(B_i) \qquad (1)$$

$$RASE = \frac{100}{M}\left[\frac{1}{n}\sum_{i=1}^{n} RMSE^2(B_i)\right]^{1/2} \qquad (2)$$

These formulae can be used for comparing errors obtained from different methods, different cases and different sensors (Wald, 2000). The ERGAS index is given as

$$ERGAS = 100\frac{dh}{dl}\left[\frac{1}{n}\sum_{i=1}^{n}\left(\frac{RMSE^2}{mean^2}\right)\right]^{1/2} \qquad (3)$$

where *dh/dl* is the ratio between the pixel sizes of the PAN and MS images (e.g., 1/4 for QB and WV data), and $\mu(i)$ is the mean of the *i* th band. Since ERGAS is a measure of distortion, its value must be as small as possible.

4. Results and discussion

Figure 4 shows the fused images obtained with the CS and MRA fusion methods for the four choices of band combinations. In visual (quantitative) analysis, it is seen that CS fusion yields relatively sharp images for both PAN and MS images of October 2011 (WV_PAN_MS) and PAN of October 2011 and MS of November 2007 (WV_PAN,QB_MS). Other results show somewhat blurred results due to temporal changes. For MRA fusion, the fusion of PAN and MS images of October 2011 (WV_PAN_MS) gives better spectral quality (i.e., fidelity of colors to original) than other three combinations, which show color distortion as compared with original MS images.

Table 3 and 4 summarize the values of RMSE, RASE, and ERGAS indexes based on the CS and MRA approaches. Smaller parameter values (ideally zero values) indicate better preservation of the original information. The resulting index values obviously depend on the MS images chosen as reference (see also Fig. 4). In the case of CS fusion, when the reference is the PAN of October 2011 and MS of November 2007 (WV_PAN, QB_MS), a better result is obtained as manifested in smaller values of RMSE, RASE and ERGAS.
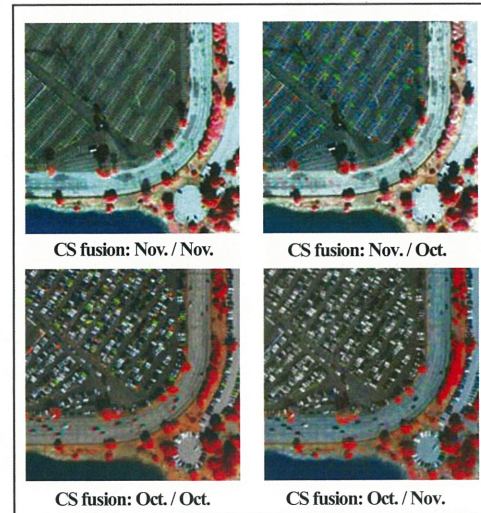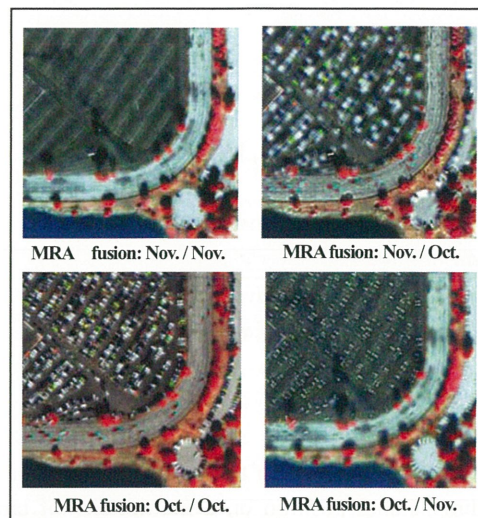
Fig. 4 Scene changes after image fusion.

Table 3. Quality index based on CS fusion.

Index	Scene changes temporal fusion			
	Nov./Nov.	Nov./Oct.	Oct./Oct.	Oct./Nov.
RMSE	1.81	7.61	1.65	**0.90**
RASE	4.46	5.10	1.22	**1.07**
ERGAS	1.91	4.72	0.29	**0.08**

Table 4. Quality index based on MRA fusion.

Index	Scene changes temporal fusion			
	Nov./Nov.	Nov./Oct.	Oct./Oct.	Oct./Nov.
RMSE	16.60	11.57	**9.84**	14.98
RASE	15.55	7.19	**6.28**	13.78
ERGAS	2.01	0.59	**0.52**	1.14

5. Conclusion and Future Research

We have investigated the multi-temporal fusion by multi-resolution analysis (MRA) and component substitution (CS) algorithms. In both quantitative and qualitative results, it has been found that the CS based method leads to better spatial quality (sharpness), whereas the MRA based method better spectral quality (fidelity to the original color). In the future research, the methodology presented in this paper can be extended to include the multi-temporal fusion of optical and synthetic aperture radar (SAR) images from satellite remote sensing.

Acknowledgements

References

1) Chibani, Y., 2007, Integration of panchromatic and SAR features into multispectral SPOT images using the 'a trous' wavelet decomposition. *Int. J. of Remote Sensing*, 28, 2295–2307.

2) Zeng, Y., Zhang, J., Van Genderen, J.L., Zhang, Y., 2010. Image fusion for land cover change detection, *Int. J. Image and Data Fusion*, 1(2), 193–215.

3) Zhu, L., Tateishi, R., 2006. Fusion of multi-sensor multi-temporal satellite data for land cover mapping, *Int. J. Remote Sensing*, 27(5), 903-918.

4) Yuhendra, Alimuddin, I., Josaphat Tetuko, S.S., Kuze, H., 2012. Assessment of pan-sharpening methods applied to image fusion of remotely sensed multi-band data, *Int. J. of Applied Earth Observation & Geoinformation*, in press.

5) Ehler, M., Klonus, S., Astrand, P.J., Rosso, P., 2010. Multi-sensor for pan-sharpening in remote sensing, *Int. J. Image and Data Fusion*, 1,1, 25-45.

6) Klonus, S., Manfred Ehlers (2007). Image Fusion Using the Ehlers Spectral Characteristics Preservation Algorithm GIScience & Remote Sensing, 44, 93-116.

7) Li, S., Li, Z., Gong, J., 2010. Multivariate statistical of measures for assessing the quality of image fusion., *International Journal of Image and Data Fusion*,1, 47-66.

8) Wald L., 2000. Quality of high resolution synthesized images: Is there a simple criterion?, In Proceedings of the third conference "Fusion of Earth data: merging point measurements, raster maps and remotely sensed images", Sophia Antipolis, France, January 26-28.

Development of 9.41 GHz Weather Radar

Adiya Sugar[1], Josaphat Tetuko Sri Sumantyo [2] Osa Kohei [3], Hiroaki Kuze [4]

[1]*Center for Environmental Remote Sensing (CEReS), Chiba University.*
1-33 Yayoi-cho, Inage-ku, Chiba-shi, Chiba 263-8522 Japan (Mongolia), sugar@graduate.chiba-u.jp
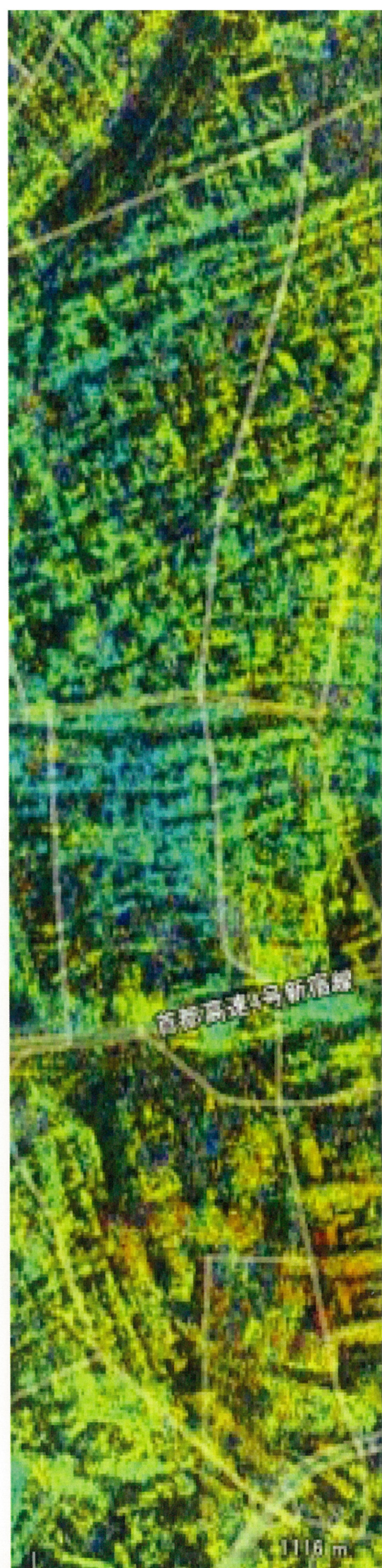[2]*Center for Environmental Remote Sensing (CEReS), Chiba University.*
1-33 Yayoi-cho, Inage-ku, Chiba-shi, Chiba 263-8522 Japan, jtetukoss@faculty.chiba-u.jp

Abstract

For this purpose, we are developing 3 dimensional weather radar (3D-WR), where this radar has capability to retrieve rain drop distribution and its characteristics in three-dimensional position on a multiplicity of targets (range, azimuth, and height). We plan to deploy this 3D radar in the near future and deliver the information for digital television weather forecasting service. The 3D-WR system consists of patch array antenna, transmitter and receiver sub system. We focus the effort in developing the patch array antenna subsystem. In the preliminary of this research, we are developing array patch antenna by using finite element method (FEM) to simulate the compact shape of antenna and its electricity characteristics (beam width, gain, input impedance etc).We develop the antenna by using Finite Element Method (FEM) (HFSS software) to simulate the radiation pattern, input impedance etc. Then the satisfied design is fabricate by using chemical etching technique. The 3D-WR works in X Band (9.41 GHz) with bandwidth 15 MHz, The antenna fabricated in array configuration with the targeted beamwidth horizontal and vertical in elevation and azimuth direction is around 6 degrees. We choose commonly available, commodity of the shelf Furuno marine radar as our model and modify it according to our design. We aim to be able to create new modified 3D weather radar and will install 1000 unit of this radar in around Japan in the future.

Keywords: 3 dimensional weather radar (3D-WR), subsystem, X Band (9.41 GHz), (FEM) (HFSS software)

首都高速4号新宿線

1116 m